

From Ice to Gas
Constraining the Desorption
Processes of Interstellar Ices

From Ice to Gas

Constraining the Desorption Processes of Interstellar Ices

Proefschrift

ter verkrijging van
de graad van Doctor aan de Universiteit Leiden,
op gezag van de Rector Magnificus prof. mr. C. J. J. M. Stolker,
volgens besluit van het College voor Promoties
te verdedigen op dinsdag 1 oktober 2013
klokke 13.45 uur

door

Edith Carine Fayolle

geboren te Clermont-Ferrand, France
in 1986

Promotiecommissie

Promotores: Prof. dr. H. V. J. Linnartz
Prof. dr. J.-H. Fillion (Université Pierre et Marie Curie, Paris, France)

Co-promotor: Dr. K. I. Öberg (Harvard University, Cambridge, USA)

Overige leden: Prof. dr. A. G. G. M. Tielens
Prof. dr. H. J. A. Rottgering
Prof. dr. J. T. Yates (University of Virginia, Charlottesville, USA)
Dr. E. Dartois (Université Paris-Sud, Orsay, France)

to all the people who inspire my dreams

**The study of the infinitely big begins with
the understanding of the infinitely small.**

Table of contents

	Page
Chapter 1. Introduction	1
1.1 Interest for molecules in space	1
1.2 Ices in the interstellar medium	2
1.2.1 The need for an ice - gas connection	2
1.2.2 The presence of ices	2
1.2.3 Ice evolution during star formation - ice sublimation affects the chemistry	5
1.2.4 Testing the ice to gas link	6
1.3 Ice sublimation in the laboratory	7
1.3.1 Thermal desorption of ices	8
1.3.2 Non-thermal desorption induced by UV photons	10
1.4 This Thesis	13
Chapter 2. Laboratory H₂O:CO₂ ice desorption data: entrapment dependencies and its parameterization with an extended three-phase model	17
2.1 Introduction	18
2.2 Desorption Model	20
2.2.1 Basic three-phase model	20
2.2.2 Extended three-phase model	22
2.3 Experiments	24
2.3.1 Experimental parameters	24
2.3.2 Experimental procedures	25
2.4 Experimental analysis	26
2.4.1 Complementarity of RAIRS and QMS	26
2.4.2 Desorption trends	28
Thickness dependency	28
Mixing ratio dependency	29
Molecular dependency	30
Heating rate dependency	30
2.4.3 Tertiary mixtures	31
2.4.4 Ice diffusion mechanisms: pore versus bulk diffusion	32
2.5 Model parametrization and performance	33
2.5.1 Parametrization	33
2.5.2 Model performance	34
Desorption trends modeling	34
Quantitative agreement	36
Predictive power	36
2.6 Astrophysical implications	37

2.7	Conclusions	39
Chapter 3. CO ice photodesorption: a wavelength-dependent study		41
3.1	Introduction	42
3.2	Experimental	43
3.3	Results	44
3.3.1	Absolute photodesorption yields for 1 eV spectral windows	44
3.3.2	CO photodesorption yield spectrum	45
3.4	Discussion	46
3.4.1	Mechanism	46
3.4.2	Astrophysical implications	47
3.5	Conclusions	48
Chapter 4. UV photodesorption of interstellar CO ice analogues: from sub-surface excitation to surface desorption		51
4.1	Introduction	52
4.2	Methods	53
4.3	Results and discussion	54
4.3.1	Pure CO ice desorption - an exclusive DIET process	54
4.3.2	Subsurface excitation	55
4.3.3	Photodesorption of solid CO on top of H ₂ O ice	58
4.4	Conclusions	61
Chapter 5. Wavelength-dependent UV-photodesorption of pure N₂ and O₂ ices		63
5.1	Introduction	64
5.2	Method	65
5.2.1	Experiments	65
5.2.2	Data analysis	66
5.3	Results	67
5.3.1	Nitrogen photodesorption	67
5.3.2	Oxygen photodesorption	70
5.4	Discussion	73
5.4.1	Photodesorption mechanisms for pure ices	73
5.4.2	Astrophysical consequences	75
5.5	Conclusions	76
Chapter 6. Indirect UV photodesorption from CO:N₂ binary ices - an efficient grain-gas process -		77
6.1	Introduction	78
6.2	Experimental methods	79
6.3	Results	82
6.3.1	Photodesorption from mixed CO:N ₂ ice	82
6.3.2	Photodesorption from layered N ₂ /CO and CO/N ₂ ices	83
6.4	Discussion and astrophysical implications	84
6.4.1	Role of ice structure and composition on absolute photodesorption rates	84

6.4.2	Implications for N ₂ and CO gas phase abundance in dense cores	87
6.4.3	Organics desorption through CO photoexcitation?	88
6.5	Summary and conclusions	88
Chapter 7. Linking the ice content and gas abundances of organic molecules in massive young stellar objects		91
7.1	Introduction	92
7.2	Observations and Analysis	94
7.2.1	Observations	94
7.2.2	Spectral extraction and rms	95
7.3	Results	96
7.3.1	Line identification and characterization	96
7.3.2	Spatial origin of the line emission	101
7.3.3	Rotational temperature, and column densities	101
7.3.4	Organics in hot core vs weak-line MYSOs	107
7.3.5	An ice-gas connection?	108
7.4	Discussion	110
7.4.1	Weak line MYSOs versus hot cores	110
7.4.2	The ice-gas connection: Observations vs. Theory	112
7.5	Conclusions	115
Bibliography		117
Nederlandse samenvatting		127
English summary		133
Résumé en français		139
Curriculum vitae		145
Publication list		147
Acknowledgments		149

Introduction

Molecules are found throughout the universe.

The discovery of molecules in space opened up a window to the chemical complexity of the interstellar medium, enabling us to explore the embedded phases of star and planet formation as well as address the origins of life on Earth and maybe elsewhere in the universe. Indeed, since life as we understand it is molecular in nature, finding organic molecules in space and more specifically in regions where stars and planets form, prompts questions about the development of life elsewhere. The molecular inventory in the interstellar medium, the processes leading to molecule formation, stability and delivery to planetary bodies are thus key questions that astrochemists are answering through a combination of observations, simulations, and laboratory experiments. The presence of icy mantles on interstellar dust grains play a key role in the formation and observation of molecules at every stage of the star-formation process. It is the ice evolution through processes encountered in space and their link with the presence of observed organic species in the gas phase that this thesis addresses.

1.1 Interest for molecules in space

A great diversity of chemical species can be found in the interstellar and circumstellar media, going from atoms, simple diatomic molecules, to large carbon edifices like fullerenes, radicals and ions¹. The first evidence for the presence of molecular species in space were unidentified optical-UV interstellar lines that had no corresponding atomic signature (Merrill 1934). These lines have later been identified as electronic transitions of the CH and CN radicals (Swings & Rosenfeld 1937; McKellar 1940). Since then, more than 200 molecular species, including isotopologues, have been detected in outer space through their rotational, vibrational and/or electronic transitions. Their identification through their emission and/or absorption features are used by astrochemists to probe the physics of the environment in which they are found. Temperature, density, kinematics and energetic fields all have an impact on the molecular energy levels population and their line shape, making these molecular species useful tracers of conditions encountered in star-forming environments.

Chemicals are used to trace the physics but they also contribute to the physical processes. Molecules are efficient coolants in the interstellar medium that are necessary to

1. See http://en.wikipedia.org/wiki/List_of_interstellar_and_circumstellar_molecules for a complete list and references.

form stars as we know them. During the gravitational collapse of dense clouds inducing the formation of a protostar, the gas pressure increases and the gas temperature should rise due to the frequent collisions of atoms and molecules. The heating of the collapsing cloud poses a dilemma: since the heated gas wants to expand, the cloud collapse could be stopped or even reversed. Molecules found in the cloud gas play thus a significant role as they can effectively transport energy outside of the cloud through collisional excitation followed by radiative de-excitation, producing photons that can escape. The photons carry this energy away thus allowing the cloud to collapse. Dominant molecular coolants include CO, O₂, H₂O (e.g. Goldsmith & Langer 1978; Neufeld et al. 1995; Goldsmith 2001).

From an astrobiological point of view, the discovery of molecules in space, and especially the complex ones has changed society's view on the origins of life, seeding the idea in people's mind that life on earth may have emerged from interstellar molecules and that our solar system might not be the only planetary system harboring a rich chemistry in the universe. Molecules are observed at every stages of star formation and complex ones are expected to be present in disks where planets and comet form. It is thus likely that they are incorporated into planetary bodies during their formation (Ciesla & Sandford 2012). Studying the chemical processes in star-forming environments and understanding the origin of molecular complexity would thus provide clues on the ordinary nature of our life-hospitable solar system.

1.2 Ices in the interstellar medium

1.2.1 The need for an ice - gas connection

Organic molecules are often associated with hot-core/corinos regions observed around high and low-mass protostars, respectively. Molecules like CH₃OH, CH₃CN, CH₃OCH₃, CH₃CHO, H₂CO, HCOOH, CH₃CH₂OH, or CH₃CH₂CN are typically observed through their rotational emission in these regions where densities are higher than 10⁷ cm⁻³ and temperatures above 100 K (e.g. Blake et al. 1987; Cazaux et al. 2003; Fuente et al. 2005). If ion-neutral reactions can explain the presence of molecules like CO, CS and small hydrocarbon chains in the interstellar medium (Herbst 1997), the high abundance of complex species in core regions around young stellar objects at relatively early stage of their formation requires other explanations since reactions rates are too low (Horn et al. 2004; Geppert et al. 2006). In addition, a fraction of these species are deuterated at levels that defy explanations by gas phase reactions alone (e.g. Ceccarelli et al. 2001; Parise et al. 2006). Ice-covered dust grains found in star-forming environments, do allow us to successfully explain these observations however, since they can act as catalyst for surface reactions.

1.2.2 The presence of ices

Submicron-sized dust grains are widely found in the interstellar medium and present distinguishable absorption features in the infrared and emission features in the submillimeter. They are composed of carbon, silicates, PAHs (e.g. Draine 2003) and are the remnants of stellar death. In the dense clouds where young stars form, they

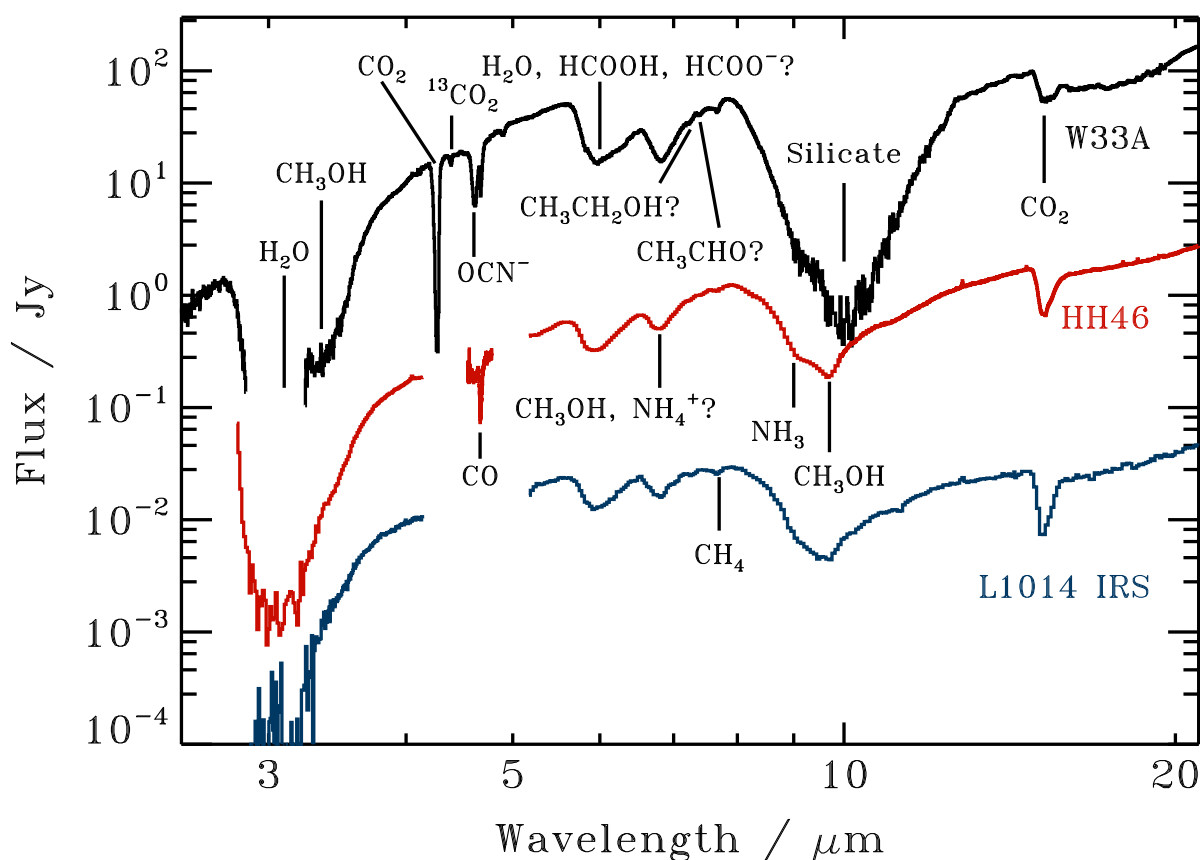


Figure 1.1: Infrared Space Observatory (ISO) spectrum acquired by the Short Wavelength Spectrometer (SWS) of the star forming region W33A, HH46, and L1014 IRS, covering the 2.5 to 20 microns region. A variety of ice mantle and refractory grain core features are evident.

account for 1% of the cloud composition ; the rest of the matter consists of gas, mainly H_2 . It is on the surface of these dust grains that most molecules will form or freeze-out in the cold regions of molecular clouds.

The hypothesis of the dust grains catalyzing molecule formation has been proposed very early on by van de Hulst (1949), who suggested that the molecular abundances should be directly related to the elemental abundances. Even though the gas grain interplay induces a more complex chemical inventory, the contribution of molecule formation mediated by the grains has been confirmed and adopted with the observation of condensed molecules along the lines of sight towards protostellar environments. The first observational evidence was the detections of solid H_2O , identified through its O-H stretching vibration at 3.08 microns (Gillett & Forrest 1973; Merrill et al. 1976). During the following decades, careful observations of ice features have been successful in identifying NH_3 , CO , OCN^- , CH_4 , CH_3OH among others as well as the presence of mixed components hinting for parent-daughter molecular relations or similar formation mechanisms. The atmospheric lines, however, prevented comprehensive surveys for ice from ground-based facilities. Breakthroughs on the relative ice mantles compo-

Table 1.1. Abundance medians^a and lower and upper quartile values of ices and individual ice components with respect to H₂O ice (Öberg et al. 2011a).

Ice Feature	Low Mass	High Mass	Background
H ₂ O	100	100	100
CO	38 ₂₀ ⁶¹ (29)	13 ₇ ¹⁹	31
CO ₂	29 ₂₂ ³⁵	13 ₁₂ ²²	38 ₃₂ ⁴¹
CH ₃ OH	7 ₅ ¹² (3)	8 ₈ ¹⁶ (4)	8 ₇ ¹⁰ (4)
NH ₃	5 ₄ ⁶	16 ₁₀ ¹⁷ (5)	...
CH ₄	5 ₄ ⁷	4 ₂ ⁴ (2)	...
XCN	0.6 ₀ ^{0.8} .2 (0.3)	0.8 _{0.4} ^{1.4} (0.6)	...
Pure CO	21 ₇ ³⁶	3 ₂ ⁶	...
CO:H ₂ O	13 ₇ ¹⁹	10 ₅ ¹²	...
CO:CO ₂	2 ₁ ³	1.3 _{0.4} ^{1.6} (0.3)	...
Pure CO ₂	2 _{0.3} ⁴	2 ₁ ²	...
CO ₂ :H ₂ O	20 ₁₅ ²³	9 ₆ ¹⁵	24
CO ₂ :CO	5 ₄ ⁷	5 ₂ ⁶	6
CO ₂ shoulder	0.8 _{0.4} ^{1.1}	1 ₁ ²	...
OCN ⁻	0.4 _{0.3} ^{0.4} (0.2)	0.6 _{0.4} ^{1.4}	...

Note. — ^a Values in parentheses include upper limits in the median calculation using survival analysis.

sitions have been obtained with the space-based Infrared Space Observatory (ISO) and its Short-Wavelength Spectrometer (SWS) instrument, allowing for spectral acquisition in the entire 2.5 - 45 microns window where vibrations of condensed molecules are intense. This survey investigated in a comprehensive way the ice abundances found along the lines of sight of intermediate to high-mass protostars (Dartois 2005, Gibb et al. 2004, and references therein). Examples of ice spectra are shown in figure 1.1 for three different interstellar regions. The ice composition is derived by subtracting the emission background due to the emitting YSO (or background star) and fitting the ice features with laboratory spectra for which the associated band strength is thus known (available for example in the Leiden data base for ice²). A follow-up ice composition survey around low-mass protostars environments and in pre-stellar cores have been realized using the Spitzer space telescope and its InfraRed Spectrometer (IRS) 5 - 30 microns (Boogert et al. 2008; Pontoppidan et al. 2008; Öberg et al. 2008; Bottinelli et al. 2010; Öberg et al. 2011a).

The typical ice compositions along the line of sight derived from all of the available ice surveys and for the various environments are presented in table 1.1 (Öberg et al. 2011a). H₂O, CO, and CO₂ are the main ice components along the line of sight of most objects. The other ice components generally found are NH₃, CH₄, CH₃OH and XCN. Interstellar ices are far from simple since some of the molecules are found in pure

2. <http://www.strw.leidenuniv.nl/lab/databases/databases%202007.htm>

phase, in water-dominated (polar) and/or in water-poor (apolar) ice phases. Moreover some of the absorption features cannot be unambiguously attributed to a single species due to the intrinsic broadness of vibrational features in the solid phase and because of the overlap in vibrational frequencies of molecules presenting similar chemical functions. Comparing the ice composition variation and abundances between star-formation stages and low- and high-mass protostellar environments provided information on the formation of the ice components and processes accompanying the ice evolution across star-formation. These findings are developed in the following subsection.

1.2.3 Ice evolution during star formation - ice sublimation affects the chemistry

A cartoon depicting the current understanding of ice evolution during star formation is presented in Fig. 1.2. At the prestellar stage, before the star is formed, molecules like H_2O , CH_4 , NH_3 form at the surface of the grain through atomic and small molecule collision and diffusion on the grains. The formation of CO_2 together with H_2O at the prestellar stage is consistent with CO_2 observed mainly in a polar environment (Knez et al. 2005). When the cloud gravitationally collapses to form the star, the temperature decreases and molecules that were initially in the gas phase freeze-out on top on the H_2O -rich layer. Since the main species to deplete at this stage is CO , an apolar layer will form on top of the already present polar ice mantle (Pontoppidan et al. 2003). At this early stage the dominant chemical reaction occurring on ices is hydrogenation since the regions are cold and deeply-embedded in the dark cloud, preventing efficient UV penetration. The hydrogenation of the CO -rich ice top layers will result in the formation of more complex species like H_2CO and CH_3OH (e.g. Tielens & Hagen 1982; Watanabe & Kouchi 2002). The observed amount of CH_3OH is in good agreement with model predictions based on CO hydrogenation schemes (Pontoppidan et al. 2003; Cuppen et al. 2011).

At the protostellar stage, the newly formed star will grow from the collapse of its envelope, inducing changes in the ice composition. The heat induced by the star will lead to thermal reactions mainly activated by diffusion within the solid. Moreover the UV radiation resulting from the interaction of cosmic rays with H_2 gas will induce in the ice a very rich chemistry since the radicals created will diffuse and react to form more complex species (Garrod & Herbst 2006; Garrod et al. 2008). In addition to the chemical changes, the icy grains will undergo sublimation induced by the protostar heating and energetic particles, which will affect the chemistry occurring on both the grains and in the gas phase. In warm regions close to the protostar where $T > 100$ K, most of the ice material on the grains sublimates into the gas phase, leading to a rich gas phase chemistry activated by the higher temperatures and densities (e.g. Charnley et al. 1992).

Some of the grains may not reach the 100 K sublimation zone but instead, follow a trajectory where they are incorporated into a disk forming around the protostar (Visser et al. 2009). In this disk, the temperatures encountered are such that ices can survive in the middle plane. The icy material will be processed by the UV and X-ray photons coming from the central object, as well as by possible vertical mixing, resulting

in ice sublimation, freeze-out cycles, and inducing a complex ice structure and composition that is yet to be understood. The dust grains in the disk coagulate to form planetesimals and some of the ice material may end up in the planets, satellites, and comets of mature planetary systems (Okuzumi et al. 2012). Understanding the evolution of the icy mantle composition and in particular the presence of complex molecules would provide valuable insights into the incorporation of prebiotic molecules during the planet and comet formation process.

1.2.4 Testing the ice to gas link

Molecules observed in the gas phase in star-forming environments are tightly linked to the physical and chemical processes occurring in the solid state. According to Herbst & van Dishoeck (2009), the formation of organics species of 6 or more atoms, so called complex organics, could either result from 1) reactions on grains through atomic bombardment during the prestellar stage and early protostellar stage (0th generations of organics), 2) energetic processing and / or heat-activated chemistry creating a the 1st generation of organics, 3) sublimation of the precursor from the ice and formation of 2nd generation of organics in the warm and dense gas-phase through neutral-neutral or ion-neutral reactions (see Fig. 1.2). In all cases, the ice composition should be linked to the observed organics in the gas phase, provided that other factors such as UV-fields are not drastically influencing the organic chemistry in the gas-phase. The presence of an ice - gas link could validate the organic formation scenario presented above but is yet to be confirmed. The small number of sources having both ice observations and gas-phase observation prevented until now the search for correlations between gas-phase organics and parent species in the ice. Chapter 7 presents new insights on how to extend this number of sources and provides tentative ice-gas correlations.

Since part of the ice organic content will end-up in planet forming regions, it is important to understand the details of this organic chemistry and particularly where the different species are formed and how. It is, however, very difficult to observe organics in the solid state due to confusion between their broad vibrational features ; the features cannot thus be unambiguously attributed to a single species. Instead, one must rely on gas phase observations where lines are quite distinct. Spatially resolved observations together with a careful analysis of the molecule excitation conditions can provide good constraints on the classification of organics into 0th, 1st, and 2nd generation as the first two will be found in the cold gas phase due to possible non-thermal desorption and the 2nd generation will only be present in the warm gas phase close to the protostar (see Fig. 1.2).

Observational constraints on the spatial location of organics and excitation conditions can be used to test chemical models predicting abundances and evolution in the ice and gas phase. Such detailed gas-grain models, require, however a good understanding of the molecular physics in the ISM. If data on gas-phase processes are mostly available, processes occurring on the grains are difficult to include in models since reaction rates, diffusion, sublimation mechanisms and efficiencies are yet to be fully constrained. It is the main goal of this thesis to investigate gas-grain processes in order to support astrochemical models.

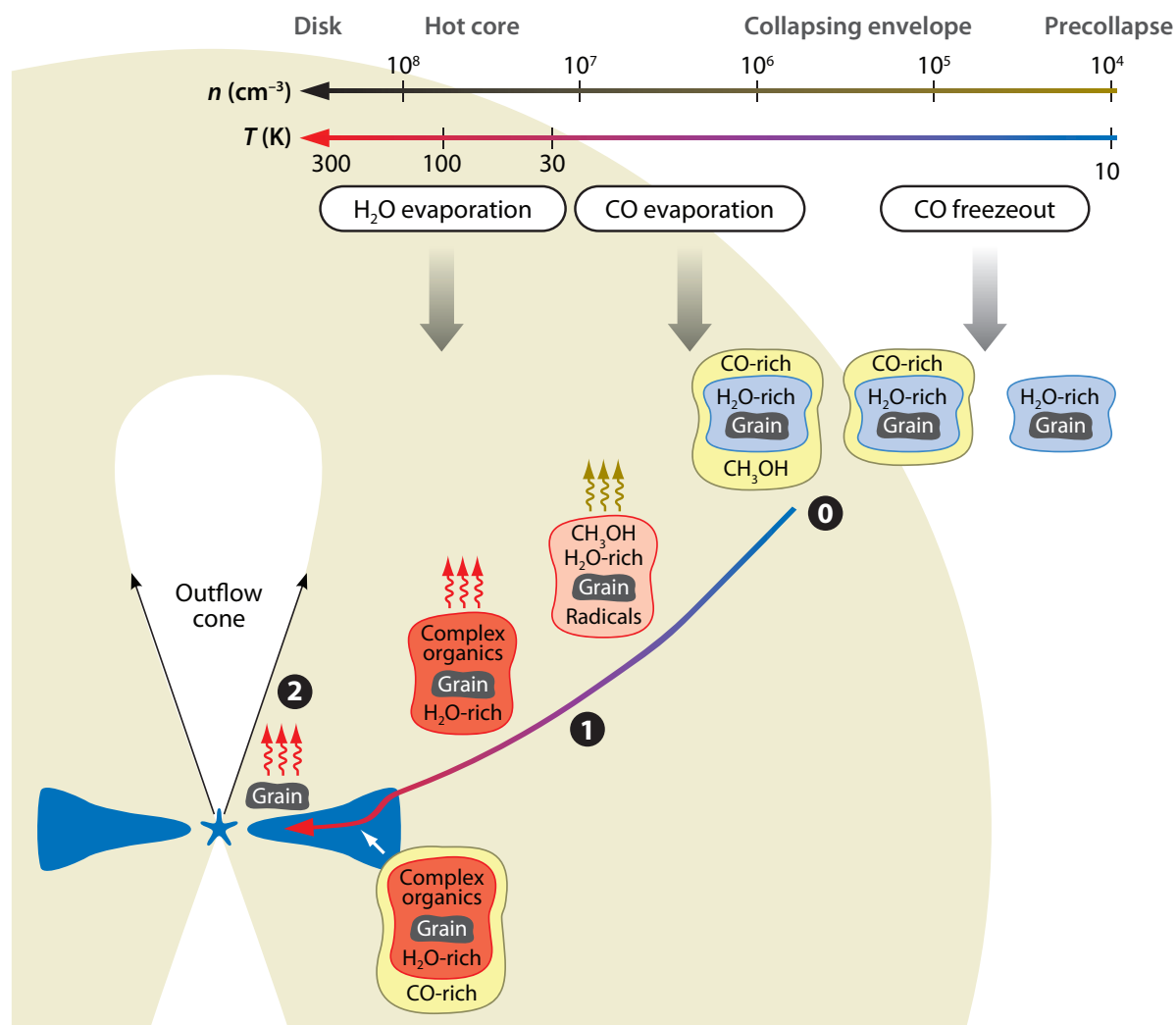


Figure 1.2: Cartoon representation of the ice evolution from the prestellar stage, through the collapsing envelope, and into a protoplanetary disk. The prestellar stage will see the formation of the first H₂O-dominated ice mantle, followed by gas-phase freeze-out during cloud collapse, forming a CO-rich mantle. The icy-grains will undergo hydrogenation, heat and UV activated reactions in the protostellar phase while flowing towards the star. Most of the icy mantle will sublimate when grains reach the 100 K region, giving rise to an active hot-core chemistry. Alternatively some of the icy grains will flow in the mid-plane of protoplanetary disks where planets and comets are formed, and the grains will be incorporated into their composition. Stages where 0th, 1st, and 2nd generation of organic molecules form are indicated. Credit E. van Dishoeck and R. Visser.

1.3 Ice sublimation in the laboratory

Ice sublimation plays an important role in the chemical evolution of star forming regions as it regulates the amount of species able to participate in the chemistry on the

grains or in the gas phase. The state in which molecules are found also provides valuable information from a physical point of view as it depends on the density, temperature, radiation conditions of the medium. Different kinds of sublimation can be distinguished: thermally-induced, photon-induced, electron-induced, high-energy particle induced (sputtering) and chemically-induced. If all of these mechanisms can trigger ice desorption to a certain extent, some of them will dominate in different regions of the ISM. The thermally-induced and UV-photon induced desorption are developed in this thesis.

1.3.1 Thermal desorption of ices

Thermal desorption of ices is the sublimation process that dominates the gas-grain interactions during the protostellar stage where the envelope collapses onto the newly formed star. The icy grains flow towards the young star and the ice mantles are warmed up. This will induce thermal desorption of the ice into the gas phase according to the binding energy of the desorbing molecules onto the surface. The thermal desorption process depends highly on intermolecular interactions and on the kinds of desorbing sites. Thus one molecular component in mixed interstellar ice is very unlikely to desorb at only one single temperature. It is not straightforward to model the desorption process in astrochemical simulations since ice parameters such as molecular composition, ice thickness, internal arrangement, must be taken into account in addition to the physical parameters of the warm-up.

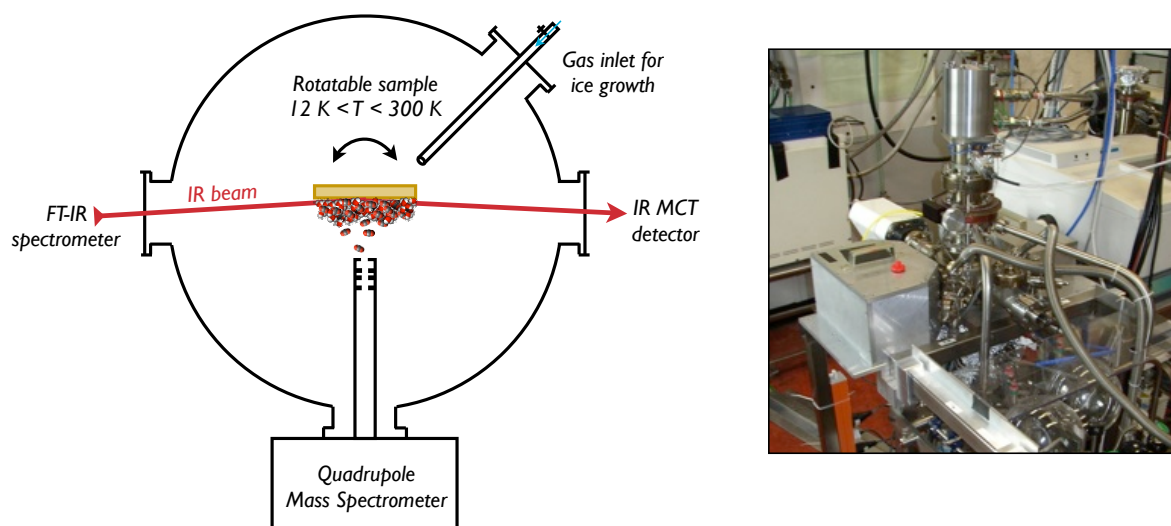


Figure 1.3: The CRYOPAD experiment from the Sackler Laboratory for Astrophysics used to perform the thermally-induced desorption experiments presented here.

Fortunately laboratory experiments based on surface science techniques can provide insights on thermal desorption mechanisms that icy grain undergo. Most of the experiments performed in this respect are done by means of Ultra-High vacuum experiments, like the set-up CRYOPAD (CRYOgenic Photoproducts Analysis Device) devel-

oped by Fleur van Broekhuizen in the Sackler Laboratory for Astrophysics in Leiden (See figure 1.3). In this low pressure environment ($\sim 10^{-10}$ mbar, $\sim 10^7$ particles per cm^{-3}), a gold sample cryogenically cooled can reach temperatures as low as ~ 12 K. Molecular ices can be grown with monolayer precision onto the sample by injecting pure or pre-mixed gas into the chamber through a capillary tube perpendicular to the sample. A heater can regulate the temperature and warm-up the sample. For the study of ice desorption, the Temperature Programmed Desorption (TPD) technique is used and consists of linearly warming-up the ice sample. The rates employed here fall between 0.5 and 5 K min^{-1} but TPD rates vary from groups to groups according to the literature. The molecules desorbing from the ice into the gas phase can be detected in CRYOPAD by Quadrupole Mass Spectrometry (QMS, model Balzers QMA 200) and Reflection Absorption InfraRed Spectroscopy (RAIRS) using a Fourier transform infrared (FTIR) spectrometer over the $4000 - 900 \text{ cm}^{-1}$ region. The infrared set-up is also used to quantify the ice thickness and ice loss during warm-up. Following the desorbing molecules from the ice (or the ice loss) with respect to the temperature provides insights on their binding energies and desorption mechanisms. These information are further incorporated into kinetic models that can be run under astrophysical warm-up time-scales, in the order of few Kelvin per century.

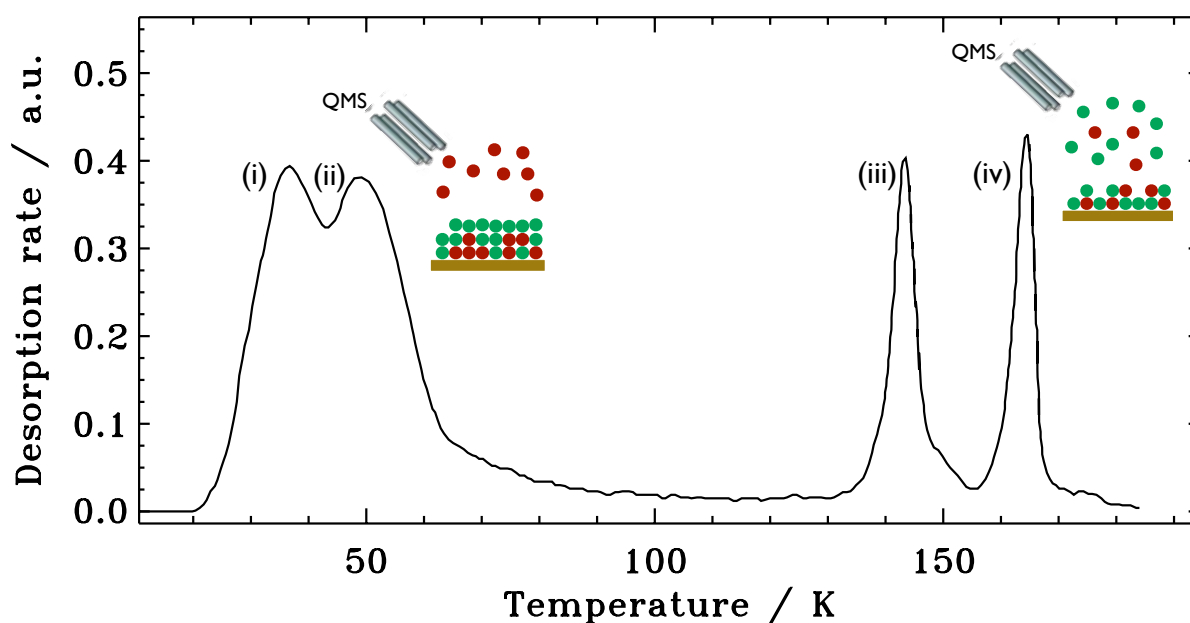


Figure 1.4: Desorption of CO from water-rich ice monitored by mass spectrometry. The four CO desorption peaks originate from (i) desorption from CO rich surface, (ii) H_2O rich surface, (iii) desorption during H_2O phase change, (iv) co-desorption with H_2O . The cartoons show the QMS detection of CO at low temperature and CO trapped with water. CO is depicted as the red species and H_2O as the red species.

Since the main component of interstellar ices is water, the thermal desorption study of molecules mixed in a water matrix is very relevant for protostellar environments

(Viti & Williams 1999). Collings, Brown, Barnun, Kimmel, among others, studied the desorption characteristics of such systems through TPD (Burke & Brown 2010). In the case of volatiles species like CO mixed with water (see for example TPD profile in 1.4), desorption of CO molecules mixed in a water matrix can occur from (i) CO surface, due to possible diffusion and segregation of volatile component to the top of the ice, (ii) from mixed CO-H₂O surface, (iii) volcano desorption during H₂O ice phase change from amorphous to crystalline, and (iv) co-desorption with H₂O. The first two release mechanisms occur around the desorption temperature of pure CO ice (starting around 30 K) while the last two occur in temperature regions where H₂O desorbs. There is thus a clear difference between the volatile material that desorbs at low temperature and the rest that stays trapped within the water ice until its desorption. This last "trapped" fraction of molecules will stay longer on the grains and can participate in surface chemical schemes while the species released at lower temperature are available for gas phase reactions (Viti et al. 2004). Quantifying and predicting the amount of volatile material that stays trapped within the water ice under astrophysical condition is thus a crucial for a good estimation of the protostellar chemical evolution and will be addressed in the chapter 2 of this thesis through laboratory experiments and modeling.

1.3.2 Non-thermal desorption induced by UV photons

In interstellar regions where the temperature is low but UV photons are present, sublimation of molecules can occur through non-thermal processes driven by UV-photons. This non-thermal desorption process can be responsible for the presence of cold gas in environments where molecules should be frozen out onto dust grains. Thus it regulates the ice-gas balance (Hollenbach et al. 2008). In particular, Willacy & Langer (2000); Dominik et al. (2005); Oka et al. (2012) among others showed that this mechanism was necessary to explain H₂O observation in protoplanetary disks. The photon distribution in star-forming environments (See Fig. 1.5) has different origins: 1) photons from the InterStellar Radiation Field (ISRF) generated by surrounding stars can penetrate the first layers of molecular clouds depending on their density (Mathis et al. 1983), 2) in inner regions shielded from the ISRF, it is the interaction of cosmic rays with H₂ that generates a local UV field composed of the Lyman and Werner photon series (e.g. Gredel et al. 1987), 3) when the protostar turns on, it will also emit UV photons that may reach the ice and 4) in protoplanetary disks, the accretion of material onto the protostar will generate a UV field dominated by Lyman- α and other characteristic emission lines (Bergin et al. 2003). These typical profiles will be altered through gas absorption and dust scattering as the photons travel to the ice regions and radiative transfer codes are necessary to predict the exact UV profiles inducing photodesorption (Guzmán et al. 2011; Fogel et al. 2011).

The photodesorption process has been studied in the laboratory and efficiencies for the main ice components have been quantified. The first detailed study that provided photodesorption rates for the interstellar medium was published by Westley et al (1995a,b) on pure H₂O ice. They found a strong dependence to the ice temperature, thickness and photon dose. To derive a photodesorption rate, they used an

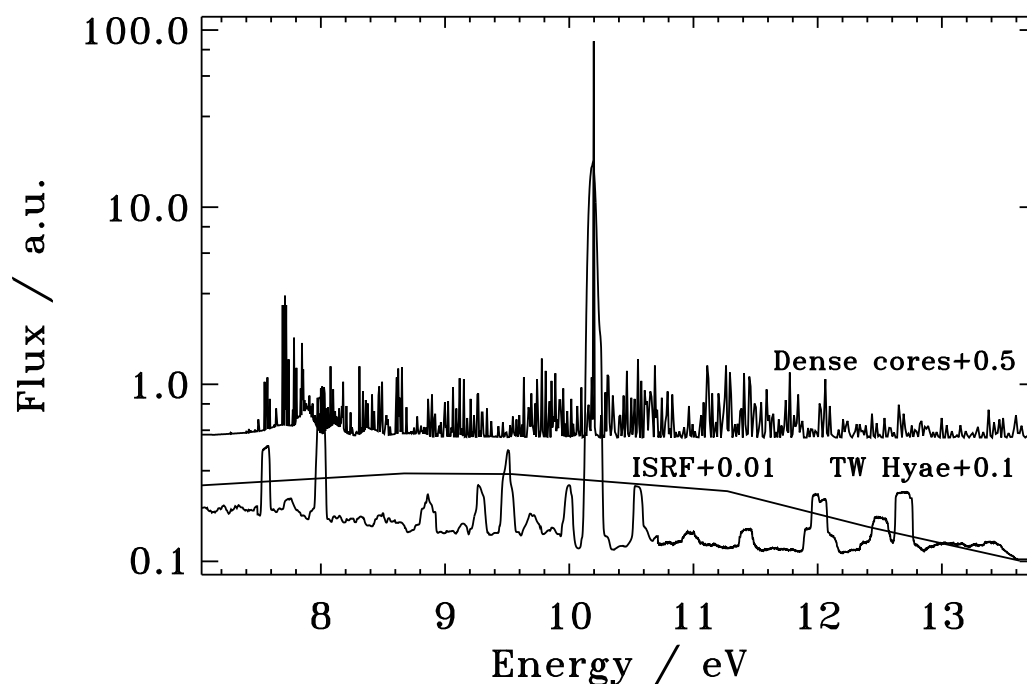


Figure 1.5: Characteristic UV fields encountered in the ISM. The dense cores spectrum is derived by Gredel et al (1987), the ISRF by Mathis et al (1983) and the protoplanetary disk TW Hydrae by Herczeg et al (2002), Valenti et al (2003) and Johns Krull & Herczeg (2007). The integrated area of each spectrum is normalized to 1 and offsets are used for clarity.

H_2 discharge lamp as the UV source, emitting mainly at Lyman alpha and a quartz microbalance to follow the ice loss. Their derived photodesorption rates are in the 10^{-3} molecules desorbed per incoming photons range, assuming that H_2O is the main species desorbing from the ice. Following studies on $\text{H}_2\text{O}/\text{D}_2\text{O}$ (Watanabe et al. 2000, Yabushita et al. 2009, Öberg et al. 2009b), CO (Öberg et al. 2007, 2009, Muñoz Caro et al. 2010), N_2 (Öberg et al. 2009), CO_2 (Öberg et al. 2009, Baragiola et al. 2012, Yuan & Yates 2013) confirmed the high photodesorption rates and investigated the various dependencies to the experimental parameters and the impact of photochemistry. Molecular dynamics simulations have also contributed to the microscopic understanding of the photodesorption process (Andersson et al. 2005, 2006, 2008, Arasa et al. 2010, 2011). For the case of CO ice, both Öberg et al. (2007, 2009) and Muñoz Caro et al. (2010) derived efficiencies that are temperature dependent but thickness and dose independent, hinting for a surface mechanism. For the absolute photodesorption values, the first study derived a rate in the 10^{-3} molecules photon^{-1} range while the other derived a higher efficiency in the 10^{-2} molecules photon^{-1} . These values are still under debate but the discrepancy could be due to different UV irradiation profiles.

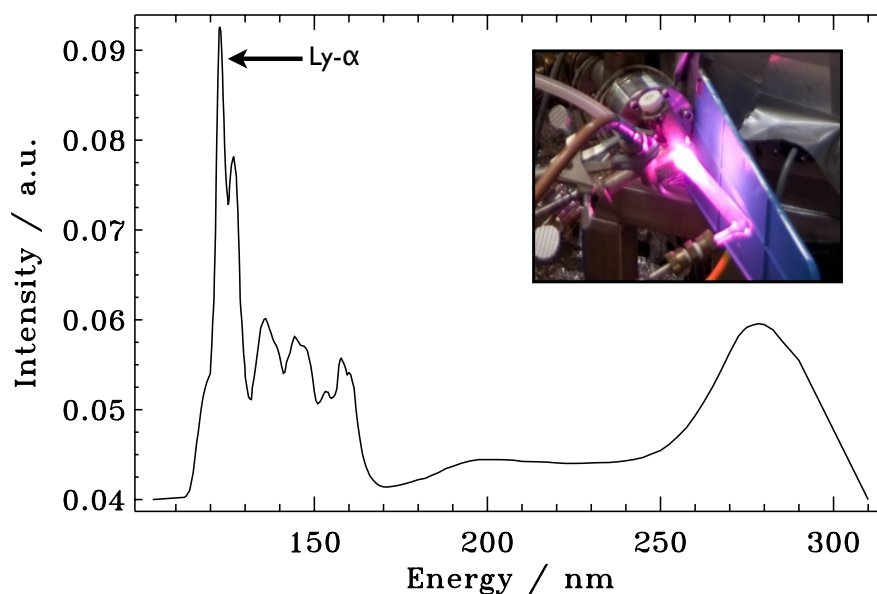


Figure 1.6: The emission profile of a broadband H₂ discharge lamp peaking at lyman alpha (Muñoz Caro & Schutte 2003).

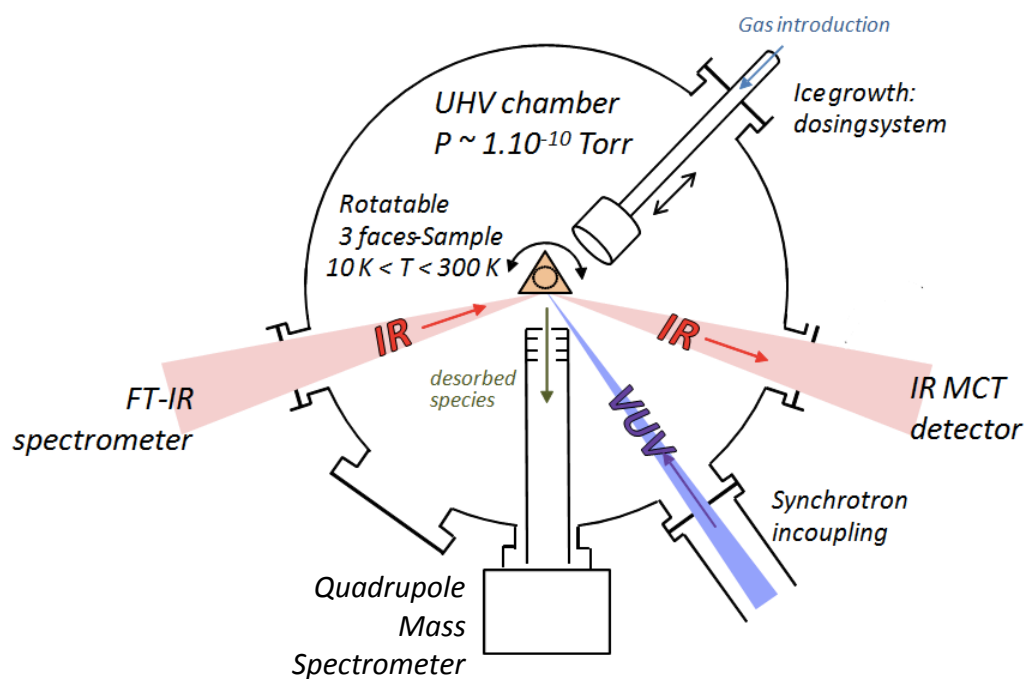


Figure 1.7: Schematic view of the set-up SPICES from the LPMAA used for the monochromatic irradiation of interstellar ice analogues at the SOLEIL synchrotron on the DESIRS beamline.

The UV energy distribution impacts on the measured photodesorption efficiency since it is the electronic excitation of molecules that induces the desorption. The pho-

photodesorption of interstellar ice analogues is traditionally studied in the laboratory using an H₂ microwave discharge lamp as source of UV photons. The set-up CRYOPAD described in the previous section is dedicated to the study of photo-processes using an H₂ lamp. Such a UV source, based on the excitation of H atoms, presents a flux high enough to induce processes that can be monitored on experimental time-scales. Figure 1.6 presents the spectrum of one of these lamps. It peaks at Lyman- α but other radiative features, in particular at 160 nm can come from the de-excitation of H₂. The spectrum profile is very sensitive to the conditions in which the lamp is used, namely H₂ pressure, microwave power, residual vacuum. Thus, a comparison of photodesorption efficiencies between experiments set-ups requires the knowledge of the lamp spectrum used for irradiation.

As an alternative to H₂ lamps, the impact of the photon energy on the ice photodesorption efficiencies and photodesorption mechanism are investigated using a tunable monochromatic light source in the VUV. The outcome of these frequency-resolved studies is presented in chapters 3 to 6 of this thesis. Successful proposals for beamtime on the DESIRS beamline at the SOLEIL synchrotron allowed us to study the photodesorption mechanism of CO, N₂, and O₂ ices using the set-up SPICES developed at the LPMAA in Paris (depicted in Fig. 1.7). The ultra-high vacuum chamber is equipped with a cryostat that can cool down a rotatable 3-face sample to temperatures as low as 10 K. Ices are grown on a polycrystalline gold surface or on Highly Oriented Pyrolytic Graphite (HOPG) at submonolayer precision using a retractable dosing line. The changes in the solid state can be monitored using RAIRS and desorbing species can be probed using a QMS. The set-up is directly coupled to the undulator-based DESIRS beamline and photon fluxes measured by calibrated photodiodes reach the 10¹⁴ photon s⁻¹ range without the use of a monochromator and reach the 10¹² photon s⁻¹ range with the monochromator. Only photons in the 7 - 13.6 eV spectral range are used since a minimum of about 7 eV is required to induce electronic transition in the species studied here and photons above 13.6 eV are absorbed by hydrogen in the ISM. It is the acquisition of calibrated photodesorption spectra that allows for the derivation of photodesorption rates with respect to the UV fields encountered in space and that provides insight into the photodesorption mechanisms of pure ices (chapters 3 to 5) and binary mixtures (chapter 6).

1.4 This Thesis

This thesis presents studies on processes bridging ice and gas-phase content for the interstellar medium. It first presents thermal desorption of water-rich ices and describes how volatile species stay trapped within the water at temperatures above their own desorption temperatures. This mimics the thermal heating that icy grains undergo during the protostellar stage. The bulk of the thesis focuses on desorption induced by UV photons as it likely occurs at the edges of molecular clouds, in prestellar cores, in the cold outer part of protostellar envelopes and mid-plane of protoplanetary disks. Synchrotron light providing monochromatic radiation in the VUV is used to derive wavelength-dependent photodesorption rates and elucidate the underlying mechanism. Finally, an observational method to test a possible ice to gas connection

around massive protostars is presented in the last chapter.

– **Chapter 2** addresses the question of how volatile molecules like CO_2 and CO desorb from the water-rich icy mantle when they are warmed-up as it would be the case during protostellar envelope collapse onto a protostar. Most models including this process assumed that each ice component would desorb at its own desorption temperature but when interacting with water, some of the volatile content can stay trapped within the water ice and desorb together with the water molecules at higher temperature. Temperature programmed desorption experiments are performed on ices of different thicknesses, volatile concentration, for different volatile components in water and for various heating rates in order to parameterize a model reproducing the volatile trapped fraction. The gas-grain model distinguishes three-phases: gas, ice surface and bulk. The desorption process occurs from the surface only and the surface is replenished by the mantle molecules, according to the enhanced diffusion of volatiles compared to water.

– **Chapter 3** presents the first wavelength-dependent investigation of ice photodesorption. The photodesorption of thin CO ice films is induced by VUV monochromatic light and the resulting photodesorption spectrum is obtained by monitoring through mass-spectrometry the desorbing molecules versus the photon energy. The photodesorption profile is tightly linked to the absorption spectrum of the ice, hinting for a Desorption Induced by Electronic Transition (DIET) process which does not involve the substrate.

– **Chapter 4** investigates in more detail the CO photodesorption mechanism. There, the photodesorption spectrum of CO is analyzed for different ice thicknesses and on different substrates, which confirms the ice-only related process and the independence to the ice thickness proposed in chapter 3. This implies a mechanism occurring in the top-most layers of the ice. The use of isotopically labeled ice layers of CO ($^{12}\text{CO}/^{13}\text{CO}$) unveiled the indirect character of photodesorption: it is the excitation of the sub-surface molecules that triggers the desorption of the surface species. The photodesorption of CO on water is also investigated and reveals that the H_2O internal structure can highly quench the photodesorption of top CO layers.

– **Chapter 5** focuses on the photodesorption of N_2 and O_2 , two diatomic species that are infrared inactive. N_2 photodesorption occurs in the same fashion as CO photodesorption: it is the electronic excitation that induces the desorption. For O_2 , the photodesorption mechanism is less straightforward since the UV irradiation can induce dissociation. The formation of oxygen radicals and ozone can lead to photodesorption in addition to the indirect process of importance for CO and N_2 .

– **Chapter 6** investigates the UV irradiation of $\text{CO}:\text{N}_2$ binary ice, which presents a first step in understanding the photodesorption of more astrophysically relevant ices. There the photodesorption of both species is investigated for the case of mixed and layered ices. The indirect mechanism found in the case of pure CO and N_2 ices is valid for binary ices. When mixed in equal proportions, both species desorb with the

same photodesorption spectrum, which is the co-addition of the single species photoabsorption spectra. This indirect mechanism where CO excitation can promote the desorption of N₂, even at wavelengths where N₂ is transparent, can explain the observed anti-correlation of cold CO and N₂ gas in prestellar cores. This study beautifully emphasizes the crucial role of the ice composition and structure, which must be taken into account when modeling photo-induced processes.

– **Chapter 7** explores the link between ice composition and gas phase observations of organics molecules around high-mass protostars. A link between the ice and organics in the gas phase should exist since most of the organics form in the solid state or through gas-phase reactions involving the evaporated ice molecules. Observationally testing this link is difficult due to the small amount of sources with both ice data and bright organic line detections, like in hot-cores. Here, observations of organics in sources that do not possess a bright core and have ice data available is attempted in order to increase the ice-gas source sample. The combination of single dish data and interferometric observations allows for the differentiation between organics present in cold protostellar envelopes and the warm compact regions close to the protostar. By combining results obtained previously for hot-core sources and our high-mass protostars sample, tentative correlations supported by a gas-grain model are presented. This study shows that it is possible to explore the ice-gas connection with more observations of both the ice and gas content around non-hot core sources.

Laboratory H₂O:CO₂ ice desorption data

Entrapment dependencies and its parameterization with an extended three-phase model

Abstract. Ice desorption affects the evolution of the gas-phase chemistry during the protostellar stage, and also determines the chemical composition of comets forming in circumstellar disks. From observations, most volatile species are found in H₂O-dominated ices.

The aim of this study is first to experimentally determine how entrapment of volatiles in H₂O ice depends on ice thickness, mixture ratio and heating rate, and second, to introduce an extended three-phase model (gas, ice surface and ice mantle) to describe ice mixture desorption with a minimum number of free parameters.

Thermal H₂O:CO₂ ice desorption is investigated in temperature programmed desorption experiments of thin (10 – 40 ML) ice mixtures under ultra-high vacuum conditions. Desorption is simultaneously monitored by mass spectrometry and reflection-absorption infrared spectroscopy. The H₂O:CO₂ experiments are complemented with selected H₂O:CO, and H₂O:CO₂:CO experiments. The results are modeled with rate equations that connect the gas, ice surface and ice mantle phases through surface desorption and mantle-surface diffusion.

The fraction of trapped CO₂ increases with ice thickness (10–32 ML) and H₂O:CO₂ mixing ratio (5:1 – 10:1), but not with one order of magnitude different heating rates. The fraction of trapped CO₂ is 44 – 84 % with respect to the initial CO₂ content for the investigated experimental conditions. This is reproduced quantitatively by the extended three-phase model that is introduced here. The H₂O:CO and H₂O:CO₂:CO experiments are consistent with the H₂O:CO₂ desorption trends, suggesting that the model can be used for other ice species found in the interstellar medium to significantly improve the parameterization of ice desorption.

2.1 Introduction

In pre-stellar cores, cold outer protostellar envelopes and protoplanetary disk mid-planes, most molecules, except for H₂, are frozen out on dust grains, forming ice mantles. The main ice component in most lines of sight is H₂O, followed by CO and CO₂, with a typical abundance of $(0.5 - 1.5) \times 10^{-4}$ for H₂O ice with respect to H₂ around solar-type protostars (van Dishoeck 2006). Infrared observations of pre-stellar cores show that most CO₂ ice and some of the CO ice is mixed with H₂O (Knez et al. 2005). The remaining CO and CO₂ are found in separate ice layers. Based on these observations, H₂O and CO₂ are thought to form simultaneously on the grain surface during the early stage of cloud formation. When the cloud becomes denser, gas phase CO freezes out on top of the water-rich ice, resulting in a bi-layered ice mantle, as described in Pontoppidan et al. (2008).

Once the pre-stellar core starts collapsing into a protostar, it heats its environment, including the icy grains. This results in the desorption of the CO-rich layer into the gas phase, in structural changes in the water-rich ice layer, and eventually in the desorption of the water-rich layer (Pontoppidan et al. 2008). Such an ice desorption scheme provides most of the gas phase reactants for the chemistry taking place at later stages in these warm regions (Doty et al. 2004). It is therefore crucial to understand ice mixture desorption and to effectively implement it in astrochemical networks. The aim of this study is to provide a laboratory basis for this process and to demonstrate how it can be modeled both in the laboratory and in space.

Laboratory experiments have provided most of the current knowledge about ice thermal desorption, including desorption energies for most pure simple ices (Sandford & Allamandola 1988, 1990; Fraser et al. 2001; Collings et al. 2004; Öberg et al. 2005; Brown & Bolina 2007; Burke & Brown 2010). Desorption from ice mixtures differs from pure ice desorption because of different binding energies between the mixture components (e.g., the CO binding energy increases from 830 K in pure ice to 1180 K in H₂O-dominated ice mixtures (Collings et al. 2003)) and because of trapping of volatile species in the H₂O hydrogen-bonding ices (Collings et al. 2004). Volatile components therefore desorb from H₂O-rich ice mixtures at a minimum of two different temperatures, corresponding to the desorption of the species from the surface of the H₂O ice and from molecules trapped inside the bulk of the H₂O ice, which only start desorbing at the onset of H₂O desorption. Additional desorption is sometimes observed at the temperature for pure volatile ice desorption and during ice re-structuring, e.g., at the H₂O phase change from amorphous to crystalline (Viti et al. 2004). This H₂O re-structuring occurs at ~140 K in the laboratory (for astrophysical timescales the re-structuring temperature and desorption temperature decrease), which is close to the onset of H₂O desorption (Collings et al. 2004).

Of the different ice mixture desorption features, the entrapment of volatile species in H₂O ice is astrochemically the most important to quantify. The trapping of CO in a water ice results in a factor of five increase in the effective desorption temperature. In a recent cloud core collapse model, this corresponds to trapped CO desorbing at 30 AU from the protostar compared to pure CO ice desorbing at 3000 AU. The case is less dramatic, but still significant, for CO₂, which desorbs at ~300 AU when pure, and at 30

AU if trapped in H₂O ice (Aikawa et al. 2008; Visser et al. 2009). Efficient ice trapping may therefore allow some volatiles to stay frozen on the dust grains during accretion of envelope material onto the forming protoplanetary disk (Visser et al. 2009).

There are only a few models that have incorporated the effects of ice mixture desorption. Collings et al. (2004) investigated the desorption of 16 astrophysically relevant species from H₂O:X 20:1 ice mixtures. Viti et al. (2004) and Visser et al. (2009) used the results of Collings et al. (2004) to split up the abundance of volatiles in up to four different flavors, with different desorption temperatures. These correspond to the fraction of each ice desorbing at the pure ice desorption temperature, from a H₂O surface, during H₂O ice restructuring and with H₂O, respectively. This approach has provided information on the potential importance of ice trapping for the chemical evolution during star formation. However, this model does not take into account specific ice characteristics such as ice thickness, volatile concentration and heating rate, on which the amount of trapped volatiles in the water ice may also depend (Sandford & Allamandola 1988). These characteristics need to be determined experimentally to correctly parameterize step models, where such are sufficient to model ice desorption. Strong dependencies on e.g. ice thickness or concentration would however warrant the development of a more continuous parameterization of ice desorption than the assignment of flavors.

These dependencies are naturally included in a few ice mixture desorption models of specific binary ices (Collings et al. 2003; Bisschop et al. 2006). The molecular specificity of these models, together with a large number of fitting parameters has, however, prevented their incorporation into larger astrochemical models. Therefore, in most gas-grain networks, desorption is still treated as if ices were pure, disregarding volatile entrapment in the water matrix (e.g. Aikawa et al. 2008).

Another problem with current gas-grain codes is that evaporation is often incorporated as a first-order process, while it is experimentally found to be a zeroth-order process with respect to the total ice abundance for ices thicker than one monolayer. Desorption models from the last decades have shown the necessity of using a zeroth order kinetics (Fraser et al. 2001; Collings et al. 2003). Incorporating ice desorption as a first-order process with respect to the total ice abundance effectively means that molecules throughout the whole ice are allowed to desorb at the same time, which is non-physical (Fraser et al. 2001; Bisschop et al. 2006). This can be solved by treating the bulk and surface of the ice as separate phases as it has been done by Pontoppidan et al. (2003) and Pontoppidan et al. (2008) for CO ice desorption and by Collings et al. (2005) for H₂O desorption and crystallization. Its successful use in astrochemical models makes this approach an attractive option to parameterize laboratory ice desorption, since the results can then be easily transferred into an astrophysical context. In this family of models, molecules are only allowed to desorb from the surface, which is continuously replenished by molecules coming from the mantle, and therefore the desorption kinetics are automatically treated correctly. This model results in a zeroth-order desorption behavior, in agreement with the experiments, since the number of molecules available for desorption remains constant in time. The model also results in trapping of volatiles in the bulk of the ice since the mantle molecules cannot desorb into the gas phase. The three-phase model we build on was first introduced by Hasegawa & Herbst (1993), but despite its advantages in treating different ice processes, it has not

been generally used for ice mixture desorption, nor has it been further developed, presumably because it did not correctly reproduce the experimentally observed amount of volatiles trapped in the water ice.

The goals of the present study are first to experimentally characterize how the trapping efficiency of CO_2 in H_2O ice depends on different ice characteristics (with complementary experiments on CO and tertiary mixtures) and second to use these experiments as a guide to improve our understanding of the trapping process within the three-phase model framework. The description of the extended three-phase model is explained in Section 2.2. The experiments used to get information on the volatile entrapment and to calibrate the model are described in Section 2.3. Laboratory results on $H_2O:CO_2$ ices, complemented by $H_2O:CO$ and $H_2O:CO_2:CO$ ice desorption results, are presented in Section 2.4. Section 2.5 presents the model fitting parameters and model results. Finally, the consequences of treating ice mixture desorption with the extended three-phase model under astrophysical conditions are discussed in Section 2.6.

2.2 Desorption Model

This study addresses the desorption of volatiles mixed with water and how to predict the fractions of volatiles in the ice and gas phase during a warm-up of the ice. The model is a system of rate equations based on the Hasegawa & Herbst (1993) model, but with the addition of diffusion. It aims at providing a solution for the amount of volatiles trapped in water with respect to the ice characteristics that can be directly included into astrochemical models, as used by Viti et al. (2004) and Visser et al. (2009). The model applies to species in the water-rich ice layer; the interface with an upper CO-rich ice layer is not treated here.

2.2.1 Basic three-phase model

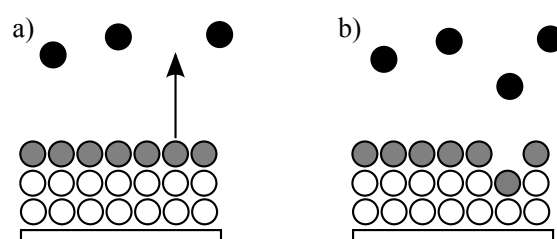


Figure 2.1: Cartoon defining the ice mantle (white), ice surface (gray), and gas phase (black) according to the Hasegawa & Herbst (1993) three-phase model. Panels a) and b) show the different phases before and after a desorption event.

The model used here to predict the trapping of volatile species in a water dominated ice is based on the three-phase model by Hasegawa & Herbst (1993). In this model, gas-grain interactions are addressed by considering three phases: the gas phase, the surface of the ice and the bulk/mantle of the ice (Fig. 1). The original model includes reactions between species in both gas and solid phase, as well as accretion from the gas to the ice and thermal and non-thermal desorption. Thermal desorption alone is

presented here. The model is based on the principle that molecules can only desorb from the surface into the gas phase and that the mantle molecules can only migrate to the surface following the desorption of a surface molecule. The time-dependent gas abundance of species i is given by

$$\frac{dn_i^g}{dt} = R_{\text{evap}} \quad (2.1)$$

where,

$$R_{\text{evap}} = (\nu e^{-E_i/T}) n_i^s \quad (2.2)$$

with n_i^g and n_i^s the gas phase and surface abundance of species i , respectively, E_i its binding energy in K, and ν a pre-exponential factor taken equal to 10^{12} s^{-1} , which is a standard value for physisorbed species (Biham et al. 2001). The surface abundance of species i can be written as:

$$\frac{dn_i^s}{dt} = -R_{\text{evap}} + R_{\text{repl}} \quad (2.3)$$

where,

$$R_{\text{repl}} = \alpha \left[\sum_j (\nu e^{-E_j/T}) n_j^s \right] \frac{n_i^m}{\sum_j n_j^m} \quad (2.4)$$

where n_i^m is the mantle abundance of species i , $\sum n_j^m$ the total number of molecules in the mantle and α is the ice coverage on the surface, which is set to 2 ML to account for surface roughness. The first term in Eq. 2.3 represents the loss of molecules i from the surface by thermal desorption. The second term is related to the replenishment of the surface sites by mantle molecules: the empty sites created by the desorption of any type of species from the surface, $\sum_j (\nu e^{-E_j/T}) n_j^s$, are statistically filled by molecules coming from the mantle. The probability for these molecules to be species of type i is equal to its mantle fraction, $\frac{n_i^m}{\sum n_j^m}$. The mantle abundance, n_i^m , of species i changes according to

$$\frac{dn_i^m}{dt} = -R_{\text{repl}}. \quad (2.5)$$

Because of the term $\frac{n_i^m}{\sum n_j^m}$, the replenishment of the surface phase by the mantle molecules during ice mixture desorption depends only on the mixing ratio of each species in this model, *e.g.*, for a $\text{H}_2\text{O}:\text{CO}_2$ 1:1 ice mixture, a molecule that desorbs into the gas phase has a 50% chance to be replaced by a water molecule and a 50% chance

to be replaced by a CO₂ molecule. This results in desorption of some volatile species around the pure ice desorption temperature and the rest remains trapped in the water ice since water molecules quickly saturate the surface phase.

The ice abundances n_i^s and n_i^m are all in cm⁻³, a unit directly related to the gas phase abundance. The abundance of species i on the surface is defined via the relation

$$n_i^s = N_i^s n^d \quad (2.6)$$

where N_i^s is the average number of molecules i on the grain surface, and n^d is the dust abundance. The same relation applies for the mantle abundance.

2.2.2 Extended three-phase model

The original three-phase model does not account for the preferred replenishment of the surface phase by volatile mantle species or that volatile species may diffuse more easily in the ice compared to water. Öberg et al. (2009b) showed that this diffusion can result in segregation of the ice components, which is important for temperatures well below the desorption energy of most volatile species in an ice mixture. This demixing mechanism changes the surface replenishment probabilities proposed in the original three-phase model by Hasegawa & Herbst (1993). Our proposed extension of the three-phase model accounts for this by introducing a mantle-surface diffusion term. Trapping of volatiles still occurs, but the surface-mantle diffusion of volatiles is enhanced compared to the original model, resulting in that more than 50 % of the empty sites are filled by volatile species. Quantitatively, this changes the surface and mantle abundances n_i^s and n_i^m as follows:

$$\frac{dn_i^s}{dt} = -R_{\text{evap}} + R_{\text{repl}} + R_i^{\text{diff}}, \quad (2.7)$$

and

$$\frac{dn_i^m}{dt} = -R_{\text{repl}} - R_i^{\text{diff}} \quad (2.8)$$

with

$$R_i^{\text{diff}} = f_i \nu \left[n_{\text{H}_2\text{O}}^s \frac{n_i^m}{\sum_j n_j^m} e^{-E_{\text{diff}}/T} - n_i^s \frac{n_{\text{H}_2\text{O}}^m}{\sum_j n_j^m} e^{-E_{\text{diff}}/T} \right], \quad (2.9)$$

and

$$E_{\text{diff}} = \left(\epsilon_{\text{H}_2\text{O}-i}^{\text{swap}} - \frac{E_{\text{H}_2\text{O}} - E_i}{2} \right) \quad (2.10)$$

for $i \neq \text{H}_2\text{O}$, and where $\epsilon_{\text{H}_2\text{O}-i}^{\text{swap}}$ is the energy barrier for a volatile molecule i and a water molecule to swap (i.e. change position) within the ice and f_i a fraction between 0 and 1 that is described below. The expression for the gas phase abundance remains unchanged (see Eq. 2.1). The diffusion term R_i^{diff} is added to the surface abundance (subtracted from the mantle abundance) to enhance the mantle to surface circulation for a volatile species i at the expense of the water, thus, R_i^{diff} is expressed differently for volatile and water molecules. The volatile ice diffusion rate depends on the balance of the probability of volatile molecules to move from the mantle to the surface at the expense of a water molecule and on the probability of the reverse process. This swapping process probability depends on the energy barrier $\epsilon_{\text{H}_2\text{O}-i}^{\text{swap}}$ of the process and on the energy difference before and after the swap, equal to $E_{\text{H}_2\text{O}} - E_i$. The diffusion rate for the water molecules is the negative sum of the diffusion rates for the volatiles, $R_{\text{H}_2\text{O}}^{\text{diff}} = -\sum_i R_i^{\text{diff}}$, since the total abundance of molecules in the mantle and in the surface is not affected by the diffusion process. A similar formalism was used to describe $\text{H}_2\text{O}:\text{CO}_2$ segregation in Öberg et al. (2009b); an exchange of a surface H_2O molecule and a mantle volatile is generally energetically favorable because H_2O forms stronger bonds than volatile species and a mantle H_2O molecule can form more bonds compared to a surface H_2O molecule.

From segregation studies of binary ices, it has become clear that only a limited fraction of the mantle participates in the mantle–surface circulation and that this fraction depends on the initial ice mixture ratio (Öberg et al. 2009b). This is represented by the fraction f_i

$$f_i = 1 - \frac{n_i^{\text{m,ini}} - c_i(x_i^{\text{ini}})^\beta}{n_i^{\text{m}}} \quad (2.11)$$

where $n_i^{\text{m,ini}}$ is the number of mantle molecules i initially in the ice, c_i an empirical factor determined for each volatile i , and x_i^{ini} the initial mixing ratio of volatiles i with respect to water. The expression $c_i(x_i^{\text{ini}})^\beta$ describes the number of mantle molecules available for segregation for a particular ice mixture before the onset of desorption and follows the form found by Öberg et al. (2009b) in ice segregation experiments when β is set equal to 2. The term $n_i^{\text{m,ini}} - c_i(x_i^{\text{ini}})^\beta$ is the number of mantle molecules protected from segregation. When the later expression exceeds the current number of volatile mantle molecules n_i^{m} , f_i reaches zero and segregation stops, i.e., the diffusion of volatile mantle molecules to the surface stops. Thus this definition results in a gradual slowdown of the ‘upward’ mantle–surface diffusion of volatile species, regulating the trapping characteristics of H_2O ice for different volatiles.

We have tested the performance of this extended three-phase model on the desorption of mixed $\text{H}_2\text{O}:\text{CO}_2$ ices by comparing model and experimental TPD experiments, where the model TPDs are constructed using the rate equations 2.1, 2.7 and 2.8. In the model TPDs the initial ice temperature is raised in steps proportional to the heating rate and at each time step the rate equations from the three-phase model are applied to calculate the temperature dependent desorption and diffusion rates. The desorption rate of the volatile is what is plotted in the TPD curves.

TPD experiments of pure ices are performed to determine the binding energies E_i . The other free parameters that are used to optimize the model are the swapping energies $\epsilon_{\text{H}_2\text{O}-i}^{\text{swap}}$ between H₂O molecules and volatiles i and the empirical factor c_i used to parameterize the diffusion of volatiles i from the mantle to the surface. These two parameters are determined by performing TPD experiments of binary ice mixtures of H₂O:CO₂ with different mixing ratios, thicknesses and heating rates and by comparing the output of the model with the experimental trends, *i.e.*, the amount of volatile species that remains trapped in the water ice at temperatures higher than the desorption temperature of the volatile species.

It is important to note that the model does not include the finite pumping speed during experiments. This will affect the derived desorption barriers and these are therefore not meant to replace the ones derived from more detailed pure ice experiments in the literature. As long as the pumping rate is constant with temperature, excluding the pumping rate will not affect the determined ice fraction that desorbs at a low temperatures versus the fraction that desorbs with H₂O. This is a reasonable assumption above the pure volatile ice desorption temperatures, where cryopumping is no longer efficient. The derivation of c_i and $\epsilon_{\text{H}_2\text{O}-i}^{\text{swap}}$ should therefore not be affected by this simplification.

2.3 Experiments

2.3.1 Experimental parameters

The experiments in this study are chosen to simultaneously provide data directly relevant to ice desorption in different astrophysical environments (with different ices) and to construct a proof-of-concept model for ice mixture desorption. The focus is on CO₂ desorption from H₂O ice mixtures, one of the most important ice systems around protostars, with supporting experiments on CO desorption. While interstellar ices are expected to be complex mixtures, it is still useful to investigate desorption from binary H₂O:volatile ice mixtures since the H₂O:volatile interactions are expected to dominate the desorption process in space, both because H₂O is the major ice constituent and because H₂O generally forms stronger bonds with itself and with volatiles than volatiles do. This hypothesis has been further tested by performing TPD experiments of two tertiary H₂O:CO₂:CO ice mixtures.

The ice thickness and structure in the experiments are chosen to be as similar as possible to the existing observational constraints on interstellar ices. Interstellar ices are estimated to be less than 100 monolayers (ML) thick from the maximum amount of oxygen available for ice formation. The experimentally grown ices are between 10 and 40 ML, since it is only possible to quantify ice thicknesses up to a certain limit (40 ML in our case) using reflection-absorption infrared spectroscopy (Teolis et al. 2007). Information on ice structure in space is limited, but the lack of a water dangling vibration at 3700 cm⁻¹ suggests a less porous ice than typically produced in the laboratory. We minimized the porosity of ice analogues by injecting gas perpendicularly to the cold surface when growing the ices (Stevenson et al. 1999; Kimmel et al. 2001).

2.3.2 Experimental procedures

All desorption experiments are performed with CRYOPAD. This set-up has been described in detail elsewhere (Fuchs et al. 2006). The set-up consists of an ultra high vacuum (UHV) chamber with a base pressure of $\sim 10^{-10}$ mbar at room temperature. Ices are grown on a gold-coated substrate situated at the center of the chamber that can be cooled down to 16 K by a close cycle He cryostat. The relative sample temperature is controlled with a precision of 0.1 K using a resistive heating element and a temperature control unit. The absolute sample temperature is given with a 2 K uncertainty. The system temperature is monitored with two thermocouples, one mounted on the substrate face, the other on the heater element.

A fourier transform spectrometer is used for reflection-absorption infrared spectroscopy (FT-RAIRS) to record vibrational absorption signatures of molecules condensed on the gold surface. The spectrometer covers $700 - 4000 \text{ cm}^{-1}$ with a typical resolution of 1 cm^{-1} and an averaged spectrum consists of a total of 256 scans. Ice evaporation is induced by linear heating of the substrate (and ice) in TPD experiments. RAIR spectra are acquired simultaneously to monitor the ice composition during the TPD. A quadrupole mass spectrometer (QMS) is positioned at 4 cm, facing the ice sample to continuously analyze the gas-phase composition mass-selectively and to obtain desorption curves of evaporating molecules during the TPD experiments.

Mixtures and pure gas samples are prepared from $^{13}\text{CO}_2$ (Indugas, min 99% of ^{13}C), CO_2 (Praxair, 99% purity), ^{13}CO (Cambridge Isotope Laboratories, 98% purity) and from gaseous water at the saturation pressure of a de-ionized liquid sample at room temperature. The de-ionized water is purified by three freeze-pump-thaw cycles. The samples are prepared separately, then injected in the chamber via an inlet pipe directed along the normal of the gold surface. In all gas samples, an isotopologue of CO was used to separate the QMS signal from background CO and N_2 . Similarly, an isotopologue of CO_2 was used to minimize the overlap in RAIR spectra between CO_2 ice and atmospheric CO_2 gas outside the UHV chamber.

H_2O and CO_2 ice amounts are determined directly using the RAIRS band strengths provided by Öberg et al. (2009,a) for CRYOPAD. From these measurements the absolute ice thicknesses are known within 50%. The relative ice abundance uncertainties are smaller, $\sim 20\%$, and due to small band strength variations with ice composition and temperature.

Table 2.1 lists the set of TPD experiments performed to calibrate and test the desorption model presented in Section 2.2. The TPD experiments begin with the deposition of pure or mixed ice samples on the gold substrate cooled to 16 – 19 K, and continue with a slow heating of the ices at a constant specified rate until the desorption of the molecules from the surface is complete. The evaporated gas phase molecules are continuously monitored by the QMS. RAIR spectra of the ices are acquired before heating to determine ice thicknesses and mixture ratios as described above. Spectra are also recorded during the warm-up as a second independent way to determine the ice composition and to monitor eventual structure modifications.

The infrared data are reduced by subtracting a local baseline around the molecular features. Mass spectrometric data are reduced by subtracting the ion current from

species present in the background for each mass channel. Absolute yields cannot be directly obtained by the QMS since it is situated away from the ice sample (4 cm) and thus some of the desorbing molecules may get pumped away before detection. All QMS desorption rate curves are therefore normalized in such a way that the time-integrated desorption rate from the various species corresponds to their infrared spectrally measured ice abundance at the beginning of each experiment.

Table 2.1: Overview of the desorption experiments

Exp.	Sample	Ratio	Thick. (ML)	Heat. rate (K.min ⁻¹)	Trapped CO ₂ /CO ice %	
					wrt. CO ₂ /CO	wrt. H ₂ O
1	H ₂ O	-	24	1	-	-
2	¹³ CO ₂	-	6	1	-	-
3	¹³ CO	-	6	1	-	-
4	H ₂ O:CO ₂	10:1	12	1	62	6.2
5	H ₂ O:CO ₂	10:1	19	1	75	7.5
6	H ₂ O:CO ₂	10:1	32	1	84	8.4
7	H ₂ O: ¹³ CO ₂	5:1	32	1	64	12.8
8	H ₂ O: ¹³ CO ₂	5:1	18	10	62	12.4
9	H ₂ O: ¹³ CO ₂	5:1	18	1	53	10.6
10	H ₂ O: ¹³ CO ₂	5:1	10	5	44	8.8
11	H ₂ O: ¹³ CO ₂	5:1	10	1	45	9.0
12	H ₂ O: ¹³ CO ₂	5:1	10	0.5	44	8.8
13	H ₂ O: ¹³ CO	10:1	14	1	43	4.3
14	H ₂ O: ¹³ CO	10:1	25	1	47	4.7
15	H ₂ O: ¹³ CO	5:1	20	1	24	4.8
16	H ₂ O: ¹³ CO	2:1	13	1	9	4.5
17	H ₂ O: ¹³ CO	1:1	17	1	4	4.0
18	H ₂ O:CO ₂ : ¹³ CO	11:4:1	16	1	32/19	12/2
19	H ₂ O:CO ₂ : ¹³ CO	20:1:1	30	1	92/96	5/5

2.4 Experimental analysis

2.4.1 Complementarity of RAIRS and QMS

Figure 2.2 illustrates the agreement between desorption curves derived from QMS and RAIRS data for CO₂ in a 5:1 water-dominated H₂O:CO₂ ice, 18 ML thick and heated at 1 K.min⁻¹ rate (Exp. 11). The upper left panel in Fig. 2.2 shows the CO₂ stretching band recorded at different temperatures during warm-up: after ice deposition at 22 K, at 62 K where segregation is known to be efficient (Öberg et al. 2009b), during the first ice desorption peak around 79 K, in the temperature interval between pure CO₂ desorption and H₂O desorption, and during desorption of the trapped CO₂. The right panel shows the desorption rate of CO₂ derived from the same experiment by mass spectrometry. The bottom panel presents the cumulative ice loss versus temperature for this experiment, obtained both by integrating the CO₂ mass signal with respect to the temperature, and by integrating the CO₂ infrared signal recorded at spe-

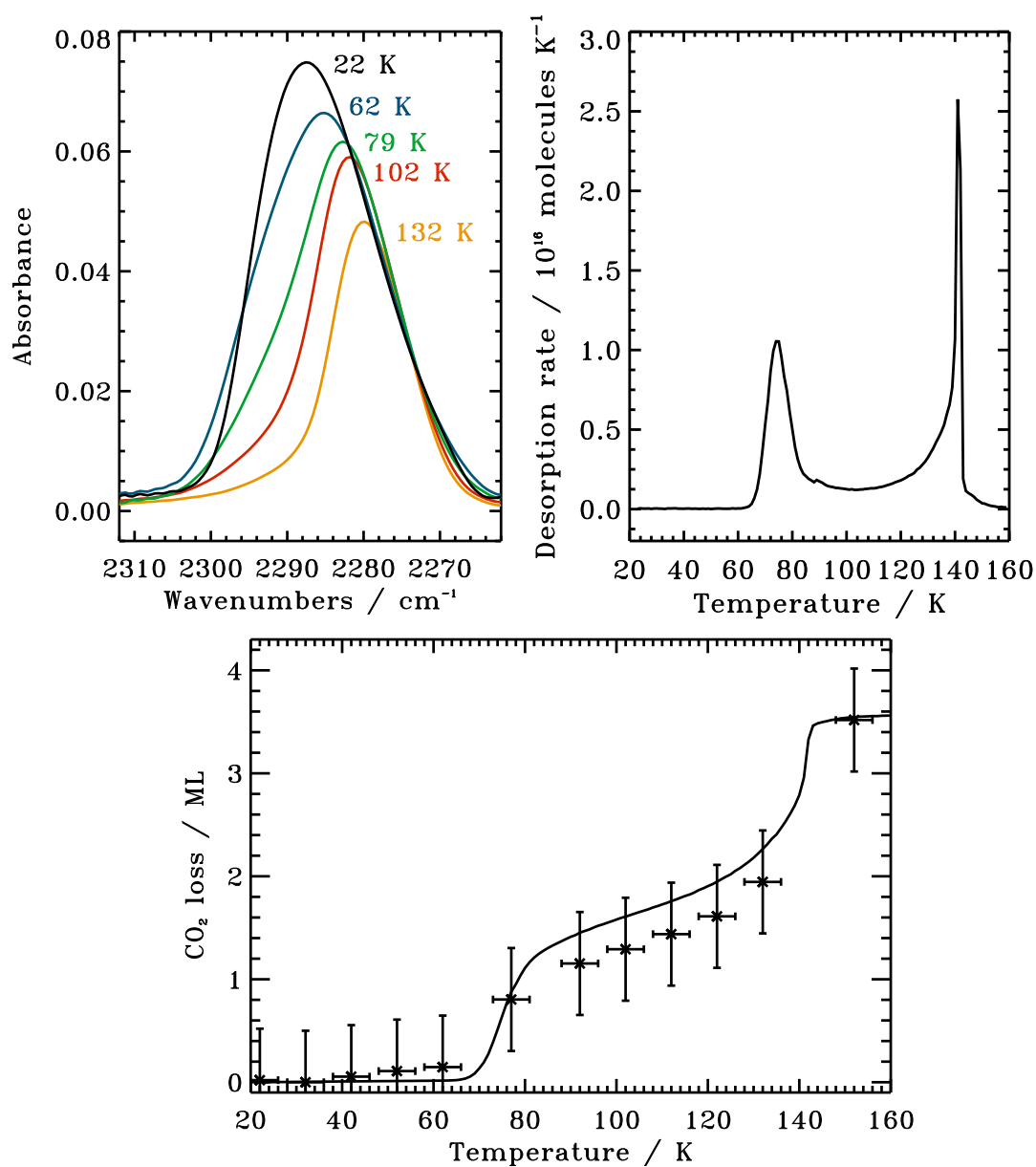


Figure 2.2: The upper left panel presents the infrared CO_2 stretching features at specific temperatures during the warm-up of 18 ML of a $\text{H}_2\text{O}:\text{CO}_2$ 5:1 ice heated at $1 \text{ K}\cdot\text{min}^{-1}$. The right upper panel presents the desorption rate of CO_2 for the same experiment obtained by mass spectrometry. The bottom panel shows the ice loss for this experiment obtained by infrared measurements (crosses) and mass spectrometry (solid line).

cific temperatures. The error bars on the infrared data are due to variable ice band strengths with temperature and composition. Within these uncertainties the fractional ice loss curves derived by infrared and by mass spectrometry agree well; there seems to be only a small systematic offset for the 80 – 130 K range. This implies that the first RAIR spectrum of the ice after deposition can be used to derive quantitative results from the TPD experiments.

Figure 2.2 also shows that there is evidence for some ice loss between the two main desorption peaks. The cumulative QMS and infrared spectroscopy signals match each other at these intermediate temperatures, which points to that the measurements trace actual ice desorption in between the pure ice desorption event and the desorption of trapped volatiles. The implications of this ice desorption process is discussed below, but it is important to note that this is not incorporated into the model framework and this may be a limitation to step-wise desorption models, whether using our parameterization or any of the previously published ones. Quantifying this process would require an additional set of experiments where the mass spectrometer is mounted closer to the substrate to allow for the detection of very low desorption rates.

2.4.2 Desorption trends

Figure 2.3 shows the desorption of CO_2 from $H_2O:CO_2$ ice mixtures of different thicknesses (a), with different CO_2 concentrations (b), and heated at different rates (d). In addition there are two CO TPD curves from $H_2O:CO$ mixtures with different CO concentrations (c). For reference, Fig. 2.3e) presents the TPD curves of pure CO, CO_2 , and H_2O ice heated at 1 K min^{-1} . The fraction of trapped volatile is obtained by integrating the QMS signal for temperatures above 110 K and dividing it by the QMS signal integrated over the entire 20–160 K range. The chosen temperature of 110 K is well below the onset of the second desorption peak and the volatiles that desorbed during the first CO_2 or CO desorption peak are (almost) entirely pumped, though as discussed above there seems to be a low-level type of desorption occurring between the main desorption peaks. Whether due to finite pumping or actual desorption this results in a 10–20% uncertainty in the determination of the trapped fraction, *i.e.*, the choice of temperature integration limits affects the estimated amount of trapped ice by $< 20\%$. The trapped percentage of volatiles in each experiment, defined with respect to the initial volatile ice content, is reported in the second last column of Table 2.1. The last column of Table 2.1 presents the trapped abundance of volatiles species with respect to the initial H_2O abundance. This value is less variable compared to the trapped amount of CO/ CO_2 with respect to the initial CO/ CO_2 abundance presented in the preceding column. Both Table 2.1 and Fig. 2.3 show that for CO_2 and CO the percentage of trapped volatile species in the H_2O ice is highly dependent on the experimental conditions; the CO_2 trapping fraction varies between 44 and 84% with respect to the initial volatile content. In the following subsections, we report and discuss these dependencies.

Thickness dependency

Figure 2.3a presents the desorption of a $H_2O:CO_2$ 10:1 ice mixture for different initial ice thicknesses and shows that the amount of trapped CO_2 (desorption around 140 K) increases with ice thickness. In contrast the amount of CO_2 desorbing around 70 K is independent of ice thickness in the experimentally investigated range. This implies that only CO_2 molecules from the top part of the ice are available for desorption at the CO_2 desorption temperature. This can be explained by either a highly porous ice that allows CO_2 to “freely” desorb from the top layers or by diffusion from the top

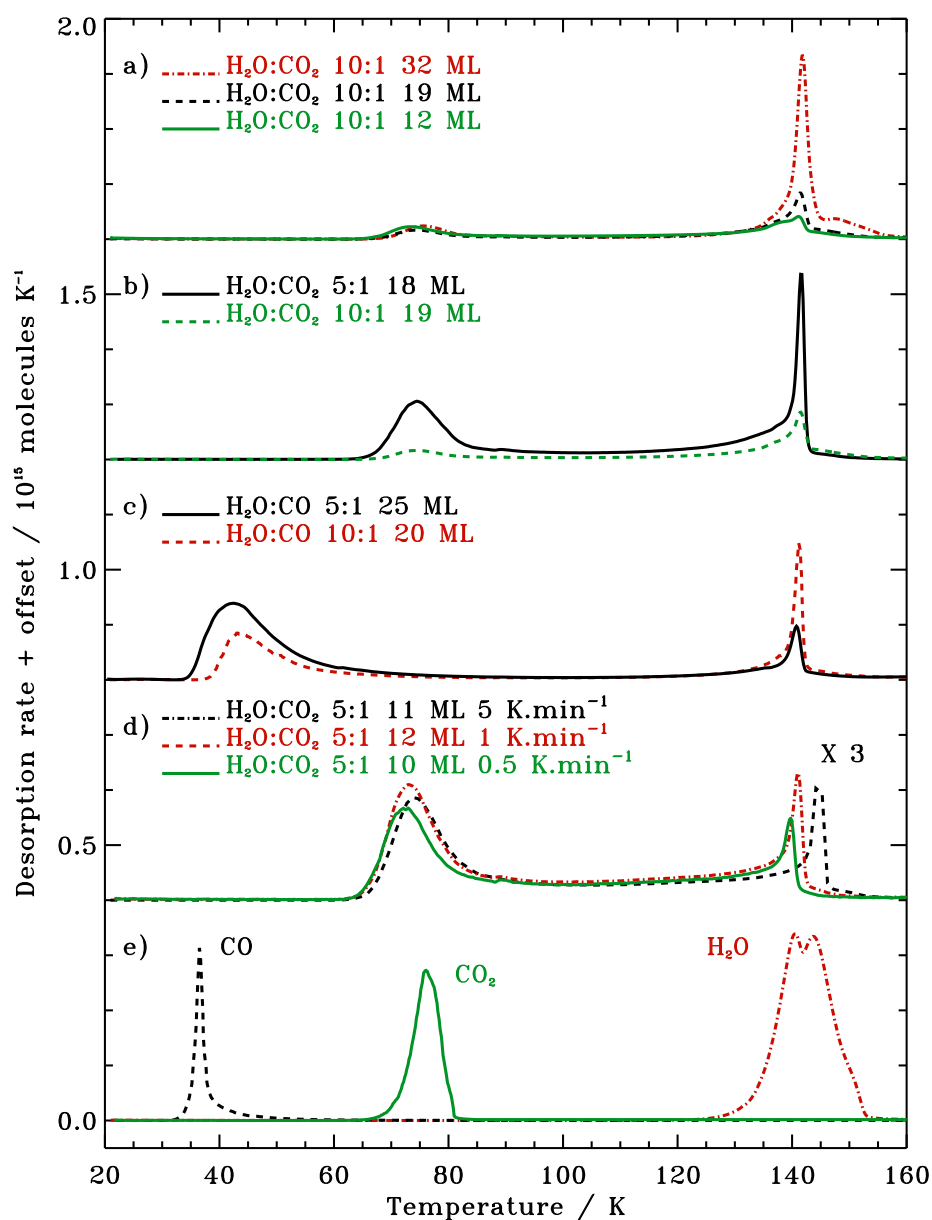


Figure 2.3: Experimental CO and CO₂ desorption curves a-d) during warm up of ice mixtures (offset for visibility) together with pure CO, CO₂ and H₂O ice TPD curves e). The heating rate is 1 K.min⁻¹ except for when specified otherwise in a), the total ice thickness and mixing ratio are listed in for each experiment.

layers of the mantle phase to the surface. In both cases the surface is eventually totally saturated by water molecules, trapping the rest of the volatiles in the ice mantle.

Mixing ratio dependency

The dependence of the volatile trapping with the mixture ratio is presented in Fig. 2.3b) for H₂O:CO₂ and in Fig. 2.3c) for H₂O:CO ice mixtures. In both cases the trapped

fraction decreases as the volatile to H_2O ratio increases. In other words, the amount of pores exposed to the surface or the diffusion length scale of volatiles in the ice must increase with increasing volatile concentration. A similar dependency was noted in Öberg et al. (2009b) when measuring segregation in ices. Increased diffusion may either be due to a gradually looser binding environment in the volatile-rich ices or a break-down of H_2O ice structure in the presence of higher concentrations of volatiles. The thick $H_2O:CO$ ice experiments (Exps. 14, 15 and 17) with initial mixture ratios of 10:1, 5:1 and 1:1 show a continuous decline of the trapping fraction, which suggests that either the ice becomes continuously more porous or that the diffusion path length increases gradually with volatile concentration.

Molecular dependency

Similarly to Sandford & Allamandola (1990) and Collings et al. (2004) we find that the trapping efficiencies of the investigated CO_2 and CO in H_2O ice are radically different. When comparing Fig. 2.3b) and c), it appears that CO is much more mobile than CO_2 in the H_2O ice as demonstrated by the higher trapping fraction of CO_2 compared to CO in similar H_2O ice mixtures. Sandford & Allamandola (1990) explained this difference from a combination of different binding energies of CO and CO_2 in H_2O ice due to molecular size, shape and electronic differences. These binding energies may equally affect the probability of escaping through an ice pore or diffusing through the bulk of the ice.

Heating rate dependency

In Fig. 2.3d), the heating rate of the ice is varied for a $H_2O:CO_2$ 5:1 ice of 10 – 12 ML between 0.5, 1 and 5 $K.min^{-1}$. This does not appreciably affect the trapping efficiency of CO_2 in the H_2O ice and implies that the process responsible for exchanges between the surface and the mantle is fast compared to the experimental warm-up time. If this was not the case, a lower heating rate would have resulted in a smaller amount of trapped CO_2 , since a slower heating means more time for the migration of mantle molecules to the surface.

The lack of a heating rate dependency on the trapped amount of volatiles (same trapped percentage in Exp. 10, 11 and 12) also implies that there is a rather sharp boundary between the molecules in the upper layers that can diffuse to the surface (whether through pores or bulk diffusion) and molecules deeper in the ice that cannot. Even if the volatiles deep in the ice can diffuse within the ice mantle, diffusion 'upwards' must quickly become slow as the surface layers saturate with H_2O molecules or alternatively all accessible pores have been emptied. This explains that the amount of desorbing CO_2 molecules at low temperatures is thickness independent (the H_2O 'ice cap' will become impenetrable after a certain amount of CO_2 molecules have desorbed) and that entrapment efficiencies are unaffected by lower heating rates.

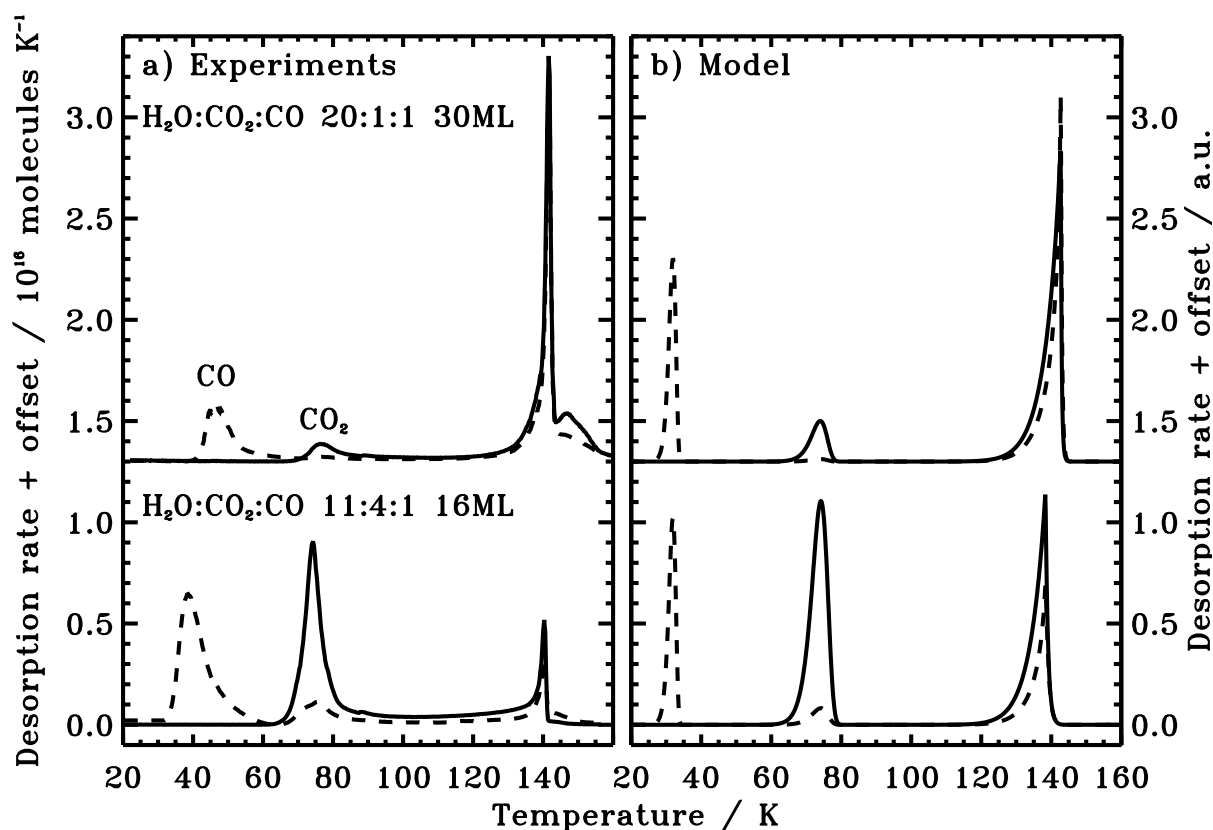


Figure 2.4: a: Desorption rate of CO_2 (solid line) and CO (dashed line) from two tertiary water dominated ice mixtures (Exps. 18 and 19) with a $1 K \cdot min^{-1}$ heating rate. - b: Implemented three-phase model desorption rate for the same experiments.

2.4.3 Tertiary mixtures

The desorption rates for the tertiary mixtures (Exps. 18 and 19) are presented in Fig. 2.4a). Similarly to the binary experiments, the trapping of volatiles is more efficient for a lower volatile to H_2O ratio. The desorption curves for CO_2 are not affected by the presence of CO. Thus the CO- CO_2 interaction does not have a significant impact on the amount of CO_2 trapped within the water matrix. Overall the TPD curves resemble the addition of desorption curves from two separate binary mixtures, except for a small fraction of CO that desorbs with CO_2 in the $H_2O:CO_2:CO$ 11:4:1 mixture (lower panel in Fig. 2.4). It is unclear whether this desorption is due to a co-desorption of CO with CO_2 or to a release of CO that has been trapped under a barrier of CO_2 surface molecules. The observed similarity supports the use of binary ice mixtures as templates to study diffusion and desorption even though they are not directly representative of interstellar ice mixtures.

When comparing the desorption of CO from a tertiary and a binary ice mixture with the same $H_2O:CO$ ratio and ice thickness, it appears that less CO is trapped in the tertiary mixture. This may be due to ice structure changes, as discussed above,

or to shielding of CO from the sticky water molecules by CO_2 molecules (the CO- CO_2 bond is weaker than the H_2O -CO one), lowering the CO diffusion barrier. The CO_2 and CO desorption curves from the dilute tertiary mixture both contain a small additional peak around 150 K, only seen elsewhere in the thickest $H_2O:CO_2$ 10:1 ice experiment. A similar double peak was noted in the 20:1 desorption experiments of Collings et al. (2004).

2.4.4 Ice diffusion mechanisms: pore versus bulk diffusion

The main mechanism behind diffusion in the ice mantle is not known and may differ between different ices. Most previous studies have focused on diffusion in cracks and pores and pore collapse has been introduced to explain ice trapping. The observation that both CO and CO_2 become trapped even though they partly desorb at their, very different, pure ice desorption temperatures is difficult to reconcile with pore collapse as the main trapping mechanism, however. That is, it would imply efficient H_2O pore collapse both at ~ 30 K and ~ 70 K.

Even if pore collapse does not provide a complete explanation of why ices become trapped, some kind of internal surface hopping may explain why molecules can diffuse out of the ice. In this scenario, the CO_2 desorption ice thickness dependency is due to that the pores and cracks that are open to the surface only go down to a certain depth, in this case a few ML for $H_2O:CO_2$ 5:1. The different CO and CO_2 trapping efficiencies may then be either due to different ice structures or to CO desorbing easier through pores compared to CO_2 . Pore diffusion may thus be consistent with these particular experimental results, but ice diffusion is present also in other ices that are known to be quite compact, e.g. CO ice (Bisschop et al. 2006). While it is possible that diffusion occurs through completely different mechanisms in different ices, the concept of ice bulk diffusion has the prospect of approximating mixing and de-mixing processes in all kinds of ices, regardless of structure.

In the bulk diffusion scenario, an amorphous ice is viewed like a very viscous liquid, whose viscosity decreases with the volatility of the ice molecules. In Öberg et al. (2009b) this was modeled as molecules swapping places with a barrier significantly higher than surface hopping. Volatile molecules will tend to swap their way towards the surface because it is energetically favorable to have the molecules that form weaker bonds in the surface layer (where fewer bonds can be made due to the ice–vacuum interface). Trapping is explained by that when volatile molecules diffuse from the top mantle layers to the surface and desorb, the top mantle layers become saturated with H_2O and therefore viscous enough to be impenetrable. The low desorption rate of volatiles between the volatile and H_2O ice desorption peaks would however suggest that under some experimental conditions, small amounts of volatiles can escape through this H_2O barrier. More experiments are required to test under which conditions this is a reasonable approximation. The model presented below is an attempt to include the most important features of this concept while still keeping the number of parameters low.

2.5 Model parametrization and performance

2.5.1 Parametrization

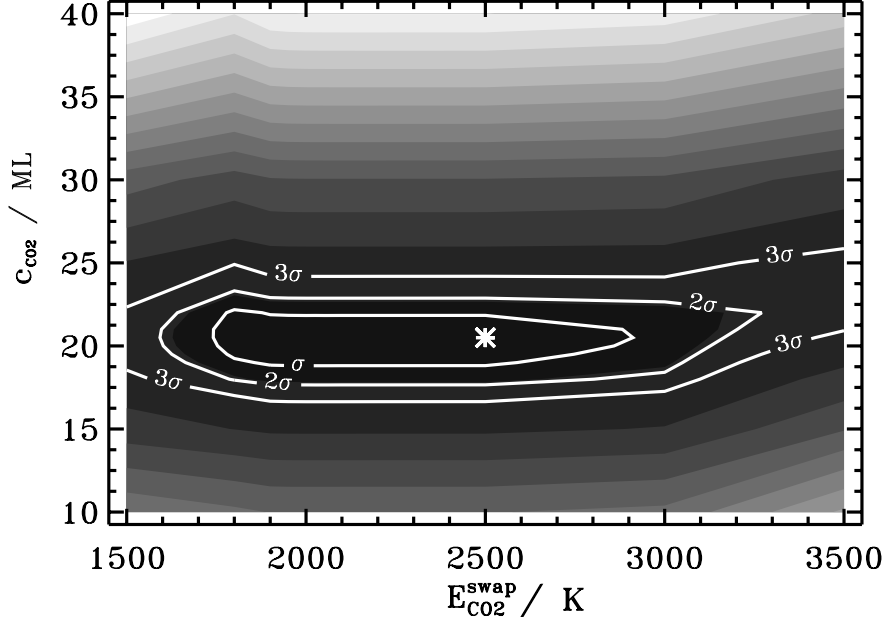


Figure 2.5: χ^2 contour plot for fitting the model parameters $\epsilon_{\text{H}_2\text{O}-\text{CO}_2}^{\text{swap}}$ (parameterizing the ability of CO_2 to switch position with a H_2O molecule) and c_{CO_2} (parameterizing the CO_2 ice thickness where swapping is fast compared to the investigated heating rates) using the experimentally determined amount of CO_2 trapped in a binary $\text{H}_2\text{O}:\text{CO}_2$ ice (Exps. 4 to 12). These two parameters regulate the distribution of the volatile molecules in the gas, surface and mantle according to Eq. 2.11 and 2.10 of Section 2.2.

The pure ice desorption energies are derived from fitting the three-phase model to the experimental pure ice desorption curves with the results: $E_{\text{H}_2\text{O}} = 4400 \text{ K}$, $E_{\text{CO}_2} = 2440 \text{ K}$ and $E_{\text{CO}} = 1010 \text{ K}$. The H_2O value is lower than the one found in Fraser et al. (2001). This discrepancy is probably due to a combination of that we use a single experiment, do not include the pumping speed and fix the pre-exponential factor to $\nu = 10^{12} \text{ s}^{-1}$ for every species here. The value in Fraser et al. (2001) should thus still be used when modeling the absolute desorption temperature. For the purpose of parameterizing the desorption fractions we prefer our value for the sake of consistency. The remaining model parameters $\epsilon_{\text{H}_2\text{O}-i}^{\text{swap}}$ and c_i are obtained separately for CO_2 and CO . This is done through a χ^2 analysis, where trapping fractions from the model are compared to those from the binary experiments for a grid of $\epsilon_{\text{H}_2\text{O}-i}^{\text{swap}}$ and c_i values. The minimum χ^2 value for CO_2 is obtained for $\epsilon_{\text{CO}_2-\text{H}_2\text{O}}^{\text{swap}} = 2500 \text{ K}$, $c_{\text{CO}_2} = 20.5 \text{ ML}$, but the swapping energy for $\text{H}_2\text{O}:\text{CO}_2$, which is linked to the ability of CO_2 to swap with H_2O within the solid phase, is not well-constrained between 1600-3200 K (Fig. 2.5). In contrast, the parameter c_{CO_2} related to available amount of CO_2 from the ice mantle that

can migrate to the surface, is well constrained which suggests that even at laboratory time scales mixture desorption is mainly governed by how large a part of the mantle is eligible for swapping with the surface, rather than the swapping barriers.

The CO experiments can be fitted with $\epsilon_{CO-H_2O}^{swap} = 960$ K and $c_{CO} = 80$ ML, but these are based on only a few experiments and the inequalities $\epsilon_{H_2O-CO}^{swap} < \epsilon_{H_2O-CO_2}^{swap}$ and $c_{CO} > c_{CO_2}$ are alone well constrained.

2.5.2 Model performance

Desorption trends modeling

Figure 2.6 shows the simulations of the binary mixture desorption using the optimized model parameters from the previous section. Generally the qualitative agreement is good and the model captures the trends that were observed experimentally. The exact shapes of the modeled and experimental desorption curves differ for several reasons. First, the model does not take into account the range of environments from which the molecules desorb, *e.g.*, the H_2O /volatile fraction changes during the desorption process and even a pure ice has a range of different binding sites. This affects both the position and the width of the peak. Second, the model does not consider the different water ice structures present at different temperatures; water ice crystallizes around 140 K (see the desorption peaks for water in Fig. 2.3e), which may affect the shape and position of the second desorption peak of the volatiles. Finally, the model does not include finite pumping speeds, which results in abundance tails in the experimental curves. While these effects may all be important under special circumstances the aim of the extended three-phase model is not to reproduce the experimental results perfectly. Rather, the goal is to capture the main characteristics of ice mixture desorption.

The increase of the trapped amount of volatiles with ice thickness and the experimental observation that the same amount of molecules desorbs around the volatile pure desorption temperature, regardless of the ice thickness, are reproduced in the model because diffusion between the mantle and surface is only allowed from a fraction of the mantle, f_i (Eq. 2.11 in Section 2.2) which depends on the kind of volatile and mixing ratio with water. This fraction is independent of the ice thickness. Thus the same amount of volatile molecules migrates to the surface regardless of ice thickness, followed by saturation of the surface phase by water molecules. The rest of the volatiles is trapped in the mantle until H_2O desorption, thus the trapped fraction depends on the ice thickness.

The observed concentration effect on the trapping efficiency is reproduced by the model because the fraction of volatiles migrating to the surface depends on the mixing ratio of the volatile with respect to water, x_i^{ini} . The lower the concentration of volatiles in the ice is, the smaller the fraction of volatile molecules make it to the surface and the more become trapped. The higher mobility of CO compared to CO_2 is also reproduced by the model as the molecular parameter c_{CO_2} is lower than c_{CO} . Thus more volatiles are able to diffuse to the surface in the case of $H_2O:CO$ mixtures.

Experimentally, a low desorption rate is sometimes observed between the volatile and H_2O desorption temperature. In the model, the diffusion barrier energy is low

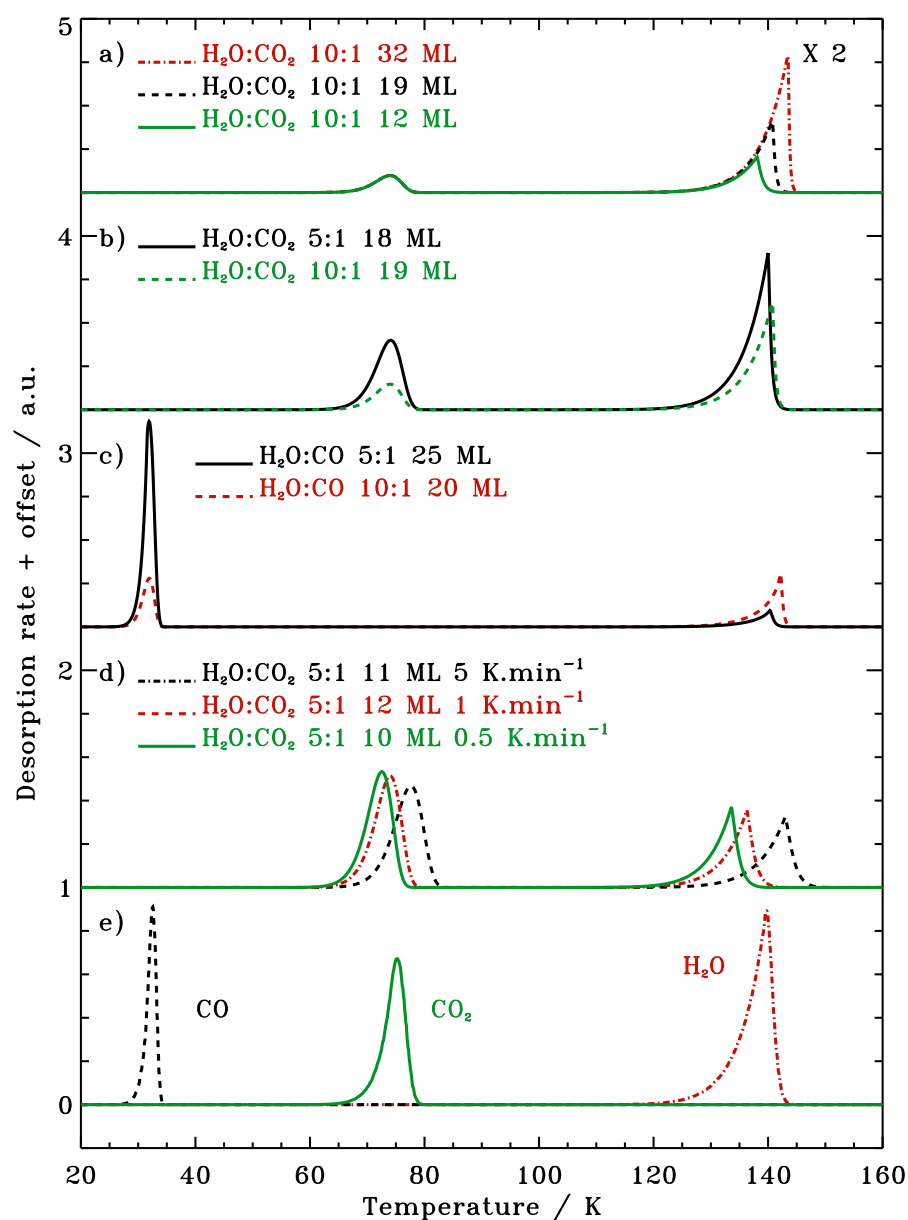


Figure 2.6: Simulated CO_2 and CO TPD curves from $\text{H}_2\text{O}:\text{CO}_2$ and $\text{H}_2\text{O}:\text{CO}$ mixtures for different thicknesses, ratios, and heating rates a-d). Panel e) presents the simulated desorption of pure H_2O , CO_2 and CO ice. This figure connects the model outputs to the experiments shown in Fig. 2.3.

enough that the diffusion process is complete before desorption of the volatile takes place and therefore there is no desorption between the pure and H_2O desorption peaks. Such a low diffusion energy barrier is needed to reproduce that the trapping efficiency is insensitive to the heating rate (within the explored heating rate range). There is probably a second diffusion process at play at these intermediate temperatures, which cannot be reproduced by the current, simple parameterization.

Quantitative agreement

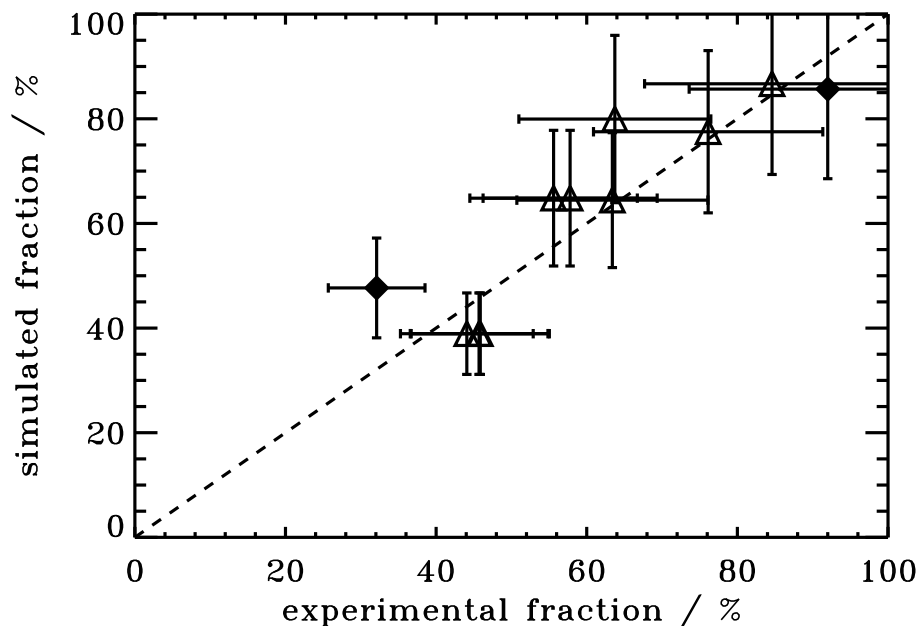


Figure 2.7: Percentage of CO_2 experimentally trapped vs the simulated one. The triangles are the trapped percentages obtained from the binary mixture experiments. The diamonds are the model predictions for the two tertiary mixtures. The one-to-one ideal relation is plotted as a dashed line.

Figure 2.7 compares the volatile trapping fractions obtained by the optimized $H_2O:CO_2$ model to those found experimentally. The error bars include the uncertainties due to the choice of the temperature from which we integrate the second QMS peak and are between 10–20% for the different experimental data points. The error bars on the model results originate from the uncertainties in the input ice thicknesses, mixing ratios and binding energies and these were obtained by varying the model input values within the experimental uncertainty ranges and then comparing the model results. In general, the uncertainty in the mixing ratio has the largest effect, resulting in model prediction uncertainties of $\sim 15\%$. We conclude that CO_2 desorption from binary mixtures is quantitatively described by the model.

Predictive power

Figure 2.4b shows the output of the model for the $H_2O:CO_2:CO$ tertiary ice mixture experiments (Exp. 18 and 19). These experiments were not used to constrain the model and are as a test of its predictive power. The concentration dependency in these experiments is reproduced by the model; an increase in the concentration of volatiles leads to a decrease in the trapping fraction.

For the higher concentration mixture, $H_2O:CO_2:CO = 11:4:1$ (Fig. 2.4b, bottom panel), the model gives a CO desorption peak around 70 K (corresponding to the pure

CO₂ desorption temperature), peak that was also experimentally observed (Fig. 2.4a, bottom panel). In the model, this peak results from the formation of free desorption sites on the surface due to desorption of surface CO₂. CO molecules that are mixed with water migrate to and desorb from the surface easily since the swapping and binding energies are very low compared to the CO₂ values.

In addition to reproducing these qualitative trends for tertiary mixtures, the three-phase model also treats correctly the desorption order of both CO₂ desorption peaks. Finally Fig. 2.7 shows that the model provides a reasonable quantitative agreement between the predicted and experimentally determined amounts of CO₂ trapped in the tertiary ice mixtures (black diamonds). This is very promising for extending this proof-of-concept model to more species and more complex mixtures.

2.6 Astrophysical implications

Trapping of volatiles in H₂O ice is a crucial parameter when predicting the chemical evolution during star and planet formation (Viti et al. 2004). The modified three-phase desorption model is used here to test the effect of different initial ice compositions and ice thicknesses on ice mixture desorption. Ultimately the three-phase model should, however, be integrated in a protostellar collapse model to simulate the ice desorption accurately during star formation. The prime advantage of the three-phase model, as initially introduced by Hasegawa & Herbst (1993) and extended here, is that it can treat surface and ice chemistry correctly, since it differentiates between surface molecules that can react with gas phase molecules, and mantle molecules that are protected from further processing.

Figure 2.8 shows the amount of CO₂ ice with respect to the original H₂O ice abundance as a function of temperature for different ice thicknesses and mixing ratios heated at 1 K per 100 years, typical for infall of material during protostar formation (Jørgensen et al. 2005).

The percentage of CO₂ entrapment in a diluted water ice is significantly affected by the initial ice thickness and mixing ratio; 50% of the initial CO₂ abundance is trapped in a 10 ML ice and 95% in a 100 ML ice. A similarly dramatic difference is seen when assuming different initial ice mixtures: 64% of the CO₂ stays trapped in the 5:1 ice and the fraction increases to 84% for the 20:1 ice.

The treatment of these trapping dependencies is one of the key strengths of the extended three-phase desorption model presented here. Figure 2.9 compares CO₂ ice desorption from a H₂O:CO₂ ice using the extended three-phase model, the original three-phase model by Hasegawa & Herbst (1993), and the Viti et al. (2004) astrochemical network. Assuming a 20 ML thick H₂O:CO₂ 5:1 ice heated at 1 K per century, our model predicts that 64 % of the initial CO₂ will be trapped by the water ice, while the model by Hasegawa & Herbst (1993) predicts an 80 % trapping amount. This difference originates from the lack of mantle-surface diffusion in Hasegawa & Herbst (1993). Its implementation is clearly important to correctly treat trapping of volatiles and to account for segregation observed around protostars (Ehrenfreund et al. 1998; Pontoppidan et al. 2008).

All the CO₂ molecules are predicted to be trapped by the water ice when simu-

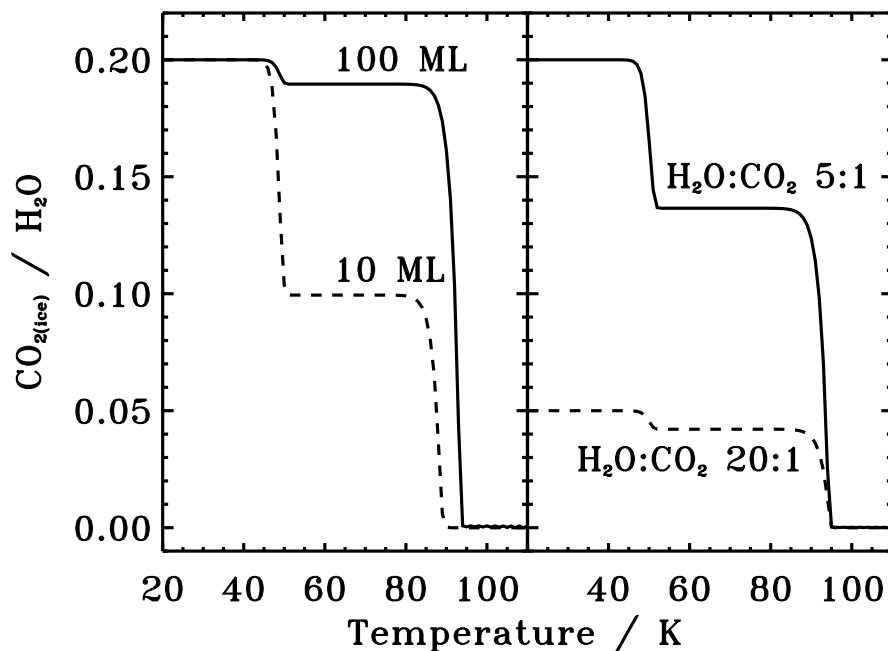


Figure 2.8: The amount of CO_2 ice during ice warm-up at 1 K per 100 years according to the three-phase model, assuming two different initial $H_2O:CO_2$ 5:1 ice mixture thicknesses (left panel) and two different 20 ML ice mixing ratios (right panel).

lating $H_2O:CO_2$ ice desorption with the Viti et al. (2004) model. The Viti et al. (2004) model assumes a different heating rate compared to the one used for the two three-phase models, but this only affects the desorption temperatures and does not affect the volatiles trapping fractions. Instead, the high trapping fraction is due to the fact that the model was parametrized based on a desorption experiment performed for a $H_2O:CO_2$ ice with a ratio of 20:1, which differs from the 5:1 – 4:1 ratio found in dense molecular clouds and protostellar envelopes (Knez et al. 2005; Pontoppidan et al. 2008). In the case of a $H_2O:CO_2$ 20:1 ices, our model outputs agree well with 100 % trapping fraction used by Viti et al. (2004), since we find that more than 95 % of the CO_2 is trapped by the water ice for 10 – 100 ML thick ices.

These different model predictions demonstrate the need for systematic laboratory studies when modelling ice desorption, since ice properties, such as ice thickness and mixing ratio, affect the desorption process. Even when using desorption step functions, the size of the step cannot be accurately decided from a single experiment. Rather the investment of multiple experiments are needed, together with their efficient parameterization, to obtain versatile models of ice desorption for arbitrary initial conditions. Already for binary ice mixtures, this results in large experimental data sets. It is therefore reassuring that using binary mixtures as templates for more complex ice mixtures results in approximately the correct trapping predictions.

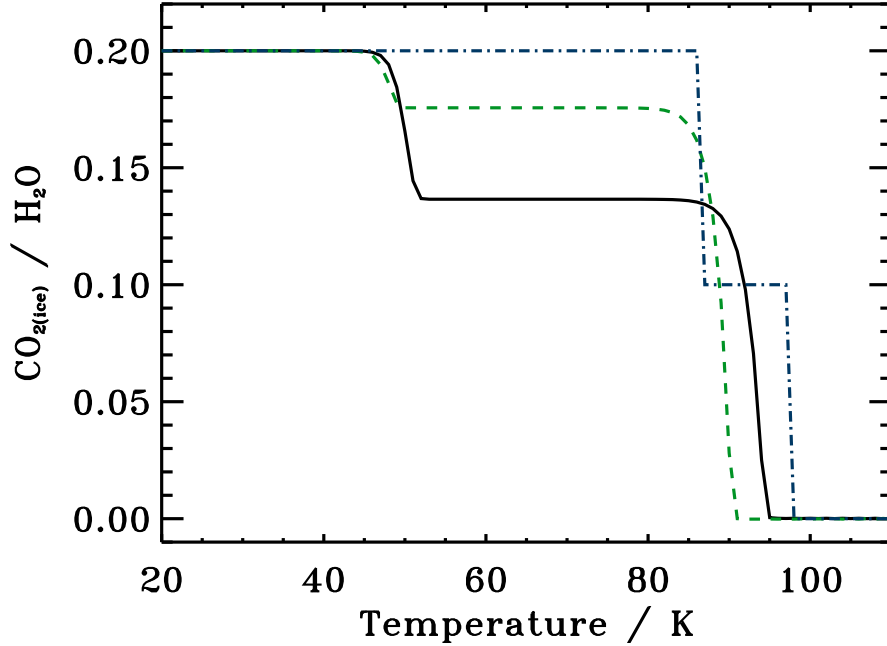


Figure 2.9: Amount of CO₂ ice during ice warm-up for a H₂O:CO₂ 5:1 ice 20 ML thick simulated by different models : the implemented three-phase model described here (black solid line), the original three-phase model by Hasegawa & Herbst (1993) (green dashed line), the Viti et al. (2004) model (blue dash-dotted line). A heating rate of 1 K per century is used in the two first models and desorption around a 5 solar masses protostar is presented from the Viti et al. (2004) model case.

2.7 Conclusions

Desorption from H₂O-rich ice mixtures is complex in that the amount of trapped ice depends not only on the species involved, but also on the mixture ratio and the ice thickness ; there is no constant fraction of volatile species trapped in a H₂O ice. This complex behavior can be reproduced by extending the three-phase model introduced by Hasegawa & Herbst (1993).

Using the H₂O:CO₂ ice system as a case study, we showed that a three-phase model that includes mantle-surface diffusion can reproduce the amount of trapped ice quantitatively in a range of binary ice mixtures. The appropriate input parameters for the H₂O:CO₂ system are a swapping energy $\epsilon_{\text{H}_2\text{O}-\text{CO}_2}^{\text{swap}}=2250$ K and a molecular parameter $c_{\text{CO}_2}=20.5$ ML, which describes from which ice depth diffusion to the surface can occur.

In the model, the different CO₂ and CO behavior can only be reproduced if $\epsilon_{\text{H}_2\text{O}-\text{CO}}^{\text{swap}} < \epsilon_{\text{H}_2\text{O}-\text{CO}_2}^{\text{swap}}$ and $c_{\text{CO}} > c_{\text{CO}_2}$. This suggests that diffusion/molecule swapping in H₂O-rich ices depends equally on the breaking of the H₂O-volatile bond (parametrized here by the swapping barrier height) and on the mass/volume of the diffusing volatile (parametrized here by the ice thickness that the molecule can diffuse through). The experimental trends found for H₂O:CO and H₂O:CO₂:CO ice mixture desorption are consistent with the H₂O:CO₂ trends, which suggests that the three-phase model is generally

appropriate to model ice mixture desorption.

However the ice desorption process is implemented in astrochemical models, this study demonstrates that it is vital to understand how ice mixture desorption depends on the ice characteristics. The extended three-phase model naturally treats ice desorption with the right kinetic order and reproduces volatile entrapment. Its use in astrochemical networks for grain-gas interactions should improve the predictions of gas-phase and grain-surface species abundances in astrophysical environments.

CO ice photodesorption: a wavelength-dependent study

Abstract. UV-induced photodesorption of ice is a non-thermal evaporation process that can explain the presence of cold molecular gas in a range of interstellar regions. Information on the average UV photodesorption yield of astrophysically important ices exists for broadband UV lamp experiments. UV fields around low-mass pre-main sequence stars, around shocks and in many other astrophysical environments are however often dominated by discrete atomic and molecular emission lines. It is therefore crucial to consider the wavelength dependence of photodesorption yields and mechanisms. In this work, for the first time, the wavelength-dependent photodesorption of pure CO ice is explored between 90 and 170 nm. The experiments are performed under ultra high vacuum conditions using tunable synchrotron radiation. Ice photodesorption is simultaneously probed by infrared absorption spectroscopy in reflection mode of the ice and by quadrupole mass spectrometry of the gas phase. The experimental results for CO reveal a strong wavelength dependence directly linked to the vibronic transition strengths of CO ice, implying that photodesorption is induced by electronic transition (DIET). The observed dependence on the ice absorption spectra implies relatively low photodesorption yields at 121.6 nm (Lyman α), where CO barely absorbs, compared to the high yields found at wavelengths coinciding with transitions into the first electronic state of CO ($A^1\Pi$ at 150 nm); the CO photodesorption rates depend strongly on the UV profiles encountered in different star formation environments.

E. C. Fayolle, M. Bertin, C. Romanzin, X. Michaut, K. I. Öberg, H. Linnartz, J.-H. Fillion,
The Astrophysical Journal Letters, 739, L36, (2011)

3.1 Introduction

Carbon monoxide, the second most abundant molecule observed in the gas phase of the interstellar medium (ISM) after H_2 , is also one of the most commonly detected molecules in the solid phase, condensed on the surface of sub-micron sized dust grains (e.g. Pontoppidan et al. 2003). Mechanisms triggering CO phase transitions under densities and temperatures encountered in star forming environments are crucial to interpret observations of CO lines. In cold parts of the ISM, most of the CO is depleted onto the grains but non-thermal desorption mechanisms, such as UV photodesorption or cosmic ray sputtering, can maintain a part of the CO budget in the gas phase, explaining the presence of CO below its thermal desorption temperature (e.g. Willacy & Langer 2000).

Desorption of CO ice induced by UV photons under astrophysically relevant conditions has recently been studied by Öberg et al. (2007, 2009), and Muñoz Caro et al. (2010) using an H_2 based broadband microwave discharge lamp as photon source and monitoring the ice loss through infrared spectroscopy during irradiation. The derived photodesorption rates are substantially higher than previously assumed (Greenberg 1973), but differ by up to a factor of 20 between the two groups. Absolute photodesorption yield values have substantial uncertainties resulting from (1) the different photon flux calibration – Öberg et al. (2007, 2009) used a NIST-calibrated photodiode whereas Muñoz Caro et al. (2010) employed a chemical actionometry method – and (2) the IR measurement of the ice sublimation, performed in transmission in the case of Muñoz Caro et al. (2010), and in reflection in the case of Öberg et al. (2007, 2009). Nonetheless, the combined uncertainties are estimated to a factor of a few and cannot fully account for the order of magnitude difference between the two groups. The different UV irradiation profiles of the two discharge lamps may instead be at the origin of this discrepancy if the photodesorption efficiency is wavelength dependent.

From these studies, excitation of CO in its first electronic state was proposed to induce desorption after energy transfer to neighboring CO molecules and rearrangement of the ice surface (M.C. van Hemert 2010, private communication). Wavelength-resolved studies are required to confirm this mechanism and to investigate whether the photodesorption mechanism of CO is wavelength dependent.

Wavelength-resolved photodesorption yields are also important for astrochemical networks. Different FUV field profiles are encountered at different star formation stages and around young stellar objects of different spectral types. The FUV can be dominated by the interstellar radiation field (ISRF) at the edge of molecular clouds, cosmic-rays excited H_2 emission in starless clouds (Gredel et al. 1987), black body emission from protostars, and emission lines due to material accretion onto the protostar or pre-main-sequence star (Bergin et al. 2003; van Dishoeck et al. 2006). Thus if photodesorption yields are wavelength-dependent, the photodesorption yield per incident UV photon may vary significantly in different star-forming environments.

In order to fully characterize the CO photodesorption process, the present work investigates for the first time the wavelength dependence of CO photodesorption yields for astrophysically relevant ices and conditions. The experimental techniques for ice preparation and synchrotron-based irradiations are explained in Section 3.2. The re-

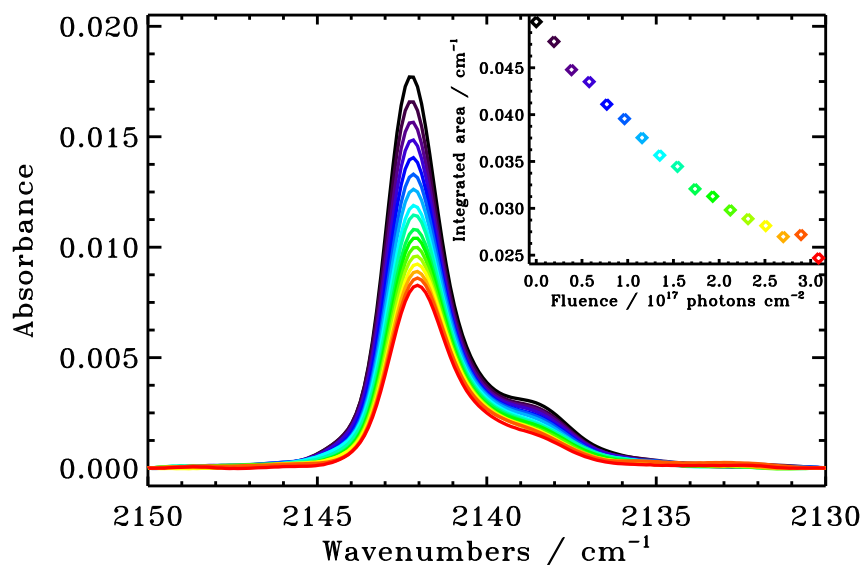


Figure 3.1: Decrease of the CO vibration RAIRS signal during irradiation of a CO ice 10 ML thick at 18 K by 9.2 eV photons. Inset shows the integrated area of the corresponding CO RAIRS band vs. UV fluence.

sults are described in Section 5.3 and the mechanism and astrophysical implications are discussed in Section 5.4.

3.2 Experimental

CO ices are grown and irradiated in the SPICES (Surface Processes in ICES) apparatus, described in detail elsewhere (Bertin et al. 2011). CO ice films are prepared under ultra high vacuum (UHV) conditions (base pressure: 5×10^{-10} Torr) on a polycrystalline gold substrate which is cooled down to 18 K by a closed cycle helium cryostat. The CO ices are grown via background deposition, i.e., by exposing the cold Au surface to a partial pressure of CO gas (Air Liquide, 99% purity) during a given time. The amount of CO deposited on the surface is monitored through Reflection Absorption InfraRed Spectroscopy (RAIRS). The thickness of the deposited ice in monolayers (ML) is obtained by performing an isothermal desorption experiment of the CO ice monitored by RAIRS, resulting in the absorbance of 1 monolayer of CO ice (Öberg et al. 2009). Complementary estimations of the CO ice thickness have also been performed using Temperature Programmed Desorption (TPD) experiments and from the exposure, assuming a sticking coefficient of unity. All techniques gave similar results, yielding ice thicknesses between 9 and 10 ML.

The set-up is equipped with two complementary photodesorption detection techniques. A Quadrupole Mass Spectrometer (QMS) allows the detection of gas phase molecules within the UHV chamber, while condensed molecules are probed by RAIRS. Simultaneous probing of the remaining condensed molecules and of the gas-phase photodesorbed molecules is therefore possible during ice irradiation. QMS measure-

Table 3.1. Energy dependent photodesorption rates for 10 ML thick CO ice at 18 K

Irradiation Energy (eV)	Relative Rate ($\text{cm}^{-1} (\text{photons cm}^{-2})^{-1}$)	Absolute Rate ($\text{molecules photon}^{-1}$)
8.2	2.19×10^{-19}	$2.8 \pm 1.7 \times 10^{-2}$
9.2	1.07×10^{-19}	$1.3 \pm 0.91 \times 10^{-2}$
10.2	0.54×10^{-19}	$6.9 \pm 2.4 \times 10^{-3}$
11.2	0.74×10^{-19}	$9.3 \pm 3.4 \times 10^{-3}$

ments are used to determine the relative photodesorption rates for all employed UV fluxes, while RAIRS provides absolute yields for UV fluxes higher than 10^{13} photons s^{-1} .

The UHV set-up is connected to the undulator-based FUV beamline DESIRS at the SOLEIL synchrotron facility in Saint-Aubin (France). In a first irradiation mode, the photon beam from the undulator stage is used directly. The high harmonics of the photon energy are filtered using a rare-gas filled chamber, set in the pass of the UV beam. Absolute incident photon fluxes are measured using calibrated photodiodes. This setting yields high photon flux (10^{14} photons s^{-1}) at selected energies with a well defined photon energy distribution (Lorentzian with FWHM of 1 eV). Irradiations at fixed photon energies (8.2, 9.2, 10.2, and 11.2 eV) are performed to monitor the CO ice loss with photon fluence using RAIR spectroscopy (see Figure 3.1). These experiments are used to derive absolute photodesorption rates for different spectral windows where CO ice absorption is known to differ (see Section 3.3.1).

In a second irradiation mode, the photons enter a 6.65 m normal incidence monochromator equipped with a 200 grooves mm^{-1} grating. In this configuration, a photon flux up to 10^{12} photons s^{-1} with a resolution of 40 meV at 10 eV for a 700 μm exit slit is achieved. The CO ice film is then irradiated by photons whose energy is linearly increased throughout the experiment, from 7 to 13.6 eV (90 to 170 nm). A relative photodesorption rate spectrum is obtained by recording the QMS signal of desorbing CO while tuning the photon energy (see upper panel of Figure 3.2 and Section 3.3.2).

3.3 Results

3.3.1 Absolute photodesorption yields for 1 eV spectral windows

Figure 3.1 shows the decrease of the CO stretching feature during irradiation of a 10 ML thick ice at 18 K by 9.2 eV photons at a flux of 1.2×10^{14} photons s^{-1} . The double-peaked structure of the infrared feature does not change during ice growth and is most likely due to the roughness of the gold substrate; the peak structure is known to be sensitive to the arrangement of adsorbed molecules on the surface (Elisabetta Palumbo et al. 2006). The evolution of the CO absorption band integrated area as a function of photon fluence is shown in the inset. The integrated band area is directly proportional to the amount of CO ice (from RAIR spectra acquired during ice growth). The loss of integrated band area during irradiation can therefore be used to quantify CO desorp-

tion.

The observed linear relationship between CO ice integrated area and photon fluence is consistent with a zeroth-order process, similar to what has been seen for broadband irradiation experiments (Öberg et al. 2007; Muñoz Caro et al. 2010). This zeroth-order kinetics is observed for the four explored irradiation energies (8.2, 9.2, 10.2, and 11.2 eV) until the ice coverage gets below 0.03 cm^{-1} integrated absorbance ($\sim 6 \text{ ML}$). The same effect has been observed by (Muñoz Caro et al. 2010). Fitting straight lines to the linear parts of the ice loss at the four investigated irradiation energies provides energy-dependent photodesorption yields.

The results from the fits are summarized in Table 3.1. The relative photodesorption yields (absorbance per incident photon flux) are converted into absolute photodesorption yields (CO molecules per incident photon) using the absorbance to ML conversion factor for the present RAIRS set-up (Section 3.2) and assuming that $1 \text{ ML} = 10^{15} \text{ molecules cm}^{-2}$. The uncertainties in the relative yields are due to the intrinsic RAIRS measurement uncertainties. The larger uncertainties on the absolute yields are due to ice thickness calibration and to differences in the FUV irradiated area versus IR probed area. Indeed, the sample area probed by the IR beam and the UV-beam spot at the surface are $1 \pm 0.1 \text{ cm}^2$ and $0.7 \pm 0.1 \text{ cm}^2$, respectively. Caution has been taken to ensure that the UV irradiated area is integrally probed by the IR beam. The photodesorption yields vary between 6.9 and $28 \times 10^{-3} \text{ molecules photon}^{-1}$ for the investigated energy range and are thus clearly wavelength-dependent. The lowest yield is obtained at 10.2 eV, which is important considering that previous photodesorption results were based on broadband UV discharge lamps, which are often dominated by photons at this excitation energy. In addition, the strong variation with photon energy motivates a more detailed investigation on the energy dependence of the photodesorption yield.

3.3.2 CO photodesorption yield spectrum

A detailed investigation of the wavelength dependence is achieved in the second kind of experiment, where a 10 ML thick CO ice sample is irradiated by a monochromatic photon beam scanning 7–13.6 eV at a constant rate, while probing photodesorption with the QMS. The QMS current resulting from the desorbing gas phase CO ($m/z = 28$) versus photon energy is presented in Figure 3.2 together with a UV absorption spectra of CO ice from Lu et al. (2005). This photodesorption spectrum is converted into molecules photon^{-1} using the absolute photodesorption yields, obtained from the first series of experiments (Section 3.3.1, Table 3.1). The scaling takes into account the exact spectral profiles in the 1 eV spectral-window experiments, which was monitored carefully for the 8.2 eV window. Figure 3.2(a) shows that when probed at a high spectral resolution, the photodesorption yield varies even more across the investigated energy range compared to the 1 eV spectral-window measurements. The lowest yield is achieved below 7.8 eV and at 10.2 eV ($< 6 \times 10^{-3} \text{ molecules photon}^{-1}$) and it is an order of magnitude lower than the peak value of $5 \times 10^{-2} \text{ molecules photon}^{-1}$ at $\sim 8.2 \text{ eV}$. The average UV profile below 10 eV results in a total photodesorption yield of $1.8 \times 10^{-2} \text{ molecules photon}^{-1}$. This value is a factor of seven higher than the previously reported yield of $2.7 \times 10^{-3} \text{ molecules photon}^{-1}$ from Öberg et al. (2009), and

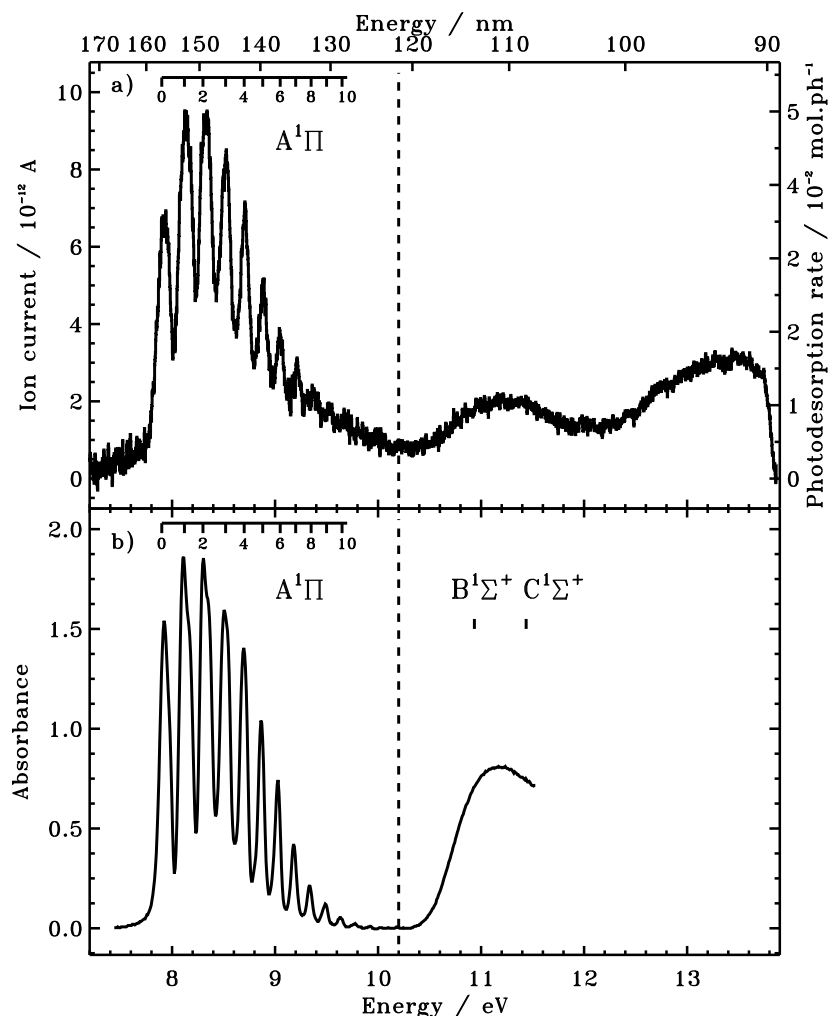


Figure 3.2: (a) Photodesorption spectrum (after background subtraction) of a 10 ML CO ice at 18 K using a resolution of 40 meV (at 10 eV) and a scan step of 12 meV every 0.5 s. (b) Absorption spectrum of solid CO at 10 K (Lu et al. 2005). The dashed line indicates photodesorption and absorption values at Ly α , 121.6 nm.

comparable within a factor of two to the yield of 3.5×10^{-2} molecules photon $^{-1}$ found by Muñoz Caro et al. (2010). The relative contribution of Ly α photons (and their inefficiency at inducing photodesorption) to the total photon flux in each experiment is a probable origin for the different yields, further stressing the importance of wavelength resolved studies.

3.4 Discussion

3.4.1 Mechanism

The photodesorption spectrum (Figure 3.2(a)) has a band structure below 10 eV that is almost identical to the absorption spectrum of pure CO ice obtained by Lu et al. (2005). The observed spectral progression is attributed to the transition from

CO ground state to vibrational levels of the first allowed electronic state ($A^1\Pi$). The striking similarity between the two spectra provides the first experimental evidence that desorption is a DIET (Desorption Induced by Electronic Transition) process, as previously suggested by Öberg et al. (2007, 2009). Desorption of condensed molecules is probably induced by subsequent relaxation of the excited molecules via energetic transfer from electronic to vibrational degrees of freedom (Avouris & Walkup 1989). This process clearly dominates the spectrum below 10 eV. Above 10 eV, the main photodesorption mechanism is expected to be more complex since the second absorption band of CO is dissociative. In this case, photodesorption may result from several relaxation pathways, including chemical recombination and desorption, as proposed in the case of water (Westley et al. 1995a; Watanabe et al. 2000; Arasa et al. 2010).

It should be noted that electrons, resulting from the interaction of incident UV photons with the metallic substrate, may also contribute to the observed CO ice desorption. Most of the UV photons can be absorbed by the metallic substrate since the ice coverage is an order of magnitude below the coverage limit for which most of the photons would be absorbed by the ice before reaching the substrate. Hot electrons resulting from electron-hole pair excitation of gold are expected to be produced for all investigated irradiation energies and may induce desorption (e.g. Bonn et al. 1999). Free electrons photo-emitted from the gold substrate may also induce CO desorption by electronic excitation or resonant electron attachment (Schulz 1973; Rakhovskaia et al. 1995; Shi et al. 1998; Mann et al. 1995). Only photons whose energy is above 10 eV can produce secondary free electrons energetic enough to trigger the latter process, since the CO-covered gold surface work function is $\sim 4.4\text{eV}$ (Gottfried et al. 2003). The importance of these electron-induced processes can be estimated from our experiment, since the production of electrons (primary photoelectrons and inelastically diffused secondary electrons) that have enough kinetic energy to trigger the CO desorption process within the ice, should increase with the photon energy. This effect is barely observed; electrons are most likely the cause of the low-level continuously increasing desorption background seen in Figure 3.2(a). In other words, DIET is the main pathway leading to the observed photodesorption below 10 eV, resulting in a strong energy dependence of the photodesorption yields.

3.4.2 Astrophysical implications

The determined strong wavelength dependence of the photodesorption yield of CO ice presented in Figure 3.2(a) demonstrates that the CO photodesorption yield is expected to vary significantly in different astrophysical environments. Incorporating this information into astrochemical networks is important to accurately predict the partitioning of CO between the gas and ice. Table 3.2 exemplifies how this wavelength dependent data can be used to predict the photodesorption efficiency in sources with characteristic UV fields. The listed photodesorption yields have been calculated by convolving UV field profiles from the literature with the CO photodesorption spectrum presented in Figure 3.2(a) between 90 and 180 nm. The UV profiles are the ISRF from Mathis et al. (1983) appropriate to model the UV field at the edges of molecular clouds, an emission spectrum of cosmic-ray-excited H_2 (Gredel et al. 1987) to mimic UV field

Table 3.2. CO Photodesorption in Different ISM Environments

Environment	Yield (molecules photon ⁻¹)	References for UV profile
Edges of clouds	1.2×10^{-2}	Mathis et al. (1983)
Pre-stellar cores	9.4×10^{-3}	Gredel et al. (1987)
Black body 10,000K	6.4×10^{-3}	van Dishoeck et al. (2006)
Tw Hydrae	6.6×10^{-3}	Bergin et al. (2003)
Pure Ly α	4.1×10^{-3}	121.6 nm

encountered in cloud cores, a 10,000 K black body for the UV field around an Herbig Ae star (van Dishoeck et al. 2006) and the emission of TW Hydrae from (Bergin et al. 2003) to illustrate photodesorption in protoplanetary disks. Pure Ly α is also added for comparison. The calculated characteristic photodesorption yields vary by a factor of four, with the lowest yields around T Tauri stars and other environments where the UV field is dominated by Ly α photons, and the highest yields per incident photon at cloud edges and next to a 10,000 K black body. The photodesorption yields used here are valid for pure CO ice thicker than ~ 6 ML, as stated in Section 3.3.1. How the CO photodesorption efficiency and mechanism change with ice thickness and/or composition should certainly be studied in order to extend the applicability of the present results to thinner pure CO ices or mixed CO containing astrophysical ices.

It is important to note that the UV spectral profile deeper into the cloud and disk may be radically different compared to the UV field incident on the cloud and disk surface because of wavelength-dependent radiative transfer. Determining accurate interstellar relevant photodesorption yields requires a combination of photodesorption spectrum and detailed UV radiative transfer. In the meantime, the presented photodesorption spectrum is recommended to calculate photodesorption yields for specific environments (Table 3.2).

3.5 Conclusions

This study provides the first photodesorption spectrum of pure CO ice, obtained by tunable synchrotron UV irradiation of CO ice under astrophysically relevant conditions. A quantitative determination of the photodesorption yields at 8.2–13.6 eV has been achieved by the simultaneous probe of the ice- and gas- phase CO concentrations coupled to either narrowband (1 eV) excitation mode at selected energies or to continuous energy scanning by monochromatic UV radiation. The resulting photodesorption yields vary by an order of magnitude over the investigated wavelength range. The CO photodesorption process is dominated by the direct electronic excitation of the condensed CO molecules (DIET) below 10 eV. Other desorption mechanisms involving secondary electrons due to UV interactions with the substrate are present, but their contributions to the total measured desorption yield are minor. Consistent with a DIET mechanism, the photodesorption yield of CO ice at Ly α is low. This may result

in different chemical evolutions in regions where the UV field is dominated by line emission compared to regions where the UV emission is due to black body radiation. The calibrated photodesorption spectrum presented here should therefore be used to determine the characteristic CO ice photodesorption yields by convolving the CO photodesorption spectrum to the UV profile found in a specific astrophysical environment. In general, the link between wavelength-dependent UV absorption of the ice and the resulting photodesorption and photochemistry is key to implement astrochemical gas-grain models and should be experimentally investigated for relevant ice species.

UV photodesorption of interstellar CO ice analogues: from subsurface excitation to surface desorption

Abstract. Carbon monoxide is after H₂ the most abundant molecule identified in the interstellar medium (ISM), and is used as a major tracer for the gas phase physical conditions. Accreted at the surface of water-rich icy grains, CO is considered to be the starting point of a complex organic presumably prebiotic chemistry. Non-thermal desorption processes, and especially photodesorption by UV photons, are seen as the main cause that drives the gas-to-ice CO balance in the colder parts of the ISM. The process is known to be efficient and wavelength-dependent, but, the underlying mechanism and the physicalchemical parameters governing the photodesorption are still largely unknown. Using monochromatized photons from a synchrotron beamline, we reveal that the molecular mechanism responsible for CO photoejection is an indirect, (sub)surface-located process. The local environment of the molecules plays a key role in the photodesorption efficiency, and is quenched by at least an order of magnitude for CO interacting with a water ice surface.

M. Bertin, E. C. Fayolle, C. Romanzin, K. I. Öberg, X. Michaut, A. Moudens, L. Philippe, P. Jeseck, H. Linnartz and J.-H. Fillion,
Physical Chemistry Chemical Physics, 14, 9929-9935, (2012)

4.1 Introduction

In cold and dense interstellar regions, i.e. circumstellar clouds, protostellar envelopes and protoplanetary disks, molecules collide with and stick to (sub)micron-sized silicate and carbonaceous particles, resulting in icy mantles (Tielens & Hagen 1982). The two most abundant species found on icy dust grains in space are CO and H₂O (Gillett & Forrest 1973; Dartois 2005; Öberg et al. 2011a). From observational ice mapping and from spectroscopic details of CO infrared features, it has been concluded that the H₂O ice layer forms first on the grain and that most CO ice is present on top of the H₂O ice (e.g. Pontoppidan et al. 2008; Cuppen et al. 2011). The resulting balance of molecules in the solid state and in the gas phase is determined by freeze-out and sublimation, and specifically the CO ice/gas balance is of great interest for several reasons. First, gas phase CO is the most commonly used tracer of density and temperature in astrophysical environments. Therefore, accurate information on conditions under which CO can be found in the gas phase is vital to interpret such observations (Bergin et al. 2001; Qi et al. 2006). Second, CO ice is seen as the precursor of CH₃OH in space, which in its turn is the proposed starting point of a rich extra-terrestrial organic chemistry with possible ties to the origins of life (Fuchs et al. 2009; Öberg et al. 2009a; Watanabe & Kouchi 2002; Herbst & van Dishoeck 2009). Consequently, third, the exact location of CO freeze-out in the protoplanetary disks is proposed to affect the composition of exoplanets (Öberg et al. 2011b). Ice sublimation can occur through both thermal (Burke & Brown 2010) and non-thermal desorption processes, and which process is finally determining the ice/gas balance depends on the temperature and radiation or particle flux. Astrophysical environments contain vacuum UV photons, cosmic-rays, and/or electrons, which all have the potential to induce ice sublimation and thus contribute to the gas-to-ice balance (e.g. Shen et al. 2004). Non-thermal desorption is expected to be especially important in cold regions ($T < 20$ K), where thermal effects are negligible; observations of rotationally cold gas-phase CO in such regions suggest the presence of an efficient non-thermal desorption process (V. Piétu et al. 2007; Oka et al. 2011). In order to quantify and model non-thermal sublimation for ices exposed to astrophysical flux levels and astronomical time scales, these processes must be understood at a molecular level. In this study we focus on vacuum UV photodesorption of CO ice, the proposed dominating non-thermal desorption process in most interstellar environments (Willacy & Langer 2000). The UV photodesorption of CO ice has been investigated in the laboratory in a number of studies using thin physisorbed CO ice films at temperatures between 10 and 25 K, irradiated by photons from broad-band H₂ discharge lamps peaking at 10.2 eV (Lyman- α). These studies have provided important empirical constraints: CO photodesorption is an efficient zeroth-order process, which depends on the ice temperature and seems confined to the ice surface or top few ice layers (Muñoz Caro et al. 2010; Öberg et al. 2007, 2009). More recently, we carried out a pilot study to investigate the photon energy dependence of the CO photodesorption yields. In those experiments synchrotron radiation was used to irradiate a CO ice with energies between 7 and 14 eV, the relevant UV range for star-forming regions, while monitoring the amount of CO photodesorbed in the gas phase. These measurements demonstrated that the UV photodesorption of CO ice is highly wavelength dependent

and directly correlated with the electronic absorption spectrum of the ice, suggesting that desorption is induced by electronic transition (DIET). Monochromatic ice photodesorption studies are thus a potentially powerful technique to probe the underlying molecular sublimation mechanism (Fayolle et al. 2011). In the present work we build on the technical developments and preliminary results available from the pilot study to obtain the first comprehensive view of the CO ice UV photodesorption process. The ultimate goal is a full mechanistic understanding, and this requires resolving the location of the relevant excitation process, determining the role of the substrate, and constraining whether excited molecules desorb themselves or distribute energy to neighboring CO molecules, resulting in an indirect desorption mechanism. Disentangling the role of the substrate and which parts of the ice are photodesorption-active are key issues that need to be addressed to accurately extrapolate the laboratory results to astronomical boundaries. In the present chapter, narrowband tunable UV radiations from the DESIRS synchrotron beamline and state-of-the-art surface science techniques are used to probe the photodesorption mechanism at a molecular level, highlighting new key-parameters that drive the efficiency of the process. Especially, different local CO environments, mimicking realistic conditions in interstellar ices (pure CO ice or CO interacting with water), are shown to have a dramatic effect on the photodesorption efficiency.

4.2 Methods

The CO ices photodesorption study is realized in the SPICES (Surface Processes & ICES) setup of the UPMC (Université Pierre et Marie Curie). Molecular ices (CO and/or H₂O) of various thicknesses are grown with monolayer precision under ultrahigh vacuum (UHV) conditions ($P < 5 \times 10^{-10}$ Torr) on a highly oriented pyrolytic graphite (HOPG) or a polycrystalline gold substrate. The two substrates are mounted on opposite sides of the tip of a turnable coldhead that is cooled down to 14 K by a closed cycle helium cryostat. The ice layers are grown by diffuse deposition of CO gas (Air Liquide, 99% purity) or H₂O vapour (high purity, liquid chromatography standard from Fluka) and the setup allows for accurate growth of different isotopic layers on top of each other. The quantities of molecules deposited on the substrate are expressed in ML_{eq} or BL_{eq} (mono/bilayer equivalents for CO and H₂O, respectively) corresponding to the density of a compact molecular layer on a flat surface, with $1\text{ML}_{\text{eq}} = 1\text{BL}_{\text{eq}} = 1 \times 10^{15}$ molecule per cm² (Collings et al. 2003a; Chakarov et al. 1995). The Temperature Programmed Desorption (TPD) method is used for the calibration of the ice thicknesses, resulting in reproducible parameters for the growth conditions with a 1 ML_{eq} precision. This technique is also employed to characterize the CO adsorption onto amorphous or crystalline water ices. The shape and position of the desorption peaks are related to CO desorption from (i) pure CO multilayers, (ii) a CO monolayer interacting with the water surface, and (iii) CO trapped within the water ice, as already studied in Collings et al. (2003a) and Collings et al. (2003b). UV photodesorption is induced through irradiation of the CO ice sample by the continuous output of the undulator-based vacuum UV DESIRS beamline of the synchrotron SOLEIL, providing photons whose energy can be continuously scanned over the 7 to

14 eV range. A narrow bandwidth of typically 40 meV is selected by the 6.65 m normal incidence monochromator implemented in the beamline. A specific gas filter equipping the beamline suppresses the high harmonics of the undulator that could be transmitted by the grating higher orders of diffraction. The absolute incident photon flux impinging onto the sample, measured by a calibrated photodiode, is about 10^{12} photons per s. The UHV setup and the beamline are directly connected, without any window, in order to prevent radiation cut-off. The photodesorption spectra are recorded in real time, i.e. during ice irradiation, monitoring the gas phase composition by means of a Quadrupole Mass Spectrometer (QMS). The desorption rate per incident photon is derived from the resulting Photon-Stimulated Desorption (PSD) spectra and the measured energy-dependent photon flux Fayolle et al. (2011). In the presented PSD spectra, the photon energy is automatically scanned from 7 to 14 eV with steps of 25 meV. Each energy step lasts 5 s. In the mean time, the QMS signal is recorded with a dwell of 1 s, which makes an average of 5 points per energy step. Caution has been taken so that, for each point, the 1 s accumulation time is much longer than the QMS mass signal build-up time, thus preventing artefacts due to the energy scan speed. Indeed, it has been verified that changing the scanning speed does not lead to a modification of the mass signal-energy correlation in the PSD spectra.

Simultaneously, the composition of the condensed phase can be monitored using Fourier Transform Reflection Absorption Infrared Spectroscopy (FT-RAIRS). At the relatively low doses used, no newly formed species has been observed during the irradiations regardless of ice (pure CO or H₂O – CO ices), neither in the condensed phase nor in the gas phase. Therefore, chemistry is not expected to play a measurable role in our PSD experiments. More experimental details on the used UHV setup SPICES are available from Bertin et al. (2011) and the use of SOLEIL/DESIRS as a VUV light source from Nahon et al. (2012).

4.3 Results and discussion

4.3.1 Pure CO ice desorption - an exclusive DIET process

Fig. 4.1 presents the Photon Stimulated Desorption spectra of pure CO ices deposited on polycrystalline gold (Fig. 4.1a) and Highly Oriented Pyrolytic Graphite (HOPG) (Fig. 4.1b) at 14 K at ice thicknesses from 3 to 250 ML_{eq}. The spectra are obtained by recording the mass signal of desorbing CO in the gas phase while irradiating a pure CO ice with UV light continuously tuned from 7 to 14 eV. From this, the CO photodesorption rate is derived as a function of the energy of the incident photons. In agreement with Fayolle et al. (2011) the CO photodesorption rate is found to be strongly wavelength-dependent, and to follow below 10.5 eV the UV absorption spectrum of condensed CO (Lu et al. 2005). The observed pattern is due to the vibronic progression of the transition from the electronic $X^1\Sigma^+(v=0)$ ground state to the first dipole-allowed excited electronic state $A^1\Pi(v'=0, 1, 2, \dots)$ of the condensed CO molecules. The recorded PSD spectrum, logically, indicates that photodesorption is triggered by an electronic excitation within the molecular ice. Since the first electronically excited $A^1\Pi$ level is a non-dissociative state (Okabe 1978; Cottin et al. 2003),

desorption triggered by the fragmentation of CO can be excluded. Thus, the desorption process must occur via a direct transfer of absorbed energy, in which the electronic excitation energy is redistributed to intra- or intermolecular vibrational modes that provide the kinetic energy for the CO ejection. This mechanism is known as a DIET process (Desorption Induced by Electronic Transition) (Avouris & Walkup 1989; Bejan 2004; Rakhovskaia et al. 1995). DIET may not be acting exclusively, however. In particular, UV-induced substrate-mediated processes may contribute - non-resonantly - to the overall CO photodesorption rate. Photoelectrons originating from the substrate may trigger CO desorption through electronic excitation or electron attachment (Rakhovskaia et al. 1995; Mann et al. 1995; Shi et al. 1998). UV-induced electronhole pairs also can contribute to the CO desorption through a strong electron - phonon coupling (Bonn et al. 1999; Funk et al. 2000). Because all these processes involve the substrate - ice interface, the potential contribution from these processes to the overall photodesorption rate is expected to be different for different substrate surfaces, and to be less prominent for thick CO ice coverage, since the number of photons reaching the substrate decreases due to absorption by the above-lying ice. Fig. 4.1a and b show that the wavelength response and intensity of the photodesorption spectra are identical for the HOPG and gold surface and that there is no thickness dependency for coverages exceeding 3 ML_{eq}. This rules out that the substrate contributes substantially to the measured photodesorption rates and confirms that CO photodesorption is thus an exclusive DIET process.

4.3.2 Subsurface excitation

The use of different ice thicknesses allows us to constrain the ice region directly associated with the photodesorption events; Fig. 4.1 shows that CO photodesorption is equally efficient within a relative spread of 5% of the desorption signal for ice coverages over two orders of magnitude, from 250 ML_{eq} down to 3 ML_{eq}. This implies that only the topmost ice layers are involved in the photodesorption process.

To further localize the photodesorption process, vacuum UV photodesorption experiments are performed on layered and isotopically labeled CO ices, comprising thin layers of ¹³CO ice, deposited at different thicknesses on top of a 10 ML_{eq} thick ¹²CO ice. PSD spectra of desorbing ¹²CO (28 amu, Fig. 4.2a) and ¹³CO (29 amu, Fig. 4.2b) directly reveal from which ice layers molecules are photodesorbed. In the experiments, 1 ML_{eq} of ¹³CO deposited on ¹²CO reduces the ¹²CO desorption yield, but does not completely quench it, and a strong ¹³CO signal is observed. The addition of a second layer of ¹³CO largely blocks all ¹²CO desorptions, while the ¹³CO desorption rate becomes comparable to that of ¹²CO from 10 ML_{eq} pure ¹²CO ice. Only molecules from the two topmost layers are thus photodesorbed. These results do not necessarily imply, however, that the actual excitation process resulting in a photodesorption event only involves molecules in the top two ice layers. Complementary information on the excitation process can be extracted from the details of the PSD spectra; the peak positions in the PSD spectrum for different ¹³CO ice coverages between 7.5 and 10.5 eV presented in Fig. 4.2c (zoom-in of Fig. 4.2b) unveil precious information on the isotopologue location of the initial excitation step. For ¹³CO coatings thinner than 2 ML_{eq},

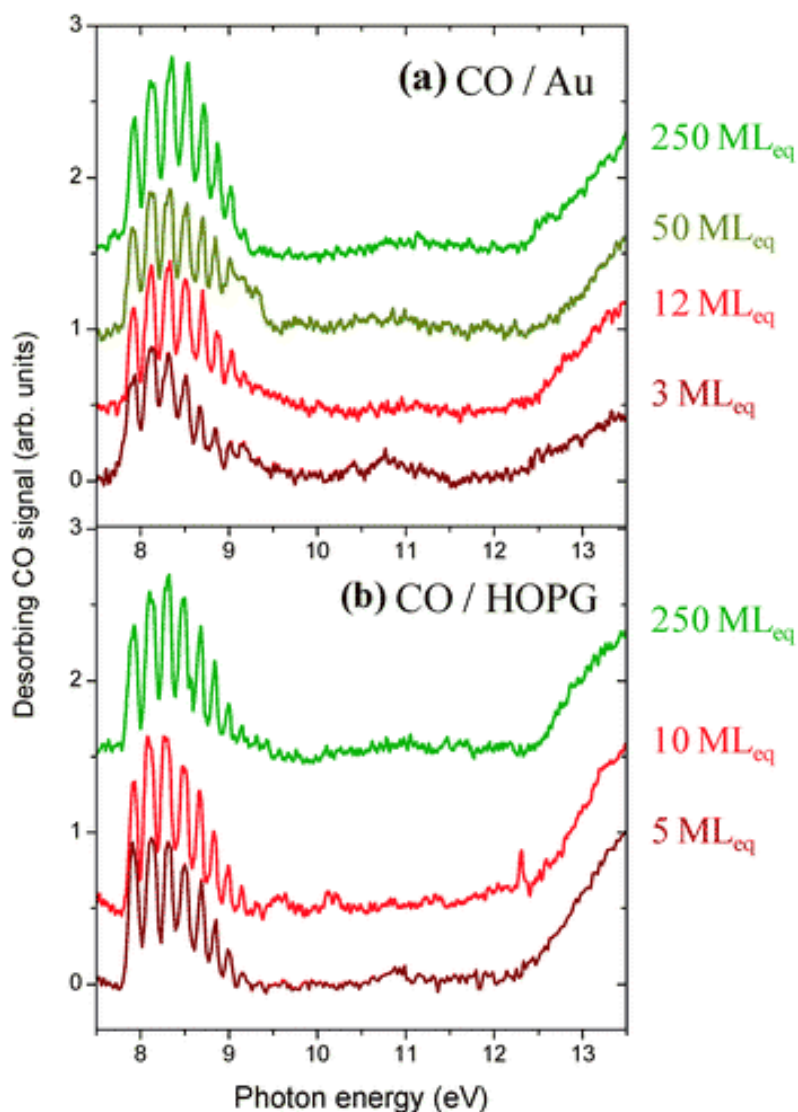


Figure 4.1: Photon-Stimulated Desorption (PSD) spectra for several thicknesses of pure CO ice deposited at 14 K on top of (a) a polycrystalline gold or (b) a highly oriented pyrolytic graphite (HOPG) surface.

the PSD spectrum matches the vibronic structure of the $A^1\Sigma(v) \rightarrow X^1\Sigma^+(v=0)$ electronic transition for condensed ^{12}CO (Lu et al. 2005). The majority of the initial photon absorption events therefore must take place in the underlying ^{12}CO ice and not in the isotopic top layer, from which the photodesorbing molecules originate; the excess energy deposited in the ^{12}CO is transferred to the surface ^{13}CO molecules. This is an indication that CO ice photodesorption is an indirect process where surface molecules are desorbed second to electronic excitation of sub-surface molecules. When the ^{13}CO cover layer exceeds 3 ML_{eq}, the spectral signature partially changes, as can be seen from the decrease in higher vibrational level spacings (Fig. 4.2c). Obviously transitions involving high v' vibrational levels in the upper electronic state are red shifted. Such a behavior is expected in the case of a heavier isotopologue excitation (^{13}CO com-

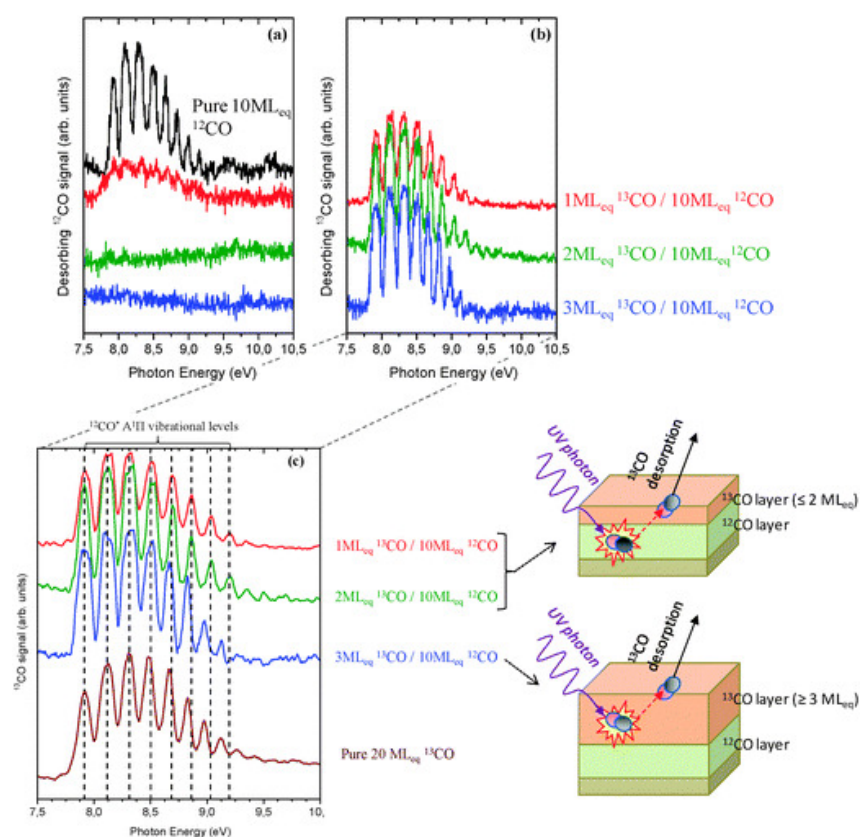


Figure 4.2: ^{12}CO (a) and ^{13}CO (b) photon stimulated desorption spectra at 14 K of 10 ML_{eq} ^{12}CO ice, covered with a layer of increasing thickness of ^{13}CO . The panel (c) shows a zoom-in of the ^{13}CO PSD spectra on the $^{13}\text{CO}/^{12}\text{CO}$ layered ice compared to the one obtained on a pure ^{13}CO ice at 14 K. The dashed lines correspond to the energies of the first vibronic levels in a pure ^{12}CO ice from Lu et al. (2005).

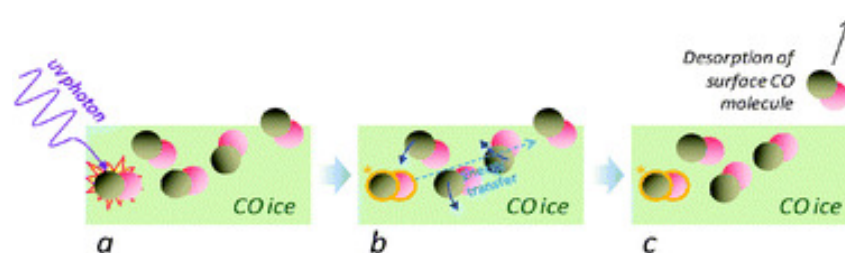


Figure 4.3: Scheme of the CO photodesorption three-step mechanism: (a) a UV photon is absorbed in the subsurface region of the CO ice, promoting a molecule into its $A^1\Pi$ electronic state, (b) the neighbouring CO rearrange around the excited molecule, resulting in the excitation of intermolecular vibrational modes, and (c) a surface CO molecule receives enough kinetic energy to be ejected from the ice.

pared to ^{12}CO), and should therefore be associated with the excitation of the $^1\Pi(v')$ levels of the condensed ^{13}CO . Indeed, the obtained PSD spectrum becomes identical to the PSD spectrum of a pure 20ML_{eq} ice of ^{13}CO . As 3 ML_{eq} of ^{13}CO are needed to ob-

serve ^{13}CO -related absorption features, it is likely that the initial excitation step occurs within the 2 to 3 topmost molecular layers. UV absorption in the top ice layer does not efficiently result in a photodesorption event; rather CO UV photodesorption is a three-step process at the investigated UV frequencies. This is schematically depicted in Fig. 4.3: (i) a subsurface-located CO molecule absorbs a UV photon and gets electronically excited, (ii) the internal excess energy of the excited molecule gets partly transferred to a surface-located CO molecule via the excitation of intermolecular vibrational modes, providing sufficient energy to (iii) eject a surface molecule into the gas phase.

This finding of an indirect DIET mechanism has important consequences concerning the carbon monoxide UV-photodesorption on interstellar grains, since it implies that the presence of other species interacting with CO molecules can potentially perturb, or even quench, the intermolecular energy transfer mechanism. This effect has therefore been tested here experimentally by determining the photodesorption efficiency of the astronomically relevant scenario of CO ices deposited on top of water ice.

4.3.3 Photodesorption of solid CO on top of H_2O ice

The CO photodesorption yield from top of H_2O ice provides an important complementary check for the proposed indirect DIET mechanism. As mentioned before CO ice in the interstellar medium is mainly found on top of H_2O -ice-coated dust grains, where it may be involved in chemical processes leading to H_2CO or CH_3OH formation. The thickness of this ice layer varies substantially, and ice observations using the Very Large Telescope (VLT) conclude that in space CO is both present in a pure CO ice phase, and in a phase that is strongly interacting through hydrogen bonding, presumably with the water molecules of the underlying ice (Pontoppidan et al. 2003,?). The two relevant photodesorption yields that need to be experimentally characterized are thus from pure CO ices, and from CO layers on top of H_2O . From the pure CO ice experiments, CO ices thicker than 2 layers are expected to desorb following a DIET indirect process, and it is unclear whether this indirect process will work if the CO molecules are interacting with subsurface H_2O in addition to other CO molecules. In order to address this question, PSD experiments of CO ice on top of H_2O have been performed using the same experimental techniques introduced for the pure ice experiments.

Fig. 4.4 shows PSD spectra for different CO ice thicknesses, deposited at 14 K on top of 250 BL_{eq} water ice films. Two different water ice phases have been investigated: an amorphous porous ice, prepared at 14 K (Fig. 4.4a), and a polycrystalline ice, grown at 140 K (Fig. 4.4b). Fig. 4.4a shows that no CO photodesorption can be observed for irradiating photon energies between 7 and 14 eV from 10 ML_{eq} CO on top of amorphous water ice. For a substantially thicker coating of 60 ML_{eq} CO ice layer on top of the same water ice, the photodesorption spectrum is almost identical to the PSD spectrum of pure CO ice (Fig. 4.4c). Obviously, the water layer can affect the CO photodesorption yield. Due to the very large specific surface of amorphous H_2O , a large amount of the CO molecules are needed to saturate the icevacuum interface of the water ice (Burke & Brown 2010; Collings et al. 2003b,a). Using studies performed

by Collings et al. (2003b,a), we evidenced from thermal desorption experiments that 10ML_{eq} of CO are clearly below the amount of molecules needed to totally recover the available surface of the amorphous water ice. As a consequence, all molecules in the 10ML_{eq} of deposited CO interact directly with the H_2O molecules, and no pure solid CO ice is grown upon deposition. This is not the case anymore when 60ML_{eq} of CO molecules are deposited on top of amorphous porous H_2O : the water specific surface is saturated, and 3ML_{eq} of a pure CO phase, i.e. multilayer of CO, grows on top of the amorphous H_2O ice. From this finding, it is concluded that a pure CO phase is needed for the photodesorption to be effective. This model is confirmed by the experiments on polycrystalline water ice. Indeed, for the same coverage the effective surface of the compact and ordered crystalline ice is much smaller than the disorganized and porous amorphous ice film surface, and the higher compactness of the ice prevents CO to penetrate in an equally efficient way as for the amorphous morphology (Rowland et al. 1991; Stevenson 1999; Dohnálek et al. 1999; Kimmel et al. 2001). 10ML_{eq} of CO are therefore a sufficient coverage to achieve a CO multilayer phase. As clearly observed from Fig. 4.4b, this phase is photodesorption-active, following the same indirect DIET process as found in the case of a pure CO ice.

The lack of observed photodesorption for CO molecules interacting with H_2O is consistent with the proposed indirect DIET mechanism. These CO molecules are located in the vicinity of the water surface, which allows either subsurface CO photoexcitation or H_2O photoexcitation/dissociation to be the first step in the photodesorption mechanism as also water ice absorbs in the 7 - 14 eV energy range (Mota et al. 2007; Mason et al. 2006). The second step requires (i) the subsequent excitation of intermolecular modes and (ii) the energy transfer towards a surface CO molecule. These steps are expected to be strongly perturbed by the presence of the water, because of the very different nature of the intermolecular interactions compared to pure solid CO; the hydrogen bridged H_2O - CO interactions are stronger than pure van der Waals interactions in solid CO, and it has recently been shown that dangling OH bonds of surface H_2O present a unique ability to rapidly and efficiently evacuate excess vibrational energy from the surface to the bulk (Zhang et al. 2011). This opens an additional relaxation pathway that competes with the intermolecular energy transfer to a surface CO molecule. Finally, in the third step, the ejection of the CO molecule, the very high corrugation of the amorphous H_2O ice may block a sublimation event; a photodesorbed CO molecule can collide with the 14 K structured water surface, and be re-trapped before being emitted into the vacuum. UV induced photochemistry at the H_2O - CO interface could play a role in the observed lack of desorption too, but this effect should be minor, since neither infrared spectroscopy nor mass spectrometry has revealed the presence of new chemical species in our experiments.

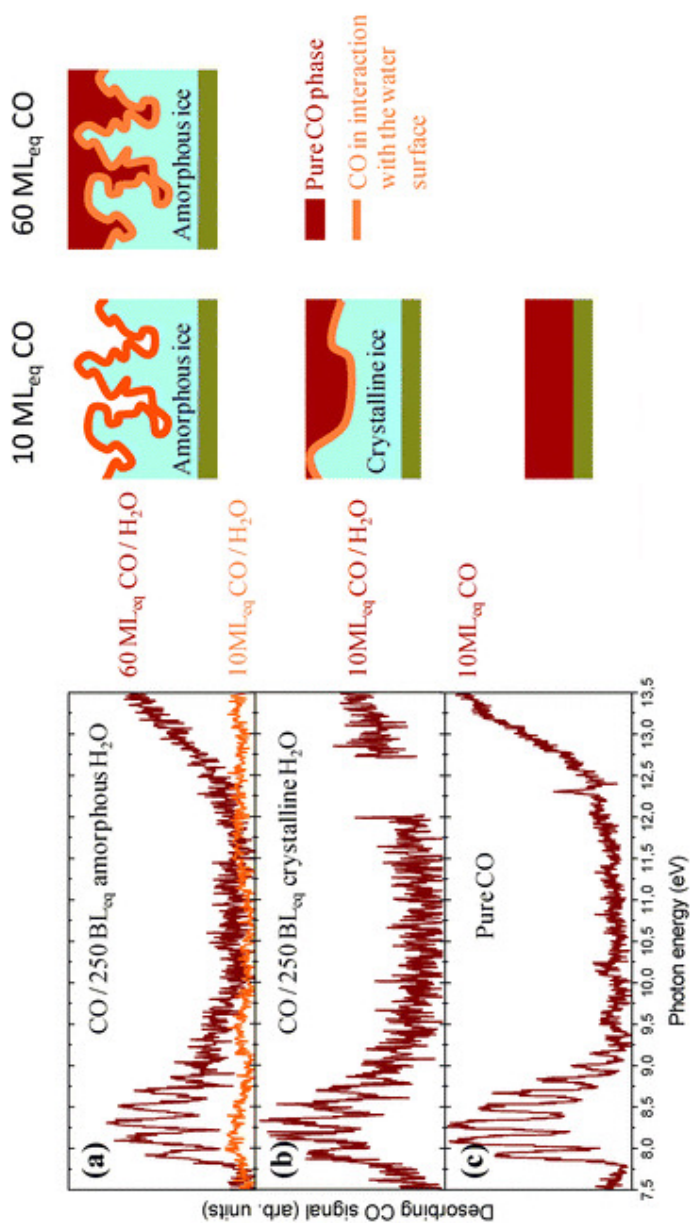


Figure 4.4: Photon stimulated desorption spectra for different amounts of CO deposited on (a) amorphous water ice, (b) polycrystalline water ice, and (c) HOPG at 14 K. The corresponding ice morphologies are schematically depicted. The CO desorption is only observed when a pure CO phase is grown upon deposition.

In astrophysical environments the UV photodesorption yield is thus expected to be substantially different for thick and thin CO ices on top of H₂O. In regions where icy grains are covered with multilayers of pure CO ice, the UV photodesorption is an efficient process (Muñoz Caro et al. 2010; Öberg et al. 2007, 2009; Fayolle et al. 2011), depending on the wavelength of the incoming radiation, and it is a plausible explanation for the observations of gas phase CO molecules in regions with temperatures below the accretion temperature of CO. The laboratory work presented here shows that this process is heavily suppressed at the CO - H₂O ice interface. The environment of the CO molecule in an interstellar ice governs its photodesorption efficiency, which needs to be taken into account when modeling the CO gas - ice balance in interstellar environments. From our PSD spectra in the 7 - 14 eV energy range and our detection limit, we estimate that the CO photodesorption yield is reduced by a factor of 15, at least, for the CO - H₂O system as compared to the pure CO multilayer film.

4.4 Conclusions

The wavelength-dependent photon stimulated desorption methods presented here offer a powerful tool to explore molecular processes involved in the photodesorption of interstellar ices. While the wavelength dependence of the desorption process allows an absolute photodesorption rate, applicable to any UV field spectrum, to be derived (Fayolle et al. 2011), it also provides valuable information on the underlying CO desorption molecular mechanism. Our studies show that the photodesorption mechanism of CO ice involves only the top-most molecular layers of the solid, and does not depend on the substrate onto which the ice is grown. Rather, the mechanism is a three-step indirect DIET process, in which the intermolecular interactions between the CO surface and sub-surface molecules govern the desorption efficiency. This last point has important consequences for the photodesorption of CO in interstellar ices. It is known from observational studies that, in the ISM, one part of the CO molecules forms a pure CO phase layer on top of water-rich icy grains, while the other part is involved in hydrogen-bound complexes with water molecules. From our finding we conclude that at least 2 pure CO layers are needed for the photodesorption process to be effective. In contrast, the efficiency of the photodesorption of CO molecules interacting with water ice surfaces is found to be reduced by at least a factor of 15 compared to pure CO ices. The presented indirect DIET mechanism implies that CO molecules interacting with the water molecules do not photodesorb efficiently, while pure CO ice molecules do.

Wavelength-dependent UV-photodesorption of pure N₂ and O₂ ices

Abstract. Ultraviolet photodesorption of molecules from icy interstellar grains can explain observations of cold gas in regions where thermal desorption is negligible. This non-thermal desorption mechanism should be especially important where UV fluxes are high.

N₂ and O₂ are expected to play key roles in astrochemical reaction networks, both in the solid state and in the gas phase. Measurements of the wavelength-dependent photodesorption rates of these two infrared-inactive molecules provide astronomical and physical-chemical insights into the conditions required for their photodesorption.

Tunable radiation from the DESIRS beamline at the SOLEIL synchrotron in the astrophysically relevant 7 to 13.6 eV range is used to irradiate pure N₂ and O₂ thin ice films. Photodesorption of molecules is monitored through quadrupole mass spectrometry. Absolute rates are calculated by using the well-calibrated CO photodesorption rates. Strategic N₂ and O₂ isotopolog mixtures are used to investigate the importance of dissociation upon irradiation.

N₂ photodesorption mainly occurs through excitation of the b¹Π_u state and subsequent desorption of surface molecules. The observed vibronic structure in the N₂ photodesorption spectrum, together with the absence of N₃ formation, supports that the photodesorption mechanism of N₂ is similar to CO, i.e., an indirect DIET (Desorption Induced by Electronic Transition) process without dissociation of the desorbing molecule. In contrast, O₂ photodesorption in the 7 - 13.6 eV range occurs through dissociation and presents no vibrational structure.

Photodesorption rates of N₂ and O₂ integrated over the far-UV field from various star-forming environments are lower than for CO. Rates vary between 10⁻³ and 10⁻² photodesorbed molecules per incoming photon.

E. C. Fayolle, M. Bertin, C. Romanzin, H. A. M. Poderoso, L. Philippe, X. Michaut, P. Jeseck, H. Linnartz, K. I. Öberg, J.-H. Fillion
Astronomy and Astrophysics, 556, 122, (2013)

5.1 Introduction

In the cold and dense regions of the interstellar medium (ISM), molecules condense onto the surfaces of submicron-sized dust grains. Upon heating or non-thermal desorption, these molecules are released into the gas phase. Constraining these desorption mechanisms is crucial since they bridge solid state and gas phase chemistry in space. In regions where heating can be neglected, non-thermal desorption pathways are required to explain the presence of molecules in the gas phase that, without such mechanisms, should remain frozen. Non-thermal desorption has been proposed to take place in star-forming regions at every evolutionary stage to explain observations of cold gas: in prestellar cores (Caselli et al. 2012), in protostellar envelopes (Kristensen et al. 2010) and in protoplanetary disks (e.g., Willacy & Langer 2000; Dominik et al. 2005; Hogerheijde et al. 2011). Non-thermal desorption in the ISM is induced by cosmic-rays, exothermic reactions, shocks, electrons, and photon irradiation. Experimental measurements of the efficiencies of these processes are a prerequisite to understand which of these pathways must be considered to predict molecular gas abundances.

Precise measurements are especially important for abundant molecules that can play key roles in gas-grain chemical networks. Two of these species are N_2 and O_2 because of their role in the formation of N- and O-bearing molecules in the gas phase and in the solid state. For instance, the presence of N_2 in the solid state leads to the formation of NH_3 (e.g., Aikawa et al. 1997; Daranlot et al. 2012). In the gas phase, the N_2 derivative N_2H^+ is a major tracer of dense cold cores (e.g., Caselli et al. 2002). Molecular oxygen plays a role in water formation in the gas phase after dissociation into atomic oxygen but also in the solid phase (Hollenbach et al. 2008). O_2 hydrogenation has been proposed as a starting point for water formation on grains by Tielens & Hagen (1982) and proven experimentally to be effective by many studies (e.g., Miyauchi et al. 2008; Ioppolo et al. 2008; Matar et al. 2008). The abundance of H_2O on the grains is thus intrinsically linked to the amount of O_2 ice, which is itself regulated by non-thermal desorption mechanisms at low temperatures.

It is difficult to put observational constraints on molecular nitrogen and oxygen abundances and guide gas-grain modeling since these species do not possess permanent dipole moments. Some O_2 electronic transitions have been observed in the far-UV (FUV) using Odin (Pagani et al. 2003) and some tentative detections have been reported in the millimeter range (Goldsmith et al. 2011; Liseau et al. 2012), resulting in low gas-phase abundances in specific environments. Molecular nitrogen has been detected by Knauth et al. (2004) in the FUV but its abundance is mainly inferred via N_2H^+ detections in the millimeter range. Since observational data on such species are rare and limited to specific ISM regions, accurate laboratory data are necessary to support gas-grain codes, including desorption efficiencies.

Among the non-thermal desorption mechanisms, UV photodesorption has been studied in detail for specific molecules by various groups. Photodesorption rates for CO (Öberg et al. 2007, 2009; Muñoz Caro et al. 2010; Fayolle et al. 2011; Bertin et al. 2012), H_2O (Westley et al. 1995a; Yabushita et al. 2009; Öberg et al. 2009b), CO_2 (Öberg et al. 2009; Bahr & Baragiola 2012), and N_2 (Öberg et al. 2009) are available for gas grain codes (for e.g. Willacy & Langer 2000; Walsh et al. 2010; Vasyunin & Herbst 2013).

However, most of the previous studies provide photodesorption rates for photons at a specific energy, mainly Lyman-alpha (121.6 nm, 10.2 eV) or for broad-band Vacuum-UV (VUV) and details on the underlying mechanisms are limited. As shown in Fayolle et al. (2011) and Bertin et al. (2012), studying photodesorption with respect to the incoming photon energy provides 1) photodesorption rates that can be used to predict the process efficiency in different phases of the ISM, taking the specific UV-field profile into account, and 2) detailed insights into the underlying molecular mechanism. Both kinds of information are needed to extrapolate photodesorption rates to astrophysical UV fluxes and time scales. In the case of CO ice, photodesorption occurs through an indirect DIET (Desorption Induced by Electronic Transition) process where surface CO desorbs through electronic excitation of subsurface molecules. This mechanism is only valid below 10 eV where photons do not induce CO dissociation. For other species (e.g. H₂O, CO₂, CH₃OH...), the dissociation of the parent molecules into radicals strongly affects the photodesorption mechanism (e.g., Westley et al. 1995a; Öberg et al. 2009b).

In the present study, N₂ and O₂ ice photodesorption is explored by performing wavelength-dependent irradiation experiments between 7 and 13.6 eV. This specific spectral window has been explored since it corresponds, for the upper limit, to the Lyman edge above which most of the radiation is absorbed by hydrogen and for the lower limit, to the minimum energy required for electronic excitation of most simple interstellar molecules. The experimental techniques that are used to measure the photodesorption rates of these non-IR active species are presented in the Method section. The results are presented separately for N₂ and O₂ in section 5.3. A discussion of the involved mechanisms, photodesorption rates, and recommendations for use in gas-grain codes is presented in section 5.4, followed by the conclusions.

5.2 Method

5.2.1 Experiments

Experiments are performed on ices grown in the ultra-high vacuum set-up SPICES (detailed description available in Bertin et al. 2011), which can reach low pressures down to 10⁻¹⁰ mbar. Ices of ¹⁴N₂, ¹⁶O₂ (both from Air liquide, alphagaz 2, pollutants < 1 ppm), ¹⁵N₂ (Eurisotop, 97% ¹⁵N), and ¹⁸O₂ (Eurisotop, 97% ¹⁸O) are grown diffusively with monolayer (ML) precision on either highly oriented pyrolytic graphite (HOPG) or a polycrystalline gold surface. Both substrates are mounted on the same rotatable cold head, which can be cooled down to temperatures as low as 14 K by a closed cycle helium cryostat. The set-up is equipped with a quadrupole mass spectrometer (QMS model 200 from Balzers) allowing for gas phase molecule detection via electron impact at 90 eV, as well as a Fourier-transform infrared spectrometer (Vector 22 model from Bruker) for reflection-absorption infrared spectroscopy (RAIRS) to probe changes in the condensed phase. Ice thicknesses are chosen to be between 30 and 60 ML, which is expected to be thicker than the photodesorption-active layers. The targeted ice thickness is achieved (within few tenths of an ML) by calibrating the rate and deposition time using the temperature program desorption (TPD) technique. The TPD curves are sensitive to the break between multilayers and monolayer desorption due

to the difference in binding energy between ice-ice and ice-substrate. Isotopolog mixtures are produced in situ by using two deposition valves connected to the deposition tube. The desired mixing ratio is achieved by monitoring the partial pressure of the gases during deposition by mass spectrometry.

Photodesorption of ices is induced by UV photons from the undulator-based DE-SIRS beamline (Nahon et al. 2012) at the SOLEIL synchrotron. In the explored 7 – 13.6 eV range, the undulator provides continuous monochromatic light with an FWHM of about 1 eV, as well as higher harmonics that are suppressed when the beam traverses a specific gas filter. For an irradiation experiment at fixed energy requiring a high flux, specific energies are chosen using the undulator, and the photons are used straight from the gas filter resulting in wavelength-fixed fluxes between 10^{13} and 5×10^{14} photons s^{-1} , and measured by calibrated photodiodes before each irradiation experiment. To acquire wavelength-dependent photodesorption spectra, a higher energy resolution is obtained using the 6.65 m normal incidence monochromator implemented on the beamline. It is possible to perform energy scans between 7 and 13.6 eV with a narrow bandwidth of typically 40 meV and intensities at the sample between 3 and 11.5×10^{12} photons $s^{-1} cm^{-2}$.

The photodesorption experiments are performed by hooking up the SPICES chamber directly to the beamline, thus avoiding any radiation cut-off due to optical components. The photon angle of incidence on the substrate is 45° , the UV beam spot is $0.7 \pm 0.1 cm^2$, and the light is in s-polarized mode (perpendicular to the plane of incidence). The photodesorption efficiency is assessed over 7 – 13.6 eV by scanning the photon energy and simultaneously recording the relative level of photodesorbed molecules by mass spectrometry. Additional high flux experiments can be performed at fixed energy, and desorption is monitored simultaneously by RAIRS and QMS.

Photodesorption data obtained from N₂ or O₂ ices are found to be identical for films grown on HOPG and Au samples, demonstrating a negligible effect of the nature of the substrate. The photodesorption spectra recorded here are mainly obtained from ices deposited on HOPG, whereas the gold substrate has been specifically used to probe the irradiated ices by IR spectroscopy.

5.2.2 Data analysis

In the case of the previous wavelength-dependent CO photodesorption studies (Fayolle et al. 2011; Bertin et al. 2012), the absolute photodesorption spectrum is found by quantifying the absolute ice loss during irradiation at a single energy and high photon flux using infrared spectroscopy. This photodesorption value at single energy is used to scale the relative photodesorption spectrum obtained by mass spectrometry following the signal of the molecular ion CO⁺ at low flux. This technique cannot, however, be directly used for N₂ nor O₂ since neither of them have permanent dipole moments and are thus not detectable in the infrared.

To derive absolute N₂ and O₂ photodesorption rates, the relative photodesorption spectra obtained from the QMS signals of the corresponding molecular ions ($m/z=28$ and 32 , respectively) are scaled using the QMS to absolute photodesorption rate factor

derived for CO and correcting it for the gas-specific ionization cross-sections¹ (Freund et al. 1990; Straub et al. 1996) as

$$Y_i = f_{i+} \times I_{i+} \quad \text{with} \quad f_{i+} = f_{\text{CO}^+} \times \frac{\sigma_{i+}}{\sigma_{\text{CO}^+}}$$

where Y_i is the absolute photodesorption rate of molecule i , I_{i+} is the QMS signal of the corresponding molecular ion, f_{i+} the QMS count to absolute photodesorption factor for species i , f_{CO^+} the same factor for CO derived by infrared spectroscopy during the same experimental runs, using identical QMS and light setting and σ_{i+} and σ_{CO^+} are the ionization by electron impact cross-sections at 90 eV for species i and CO.

Using CO measurements to calibrate N_2 and O_2 photodesorption is a reasonable approach because N_2^+ , O_2^+ , and CO^+ fragments have very close masses. The apparatus function of the QMS (mainly dominated by the gain due to the secondary electron multiplier (SEM) and fragment transmission efficiency) should thus be similar (within few percents) for a given ionization energy. The gas phase velocity distribution of the desorbing species may influence the QMS detection efficiency. In the present experiments, velocities of the photodesorbed molecules were not specifically determined, but are expected to be of the same order of magnitude for CO, O_2 , and N_2 that all three have very similar masses and ice binding energies. Consequently, the mass signal ratios of N_2^+ or O_2^+ over CO^+ only depends on the respective gas partial pressures and on the 90 eV ionization cross-sections by electron impact of the corresponding gases (Kaiser et al. 1995).

Great care has been taken to insure that the QMS signal used to probe the photodesorption rates unambiguously originates in the parent desorbing molecules (i.e. N_2 , O_2 , or CO). The absence of QMS signals that could be attributed to N_3^+ , O_3^+ , or CO_2^+ in low light flux conditions experiments clearly indicates that the molecular ion signals are not contaminated by secondary fragmentation in the QMS of N_3 , O_3 , or CO_2 , respectively; the electron impact fragmentation patterns of these neutral species at 90 eV have been considered for this purpose (for example, see Cosby 1993; Bennett & Kaiser 2005; Ennis et al. 2011, for detailed analysis of O_3 fragmentation).

A first source of uncertainty in the photodesorption yields comes from the QMS signal-to-noise ratio and small residual gas fluctuations. The root mean square of the spectra reaches 4×10^{-4} molecules photon⁻¹ for $^{15}\text{N}_2$ and 6×10^{-4} molecules photon⁻¹ for O_2 . In addition, there is a 40 % systematic uncertainty inherent to the calibration method from relative QMS count to absolute photodesorption rates for CO (see Fayolle et al. 2011).

5.3 Results

5.3.1 Nitrogen photodesorption

The photodesorption spectrum of a 60 ML-thick $^{15}\text{N}_2$ ice at 15 K is shown in Fig. 5.1. It shows a strong wavelength dependency and presents a highly structured sig-

1. The ionization cross sections by electron impact at 90 eV used for calibration here are: 1.73 \AA^2 for CO and 1.78 \AA^2 for N_2 from Freund et al. (1990) and 1.64 \AA^2 for O_2 from (Straub et al. 1996)

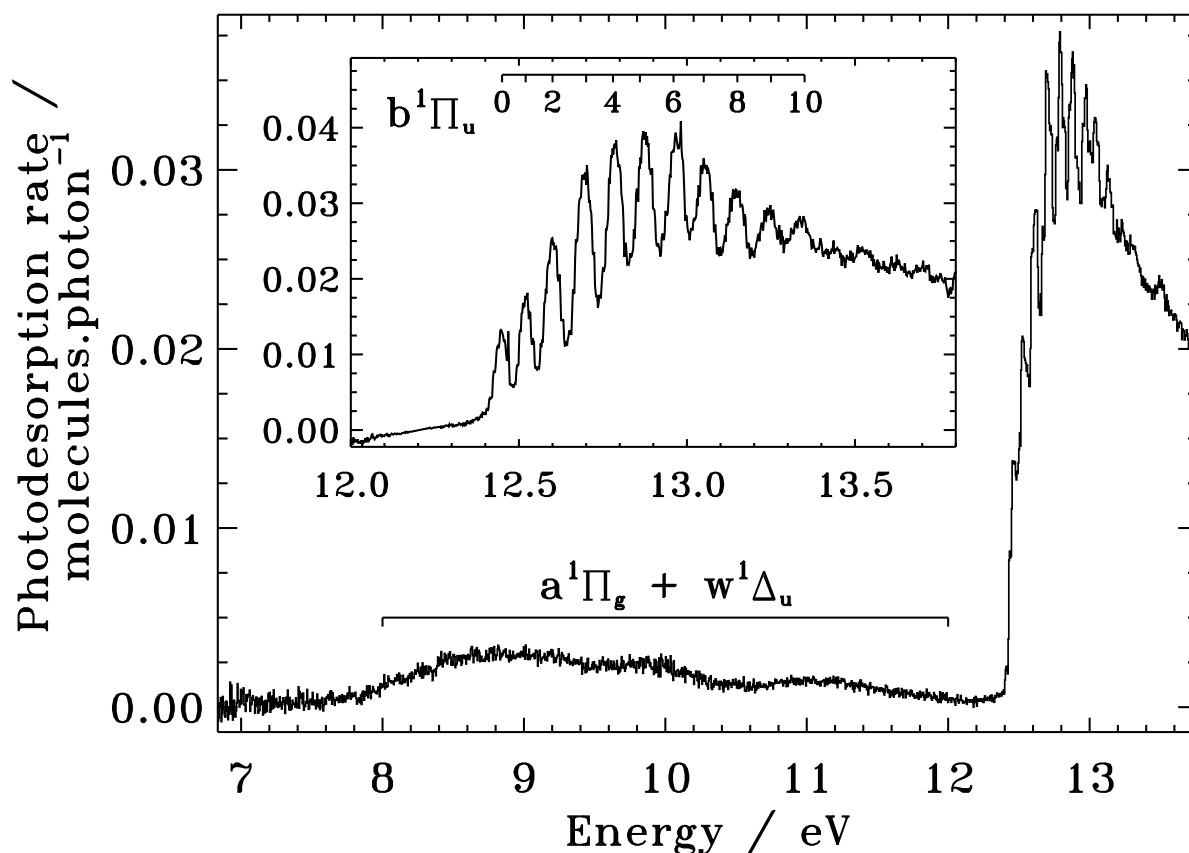


Figure 5.1: Photodesorption spectrum of 60 ML-thick $^{15}N_2$ ice at 15 K between 7 and 13.6 eV. Spectroscopic assignments from Haensel et al. (1971), adapted from $^{14}N_2$ to $^{15}N_2$, are overplotted.

nal above 12.4 eV, as well as a clear efficiency break of more than an order of magnitude compared to the minor shallow bands between 8 and 12 eV. The photodesorption maximum is found at 12.8 eV and reaches $3.77 \pm 1.13 \times 10^{-2}$ molecules photodesorbed per incoming photon. For energies below 12.4 eV, the photodesorption rates do not exceed 4×10^{-3} molecules photon $^{-1}$. At Lyman-alpha, the rate of $1.5 \pm 0.9 \times 10^{-3}$ molecules photon $^{-1}$ found here is higher than the one derived by Öberg et al. (2009) but is in agreement within the experimental uncertainties. To understand the origin of the N_2 photodesorption spectrum, one needs to compare it to the corresponding photoabsorption spectrum (Haensel et al. 1971). The structured photodesorption signal above 12.4 eV is also observed in the N_2 absorption spectrum. This absorption band corresponds to the vibrational progression of the dipole-allowed $b^1\Pi_u \leftarrow X^1\Sigma_g^+$ electronic transition. The similarity between the photoabsorption and photodesorption spectra indicates that N_2 photodesorption is triggered by the excitation of N_2 in the $b^1\Pi_u$ state. This transition is, however, predissociative in the gas phase due to a valence-Rydberg coupling (James et al. 1990) and leads to the formation of atomic $N(^2D)$ and $N(^4S)$. The dissociation energy of N_2 in the gas phase is 9.6 eV, lower than the observed photodesorption band. However, neither ^{15}N atoms nor $^{15}N_3$ molecules

are detected by the QMS during ice irradiation, which suggests a photostability of N_2 in the ice up to 13.6 eV.

To further test whether N_2 photodesorption could be initiated by photodissociation, a 1:1 $^{15}\text{N}_2$: $^{14}\text{N}_2$ mixture of 60 ML at 15 K was irradiated, and the photodesorption measurements of $^{15}\text{N}_2$, $^{14}\text{N}_2$, and $^{15}\text{N}^{14}\text{N}$ are presented in Fig. 5.2a. The desorption of $^{15}\text{N}^{14}\text{N}$ is negligible during irradiation and the low percentage detected during a TPD experiment following irradiation is consistent with the gas impurity level indicated by the $^{15}\text{N}_2$ gas provider. This implies an inefficient dissociation of N_2 or a very efficient and immediate recombination of dissociated N_2 due to cage effects in the solid phase. The formation of azide (N_3) after UV photolysis of solid N_2 has been reported by Wu et al. (2012) in a similar UV irradiation experiment but using a higher photon flux. In the present case, additional high flux irradiation experiments with a photon distribution peaking at 13 eV (1 eV width and 2.9×10^{13} photons $\text{s}^{-1} \text{cm}^{-2}$ intensity) were performed on a 60 ML $^{15}\text{N}_2$: $^{14}\text{N}_2$ 1:1 film and monitored using RAIRS for 40 minutes, followed by a TPD experiment. None of the N_3 isotopologs have been detected in the infrared spectra. This does not contradict the results from Wu et al. (2012) since the fluence they employed was about 19 times higher than what is used in the present experiments and our non-detection also agrees with the non-detection reported in a H_2 -discharge lamp-based UV irradiation study by Hudson & Moore (2002).

Figure 5.2b presents the photodesorption spectra of $^{15}\text{N}_2$ and $^{14}\text{N}_2$ from pure 30 ML-thick ice films at 14 K. A comparison of the two spectra clearly shows an isotopic shift in the vibrational progression for both species upon excitation towards the $b^1\Pi_u$ state. This supports a mechanism similar to what has been discussed for CO by Bertin et al. (2012), where similar behavior was observed for ^{12}CO and ^{13}CO . This isotopic shift is not visible in the 1:1 $^{15}\text{N}_2$: $^{14}\text{N}_2$ photodesorption spectra (Figure 5.2a), since here the photodesorption pattern of both isotopologs overlaps. This overlap is easily explained by the fact that in mixed ice films, the desorption of any N_2 molecule can be induced by both isotopologs.

The evidence of vibronic excitation in the N_2 photodesorption spectrum and the lack of recombined $^{15}\text{N}^{14}\text{N}$ or N_3 isotopologues indicate that the underlying mechanism is a desorption induced by electronic transition (DIET) process. The mechanism above 12.4 eV is similar to the mechanism found for CO photodesorption below 10 eV by Fayolle et al. (2011) and Bertin et al. (2012) and is discussed further in Section 5.4.

The minor photodesorption signal obtained for energies lower than 12 eV may be due to the excitation of the forbidden Lyman-Birge-Hopfield $a^1\Pi_g \leftarrow X^1\Sigma_g^+$ and Tanaka $w^1\Delta_u \leftarrow X^1\Sigma_g^+$ transitions according to Wu et al. (2012). These very weak transitions have also been reported in absorption in the solid phase by, e.g., Brith & Schnepf (1965), Roncin et al. (1967), and Mason et al. (2006). The two vibronically resolved progressions associated to the excitation of $a^1\Pi_g$ and $w^1\Delta_u$ observed in absorption spectrum of solid N_2 (Mason et al. 2006) are not seen in our photodesorption spectrum. These transitions, which are both electronically dipole forbidden in the gas phase, are weak in the solid state. It is possible that these narrow bands are buried in the continuum that is visible between 8 and 12 eV in Fig. 5.1.

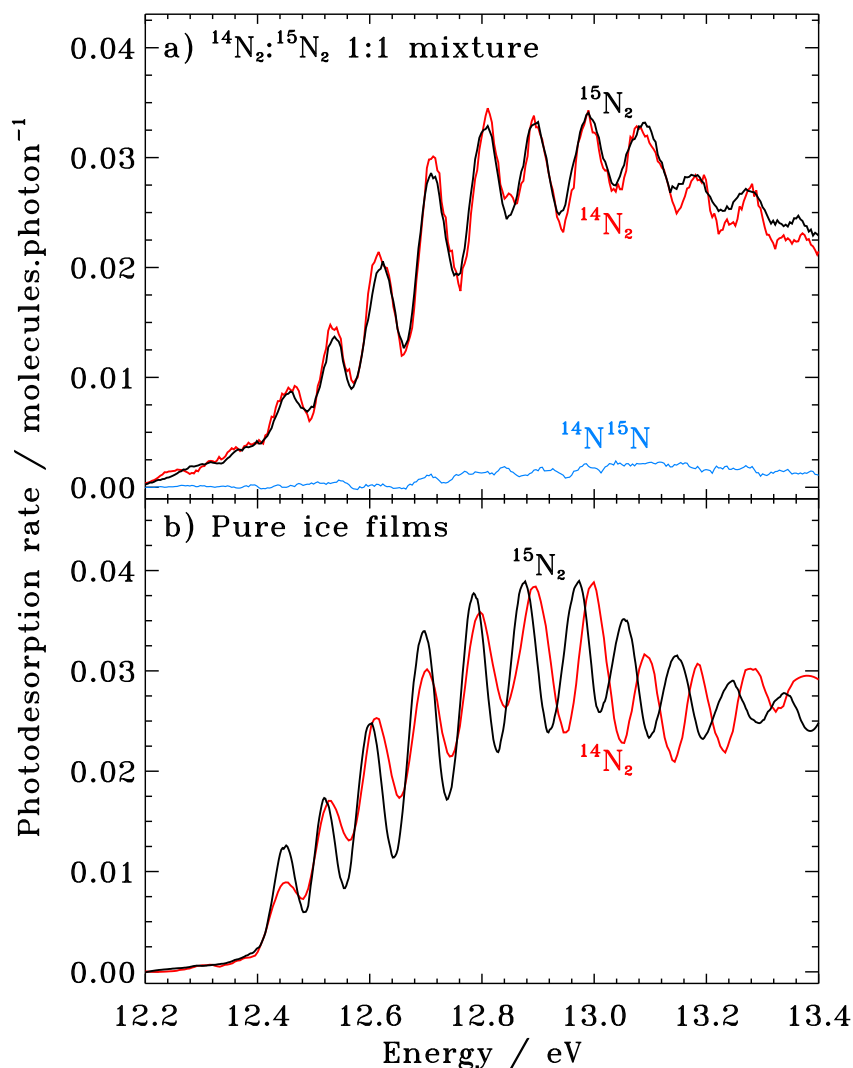


Figure 5.2: Photodesorption spectra of $^{15}N_2$ (back line), $^{14}N_2$ (red line), and $^{15}N:^{14}N$ (blue line) between 12.2 and 13.4 eV from a) a 60 ML-thick $^{15}N_2:^{14}N_2$ 1:1 ice at 14 K and b) pure 30 ML-thick $^{15}N_2$ and $^{14}N_2$ ice films at 14 K. The photodesorption spectra have been smoothed to facilitate comparisons between the vibrational progressions.

5.3.2 Oxygen photodesorption

Figure 5.3 shows the photodesorption spectrum of a 30 ML-thick O_2 ice at 15 K. The spectrum displays a strong, broad and unstructured desorption pattern with clearly no evidence of any vibrational structure. The photodesorption value exceeds 5×10^{-4} molecules photon $^{-1}$ for all photon energies in the studied spectral window between 7.5 and 13.6 eV, with a starting value of $\sim 1.5 \times 10^{-3}$ molecules photon $^{-1}$ around 7.5 eV that hints for a photodesorption onset at lower energies. Molecular oxygen dissociates in the solid phase as is shown by the detection of atomic oxygen in the gas phase during irradiation. The signal of $m/z=16$ has been recorded during irradiation and an upper limit of the amount of desorbing atomic oxygen is derived by also taking

the fragmentation pattern of O_2 into O^+ and O_2^+ in the QMS into account; oxygen atoms desorbing from the surface are detected with a concentration lower than 8 % with respect to desorbing molecular O_2 . The detection of O-atoms stemming from the UV photolysis hints at an excitation mechanism followed by dissociation. The O_2 and O recombination should yield ozone, but no significant $m/z=48$ signal is observed during irradiation or subsequent TPD. Ozone likely forms but in very small amounts considering the low fluence employed in the present experiment; the flux amounts to a few 10^{12} photons $s^{-1} cm^{-2}$ during 20 minutes scanning the 7 to 13.6 eV range.

There is a good agreement between the O_2 photodesorption spectrum presented here and the VUV absorption spectrum recorded by Mason et al. (2006) over the 7 - 10.5 eV range, and both spectra are dominated by a broad structure peaking at 9.3 eV (see also Fig. 5.3). This band may link to the $B^3\Sigma_u^- \leftarrow X^3\Sigma_g^-$ Schumann-Runge continuum as proposed by Mason et al. (2006), who discuss the difference between solid state and gas phase properties. Indeed, direct dissociation via the Schumann-Runge continuum produces $O(^3P)$ and $O(^1D)$ above 7.01 eV in the gas phase (Parker 2000), which is consistent with the observation of atomic oxygen desorbing from the O_2 ice film upon VUV irradiation. An alternative or possible parallel explanation is that the broad 9.3 eV desorption peak is associated with an excitation towards the $E^3\Sigma_u^-$ transition with maximum absorption energies in the gas phase around 9.5 and 11 eV. This electronic transition would also lead to the formation of $O(^1D)$ atoms through dissociation (Lee & Nee 2000). In Mason et al. (2006), oxygen dimers $(O_2)_2$ have also been proposed as a possible starting point for desorption, particularly for lower energies, but this cannot be verified here.

For energies above 10.5 eV, the molecular origin of the O_2 photodesorption mechanism is more ambiguous because UV absorption data are not available in the condensed phase. We observe a minimum around 10.5 eV that coincides with the ionization threshold of molecular oxygen in the condensed phase (Himpsel et al. 1975). This would mean that ionic species are involved in the desorption mechanism. However, since the first ionic states are non-dissociative (Yang et al. 1994), reactions involving the O^+ ion can be ruled out. Moreover, a fast neutralization is expected upon single ionization (Avouris & Walkup 1989), consequently ionic states may relax to neutral states (below 10.5 eV), allowing a desorption mechanism that is fairly similar to the one observed in the neutral case. It will be interesting to perform additional experiments to confirm this scenario.

Figure 5.4 presents the photodesorption signal of $^{16}O_2$, $^{18}O_2$, and $^{16}O^{18}O$ from a 1:1 $^{16}O_2$: $^{18}O_2$ ice mixture at 15 K and 60 ML thick. The photodesorption signal of the initial $^{16}O_2$ and $^{18}O_2$ isotopologs overlap and a contribution of the $^{16}O^{18}O$ isotopolog, stemming from the dissociation and recombination of the initial mixture components, is clearly visible. This shows that the O_2 photodesorption mechanism involves non-negligible channels due to O_2 dissociation.

When irradiating the 60 ML thick 1:1 $^{16}O_2$: $^{18}O_2$ mixture at 15 K with 9.2 eV photons using the undispersed radiation (1 eV FWHM) mode with high photon flux (4.3×10^{14} photons $s^{-1} cm^{-2}$ at 9.2 eV), the formation of ozone is observed by RAIRS. Figure 5.5 shows all O_3 isotopologs forming during the irradiation of an 1:1 $^{16}O_2$: $^{18}O_2$ ice mixture. The assignment of the various isotopologs is possible by using gas phase

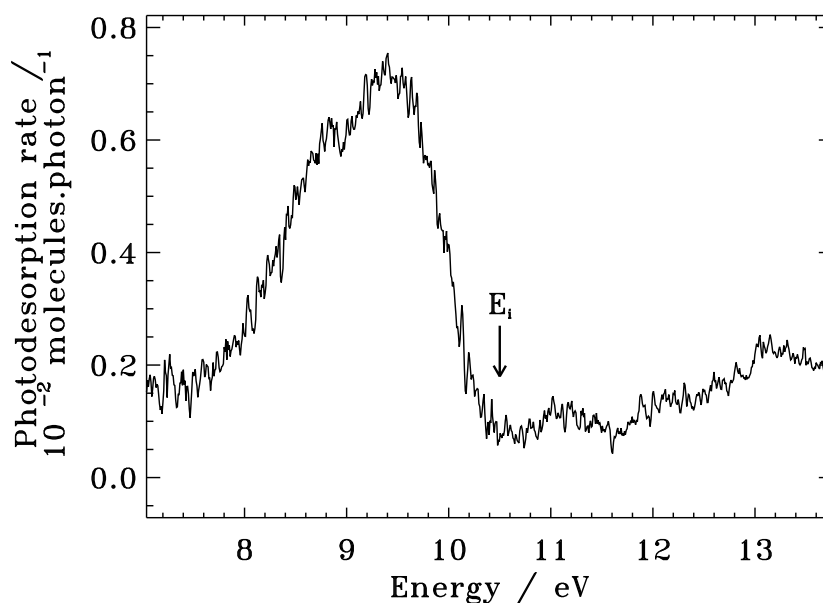


Figure 5.3: Photodesorption spectrum of O_2 for a 30 ML ice film at 15 K between 7 and 13.6 eV. The E_i arrow presents the ionization threshold O_2 in the solid state.

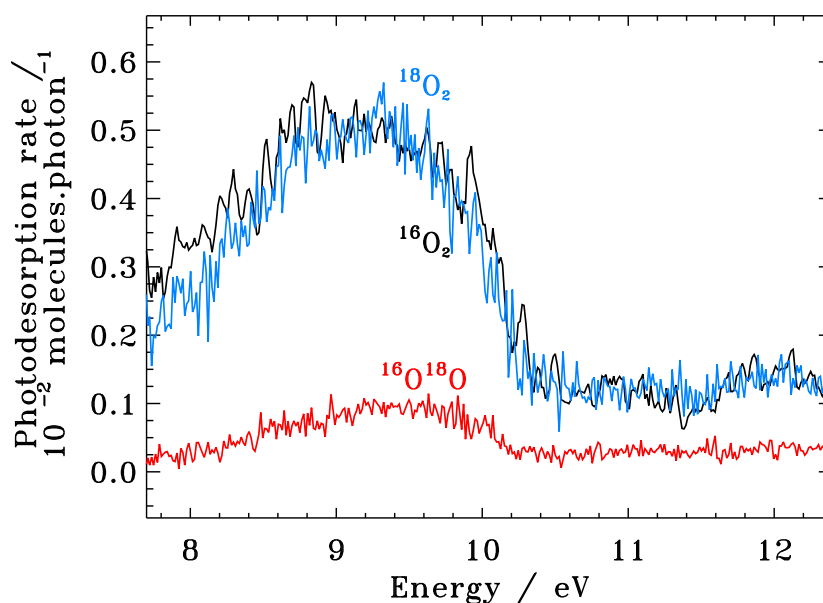


Figure 5.4: Photodesorption spectrum of $^{16}O_2:^{18}O_2$ 1:1 at 15 K, 60 ML between 7.5 and 13.6 eV.

data obtained by Dimitrov et al. (1998). As shown by the presence of the six ozone bands, all combinations of ^{16}O and ^{18}O are formed. O atoms attack molecular oxygen to produce significant amounts of O_3 , and the formation of $^{16}O^{18}O^{16}O$ and $^{18}O^{16}O^{18}O$ can result either from an addition or inclusion of atomic oxygen to molecular oxygen. Gas phase experiments show a strong isotopic dependence of the formation of

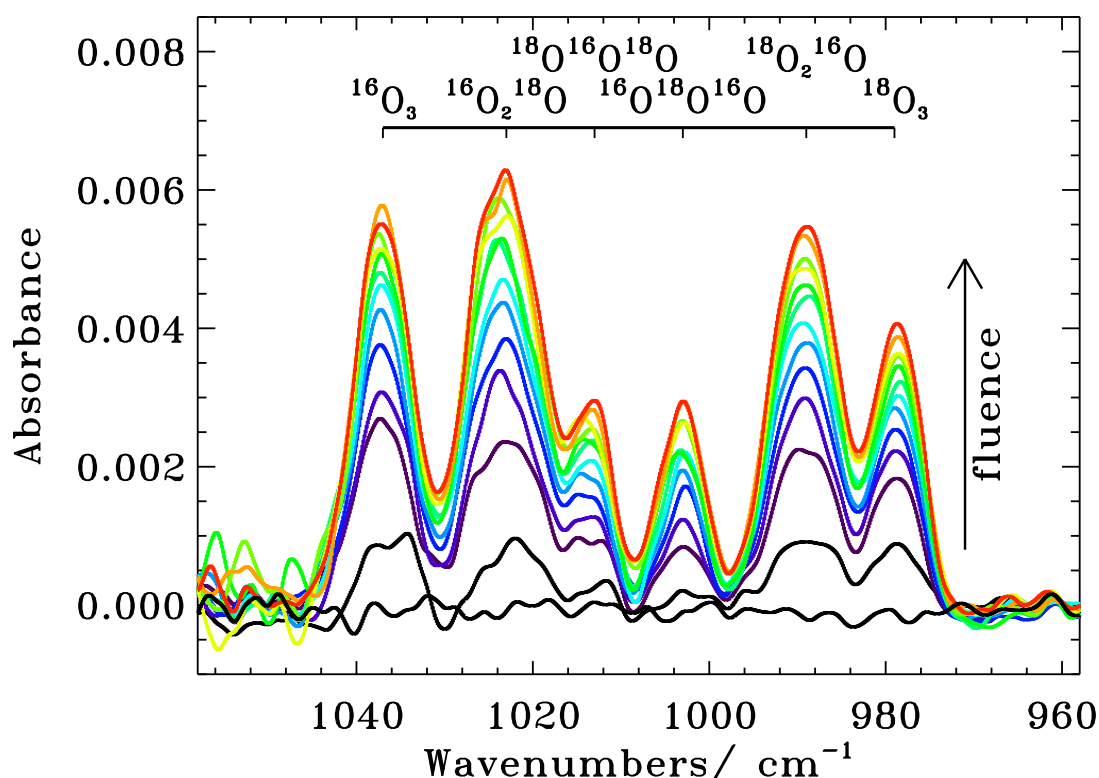


Figure 5.5: RAIRS spectra of O_3 isotopolog formation for increasing UV fluence (from black to red) from a 60 ML thick $^{16}\text{O}_2$: $^{18}\text{O}_2$ 1:1 ice irradiation experiment at 9.2 eV.

ozone (Janssen et al. 1999; Mauersberger et al. 2003), and recent experiments on ozone synthesis in the solid state induced by electron bombardment yield an even stronger isotopic enrichment (Sivaraman et al. 2010) in favor of the heavier isotopolog. The O_2 photodesorption rate will depend directly on the branching ratio between desorption and dissociation, so more detailed studies on this isotope effect are warranted.

5.4 Discussion

5.4.1 Photodesorption mechanisms for pure ices

Photodesorption is a wavelength-dependent process. The similarities between the absorption and the photodesorption spectra for N_2 , O_2 , and CO (Fayolle et al. 2011; Bertin et al. 2012) clearly show that photodesorption in the VUV is induced by electronic excitation of the condensed molecules. The nature of the excited state reached after UV irradiation determines the mechanism leading to photodesorption. Two different families of molecules can be distinguished: a first class where molecules do not dissociate (e.g., CO , N_2) and a second class where dissociation occurs (e.g., O_2 , H_2O , CH_3OH , e.g., Westley et al. 1995a; Öberg et al. 2009a). The photodesorption of both types is triggered by the initial photon absorption, but they differ in the energy redistribution mechanisms from excited to desorbing species. Desorption induced by ionization is not discussed here since the ionization potential of most simple molecules

found in interstellar ices is above or at the high end of the investigated energy range.

In the case where absorption of a UV photon does not lead to dissociation, excited molecules can induce a sudden rearrangement within the ice lattice when returning to the ground state and eject some of the surface molecules into the gas phase. This indirect DIET process has been highlighted in Bertin et al. (2012), where a layer of ¹³CO deposited on a thicker ¹²CO ice film was irradiated between 7 and 13.6 eV. Molecules desorbing in this case are mainly ¹³CO, but they follow the excitation pattern of subsurface ¹²CO. The same mechanism is observed in the case of N₂ for the excitation to the b¹Π_u state. The photodesorption efficiency of this subsurface excitation inducing surface desorption mechanism is thus directly linked to the efficiency of the energy redistribution between the excited molecule and the surface. Investigating the energy-coupling efficiency between different kinds of molecules is crucial since the excitation of one species could induce the desorption of another.

In the second case where molecules are dissociated after UV photon absorption, there are additional pathways to bring condensed molecules into the gas phase. Similar to what has been seen in molecular dynamic simulations for the case of H₂O (Andersson & van Dishoeck 2008; Andersson et al. 2011), the formation of oxygen radicals affects the O₂ photodesorption mechanism. O₂ photodesorption can come from

1. Photon absorption $O_{2(s)} \xrightarrow{h\nu} O_{2(s)}^*$;
2. Redistribution of the energy that induces
 - i) an indirect DIET process $O_{2(s)}^* \rightarrow O_{2(g)}$;
 - ii) O₂ dissociation $O_{2(s)}^* \rightarrow O + O$
 - 1) $O + O \rightarrow O_{2(g)}$
exothermic recombination;
 - 2) $O_{2(s)} + O \rightarrow O_{2(g)} + O$
kick-out by atomic oxygen;
 - 3) $O_{2(s)} + O \rightarrow O_{3(s)} \xrightarrow{h\nu} O_{2(g)} + O$
photoinduced dissociation of ozone.

The additional photodesorption pathways accessible by the formation of atomic oxygen are ii) 1) recombination of oxygen radicals to reform molecular oxygen followed by desorption to dissipate excess of energy, ii) 2) kick out of molecular oxygen from the surface induced by mobile atomic oxygen, and ii) 3) reaction of atomic oxygen with a molecular oxygen to form ozone, which can be photolyzed into O₂ with enough energy to desorb. The recombination of oxygen atoms, reaction ii) 1), is related to the probability that two oxygen atoms meet and react. This reaction channel depends highly on the diffusion of oxygen atoms, as well as on their concentration in the ice, thus it is expected to be flux dependent. In addition, the photodesorption channel involving the photolysis of ozone, ii) 3), will only be effective for a high photon dose. In the low flux experiments presented here, very little O₃ is formed compared to the high flux experiments. Additional studies investigating O₂ photolysis and desorption with respect to the photon flux are required to confirm and quantify a flux dependency of each reaction channels.

5.4.2 Astrophysical consequences

The measured photodesorption spectra of N_2 , O_2 , and CO (present study and Fayolle et al. 2011; Bertin et al. 2012) is wavelength dependent, which implies that the photodesorption efficiency in space will depend on the FUV field profile. Photodesorption in the ISM is expected to be the most efficient in the 7.0 – 13.6 eV range. The 7.0 eV lower limit of this range corresponds to the minimum energy required for an electronic transition of most small molecules found in the ISM, while the 13.6 eV upper limit corresponds to the Lyman edge where radiation in molecular clouds is absorbed by hydrogen. Table 5.1 exemplifies how the photodesorption rates of N_2 , O_2 , and CO can change with respect to the FUV field encountered in different environments. Values are obtained by convoluting the FUV profiles to the photodesorption spectra between the 92 and 172 nm (7.2 - 13.6 eV). In other words, these calculations weight the photodesorption rate derived from the laboratory experiments by the fraction of photons at discrete energies in various ISM regions. For the calculations performed in Table 5.1, the FUV profile for the interstellar radiation field at the edge of the molecular clouds is provided by Mathis et al. (1983), the Lyman and Werner series used for the prestellar cores calculation are taken from Gredel et al. (1987), and the TW hydrae spectrum used here has been collected by Herczeg et al. (2002), Valenti et al. (2003), and Johns Krull & Herczeg (2007). A 10000 K black body curve is taken to approximate the emission from a Herbig Ae star, and photodesorption rates at pure Lyman-alpha are presented as well. Values presented for CO are similar to those reported by Fayolle et al. (2011) except for the 10000 K black body case where the Planck equation used in the previous study was incorrect.

In general, the photodesorption rates calculated here are significantly higher than those employed in current astrochemical models, especially for CO (e.g. Guzmán et al. 2011; Vasyunin & Herbst 2013). This is the case because most experimental values derived in the past were obtained using an hydrogen discharged lamp emitting photons mainly at Lyman-alpha. As proven by the photodesorption spectra obtained experimentally, it appears that photodesorption rates are in general lower at this particular wavelength than at other FUV wavelengths.

When comparing CO, N_2 , and O_2 , the change in photodesorption rates between the different ISM environments is most significant for CO ice between the edge of the molecular clouds and when exposed to radiation at pure Lyman-alpha. In the former case, many of the UV photons are in resonance with CO $A^1\Pi$ electronic state, while CO photodesorption has a minimum at 10.2 eV. N_2 and O_2 photodesorption rates vary less in the FUV (less than a factor 4) and have a lower rate than CO in all regions. This implies that in regions where the main desorption mechanism is photodesorption, the gas-to-pure ice ratio will be higher for CO than for N_2 or O_2 .

Care has to be taken when using the present laboratory spectra to derive photodesorption efficiencies with respect to the local FUV field since these values are only given for pure ices. Where ices are mixed, detailed chemical modeling that takes the excitation-desorption mechanism of each species into account has to be used to predict photodesorption efficiencies. For species that do not dissociate (e.g., N_2 , CO), the subsurface molecules will induce the desorption of surface molecules, while in the

Table 5.1: Photodesorption rates of pure N₂, O₂, and CO ice for different ISM environments.

Environment	N ₂ molecules photon ⁻¹	O ₂ molecules photon ⁻¹	CO molecules photon ⁻¹
Edges of clouds ^a	2.6×10^{-3}	3.3×10^{-3}	1.3×10^{-2}
Prestellar cores ^b	2.2×10^{-3}	2.6×10^{-3}	1.0×10^{-2}
Black body 10,000 K	5.3×10^{-3}	2.3×10^{-3}	6.4×10^{-3}
TW Hydrae ^c	2.1×10^{-3}	2.3×10^{-3}	7.2×10^{-3}
Lyman-alpha	1.5×10^{-3}	2.1×10^{-3}	4.2×10^{-3}

a. using the ISRF from Mathis et al. (1983)

b. using the spectrum calculated by Gredel et al. (1987)

c. using the spectrum collected by Herczeg et al. (2002), Valenti et al. (2003), and Johns Krull & Herczeg (2007)

case of dissociation (O₂, H₂O), the radicals created can induce chemistry that will affect photodesorption efficiencies. For example, (Hollenbach et al. 2008) use a value of 10^{-3} molecules photon⁻¹ for the photodesorption rate of O₂, which is very close to the value derived experimentally for pure O₂ ice. In mixed ices, however, the photodesorption of O₂ could be perturbed: on one hand, the atomic oxygen produced upon irradiation can recombine with other molecules or radicals, lowering photodesorption induced by exothermic oxygen recombination; on the other hand, the presence of additional excited species and radicals may enhance indirect O₂ photodesorption via DIET or kick-out mechanisms. It is not obvious how these effects could balance each other. More experiments and molecular dynamics simulations are required to treat photodesorption in mixed ices accurately. The present study offers a firm first step in this direction.

5.5 Conclusions

The UV induced photodesorption of pure N₂ and O₂ ices are principally different. N₂ does not significantly dissociate upon irradiation between 7 and 13.6 eV. Its transition to the first allowed electronic state (above 12.4 eV) induces desorption through an indirect process where the excited molecules eject surface molecules into the gas phase. In the case of O₂, photodissociation already occurs below 7 eV, and oxygen radicals induce chemical pathways driving the photodesorption mechanism. The formation of ozone in the case of high flux irradiation affects the photodesorption of O₂ by adding an additional channel for molecular oxygen desorption induced by ozone photolysis. Absolute wavelength-dependent photodesorption rates can be used to estimate photodesorption in various star-forming environments, but it is important to note that the presented results apply to pure ices only. A detailed modeling of neighbor interaction and radical-induced chemistry is required to predict photodesorption efficiencies in the case of mixed ices.

Indirect UV photodesorption from CO:N₂ binary ices - an efficient grain-gas process -

Abstract. UV ice photodesorption is an important non-thermal desorption pathway in many interstellar environments that has been invoked to explain observations of cold molecules in disks, clouds and cloud cores. Systematic laboratory studies of the photodesorption rates, between 7 and 14 eV, from CO:N₂ binary ices, have been performed at the DESIRS vacuum UV beamline of the synchrotron facility SOLEIL. The photodesorption spectral analysis demonstrates that the photodesorption process is indirect, i.e. the desorption is induced by a photon absorption in sub-surface molecular layers, while only surface molecules are actually desorbing. The photodesorption spectra of CO and N₂ in binary ices therefore depend on the absorption spectra of the dominant species in the sub-surface ice layer, which implies that the photodesorption efficiency and energy dependence are dramatically different for mixed and layered ices compared to pure ices. In particular, a thin (1-2 ML) N₂ ice layer on top of CO will effectively quench CO photodesorption, while enhancing N₂ photodesorption by a factors of a few (compared to the pure ices) when the ice is exposed to a typical dark cloud UV field, which may help to explain the different distributions of CO and N₂H⁺ in molecular cloud cores. This indirect photodesorption mechanism may also explain observations of small amounts of complex organics in cold interstellar environments.

M. Bertin, E. C. Fayolle, C. Romanzin, H. A. M. Poderoso, X. Michaut, L. Philippe,
P. Jeseck, K. I. Öberg, H. Linnartz and J.-H. Fillion,
submitted to the Astrophysical Journal

6.1 Introduction

In cold and dense regions of the interstellar medium (ISM), characteristic of star and planet formation, gaseous atoms and molecules stick onto dust grains forming ice mantles in relatively short time scales. At these very low temperatures (< 20 K), thermal desorption is negligible for all molecules except H₂. Yet, molecules are detected in the gas phase for temperatures below their condensation temperature and this implies the existence of efficient non-thermal desorption processes. These comprise desorption induced by cosmic rays, chemically-induced desorption and vacuum UV photodesorption. The latter has been proposed as an important desorption pathway, particularly in the surface layers of proto-planetary disks (Willacy & Langer 2000; Dominik et al. 2005; Hogerheijde et al. 2011). It may also account for the gas-to-ice abundance ratio for a number of species as observed in other dense regions of the ISM (Coutens et al. 2012; Hollenbach et al. 2008), including the edges of molecular clouds where external UV photons can alter the ice mantle formation, or in the inner part of dense molecular clouds where UV photons are produced by the cosmic-ray ionization of H₂ (Caselli et al. 2012). Photodesorption, therefore, is of general importance, influencing the chemistry at different locations in denser regions in space.

Quantitative photodesorption yields from low temperature ices were first obtained experimentally for H₂O (Westley et al. 1995a,b). Over the last five to seven years photodesorption rates have been determined for other pure ice samples using broad band, hydrogen discharge lamps; CO (Öberg et al. 2007; Muñoz Caro et al. 2010), H₂O/D₂O (Öberg et al. 2009b), N₂ and CO₂ (Öberg et al. 2009; Bahr & Baragiola 2012; Yuan & Yates 2013), O₂ and O₃ (Zhen et al, submitted). Molecular dynamics calculations have been performed for water ice (Andersson et al. 2006, 2005; Arasa et al. 2010, 2011) and are in good agreement with the experimental findings. More recently, wavelength-specific studies have been performed and for CO, N₂ and O₂ absolute photodesorption rates have been determined between 7 and 14 eV (Fayolle et al. 2011, Fayolle et al in press). The spectral dependence of the photodesorption yield is of fundamental interest for modeling regions in space with different spectral energy distributions. Moreover, this approach has been very successful to link the photodesorption process in the ice to the solid state mechanisms at play, highlighting the physical-chemical parameters governing the photodesorption process. In the case of CO and N₂ the wavelength dependent intensity of the measured Photon-Stimulated Desorption signals (PSD) follows directly the electronic transitions in the condensed molecules (Fayolle et al. 2011, Fayolle et al in press). This is a signature of a mechanism known as DIET (desorption induced by electronic transition), not (substantially) involving dissociation/recombination in the ices. An even more detailed picture of the involved surface processes has been derived from the investigation of layered ¹³CO/¹²CO films (Bertin et al. 2012) showing that the photodesorption is mediated by the ice lattice. This study pointed out a sub-surface excitation mechanism in which electronically excited molecules release their energy through intermolecular vibrational motion into a desorption channel. Recently, Yuan & Yates (2013) addressed the crucial role of this energy transfer from the ice lattice by comparing Lyman- α photodesorption at 75 K for pure ¹²CO₂, pure ¹³CO₂ and ^{12/13}CO₂ mixed ices.

In the present work we go one step further and study the photodesorption efficiency of a binary ice mixture made of different chemical species. We present wavelength dependent photodesorption measurements from CO and N₂ binary ices (layered and mixed) at 10 K. This is interesting from a physical-chemical point of view; their masses are nearly equivalent, their photodesorption mechanisms are similar and their binding energies to the solid are comparable, but the two molecules have strong, non-coinciding photodesorption features in the VUV (around 8.5 and above 12.3 eV for CO and N₂, respectively) in their pure solid phase. The choice for a CO:N₂ ice is particularly relevant from an astronomical point of view. CO is highly abundant, both in the gas phase and in the solid state, representing the main molecular component after H₂. Molecular nitrogen, N₂, is not directly detectable due to its lack of a permanent dipole moment, but is considered as one of the main reservoir of nitrogen in the gas phase, due to its high stability. Its presence in the ISM is evidenced by the detection of N₂H⁺ resulting from a proton transfer reaction involving H₃⁺ (Bergin et al. 2002; Flower et al. 2006; Hily-Blant et al. 2010). Moreover, N₂ stands at the origin of other processes leading to the formation of more complex N-bearing molecules (Persson et al. 2010, 2012; Hily-Blant et al. 2013). As both CO and N₂ are highly volatile, with accretion temperatures in the 16-20 K regime under ISM conditions and sticking coefficients close to unity, they are the last species to freeze onto dust grains, generating a top layer that can be considered as a binary interstellar ice (Öberg et al. 2005; Bisschop et al. 2006). Nevertheless, observational studies of N₂H⁺ and other N-containing species in dense cores indicates that N₂ depletion onto the grains occurs later, i.e. at higher density, than for CO (Bergin et al. 2002; Pagani et al. 2005, 2012). Therefore, it has been suggested that a mechanism leads to a continuous enrichment of gas phase N₂, counterbalancing its accretion on the grains. Chemistry involving CN + N reactions, constantly forming N₂ in the gas, is invoked (Hily-Blant et al. 2010), but, photodesorption processes, preferentially ejecting N₂ instead of CO in the gas phase from a condensed mixture of N₂ and CO, may be an equally important channel.

In this chapter, a laboratory based study of vacuum UV irradiated CO:N₂ binary ice samples as a function of the wavelength is presented. This approach follows successful experiments on pure CO, N₂ and O₂ ice (Fayolle et al. 2011, Fayolle et al. in press). In the next section experimental details are given. The results are presented in section 3 and are discussed from a physical-chemical and an astrophysical point of view in section 4.

6.2 Experimental methods

The photodesorption studies are realized in the SPICES (Surface Processes & ICES) setup of the UPMC (Université Pierre et Marie Curie), under ultrahigh vacuum (UHV) conditions ($P \sim 1 \times 10^{-10}$ Torr). The substrate on which ices are grown is a Highly Oriented Polycrystalline Graphite (HOPG) surface. It is mounted on the tip of a turnable cold head that can be cooled down to ~ 10 K by means of a closed cycle helium cryostat. The ice layers are grown in-situ by exposing the cold HOPG substrate to a partial pressure of CO and/or N₂ gases. A dosing tube, placed 1 mm in front of the substrate, allows a local exposure of the gases onto the cold sample without contami-

nating the whole UHV chamber. The isotopologues ¹³CO (Eurisotop, 99.6 % ¹³C) and ¹⁵N₂ (Eurisotop, 97 % ¹⁵N) are used in order for them to be distinguishable by mass spectrometry. The quantities of molecules deposited on the substrate are expressed in ML_{eq} (monolayer equivalent) corresponding to the surface density of a compact molecular layer on a flat surface, with 1 ML_{eq} ≈ 1 × 10¹⁵ molecule.cm⁻². Temperature Programmed Desorption (TPD) is used for the calibration of the ice thicknesses, resulting in reproducible parameters for the growth conditions with a precision better than 1 ML_{eq}.

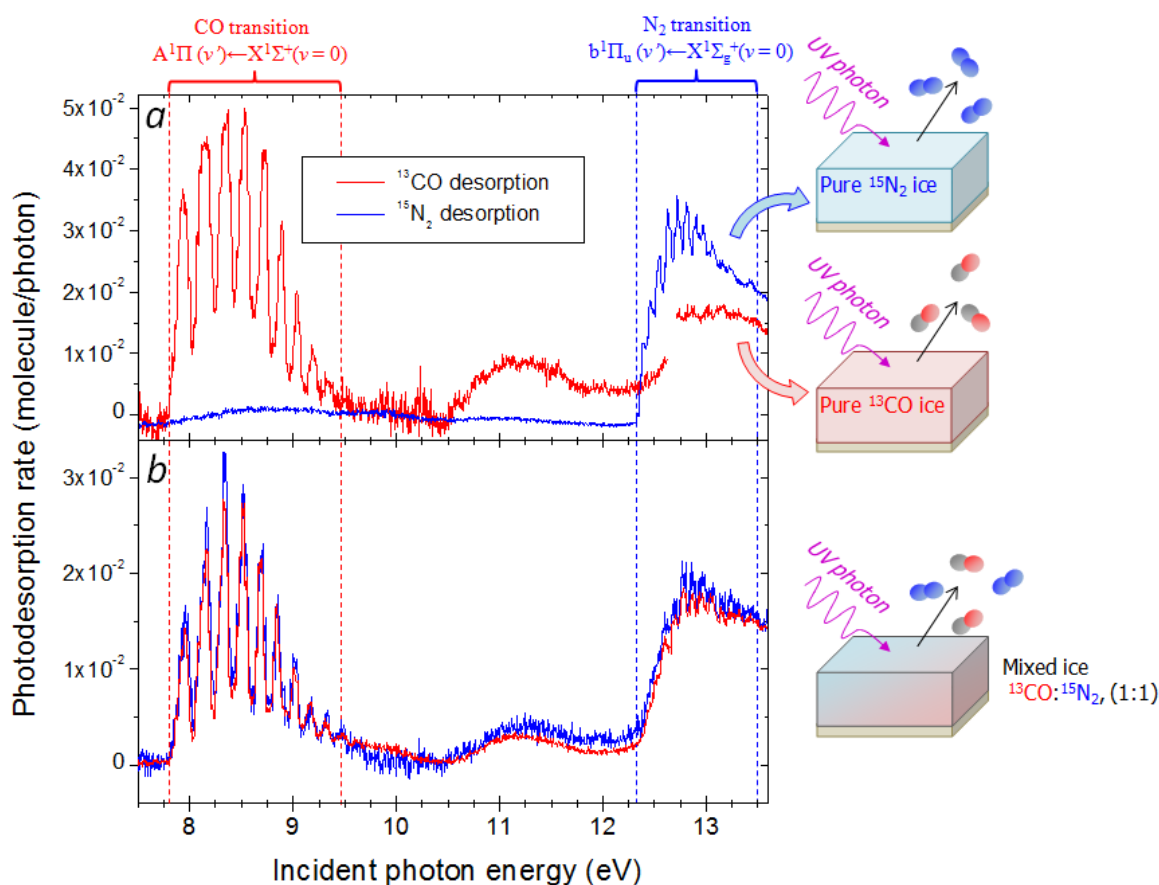


Figure 6.1: Photon-Stimulated Desorption (PSD) spectra of ¹³CO (red) and ¹⁵N₂ (blue) from 30 ML of pure ¹³CO and ¹⁵N₂ ices (a), and from a mixed ¹³CO:¹⁵N₂ ice, in proportion 1:1 (b). The electronic transitions in condensed CO and N₂ associated with the main photodesorption features are indicated. All spectra have been obtained for ices kept at 15 K and deposited on HOPG.

UV photodesorption is induced through irradiation of the ice sample by the continuous output of the undulator-based vacuum UV DESIRS beamline of the synchrotron SOLEIL (Nahon et al. 2012), providing photons with an energy that can be continuously scanned over the 7 - 14 eV range. A narrow bandwidth of typically 40 meV is selected by the 6.65 m normal incidence monochromator that is implemented on the

beamline. A gas filter in the beamline suppresses the harmonics of the undulator that can be transmitted in higher diffraction orders of the grating. The absolute incident photon flux per surface unit impinging onto the sample is measured by a calibrated photodiode and varies for a given spectral bandwidth of 40 meV between 0.3 and 1.1×10^{13} photons.s⁻¹.cm⁻² depending on the photon energy. In order to prevent radiation cut-off, the DESIRS beamline is directly connected to SPICES, i.e., without any window.

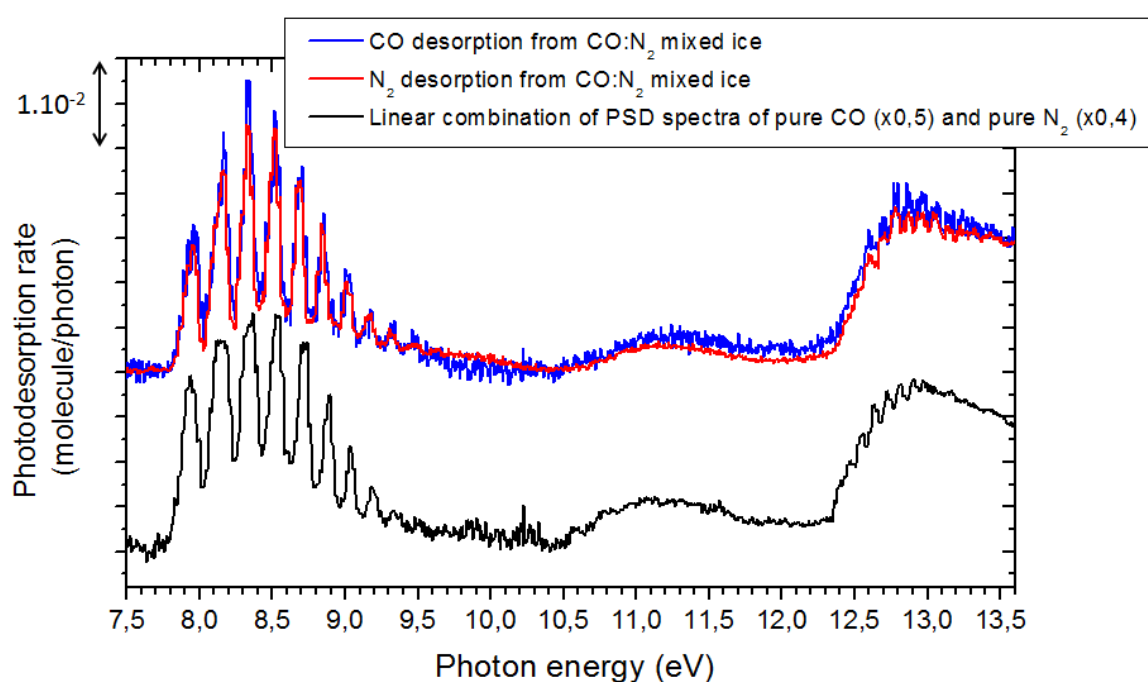


Figure 6.2: Photon-stimulated spectra of N₂ and CO from a mixed CO:N₂ ice, in proportion 1:1, compared with a linear combination of PSD spectra obtained from pure CO ice ($\times 0.5$) and pure N₂ ice ($\times 0.4$). The spectra have been acquired from ices deposited on HOPG kept at 15 K.

Photon-stimulated desorption spectra, are recorded in real time during ice irradiation, monitoring the gas phase composition upon evaporation by means of a Quadrupole Mass Spectrometer (QMS), as a function of the incident photon energy. In the presented PSD spectra, the photon energy is automatically scanned from 7 to 14 eV with steps of 25 meV. Each energy step lasts ~ 5 s. In parallel, the QMS signal is recorded with a dwell of 1 s, which makes an average of 5 points per energy step. Caution has been taken to ensure that for each data point the 1 s accumulation time is substantially longer than the QMS mass signal build-up time, preventing eventual artifacts due to fast wavelength scanning. The mass resolution of the QMS, as taken

from the Full-Width-at-Half-Maximum (FWHM) of the Gaussian mass peaks associated with ¹³CO ($m = 29$ amu) and ¹⁵N₂ ($m = 30$ amu) is ~ 0.3 amu. It therefore allows for a fine separation of ¹³CO and ¹⁵N₂ signals with negligible overlap. The energy-dependent desorption rate per incident photon is derived from the PSD spectra and the measured energy-dependent photon flux, following the methods described in detail previously (Fayolle et al. 2011, Fayolle et al. in press). Additional information on the composition of the condensed phase can also be obtained by monitoring simultaneously Reflection-Absorption-Infrared Spectra (RAIRS) using a Fourier transform infrared (FT-IR) spectrometer.

6.3 Results

Figure 6.1a shows PSD spectra obtained upon VUV irradiation of the pure ¹³CO and ¹⁵N₂ ices. These spectra have already been presented and discussed in previous studies. The photodesorption rates exhibit energy-dependent efficiencies that follow closely the VUV absorption of the pure molecular solids, with patterns that are associated with electronic transitions of the condensed molecules. For instance, the features observed between 7.9 and 9.5 eV in the CO PSD spectrum are due to vibronic bands in the $A^1\Pi - X^1\Sigma^+(v',0)$ electronic transition, each peak being associated with a transition towards a vibrational sub-level v' in the A-state of solid ¹³CO (Fayolle et al. 2011). In a similar way, the main feature responsible for the photodesorption of solid ¹⁵N₂ (above 12.3 eV) is associated with the $b^1\Pi_u - X^1\Sigma_g^+(v',0)$ transition in pure nitrogen ice (Fayolle et al., in press). The observation of such structures in the energy-resolved photodesorption rates is a clear signature for a DIET mechanism, as discussed in (Fayolle et al. 2011, Fayolle et al. in press). It has been shown that the excitation mainly takes place in a subsurface region of the ice (2-3 upper molecular layers), while only the molecules from the topmost layer are ejected into the gas phase. A short-range energy transfer from the excited to the desorbing molecules is therefore expected to occur, presumably through the coupling between the relaxation of the excited species and the excitation of intermolecular collective vibrational modes (Bertin et al. 2012). It should be noted that the thickness of our samples is less than the photon penetration depth, implying that photons can excite molecules deeper within the ice and even reach the graphite substrate. However, according to (Bertin et al. 2012), neither the substrate nor underlying layers are contributing to the desorption features observed here. The question that is addressed here is how these properties translate in a mixed ice, consisting of both CO and N₂.

6.3.1 Photodesorption from mixed CO:N₂ ice

Figure 6.1b displays the PSD spectra for both ¹³CO and ¹⁵N₂ desorbing upon VUV irradiation of an ice grown from a 1:1 CO:N₂ mixture. There is a clear difference between the results for the pure and mixed ice irradiation. As discussed above, the pure ice spectra are very different, whereas, for the mixed ice, the PSD spectra are identical. A comparison with Fig. 6.1a shows that the photodesorption spectra of the CO:N₂ ice mixture results in a superposition of the PSD spectra of the two pure constituents.

The ejection of any surface molecule in the mixed ice, clearly, is initiated by the electronic excitation of any other molecule. In particular, the PSD spectra of the mixed ice show that the excitation of solid CO into its $A^1\Pi$ state leads to the desorption of surface N_2 (7.9 - 9.5 eV), and that solid N_2 excitation into its $b^1\Pi_u$ state initiates CO desorption above 12.3 eV. This finding is fully consistent with the previously introduced concept of an indirect DIET mechanism; part of the excess energy deposited in the ice by the vacuum UV photon absorption is transferred from one to the other molecule independently of its chemical nature - causing desorption. Within this respect, the process shows similarities with the *indirect adsorbate-mediated photodesorption* proposed by Thrower et al. (2008) in which the energy of a laser pulse absorbed by benzene molecules is transferred to water molecules enhancing their desorption.

For a given energy, the absolute photodesorption rates of CO and N_2 from the mixed ice are lower by a factor of 2 than the corresponding value derived for the pure ices. In fact, the PSD spectra of the mixture can be fitted with a very good agreement by a linear combination of the desorption spectra of pure $^{15}N_2$ and pure ^{13}CO in which each constituent contributes to about ~ 0.5 of the overall desorption signal (Fig. 6.2). As the surface of the mixed film is expected to be composed of half CO and half N_2 molecules, and as the adsorption energies of CO and N_2 are very close (Bisschop et al. 2006), this shows that the amount and efficiency of the energy transfer to surface molecules upon subsurface CO excitation or N_2 excitation are about the same.

6.3.2 Photodesorption from layered N_2/CO and CO/N_2 ices

Photon-stimulated desorption spectra of ^{13}CO (left panel) and $^{15}N_2$ (right panel) obtained from a pure 25 ML_{eq} ^{13}CO ice covered by an increasing layer of $^{15}N_2$ are shown in Fig. 6.3. In the case of pure CO or N_2 ice (top left and bottom right, respectively) the characteristic desorption profiles around 8.5 and above 12.3 eV are seen. When the CO ice is covered by 0.9 ML_{eq} of N_2 , the CO desorption yield drops substantially, and it is almost entirely suppressed above ML_{eq} . This behavior, also observed in the case of layered $^{13}CO/^{12}CO$ (Bertin et al. 2012), shows that mostly the surface molecules are susceptible to desorb upon UV irradiation.

When investigating the PSD of $^{15}N_2$ for a low thickness of N_2 overlayer (0.9 ML_{eq}), one can see that its photodesorption pattern mimicks almost completely the one of the pure CO ice, demonstrating that its photodesorption is triggered only by the absorption of the underlying CO molecules. In particular, its photodesorption in the 7.9 - 9.5 eV range, associated with the excitation of the $A^1\Pi$ state of solid CO, becomes the dominant contribution, although pure solid N_2 does not photodesorb at these energies. In contrast, photodesorption initiated by the N_2 excitation in the $b^1\Pi_u$ state (> 12.3 eV) is not clearly observed. The adsorption of a small quantity of N_2 onto a CO ice therefore drastically modifies the energy-dependence of its photodesorption process. For increasing thickness of the $^{15}N_2$ overlayer, the N_2 excitation contribution to the N_2 PSD spectra gradually recovers the one of the pure N_2 ice. The contribution of the CO excitation becomes very weak for N_2 thicknesses above ML_{eq} , showing that the range for an efficient energy transfer involves less than 3 molecular layers.

Figure 6.4 shows the results of layered experiments in which 25 ML_{eq} $^{15}N_2$ ice is

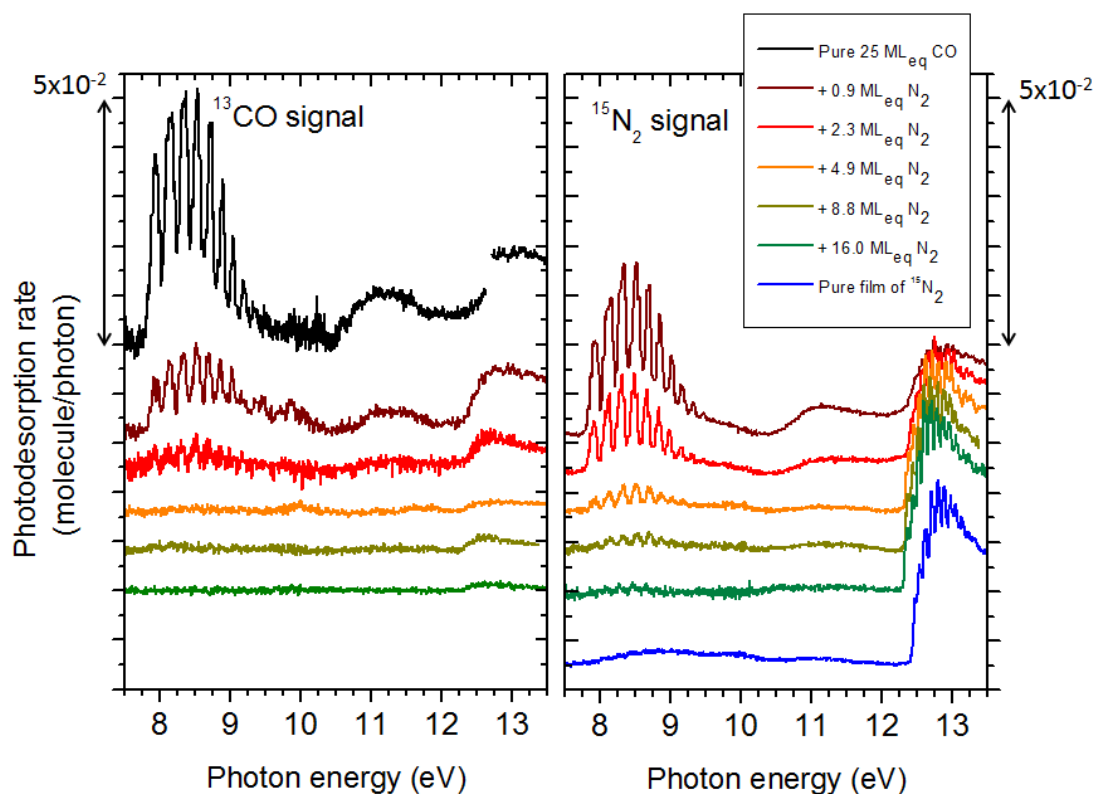


Figure 6.3: Photon-stimulated desorption spectra of ^{13}CO (left) and $^{15}\text{N}_2$ (right) from 25 ML_{eq} of ^{13}CO ice covered by an increasing $^{15}\text{N}_2$ layer on top. The PSD spectrum obtained from a pure 25 ML_{eq} $^{15}\text{N}_2$ ice is also presented for comparison. All spectra are recorded for 15 K ices, deposited on HOPG.

covered by an increasing layer of ^{13}CO . The experiment is essentially identical to the previous one (fig. 6.3), but the role of N_2 and CO are exchanged. The N_2 photodesorption signal vanishes for a larger CO coverage and a clear vibrational progression in the ^{13}CO desorption channel is found that corresponds to an excitation into the $b^1\Pi_u$ state of N_2 . This feature is superimposed over a continuous desorption of ^{13}CO observed above 12.5 eV in pure CO samples (Fayolle et al. 2011). As for the 25 ML_{eq} ^{13}CO ice covered by $^{15}\text{N}_2$ the spectra are fully consistent with a process in which only surface molecules desorb after excitation of sub-surface species.

6.4 Discussion and astrophysical implications

6.4.1 Role of ice structure and composition on absolute photodesorption rates

The VUV photodesorption of coadsorbed N_2 and CO presents very different energy-dependent profiles and efficiencies compared to pure N_2 and CO ices. Both molecules mainly desorb through an indirect mechanism, where the excitation of a subsurface

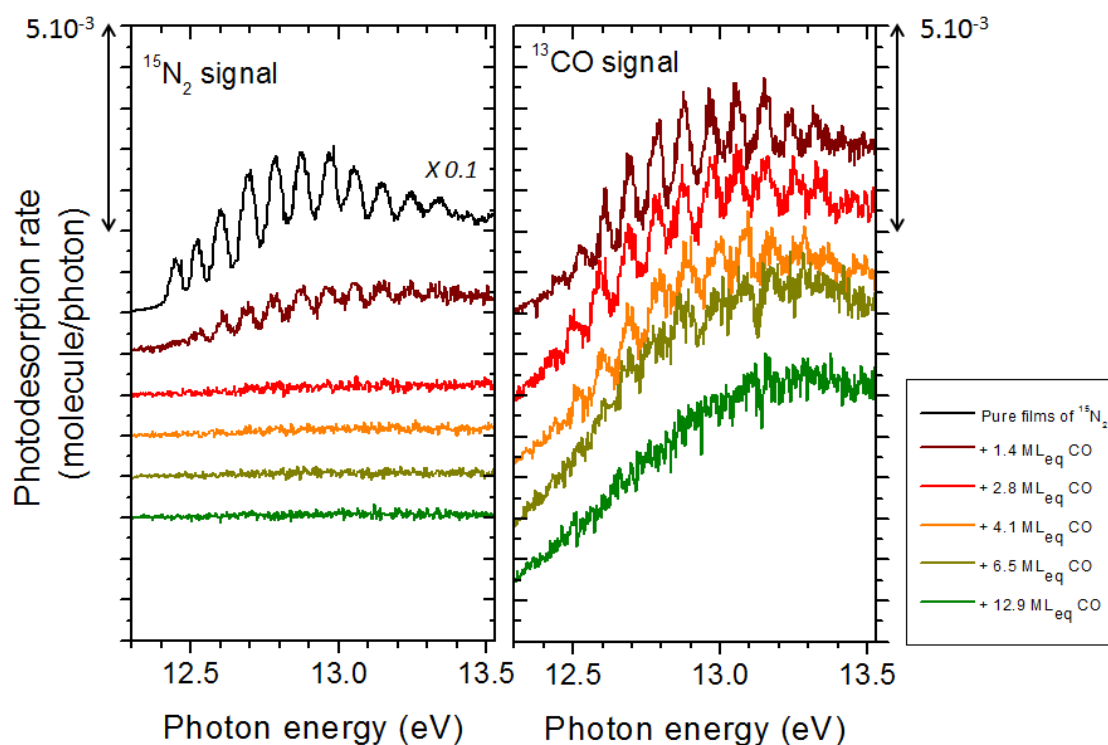


Figure 6.4: Photon-stimulated desorption spectra of $^{15}\text{N}_2$ (left) and ^{13}CO (right) from 25 ML_{eq} of $^{15}\text{N}_2$ ice covered by an increasing layer of ^{13}CO ice on top. All spectra are recorded for 15 K ices, deposited on HOPG.

molecule, whether CO or N_2 , leads to the desorption of N_2 and CO surface molecules. Because this indirect mechanism involves energy transfer from the excited molecule to the desorbing one, presumably by collective vibrational mode excitation, the photodesorption energy-dependence and efficiency depend strongly on the nature of the intermolecular interactions. In general intermolecular interactions in solids may promote the photodesorption, but also quench it. This has been demonstrated for CO_2 in interaction with other isotopologues or rare gas matrices (Yuan & Yates 2013), and for CO in interaction with H_2O ice (Bertin et al. 2012). For the latter case, an explanation has been proposed, stating that the photodesorption efficiency is driven by the competition between two excess energy relaxation pathways: (i) relaxation by intermolecular phonon modes of the ice, coupled to desorption and (ii) relaxation by transfer to intramolecular vibration modes of neighboring molecules. If the first relaxation pathway is dominant, the photodesorption will be efficiently triggered by UV absorption of neighboring molecule. If the latter pathway dominates the relaxation process, as it is the case when excited CO transfers efficiently its excess energy to the O-H dangling bond vibrations of neighboring water molecules, then the photodesorption gets hindered. In both cases, the constructive and destructive matrix effects are a consequence

Table 6.1: Energy-integrated photodesorption rates of CO and N₂ in several regions of the ISM for pure ices, mixed CO:N₂ ices in a proportion of 1:1, and 0.9 monolayer equivalent (ML_{eq}) of N₂ deposited on top of a CO ice. The rates are for ices kept at 15 K. All values are given in desorbed molecules per incident photon.

Environment	Pure CO ice ^a	Pure N ₂ ice ^b	CO from		N ₂ from	
			Mixture CO:N ₂ 1:1	0.9 ML _{eq} N ₂ on CO	Mixture CO:N ₂ 1:1	0.9 ML _{eq} N ₂ on CO
Edges of clouds ^a	1.3×10^{-2}	2.6×10^{-3}	5.7×10^{-3}	5.3×10^{-3}	5.5×10^{-3}	8.0×10^{-3}
Prestellar cores ^b	1.0×10^{-2}	2.2×10^{-3}	3.0×10^{-3}	3.9×10^{-3}	3.0×10^{-3}	5.1×10^{-3}
Protoplanetary disk ^c	7.2×10^{-2}	5.3×10^{-3}	2.3×10^{-3}	3.0×10^{-3}	2.1×10^{-3}	2.7×10^{-3}

Note. — Using UV field from ^aMathis et al. (1983), ^bGredel et al. (1987), ^cHerczeg et al. (2002); Valenti et al. (2003); Johns Krull & Herczeg (2007). ^d and ^e are values from Fayolle et al. (2011) and Fayolle et al. (in press) respectively

of the indirect character of the photodesorption mechanism.

Because the intermolecular coupling in the ice between excited and surface molecules can drastically modify the photodesorption process, it is expected that different composition, but also different structure of the ice, will modify the energy-integrated photodesorption yield for a given UV field. This is illustrated for the N₂/CO binary ices. As shown in Figs. 1 and 3, coadsorption of N₂ with CO promotes N₂ desorption in the 7 - 11.5 eV range whereas it decreases the desorption efficiency of CO in the same energy range. To quantify this effect, energy-integrated photodesorption rates have been derived from our PSD curves for three types of interstellar vacuum UV profiles as a function of the CO:N₂ layered/mixed ices composition. The results are displayed in Table 1. To obtain these values, our energy-resolved desorption rates have been convoluted with vacuum UV profiles describing the interstellar radiation field (ISRF) at the edge of clouds (Mathis et al. 1983), the effect of secondary photons from cosmic ray impacts in dense cores (Gredel et al. 1987), and a TW Hydræ radiation field as model for the UV field in proto-planetary disks (Herczeg et al. 2002; Valenti et al. 2003; Johns Krull & Herczeg 2007). The resulting photodesorption rates are varying depending on (i) the UV field considered, (ii) the ice composition and (iii) the internal ice organization (layered versus mixed). Compared to pure ices the photodesorption rates from the binary ices change by up to an order of magnitude. The general trend is to decrease the CO photodesorption rate from $> 1 \times 10^{-2}$ to $2-6 \times 10^{-3}$ molecules.photon⁻¹, and to increase the N₂ photodesorption rate by a factor of 2-3. This shows that a proper description of the VUV photodesorption process has to take into consideration the structure and composition of the ice on which the molecules are adsorbed; the photodesorption rates extracted from pure molecular solids may not be realistic in the case of more complex ices, as typically present in the interstellar medium.

6.4.2 Implications for N₂ and CO gas phase abundance in dense cores

In dense cores, non-thermal desorption, including photodesorption, is constantly enriching the gas phase, competing with gaseous species freezing-out on the grains. Thus a variation of the photodesorption rate with chemical composition and ice morphology directly influences the steady state between the two processes. The details of the processes that determine the steady-state are especially important for N₂ because of the longstanding question why N₂ molecules remain (partially) in the gas-phase in cold interstellar regions where CO is found to be completely frozen out on grain surfaces (Bergin et al. 2002; Pagani et al. 2012). This cannot be explained by thermal processes alone, since N₂ and CO are expected to condense on icy grains less than 2 K apart, and with the same efficiency (Öberg et al. 2005; Bisschop et al. 2006). The photodesorption rates as extracted from pure CO and N₂ ices are not resolving the issue either since the photodesorption rate is substantially lower for pure N₂ than for pure CO for realistic dark cloud UV fields (Table 6.1). However, considering pure ices may be inappropriate, as discussed in section 4.1, since the ice structure and composition may impact the CO and N₂ photodesorption rates.

Since CO and N₂ are expected to freeze-out in the same temperature range, it is rather unlikely that the top layers of the ices are composed of solely pure N₂ or pure CO thick layers. Instead, we expect that both species are coadsorbed at the surface of the icy grains. The exact nature of the top layers depends on the abundance of N₂ as compared to CO, as well as on the proximity in time and space of CO and N₂ freeze-out. The amount of N₂ being relatively low compared to CO (Bergin et al. 2002; Maret et al. 2006), it is expected that solid N₂ is frozen on or into a CO-rich environment. Whether the outer layers of the grain will be layered or mixed is not that easy to answer, and is likely source-dependent. N₂ is expected to condense for 2 K lower temperatures, compared to CO (Flower et al. 2006; Hily-Blant et al. 2010), which would, for low cooling speed of the cloud, lead to the growth of a thin N₂ layer on top of CO-rich ice. In the case of a shorter cooling time, such a temperature difference would not be sufficient to result in segregated layers, and N₂ would be embedded in a CO matrix.

As explained before, the photodesorption rates extracted from pure CO and pure N₂ in prestellar cores cannot explain the N₂ constant gas phase enrichment in region where CO is totally frozen: the pure N₂ photodesorption is substantially less efficient than for pure CO. If we consider instead a mixed CO:N₂ 1:1 ice, the photodesorption rates of CO and N₂ in prestellar cores become identical, as shown on Table 6.1. In the case of a more realistic system, i.e. a small amount (0.9 ML_{eq}) of N₂ on CO ice, then, the CO photodesorption rate strongly decreases, whereas the N₂ photodesorption rate is promoted. Then, the N₂ desorption becomes more efficient than the CO one, and photodesorption can explain gas phase N₂ enrichment. Thus, under interstellar conditions N₂ will be photodesorbed at least as efficiently as CO as long as they are coadsorbed, and in many core environments, the N₂ photodesorption may exceed that of CO providing a natural explanation to why N₂ is maintained longer in the gas phase compared to CO.

6.4.3 Organics desorption through CO photoexcitation?

The indirect nature of the photodesorption process may have more general implications beyond the explanation of the CO and N₂ abundances in the ISM. The ability of CO ice to transfer part of the absorbed energy to a surrounding molecule may act as an important indirect photodesorption channel of other species as well, and in particular of formaldehyde H₂CO, methanol CH₃OH, and possibly more complex organic molecules, providing a non-dissociative non-thermal desorption pathway. Indeed, these species are expected to form into the CO-rich icy mantles, by hydrogenation processes (Watanabe & Kouchi 2002; Fuchs et al. 2009; Herbst & van Dishoeck 2009; Taquet et al. 2013). Moreover, in (Cuppen et al. 2011), it was spectroscopically shown that interstellar CO ice gets intimately mixed with methanol and that the outer CO layer of the ice is essentially water free.

Organic molecules are expected to efficiently photodissociate upon UV photon irradiation, as it the case for instance for CH₃OH (Öberg et al. 2009a), leading to the formation of photoproducts that can eventually desorb. Photochemistry in the ice represents an important decay channel upon UV excitation and is in direct competition with the photodesorption of the intact molecule. When the photodestruction is dominating, it can even prevent the intact molecule to be ejected in the gas phase, making the photodesorption decay channel totally inactive. Embedded in a CO-rich environment, however, such molecules may react differently under UV irradiation: even when the direct UV absorption of organics leads to their destruction, a photon absorption by the surrounding and more numerous CO molecules could lead to the desorption of the surface-located organics via a similar mechanism as highlighted for CO:N₂. The CO would then act as a 'seed' for intact molecular photodesorption, preventing their destruction in the ices and thus enriching the gas phase with small organics. Such a process could then explain the observed gas abundances of organics, observed in the cold regions of the ISM (Öberg et al. 2010; Bacmann et al. 2012; Tercero et al. 2013). Whether this indirect photodesorption process can be generalized to heavier and more strongly bound species than CO and N₂ needs to be experimentally verified, however.

6.5 Summary and conclusions

From a systematic set of energy (7 - 14 eV) resolved (40 meV) photodesorption laboratory studies on CO:N₂ binary ices, both mixed and layered the following conclusions can be made:

- The desorption is induced by a photon absorption in the topmost molecular layers, while only surface molecules are actually desorbing. This implies an energy transfer from the subsurface excited molecule to the surface ones. Thus, the photodesorption rate is not linked to the absorption spectrum of the desorbing molecule, but is instead associated to the absorption profile of the surrounding species, located deeper in the ice. When N₂ and CO are mixed in equal proportions, their photodesorption spectra become superimposable, and reflect a linear combination of the photodesorption spectra of both pure ices. When a small quantity of N₂ is deposited at the surface of a CO ice, then, its photodesorption spectrum reflects mostly the one of

pure CO. This is remarkable since, in this case, the N_2 major desorption feature lies in the 7.9 - 9.5 eV energy range, in which pure solid N_2 does not absorb.

– This indirect desorption mechanism and its dependence on ice structure and wavelength influence the (overall) desorption efficiency in space. Considering the range of indirect photodesorption processes, we suggest that the photodesorption rates experimentally obtained from pure ices should only be used for molecules which can form pure phases in the ISM ices, exceeding at least two to three molecular toplayers, as it may be the case for CO in some cold regions. Below this thickness, or when molecules are mixed with others, photodesorption rates obtained from a more realistic composite ice should lead to a more accurate description of the non-thermal desorption. Here both chemical composition and molecular organization play a role.

– The results presented here provide a way to replenish nitrogen in the prestellar cores, contributing to the unexplained low depletion rate of N_2 as compared to CO. If the rates derived for pure CO and N_2 are used, CO should desorb with an efficiency that is almost one order of magnitude higher than for N_2 . This is not in agreement with observations concluding that gaseous CO depletes on the grains with a higher rate than N_2 . When considering the rates extracted from a more realistic system, most probably a layered N_2 /CO structure with a small amount of N_2 , as presented here, gaseous N_2 will be enriched with respect to CO. A detailed astrochemical modeling is required to quantify the extent of this N_2 enrichment.

– Finally, the mechanism introduced here may explain observation of organic species in the gas phase in very cold environments of space. Indirect photodesorption could indeed result in the release of gas phase intact organic species by UV absorption of neighboring molecules, whereas direct UV photo-excitation of this species may lead to its destruction through photolysis.

Linking the ice content and gas abundances of organic molecules in massive young stellar objects

Abstract. Sources of complex organic molecules display a large chemical diversity, including small-scale differentiation between nitrogen and oxygen bearing complex species. We aim to test whether complex chemical differences can be explained by different initial ice conditions in different lines of sight.

We use the IRAM 30m and the Submillimeter Array to search for complex organic molecules in three massive young stellar objects (MYSOs) with known ice abundances, but without luminous hot cores, to expand the existing sample of MYSOs with both ice and complex gas observations.

Complex molecules are detected toward all three MYSOs at comparable abundances with respect to CH_3OH as in classical hot core sources. The N-bearing molecules are generally concentrated toward the source center, while most O- and C-bearing molecules are present both in the center and in the colder envelope. $\text{HNCO}/\text{CH}_3\text{OH}$ gas ratios tentatively depend on the $\text{OCN}^-/\text{CH}_3\text{OH}$ and $\text{NH}_3/\text{CH}_3\text{OH}$ ice ratios, while $\text{CH}_3\text{CN}/\text{CH}_3\text{OH}$ gas ratios do not. This is consistent with new model predictions. Both theory and observations suggest that gas temperature and initial abundances are important factors for complex organic distributions toward MYSOs. To quantify their relative impact requires a large spatially resolved survey of YSOs with ice detections.

E. C. Fayolle, K. I. Öberg, R. T. Garrod, E. F. van Dishoeck and S. E. Bisschop
in preparation

7.1 Introduction

Organic molecules containing more than 6 atoms, so-called complex organics (Herbst & van Dishoeck 2009), are commonly found in the warm and dense gas phase ($T > 100$ K, $n > 10^6$ cm⁻³) around young stellar objects (YSOs) (e.g. Blake et al. 1987; Cazaux et al. 2003; Fuente et al. 2005). Abundances and abundance ratios of complex organics are found to vary substantially between (Helmich & van Dishoeck 1997) and within YSOs (e.g. Wyrowski et al. 1999), suggestive of formation and/or destruction routes that are highly environment specific as well as a possible variation in chemical initial conditions. The potential dependencies together with the fact that complex organics present large numbers of lines, spanning most excitation conditions found in space, entails that these molecules have a great potential to provide useful clues on the physical conditions where they are found, as well as the chemical and physical history (Nomura & Millar 2004). Complex molecules are also of high interest for origins of life theories since they are the precursors of even more complex prebiotic material (Ehrenfreund & Charnley 2000). Molecular probe development and advancements in prebiotic evolution from organics rely both on a detailed understanding of complex organic chemistry. The formation and destruction mechanisms of most complex organics and the corresponding process efficiencies are, however, poorly constrained.

The formation of organic molecules around massive YSOs (MYSOs) was first thought to proceed through gas phase reactions in dense hot cores, following evaporation of ice grain mantles (e.g. Charnley et al. 1992). Recent laboratory experiments and modeling efforts point now toward a more complicated sequential scenario which relies to a greater extent on surface formation routes on sub-micron sized dust particles. Herbst & van Dishoeck (2009) classified complex organic molecules in terms of generations according to the following scenario: In interstellar clouds and in the deeply embedded early phases of star formation, atoms and molecules accrete or form on the surface of dust grains, building up an icy mantle of simple species like H₂O, CH₄, NH₃ (Tielens & Hagen 1982). This icy molecular mantle is processed at low temperature by atoms, which can diffuse even at the low temperatures in cloud cores, creating the 0th generation of organic molecules. A good example of this species is CH₃OH, which is efficiently formed at low temperature by the hydrogenation of CO ice (Watanabe & Kouchi 2002; Watanabe et al. 2003, 2004; Fuchs et al. 2009; Cuppen et al. 2009). 1st generation complex organics form during heating up the cold envelope by the increasing luminosity of the central source and is due to a combination of photo-processing of the ice - resulting in radical production - and a warming up (20 to 100 K) of the grains - enhancing mobility of radicals and molecules (Garrod et al. 2008; Öberg et al. 2010). When the icy grains move inward and reach a regions warmer than 100 K, the icy mantle evaporates, bringing the 0th and 1st generation organics into the gas phase, where additional chemical reactions give rise to the formation of the 2nd generation complex organics (e.g. Charnley et al. 1992; Viti et al. 2004, Doty et al. 2002).

In the proposed scenario of complex molecule formation, the initial ice mantle plays a critical role. The exact composition of this ice may therefore have a large effect both on the product composition of formed organics and on their overall formation efficiency. Garrod et al. (2008) and Öberg et al. (2009a) find for example that CH₃OH

ice is a key starting point for most complex organic formation. Rodgers & Charnley (2001) have shown that the relative amount of NH_3 in the ice has a large impact on the $\text{CH}_3\text{CN}/\text{CH}_3\text{OH}$ abundance ratio in the protostar using a hot core chemistry model. Observationally testing these relationships would provide key constraints on the formation pathways of complex organic molecules.

Isolated MYSOs with warm inner envelopes are good laboratories to test this hypothesis as these sources are bright enough to observe a wide variety of organics and some of them present ice feature from the cold outer protostellar envelope (Gibb et al. 2004). Sources presenting both complex gas and ice features are, however, rare as the sources need to be evolved to possibly display a bright hot core chemistry and young enough such that the ice material has not been completely consumed by accretion, warm up and envelope-dispersal. In the massive YSO sample studied by Bisschop et al. (2007), only three hot cores present ice spectra. Such a small number prevents any analysis of correlation between ice and gas content and motivates our search for other objects displaying both ice features and gas phase organics.

To extend the sample of sources with both complex organics and ice observations, we propose to explore the presence of gas phase organics species around massive young sources with available ice observations, but without that a bright hot core phase. Massive objects NGC7538 IRS9, W3 IRS5, and AFGL490 have been observed in the mid-infrared by ISO and analyzed for ice abundances by Gibb et al. (2004). NGC7538 IRS9 is a $6 \times 10^4 L_\odot$ luminous object located in Perseus. It is close to hot core source NGC7538 IRS1 and displays at least 3 bipolar outflows, shows evidence for accretion (Sandell et al. 2005) as well as a hot component close to the central object. W3 IRS5 is associated with five young stellar objects, two of which are massive (van der Tak et al. 2005; Megeath et al. 2005; Rodón et al. 2008; Chavarría et al. 2010). It has a luminosity of $17 \times 10^4 L_\odot$ and presents strong S-bearing molecular lines. AFGL490 is a very young medium-mass YSO of $4.6 \times 10^3 L_\odot$, in transition to an Herbig Be star, which drives a high-velocity outflow (Mitchell et al. 1995) and shows evidence of a rotating disk (Schreyer et al. 2006). These three objects are considered to be at a different evolution stage compared to the hot-core sources and it is unclear a priori what level of complex organic activity is expected and where in the protostellar envelope any detected emission originates.

In this study we use a combination of single dish IRAM 30m data and spatially resolved observations from the Submillimeter Array¹ to search for organic molecules around these three MYSOs and report on their complex organic abundances in the cool protostellar envelope and in a warmer region closer to the star. A subset of this data was used in the Öberg et al 2013 (in press) to study the radial distribution of molecules in NGC7538 IRS9, while the present study focuses on the overall detection rate of organics in these weak-line sources, and chemical connections to the initial ice chemistry and to traditional hot core sources. The chapter is organized as follow: the observations are described in Section 7.2, the results of the line analysis is shown in Sections 7.3.1, 7.3.2 and 7.3.3. The chemistry in our sample is compared to the chemistry in

1. The Submillimeter Array is a joint project between the Smithsonian Astrophysical Observatory and the Academia Sinica Institute of Astronomy and Astrophysics. It is funded by the Smithsonian Institute and the Academia Sinica.

traditional hot-core sources in Section 7.3.4. Section 7.3.5 presents correlation studies between ice and gas column densities and abundances, testing the impact of initial ice compositions on the complex chemistry. A discussion on the use of these line-poor sources to underpin the origins of complex chemistry is presented in Section 7.4, which is followed by the conclusions of this study.

7.2 Observations and Analysis

7.2.1 Observations

Table 7.1: Source characteristics and ice abundances

Source	d kpc	L $10^4 L_{\odot}$	$N_{\text{H}_2\text{O}}$ 10^{17} cm^{-2}	X / % $N_{\text{H}_2\text{O}}$			
				CH_3OH	CH_4	NH_3	OCN^-
NGC7538 IRS9	2.7	3.5	70	4.3 ± 0.6	2 ± 0.4	15 ± 2.7	1.7 ± 0.5
W3 IRS5	2.0	17	51	<3.3	<1.3	<5.7	<0.23
AFGL490	1.4	0.46	6.2	11 ± 4	<2.4	<16	<1.2
W33A	3.8	5.3	110	14 ± 4	1.5 ± 0.2	15 ± 4	6.3 ± 1.9
AFGL2591	3.3	18	12	14.2 ± 2	<2.7	<2.3	–
NGC7538 IRS1	2.4	15	22	<4	1.5 ± 0.5	<17	<0.5
Orion IRc2	4	1.0	24.5	10 ± 3	–	–	2 ± 0.6
G24.78	7.7	1.2	–	–	–	–	–
G75.78	1.9	19	–	–	–	–	–
NGC6334 IRS1	1.7	11	–	–	–	–	–

The MYSOs NGC7538 IRS9, W3 IRS5, and AFGL490 located in Perseus NGC7538 at 2.7 kpc, in Perseus W3 at 2.0 kpc and in Camelopardalis OB1 at 1.4 kpc respectively (see Table 7.1) have been observed with the IRAM 30m and the Submillimeter Array (SMA).

NGC7538 IRS9 was observed with the IRAM 30m telescope on February 19–20, 2012 using the EMIR 230 GHz receiver and the new FTS backend. The two sidebands cover 223–231 GHz and 239–247 GHz at a spectral resolution of $\sim 0.2 \text{ km s}^{-1}$ and with a sideband rejection of -15dB (Carter et al. 2012). Pointing was checked every 1–2 hours and found to be accurate within 2–3". Focus was checked every 4 hours, and generally remained stable through most of the observations, i.e. corrections on the order of 0.2–0.4" were common, but a correction of 0.7" was required once. Spectra were acquired in both position switching and wobbler switching modes. The resulting spectra had similar relative line intensities, indicative of no emission in the wobbler off position. The wobbler switching mode was considerably more stable and these data alone are used for the quantitative analysis. The raw IRAM spectra were converted to main beam temperatures and fluxes using forward and beam efficiencies and antenna temperature to flux conversion values listed at www.iram.es/IRAMES/mainWiki/Iram30mEfficiencies. The spectra were reduced using CLASS. A global baseline was fitted to each 4 GHz spectral chunk using 4–7 windows. The individual scans were baseline subtracted and

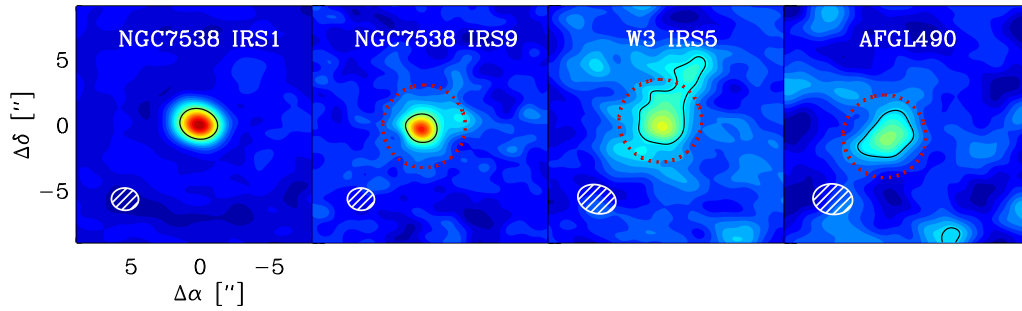


Figure 7.1: Image of the CH₃CN emission using the 239.138 GHz line acquired by the SMA for NGC7538 IRS1, NGC7538 IRS9, W3 IRS5, and AFGL490. The black contour presents the 50 % line intensity, and the synthesized beam is shown in white at the bottom left. A 2'' radius mask is over plotted in dashed red which is used to extract spectra.

averaged. The absolute flux scale of the lines were then set using calibrated SMA data as outlined in detail by Öberg et al (in press).

SMA observations were acquired in the compact and extended array configurations. The data in the compact configuration were taken on the 15th of October 2011 for all sources and with 7 antennas, resulting in baselines between 16 - 77 m. The data in the extended configuration were obtained using 8 antennas, resulting in 44 - 226 m baselines and were acquired on the 29th of July 2011 for W3 IRS5 and AFGL490 and on the 15th of August 2011 for NGC7538 IRS9. The SMA correlator was set-up to obtain a spectral resolution of $\sim 1 \text{ km s}^{-1}$ using 128 channels for each of the 46 chunks covering 227-231 GHz in the lower sideband and 239-243 GHz in the upper sideband. The $\tau_{225 \text{ GHz}}$ was 0.09 on the 29th of July, 0.1 on the 15th of August, and 0.07 on the 15th of October 2011.

The MIR package has been used to perform the first data reduction steps (flux calibration and continuum subtraction). Absolute flux calibration has been done with Calisto and band pass calibrators were 1924-292 and 3c84 for the compact observations, and 3c454.3 and 3c279 were used for the 29th of July and 15th of July observations respectively. Gain calibrators for NGC7538 IRS9 include 0014+612 and 0102+584, and the objects 0244+624, 0359+509, and 0102+584 have been used for W3 IRS5 and AFGL490. The compact and extended data were combined for each source with MIRIAD using natural weighting, which resulted in synthesized beam sizes of $2.0'' \times 1.7''$ for NGC 7538 IRS 9, $2.2'' \times 2.8''$ for W3 IRS5, and $2.3'' \times 2.9''$ for AFGL490.

7.2.2 Spectral extraction and rms

Both the IRAM and SMA data have been frequency calibrated using the bright 5-4 CH₃OH ladder around 241.7 GHz, correcting for the intrinsic velocity of the different sources. The SMA spectra are extracted using a 2'' mask around the center phase of each source. The mask dimension is chosen to encompass all CH₃CN line emission at 239.318 GHz that can be associated with a centrally condensed component, as shown

in Figure 7.1.

The rms for the IRAM and SMA observation of each source has been derived by determining the standard deviation in a line free region of several hundred channels: the 229.37-229.445 GHz region for the lower side band and the 240.7 - 240.75 GHz region for the upper side band. The rms derived for these very deep IRAM observations is between 15 and 20 mK. For the SMA data, the rms for the lower side band is ~ 70 mK, and ~ 100 mK for the upper side-band.

7.3 Results

7.3.1 Line identification and characterization

Figure 7.2 shows the 239-243 GHz spectral region for the three targeted line-poor MYSOs and the traditional hot-core source NGC7538 IRS1 using the IRAM 30m. The MYSOs present a lower line density as well as some line overlaps with the traditional hot core. Lines from complex organics listed by Bisschop et al. (2007) found in traditional hot-core sources were searched for in the MYSOs spectra. CH_3OH , CH_3CN , CH_3CCH , HNCO , CH_3OCH_3 , and CH_3CHO lines were identified in at least one of the MYSOs using the splatalogue catalogue tool and the CDMS and the JPL spectral databases (Müller et al. 2001; Pickett et al. 1998). All available lines in the observed spectral range have been used for the quantitative analysis except for CH_3OH where only the lines from the 5-4 ladder are used to simplify the excitation analysis.

Identified lines are fitted with a Gaussian function in IDL using the routine `gaussfit` for isolated lines and `mpfitfun` when a multiple gaussian fit was required because of overlapping lines. A local baseline component was added to the fits when needed and the presented uncertainties are output by the fitting routines. 3σ upper limits are calculated using average FWHM for the different sources. Unresolved multiplets are treated in one out three ways depending on the nature of the overlapping lines: 1) if one of the possible contributing lines has a very low Einstein coefficient or high upper energy level and that a line presenting the same characteristics elsewhere in the spectrum is not clearly resolved, then it is discarded and only the rest of the multiplet is fitted 2) if the lines are coming from the same species and the upper energy level and Einstein coefficients are identical or close to identical, then the degeneracies are added and the feature is treated as a single line, 3) if none of the two previous conditions are met, the multiplet is discarded.

Line upper energy levels, Einstein coefficients, degeneracies from Splatalogue are listed together with derived line intensities and FWHM in Table 7.2 for CH_3OH from the single dish observation, in Table 7.3 for CH_3OH from the SMA spectra, in Table 7.4 for CH_3CN , in Table 7.5 for CH_3CCH and Table 7.6 for HNCO , CH_3OCH_3 and CH_3CHO . No other complex molecules were detected towards any of the sources. For molecules with weak lines, only the IRAM data have been used since the SMA observations have lower spectral resolution and a higher rms.

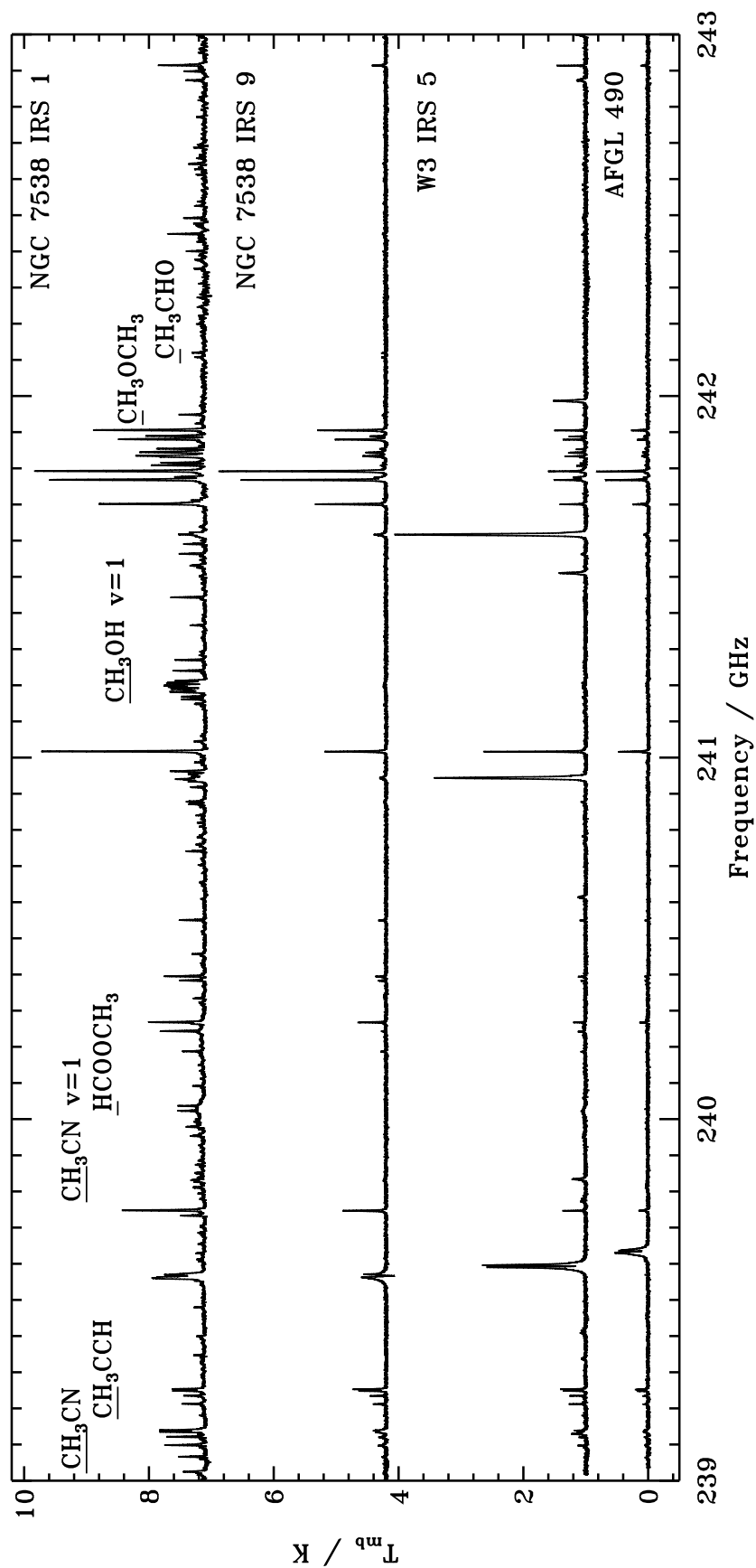


Figure 7.2: The 239-243 GHz spectral window from the IRAM 30m displaying emission lines for typical hot core source NGC 7538 IRS 1 and weak line MYSOs NGC7538 IRS9, W3IRS5, AFGL490.

Table 7.2: CH₃OH lines data from IRAM 30m spectra.

Freq (GHz)	E_{up} (K)	log A	g_u	NGC7538 IRS9		W3 IRS5		AFGL490	
				$\int T_{mb}dV$ (K)	FHWM (km s ⁻¹)	$\int T_{mb}dV$ (K)	FHWM (km s ⁻¹)	$\int T_{mb}dV$ (K)	FHWM (km s ⁻¹)
239.746	49.1	-4.25	11	4.08±0.05	3.70±0.03	1.21±0.03	2.32±0.04	0.91±0.04	4.4±0.2
241.700	47.9	-4.22	11	6.08±0.05	3.47±0.02	1.41±0.03	2.43±0.04	1.33±0.04	3.53±0.07
241.767	40.4	-4.24	11	11.97±0.04	3.37±0.01	2.20±0.04	2.98±0.03	3.30±0.04	3.11±0.02
241.791	34.8	-4.22	11	13.65±0.04	3.37±0.01	2.49±0.04	2.91±0.03	4.00±0.03	3.09±0.02
241.807	115.2	-4.66	22	0.45±0.06	4.5±0.4	0.32±0.03	1.58±0.09	< 0.27	-
241.813	122.7	-4.66	11	0.21±0.05	3.6±0.6	0.23±0.03	1.7±0.2	< 0.27	-
241.830	130.8	-4.66	11	< 0.21	-	0.26±0.03	2.0±0.2	< 0.27	-
241.833	84.6	-4.41	22	2.62±0.05	4.61±0.06	1.09±0.03	2.18±0.04	0.71±0.05	4.9±0.2
241.842	72.5	-4.29	11	2.00±0.08	5.5±0.1	0.63±0.04	1.90±0.08	0.52±0.06	6.8±0.5
241.844	82.5	-4.41	11	0.48±0.06	3.3±0.3	0.64±0.04	2.2±0.1	0.29±0.03	3.50±0.02
241.852	97.5	-4.41	11	0.64±0.06	5.5±0.4	0.44±0.03	2.1±0.1	0.30±0.05	6.5±0.8
241.879	55.9	-4.22	11	4.64±0.05	3.64±0.02	1.32±0.04	2.58±0.05	1.02±0.04	4.1±0.1
241.888	72.5	-4.29	11	1.68±0.05	4.28±0.09	0.75±0.03	2.04±0.06	0.50±0.05	5.2±0.3
241.904	60.7	-4.29	11	3.14±0.02	3.66±0.02	0.98±0.02	2.57±0.03	0.76±0.02	3.85±0.07
241.905	57.1	-4.30	11	3.14±0.02	3.66±0.02	0.98±0.02	2.57±0.03	0.76±0.02	3.85±0.07

Table 7.3: CH₃OH lines extracted from SMA observation from the 2'' radius compact region.

Freq (GHz)	E _{up} (K)	logA	g _u	NGC7538 IRS9		W3 IRS5		AFGL490	
				∫T _{mb} dV (K)	FHWM (km s ⁻¹)	∫T _{mb} dV (K)	FHWM (km s ⁻¹)	∫T _{mb} dV (K)	FHWM (km s ⁻¹)
239.746	49.1	-4.25	11	10.1± 0.5	4.6± 0.2	3.1± 0.4	1.9± 0.2	4.0± 0.5	4.6± 0.5
241.700	47.9	-4.22	11	9.6± 0.4	4.1± 0.2	3.6± 0.4	2.4± 0.2	4.8± 0.6	5.9± 0.5
241.767	40.4	-4.24	11	10.7± 0.4	3.5± 0.1	4.2± 0.4	2.3± 0.2	2.3± 0.4	2.6± 0.3
241.791	34.8	-4.22	11	9.3± 0.4	3.16± 0.09	4.6± 0.5	2.9± 0.2	3.1± 0.5	4.9± 0.7
241.807	115.2	-4.66	22	2.7± 0.6	6± 1	1.8± 0.5	2.4± 0.5	< 1.5	-
241.813	122.7	-4.66	11	1.3± 0.4	3.6± 0.9	1.3± 0.5	2.8± 0.8	< 1.5	-
241.830	130.8	-4.66	11	<1.1	-	<1.4	-	< 1.5	-
241.833	84.6	-4.41	22	8.4± 0.6	4.7± 0.3	4.0± 0.5	2.9± 0.3	2.4± 0.5	4.6± 0.8
241.852	97.5	-4.41	11	2.5± 0.5	3.4± 0.5	1.8± 0.5	1.5± 0.4	< 1.5	-
241.879	55.9	-4.22	11	7.2± 0.4	3.4± 0.2	3.4± 0.4	2.3± 0.2	2.5± 0.5	4.7± 0.7
241.888	72.5	-4.29	11	6.0± 0.5	5.2± 0.3	2.1± 0.4	1.6± 0.2	2.4± 0.7	7± 2
241.904	60.7	-4.29	11	6.9± 0.3	4.5± 0.1	2.2± 0.2	2.2± 0.2	2.2± 0.3	5.2± 0.5
241.905	57.1	-4.30	11	6.9± 0.3	4.5± 0.1	2.2± 0.2	2.2± 0.2	2.2± 0.3	5.2± 0.5

Table 7.4: CH₃CN lines data from IRAM 30m spectra.

Freq (GHz)	E _{up} (K)	logA	g _u	NGC7538 IRS9		W3 IRS5		AFGL490	
				∫T _{mb} dV (K)	FHWM (km s ⁻¹)	∫T _{mb} dV (K)	FHWM (km s ⁻¹)	∫T _{mb} dV (K)	FHWM (km s ⁻¹)
239.023	258.9	-3.00	54	0.31± 0.07	9± 2	< 0.2	-	<0.3	-
239.064	194.6	-2.97	54	0.4± 0.1	9± 2	0.17 ± 0.05	6 ± 2	0.23± 0.05	6± 2
239.096	144.6	-2.95	108	1.04± 0.05	6.0± 0.3	0.44± 0.04	2.2± 0.2	0.48± 0.08	8 ± 1
239.120	108.9	-2.94	54	0.88± 0.05	5.7± 0.3	0.34± 0.04	2.8± 0.3	0.29± 0.07	6± 2
239.133	87.5	-2.93	54	1.14± 0.05	4.6± 0.2	0.47± 0.03	2.4± 0.2	0.42± 0.05	4.9± 0.5
239.138	80.3	-2.93	54	1.46± 0.05	5.2± 0.2	0.52± 0.03	2.1± 0.2	0.47± 0.05	5.4± 0.5

Table 7.5: CH₃CCH lines data from IRAM 30m spectra.

Freq (GHz)	E _{up} (K)	logA	g _u	NGC7538 IRS9		W3 IRS5		AFGL490	
				∫T _{mb} dV (K)	FHWM (km s ⁻¹)	∫T _{mb} dV (K)	FHWM (km s ⁻¹)	∫T _{mb} dV (K)	FHWM (km s ⁻¹)
239.029	439.8	-4.97	58	< 0.21	-	< 0.14	-	< 0.19	-
239.088	346.1	-4.07	16	< 0.21	-	< 0.14	-	< 0.19	-
239.179	201.7	-4.88	58	0.19± 0.05	3.4± 0.6	0.17± 0.05	2.5± 0.6	<0.19	-
239.211	151.1	-4.00	16	0.92± 0.04	3.1± 0.2	0.78± 0.03	2.00± 0.06	0.29± 0.04	3.5± 0.4
239.234	115.0	-4.85	58	1.00± 0.04	2.71± 0.08	0.72± 0.03	1.98± 0.07	0.30± 0.04	3.0± 0.3
239.248	93.3	-4.84	58	1.77± 0.04	2.92± 0.05	1.15± 0.03	2.2± 0.05	0.53± 0.03	2.3± 0.1
239.252	86.1	-4.84	58	2.01± 0.04	2.74± 0.04	1.26± 0.03	2.12± 0.04	0.73± 0.03	2.9± 0.1

Table 7.6: HNCO, CH₃CHO, and CH₃OCH₃ lines data from the IRAM 30m spectra and HNCO acid line data from the SMA 2'' radius compact region.

Species	Freq (GHz)	E _{up} (K)	logA	g _u	NGC7538 IRS9 ∫T _{mb} dV (K)	FWHM (km s ⁻¹)	W3 IRS5 ∫T _{mb} dV (K)	FWHM (km s ⁻¹)	AFGL490 ∫T _{mb} dV (K)	FWHM (km s ⁻¹)
HNCO	240.876	112.6	-3.72	23	0.46±0.08	13±2	0.41±0.05	5.5±0.5	<0.19	-
	241.704	239.9	-3.74	23	<0.21	-	<0.22	-	<0.19	-
	241.708	239.9	-3.74	23	<0.21	-	<0.22	-	<0.19	-
	241.774	69.6	-3.71	23	0.38±0.05	2.7±0.3	0.86±0.05	3.8±0.2	0.22±0.04	2.7±0.4
	242.640	113.1	-3.71	23	<0.21	-	0.49±0.06	8.9±0.8	<0.19	-
SMA	240.876	112.6	-3.72	23	<1.4	-	<1.4	-	<1.3	-
	241.774	69.6	-3.71	23	4.2±0.5	5.8±0.6	5.7±0.6	5.2±0.4	<1.3	-
	242.640	113.1	-3.71	23	2.4±0.6	10±2	<1.4	-	<1.3	-
CH ₃ OCH ₃	225.599	69.8	-3.88	450	0.34±0.04	4.2±0.4	0.12±0.04	2.6±0.6	0.29±0.07	8±2
	240.985	26.3	-3.99	154	<0.22	-	<0.15	-	<0.25	-
	241.529	26.3	-3.99	198	<0.22	-	<0.15	-	<0.21	-
	241.947	81.1	-3.78	378	0.22±0.06	3.5±0.8	0.07±0.02	1.2±0.3	0.25±0.07	6±2
	223.650	72.3	-3.41	50	0.22±0.03	2.8±0.3	<0.18	-	<0.19	-
CH ₃ CHO	223.660	72.2	-3.41	50	0.28±0.04	3.2±0.3	<0.18	-	<0.19	-
	226.552	71.4	-3.39	50	0.29±0.03	2.9±0.3	<0.18	-	<0.19	-
	226.593	71.3	-3.39	50	0.33±0.04	3.5±0.3	<0.18	-	<0.19	-
	229.775	61.5	-4.29	46	<0.19	-	<0.18	-	<0.19	-
	230.302	81.0	-3.38	50	0.20±0.03	2.5±0.3	<0.18	-	<0.19	-
	230.316	81.1	-3.38	50	0.19±0.03	2.3±0.3	<0.18	-	<0.19	-
	242.118	83.8	-3.30	54	0.28±0.04	3.7±0.5	<0.18	-	<0.19	-
	244.789	83.1	-3.29	54	0.24±0.04	3.7±0.5	<0.18	-	<0.19	-
	244.832	83.1	-3.29	54	0.24±0.07	4.2±0.9	<0.18	-	<0.19	-
	244.854	72.3	-4.19	50	<0.19	-	<0.18	-	<0.19	-
242.106	83.9	-3.30	54	0.22±0.05	2.6±0.5	<0.18	-	<0.19	-	

7.3.2 Spatial origin of the line emission

Figures 7.3, 7.4, and 7.5 present the line fluxes of key molecules from both the single-dish observation and the extracted spectra from the SMA observations of the inner regions around the 3 MYSOs. In the higher signal-to-noise ratio (SNR) spectra in Fig. 7.3, the IRAM spectra are clearly not a scaled up versions of the SMA spectra for any of the targeted molecules. This puts qualitative constraints on the origin of the emission from the different molecules. CH_3CN emission from the IRAM and SMA overlap, indicative that most CH_3CN emission originates at the source center, while CH_3CCH flux from the IRAM is not recovered by the SMA, indicative of extended emission. CH_3OH lines display a mixed behavior; lines with higher upper energies show more overlap between the IRAM 30m and SMA spectra than the colder lines. The HNC line flux is very similar for NGC7538 IRS9 and W3 IRS5, but none of the IRAM 30m flux is recovered by the AFGL490 SMA observations, and this molecule thus seems to be present at different scales in different sources.

In Fig. 7.5 the SNR is generally lower, but it is still clear that CH_3CHO toward NGC7538 IRS9 only has extended emission since none of the IRAM 30m line flux is recovered in the SMA spectra. No CH_3CHO lines are detected in the other two MYSOs in the spectral range where IRAM 30m and SMA observations overlap. CH_3OCH_3 is detected toward NGC7538 IRS9 and AFGL490, and in both cases tentative SMA detections suggest that the emission originates from the source centers. Based on the different emission patterns, the molecules found in these spectra are classified as follows: CH_3CCH and CH_3CHO are envelope organics, CH_3CN and CH_3OCH_3 are core organics and CH_3OH and HNC are intermediate cases with significant core and envelope contributions.

7.3.3 Rotational temperature, and column densities

The core and envelope classifications based on spatial emission patterns should be reflected in the rotational temperatures of the different molecules. Rotational diagrams were constructed for molecules with sufficient number of line detections, i.e. CH_3OH (extracted from IRAM and SMA), CH_3CN , CH_3CCH , according to the method described in Goldsmith & Langer (1999). A 10% uncertainty was added to the line integrated area (not listed in the line tables) to account for the fact that the line shapes are not necessarily Gaussian. We used the `linfit` routine in IDL to derive the rotational temperatures as well as the column densities and the routine returned the corresponding uncertainties.

Table 7.7 presents the column densities and rotational temperatures derived for these molecules. The beam-averaged CH_3OH column densities and rotational temperatures derived from the IRAM 30m spectra are in agreement with those found by van der Tak et al. (2000) using the JCMT single dish telescope, including higher frequency lines. The rotational temperature and column densities derived for CH_3OH from the SMA data are always higher than those derived by the IRAM 30m, consistent with that the SMA observations probe material closer to the MYSO center. The third row of Table 7.7 presents the derived temperatures and column densities for CH_3CN

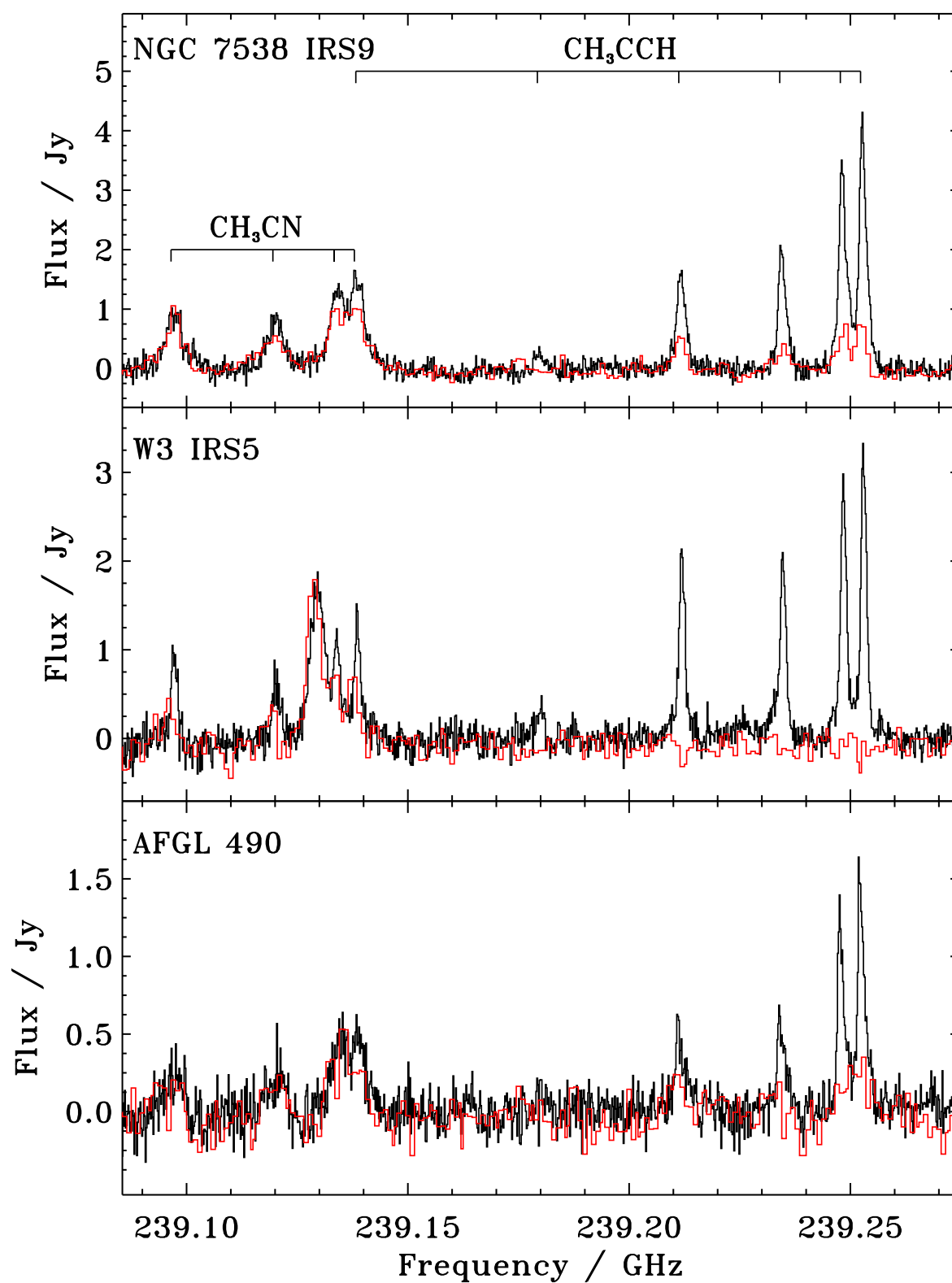


Figure 7.3: Spectral window with several CH_3CN and CH_3CCH lines from the single dish (black lines) and the 2'' interferometric data (red line).

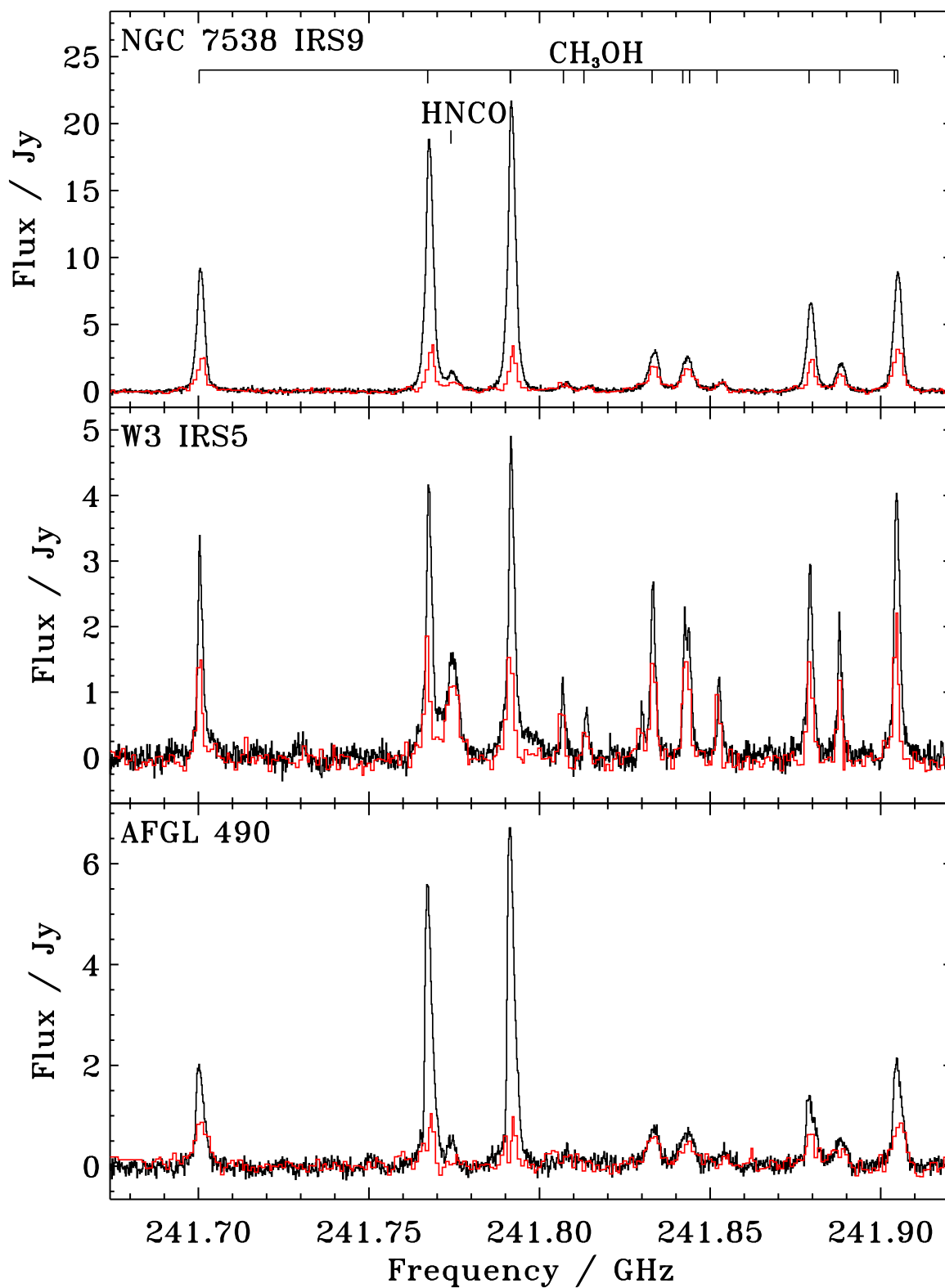


Figure 7.4: Spectral window with several CH₃OH lines from the single dish (black lines) and the 2'' interferometric data (red line).

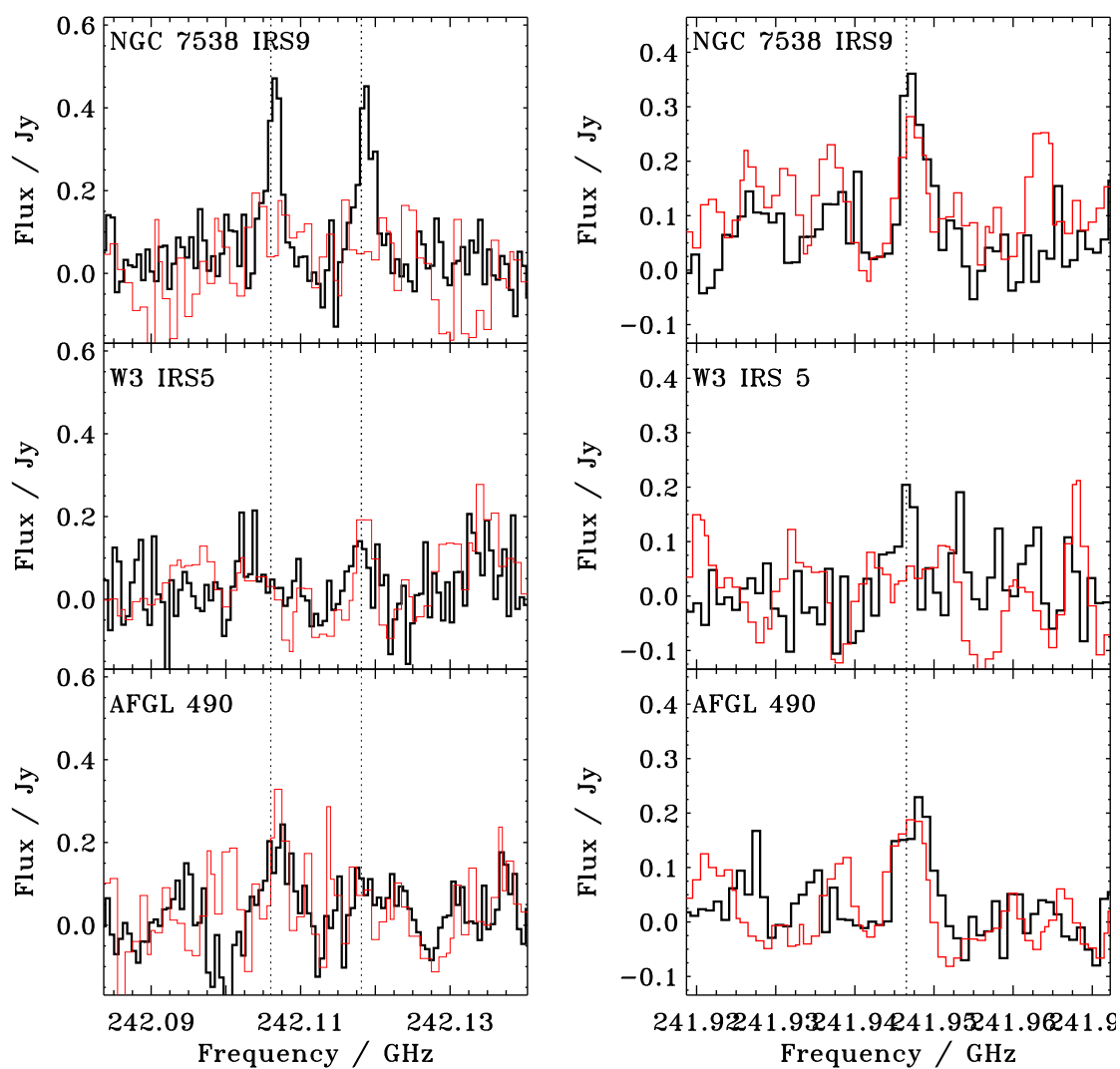


Figure 7.5: Spectra of two CH_3CHO lines at 242.106 GHz and 242.118 GHz (left panel) and the CH_3OCH_3 line at 241.946 GHz (right panel) from the single dish (black line) and $2''$ interferometric data (red line). The three line frequencies are marked by black dotted line.

from the IRAM data assuming that the emission is only coming from the 2'' radii encompassed by the SMA beam, i.e. we apply a dilution factor of 0.16 to account for the SMA extraction mask area (2'' radius) to IRAM beam (5'' radius) ratio. This assumption is justified by the hot-core like rotational temperatures of 80–110 K toward the different MYSOs, which are also consistent with the CH₃OH excitation temperature derived from the SMA spectra. The IRAM data are used here since they present much higher spectral resolution and SNR, and the beam dilution factor is motivated by the observed overlap between the IRAM and SMA line fluxes (see Figure 7.3). The last row shows the rotational temperatures and column densities obtained for the CH₃CCH 14-13 ladder from the IRAM spectra. The rotational temperature of ~50 K toward all sources is consistent with an envelope origin, but suggests that it is mainly present in the luke-warm envelope regions rather than the outermost cold region.

For HNCO, CH₃CHO and CH₃OCH₃, no rotational diagrams can be build due to the very small upper level energy range of the observed transitions, and column densities are calculated using the envelope temperature (the CH₃OH IRAM 30m rotational temperature) if the molecule was classified as an envelope molecule, the core temperature (the CH₃CN rotational temperature) if the molecule was classified as a core molecule, and both rotational excitation temperatures if the molecule is classified as intermediate. For core molecules, the same dilution factor as for CH₃CN was applied (see Table 7.8). For molecules with multiple line detections, the column densities are derived by averaging the individual column densities found for each detected line and taking as uncertainty the square root of the sum of the individual uncertainties squared. Only the IRAM data are used to calculate these column densities since these data present a better SNR.

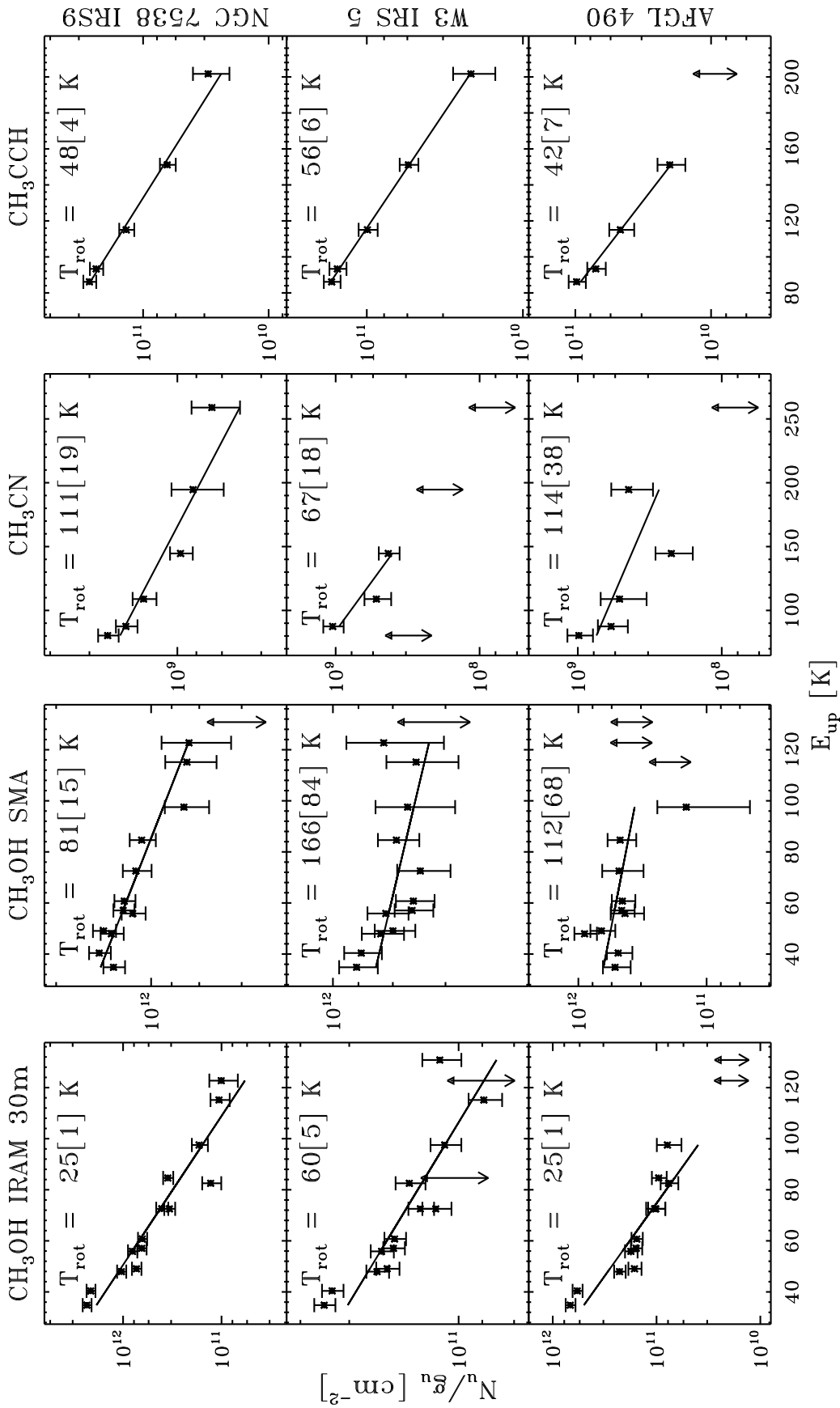


Figure 7.6: Rotational diagrams of CH₃OH from the single dish data (first column), for CH₃OH from the SMA spectra extracted with a 2" mask (second column), and CH₃CN from the single dish data (third column), and CH₃CCH (fourth column) and for the sources NGC7538 IRS9 (first row), W3 IRS5 (second row), and AFGL490 (third row).

Table 7.7: Rotational temperatures and column densities for CH₃OH, CH₃CN, and CH₃CCH derived from the rotational diagrams presented in Fig. 7.6.

Species	NGC7538 IRS9		W3 IRS5		AFGL490	
	T _{rot} (K)	N (cm ⁻²)	T _{rot} (K)	N (cm ⁻²)	T _{rot} (K)	N (cm ⁻²)
CH ₃ OH (IRAM)	25 ± 2	9 ± 1 × 10 ¹⁴	64 ± 6	3.2 ± 0.4 × 10 ¹⁴	25 ± 2	2.4 ± 0.4 × 10 ¹⁴
CH ₃ OH (SMA)	81 ± 16	2.5 ± 0.4 × 10 ¹⁵	166 ± 84	2.4 ± 0.5 × 10 ¹⁵	102 ± 67	1.2 ± 0.5 × 10 ¹⁵
CH ₃ CN ^b	111 ± 20	7 ± 2 × 10 ¹³	92 ± 23	2.4 ± 0.8 × 10 ¹³	164 ± 78	3.6 ± 1.2 × 10 ¹³
CH ₃ CCH	47 ± 5	1.2 ± 0.3 × 10 ¹⁵	58 ± 8	7 ± 2 × 10 ¹⁴	42 ± 7	4.2 ± 1.7 × 10 ¹⁴

^b Derived from IRAM 30m spectra rotational diagrams and applying a dilution factor corresponding to size the SMA 2'' mask radius over IRAM 10'' beam diameter.

Table 7.8: Column densities for HNCO, CH₃CHO, CH₃OCH₃ using excitation temperatures from Table 7.

Species	NGC7538 IRS9	W3 IRS5	AFGL490
	N (cm ⁻²)	N (cm ⁻²)	N (cm ⁻²)
HNCO _{ext}	4.0 ± 1.3 × 10 ¹³	1.8 ± 0.3 × 10 ¹³	6.0 ± 2.2 × 10 ¹²
HNCO _{comp}	1.1 ± 0.3 × 10 ¹⁴	1.4 ± 0.6 × 10 ¹⁴	< 4 × 10 ¹³
CH ₃ OCH ₃	3.3 ± 1.0 × 10 ¹⁴	9.7 ± 4 × 10 ¹³	4.5 ± 1.9 × 10 ¹⁴
CH ₃ CHO	3.1 ± 0.4 × 10 ¹³	< 1.1 × 10 ¹³	< 1.3 × 10 ¹³

7.3.4 Organics in hot core vs weak-line MYSOs

Per definition the line-poor MYSOs reported in this study have less intense emission of complex organic molecules compared to traditional luminous hot core sources. The question for this section is whether the chemical composition with respect to CH₃OH is different between the two source families. The CH₃CN, CH₃CCH, HNCO, CH₃CHO, and CH₃OCH₃ abundances with respect to CH₃OH obtained here for the three MYSOs are compared to the hot core abundances derived by Bisschop et al. (2007) in Figure 7.7. For the 3 MYSOs sources, the molecular abundances with respect to CH₃OH are calculated using the CH₃OH column densities derived for the envelope if the molecule has been classified as 'envelope' molecules and using the CH₃OH column density derived for the core (SMA-based) in the case of a core molecule. For the hot core sources, Bisschop et al. (2007) applied a dilution factor corresponding to the region where T > 100 K for CH₃OH, CH₃CN, HNCO and CH₃OCH₃, but not for CH₃CCH and CH₃CHO. To calculate CH₃CCH and CH₃CHO abundances with respect to CH₃OH we removed the dilution factor for CH₃OH applied by Bisschop et al. (2007). All other abundances are taken directly from Bisschop et al. (2007).

The histograms in Figure 7.7 show that the CH₃CN, CH₃OCH₃, and HNCO core abundances with respect to CH₃OH are similar for the young MYSOs and the hot-core sources. In contrast, the young MYSOs show higher envelope abundances with respect to CH₃OH compared to the hot core sources. This difference is most likely due to that we could not separate CH₃OH core and envelope emission in the study by Bisschop et al. (2007), resulting in artificially low envelope ratios with respect to CH₃OH when all CH₃OH is implicitly assumed to originate in the envelope; in reality

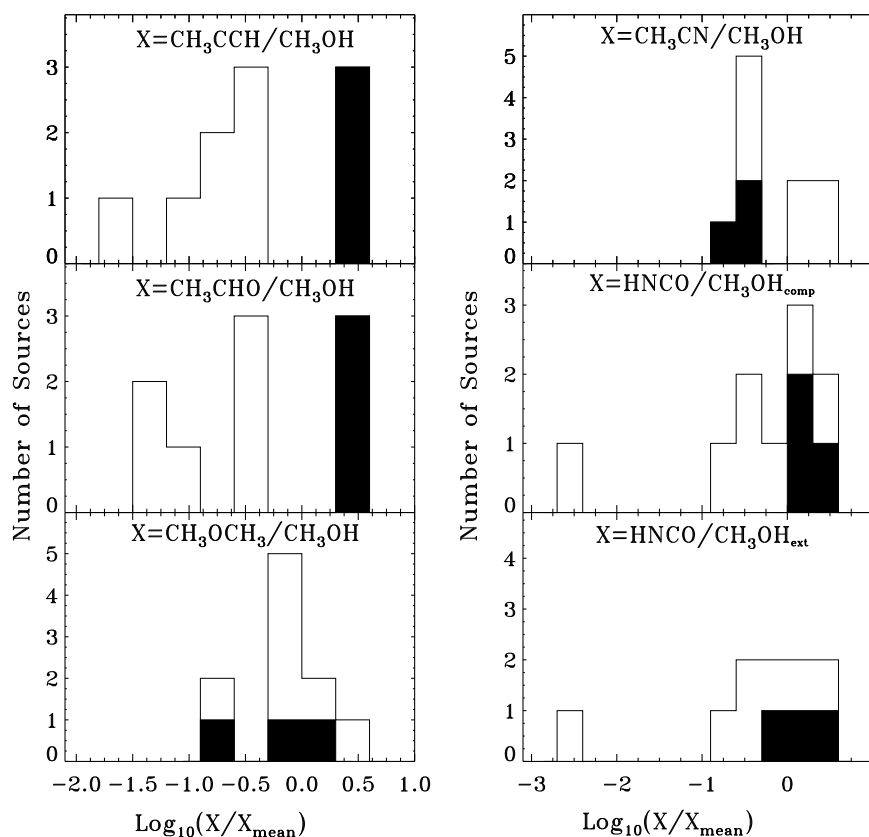


Figure 7.7: The solid filled histograms correspond to sources observed and analyzed here, the black contour histograms correspond to sources from Bisschop et al. (2007)

the high excitation temperature of CH_3OH in the hot core sources suggest that most of it really comes from the core.

Some of the same trends are visible for the log-log correlations of molecular abundances with respect to CH_3OH showed in Figure 7.8. In addition, these plots show that there is no clear correlation between the two N-bearing organics CH_3CN and HNCO and ratios span about one order of magnitude. There is also no correlation between the two O-bearing complex species CH_3OCH_3 and CH_3CHO , which is consistent with their different origins in the MYSOs. In contrast, there seems to be a correlation between envelope molecules CH_3CHO and CH_3CCH , but this potential trend is probably exaggerated by the different abundance derivations with respect to CH_3OH for the hot cores and the weak-line MYSOs.

7.3.5 An ice-gas connection?

The CH_3OH ice content may be an important factor on whether a hot core chemistry developed and we therefore compare the CH_3OH core column density toward weak-line MYSOs and hot cores with their CH_3OH ice abundance with respect to H_2O (Gibb et al. 2004) (see Table 7.1). In the hot cores the majority of the CH_3OH gas originates from the core and we use the derived column densities from Bisschop et al. (2007),

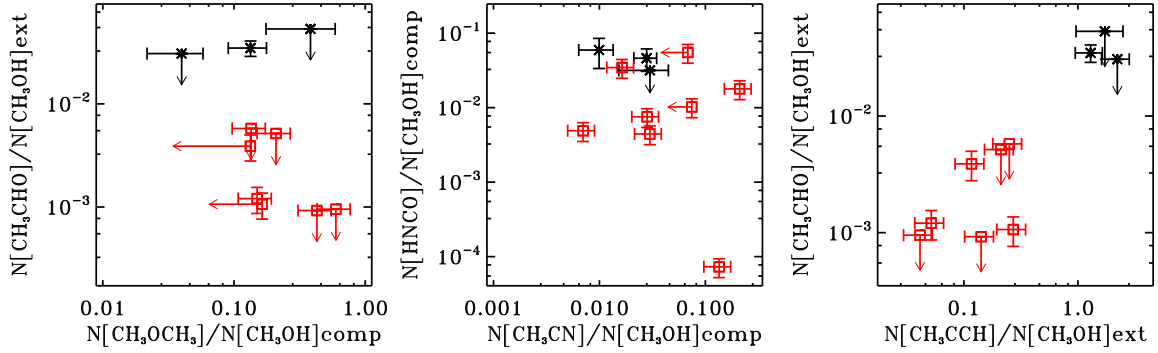


Figure 7.8: Gas abundance correlation between organics including upper limits. The black crosses are the abundances derived for the MYSOs, the red squares are derived by Bisschop et al. (2007). An arbitrary error of 20% has been taken for the latest values.

where all CH_3OH emission is assumed to originate from the central region where the temperature is higher than 100 K. For the MYSOs studied here, the regions where the temperature is higher than 100 K is derived using a relation between luminosity and temperature $R_{T=100\text{K}} \approx 2.3 \times 10^{14} (\sqrt{L/L_\odot})$, which was shown by Bisschop et al. (2007) to approximate the 100 K radius well toward their source sample. We further assume that all SMA CH_3OH line flux originate from these regions, based on the derived rotational temperatures, and use an appropriate dilution factor when the 100 K area is smaller than the $2''$ mask used for spectral extraction. Figure 7.9 presents the resulting column density of hot CH_3OH gas versus the initial CH_3OH abundance on the grains. No strong correlation is observed but more sources with information on the spatial distributions of CH_3OH are needed to reach a conclusive answer on the importance of the initial CH_3OH abundance.

The initial ice composition may also affect the complex organic composition in both hot cores and weak-line MYSOs. Figures 7.10 presents correlation plots between ratios of the N-bearing organics and CH_3OH in the ice and gas-phase. The two gas-phase N-bearing organics are HNCO and CH_3CN , and the two ice species are OCN^- and NH_3 . The ice abundances are listed in Table 7.1 and have been obtained by Gibb et al. (2004). A limited sample of 7 MYSOs have overlapping ice and gas observations. Moreover, only a fraction of them can be used in each plot due to multiple ice abundance upper limits. The top left panel of Figure 7.10 shows a tentative correlation between OCN^- ice and HNCO in the gas phase with respect to CH_3OH (the outlier is due to HNCO in the AFGL 490 envelope, while all other points trace HNCO in the cores). HNCO and OCN^- are linked through efficient thermal reaction within the ice (van Broekhuizen et al. 2004), and the gas-phase $\text{HNCO}/\text{CH}_3\text{OH}$ ratio may simply reflect the ice abundance ratio before evaporation, and a correlation between the ice and gas ratios is thus expected. The top right panel of Figure 7.10 shows the gas phase abundance of HNCO over CH_3OH with respect to NH_3 , another N-bearing molecule that could play a role in the HNCO/OCN^- formation scheme because it is a major source of nitrogen in the ice (van Broekhuizen et al. 2004); and again a tentative correlation is observed. The

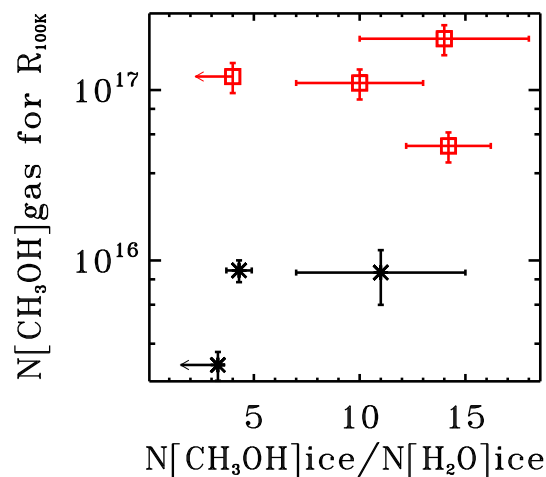


Figure 7.9: CH_3OH column density in the inner core versus CH_3OH ice abundance over H_2O ice in the envelope.

relation between OCN^- in the ice and CH_3CN in the gas is explored in the bottom left panel of Figure 7.10. These molecules are not correlated for the 4 sources presented here, despite both containing a CN functional group. Finally, the bottom right panel presents the $\text{CH}_3\text{CN}/\text{CH}_3\text{OH}$ gas ratio versus the $\text{NH}_3/\text{CH}_3\text{OH}$ ratio in the ice. There is no correlation, which is in contradiction with the predictions from Rodgers & Charnley (2001).

7.4 Discussion

7.4.1 Weak line MYSOs versus hot cores

Previous observations of complex molecules toward MYSOs have generally focused on sources with a well-developed hot core that is responsible for most of the molecular emission. In such cases either interferometric *or* single dish observations are sufficient to determine complex organic abundances as long as the radius of the evaporation front close to the central protostar is known. Single-dish observations combined with the rotational diagram technique can also be used to derive abundances of molecules that are pre-dominantly present in the outer envelope, since then beam-averaged abundances can be assumed. The real difficulty is the molecules that are distributed throughout the envelope and core. For such molecules, single-dish and interferometric observations need to be combined to deduce what fraction of the molecular emission originates in the envelope and in the core respectively, and then use these fractions to calculate the chemical composition of the two physically and chemically different regions. Based on this study, this class of molecules seems to mainly encompass 0th generation ices, i.e. CH_3OH and HNCO , but as our sensitivity increases we expect, based on model results, that many classical hot core molecules will present a

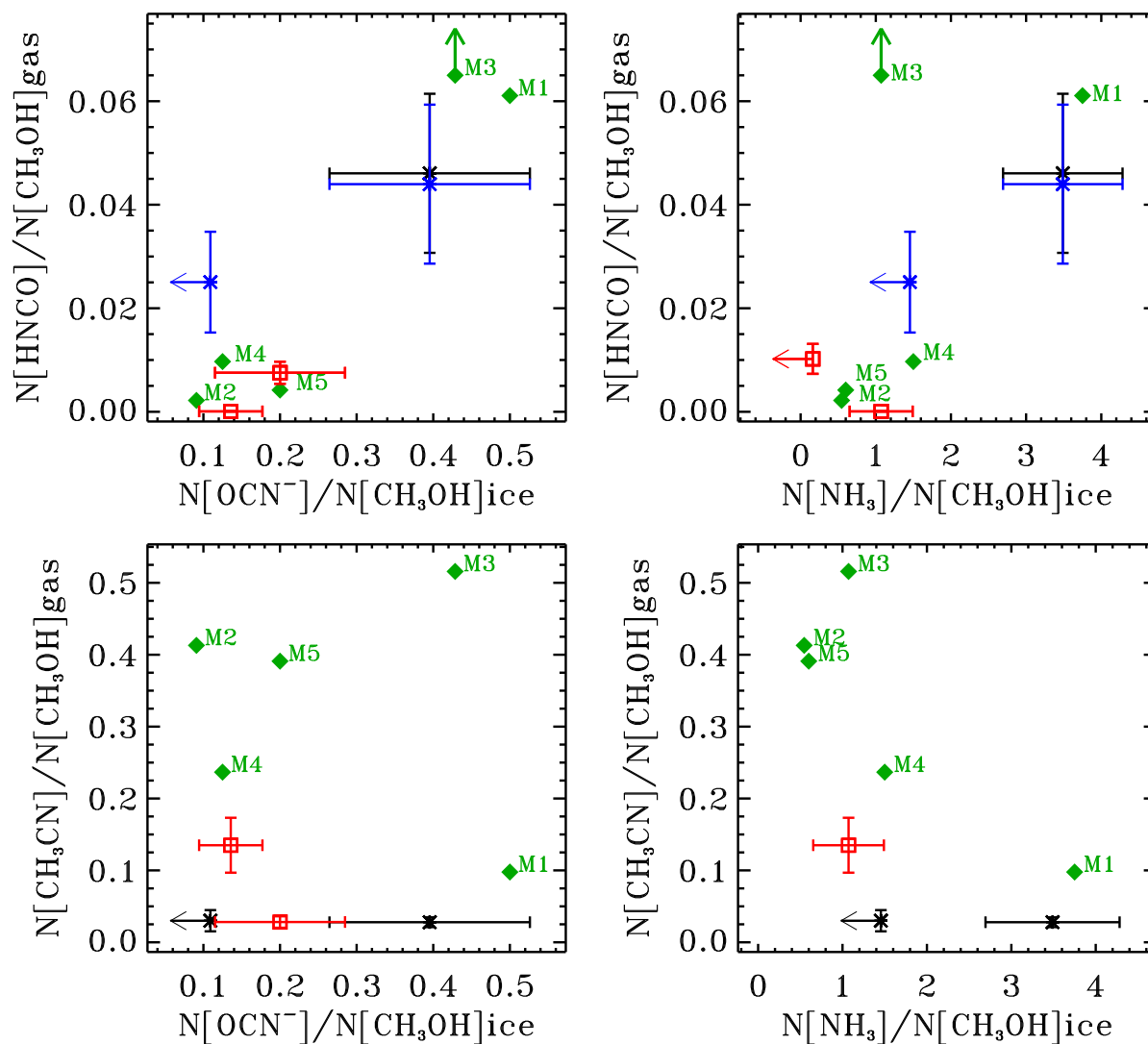


Figure 7.10: Ice versus gas abundance correlation for N-bearing species with respect to CH₃OH. The crosses are abundances derived respectively for the MYSOs, the red squares are the values derived by Bisschop et al. (2007). An arbitrary error of 20% has been taken for the latest values. For the two top plots the black crosses represent the HNCO over CH₃OH abundance derived for the compact component while the blue crosses correspond to the HNCO abundance calculation for an extended component. The green diamonds represent the model results for five initial abundance M1 to M5 reported in Table 7.9. The arrows for model M3 in the top panels are included to represent the high [HNCO]/[CH₃OH] abundance ratio of 0.3 in M3.

significant envelope emission profile as well.

Using the IRAM 30m and SMA spectra we could classify several complex organic molecules into belonging to the core, envelope and both. The two envelope molecules, CH_3CHO and CH_3CCH were similarly classified by Bisschop et al. (2007) based on excitation temperatures alone, suggesting that the envelopes around line-poor MYSOs and hot cores are chemically similar. In contrast we find that in the line-poor MYSOs, CH_3OH and sometimes HNCO have significant emission contributions from the envelope, while Bisschop et al. (2007) found that in hot core sources they have excitation temperatures above 100 K, and were thus classified as originating exclusively from the core region; these sources have probably a similar envelope line flux as observed for the line-poor MYSOs, but in single dish studies, this emission contribution is drowned out by the hot cores.

Overall, the chemistry in the young MYSOs is remarkably similar to what is observed in the hot cores, which suggests that they may be hot core pre-cursors. CH_3CN , CH_3CCH , CH_3CHO , HNCO , CH_3OCH_3 are observed in both kinds of sources at comparable abundances with respect to CH_3OH . $\text{CH}_3\text{CH}_2\text{OH}$ and HCOOCH_3 - two typical hot-core molecules - are not seen in the line-poor MYSOs, but typical abundance of these molecules with respect to CH_3OH from Bisschop et al. (2007) are consistent with non-detections. The hot-core pre-cursor interpretation is also consistent with the observed lack of CH_3OH core column density or hot-core activity on the initial CH_3OH ice abundance.

7.4.2 The ice-gas connection: Observations vs. Theory

Whether or not the overall hot-core chemistry depends on the initial ice composition, we expect that the ice composition will have an effect on the chemical composition in both hot cores and line-poor MYSOs. This dependence may look very different for complex molecules that form in the gas-phase from evaporated ices compared to products of complex ice chemistry. The fact that we do not observe a clear trend between NH_3 in the ice and CH_3CN in the gas suggests that the model of Rodgers & Charnley (2001) is missing important complex molecule formation pathways. We have therefore used the state-of-the-art *MAGICKAL* model (Garrod 2013) to explore the connection between ice and gas-phase species further. The model is based on rate-equations/modified rate-equations that treat the gas-grain chemistry by differentiating the gas-phase, the ice surface and the bulk of the ice.

We have run the *MAGICKAL* code for using the fiducial physical model from Garrod (2013), and a standard H_2O ice abundance, but varying the remaining ice composition to span the observed ranges in the combined line-poor MYSOs and hot cores sample (see M1 to M5 in Table 7.9). The resulting gas-phase abundance of HNCO , CH_3CN , and CH_3OH are reported at different temperatures during warm-up in table 7.10.

The relationships during protostellar warm-up between gas-phase HNCO and CH_3CN with respect to CH_3OH , and OCN- and NH_3 initial ice abundances with respect to CH_3OH ice are shown in Figure 7.11, for temperatures between 20 K and 100 K. Since the model does not treat ion chemistry in the ice, a full conversation rate

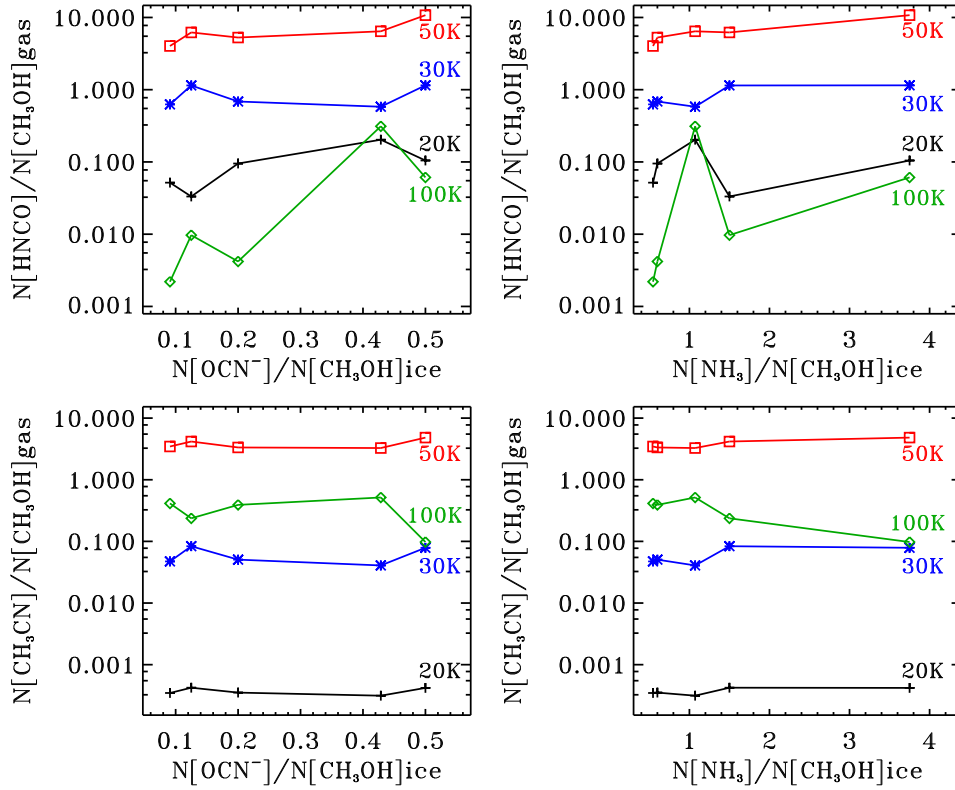


Figure 7.11: Model ice versus gas abundance correlation from the MAGICKAL model Garrod (2013). Five initial ice abundances are used to run the models and derived N-bearing abundances with respect to CH_3OH . The black plus signs present the results at 20 K, the blue crosses are the model results at 30 K, the red squares represents 50 K and the green diamonds are the results at 100 K.

Table 7.9: Initial ice abundances with respect to water used for the five chemical model simulation M1-5. The three phase model assumes a H_2O abundance with respect to hydrogen of $2.66 \times 10^{-7} n_{\text{H}}$ for the ice surface and $1.46 \times 10^{-4} n_{\text{H}}$ for the ice bulk.

Species ratio	M1	M2	M3	M4	M5
$\text{CH}_3\text{OH}/\text{H}_2\text{O}$	4	11	14	4	10
$\text{CH}_4/\text{H}_2\text{O}$	2	2	2	2	2
$\text{HNCO}/\text{H}_2\text{O}$	2	1	6	0.5	2
$\text{NH}_3/\text{H}_2\text{O}$	15	6	15	6	6

of HNCO ice into OCN^- has been assumed based on the efficient HNCO to OCN^- conversion derived experimentally by van Broekhuizen et al. (2004). Figure 7.11 shows that both ice composition and temperature have strong impacts on gaseous abundance ratios and it is therefore clearly important to compare the simulation outputs and gas-phase observational data at similar gas temperatures.

Observationally, most HNCO and CH_3CN appears to originate at high temperatures and we therefore focus on the predictions at 100 K. The gas-phase abundances at 100 K derived from the simulations are over-plotted on the observational data in Figure

Table 7.10: Gas abundances with respect to hydrogen at various temperatures derived by the Garrod (2013) model for the initial ice abundances presented in Table 7.9

Model	Species	$n(20\text{ K})/n_H$	$n(30\text{ K})/n_H$	$n(50\text{ K})/n_H$	$n(100\text{ K})/n_H$
M1	CH ₃ OH	1.630×10^{-11}	1.082×10^{-12}	4.906×10^{-11}	3.165×10^{-9}
	HNCO	1.706×10^{-12}	1.243×10^{-12}	5.273×10^{-10}	1.933×10^{-10}
	CH ₃ CN	6.841×10^{-15}	8.522×10^{-14}	2.367×10^{-10}	3.092×10^{-10}
M2	CH ₃ OH	1.961×10^{-11}	1.880×10^{-12}	1.129×10^{-10}	6.814×10^{-9}
	HNCO	1.013×10^{-12}	1.177×10^{-12}	4.546×10^{-10}	1.497×10^{-11}
	CH ₃ CN	6.810×10^{-15}	8.898×10^{-14}	3.908×10^{-10}	2.814×10^{-9}
M3	CH ₃ OH	2.173×10^{-11}	2.617×10^{-12}	1.139×10^{-10}	7.291×10^{-9}
	HNCO	4.412×10^{-12}	1.521×10^{-12}	7.323×10^{-10}	2.272×10^{-9}
	CH ₃ CN	6.821×10^{-15}	1.065×10^{-13}	3.723×10^{-10}	3.761×10^{-9}
M4	CH ₃ OH	1.613×10^{-11}	9.645×10^{-13}	5.875×10^{-11}	3.724×10^{-9}
	HNCO	5.362×10^{-13}	1.104×10^{-12}	3.644×10^{-10}	3.611×10^{-11}
	CH ₃ CN	6.822×10^{-15}	8.053×10^{-14}	2.449×10^{-10}	8.813×10^{-10}
M5	CH ₃ OH	1.938×10^{-11}	1.828×10^{-12}	9.365×10^{-11}	6.373×10^{-9}
	HNCO	1.842×10^{-12}	1.254×10^{-12}	4.935×10^{-10}	2.671×10^{-11}
	CH ₃ CN	6.829×10^{-15}	9.242×10^{-14}	3.127×10^{-10}	2.492×10^{-0}

7.10. The first thing to note is that the model predictions generally agree with observations within a factor of a few. Furthermore, the model predicts a correlation between OCN⁻ in the ice and warm HNCO in the gas phase with respect to CH₃OH, which is in agreement with observations. The relatively high HNCO/CH₃OH gas-phase abundance, compared to the initial ice abundance, in AFGL490 envelope is consistent with model predictions at lower temperatures.

The link between gas-phase HNCO and NH₃ ice is also suggested by the model except for the M3 run. The reason M3 deviates is not fully understood and a more in-depth theoretical study is required to explore the expected scatter in this relationship. In contrast to what has been proposed by Rodgers & Charnley (2001), the abundance of CH₃CN with respect to CH₃OH does not correlate with the NH₃ ice content in the MAGICCAL code output, and neither does the cyanide ice related species OCN⁻. This agrees with the observational results and is most likely due to CH₃OH is involved in the formation of CH₃CN.

Figure 7.10 presents an encouraging agreement between theory and observations, but currently both the explored model parameter space and the observational sample are small. The case is complicated further by indications from both theory and observations that gas-phase abundance ratios depend strongly on both the initial ice composition and the local temperature. A large sample of spatially-resolved gas-phase observations together with ice observations of the same object is therefore needed to conclusively establish how the complex gas-phase chemistry depends on the ice composition. As shown here, line-poor MYSOs contain detectable amounts of complex organic material and present a similar chemistry to hot cores. Most MYSOs with ice observations from ISO could therefore be used to expand the sample. SOFIA could potentially also be used to expand the sample of MYSO ice sources. In addition, a larger

grid of simulations is necessary to investigate systematically the theoretical impact of the different ice components on the gas-phase species and identify ice-gas correlations that should be tested observationally.

7.5 Conclusions

1. We detect complex organic molecules CH_3CN , CH_3CCH , CH_3CHO , CH_3OCH_3 together with HNCO and CH_3OH toward three young MYSOs without any previous evidence for hot-core activity.
2. Using a combination of single dish and interferometry observations, we find that CH_3CN and CH_3OCH_3 emission originates in the central core region, CH_3CHO and CH_3CCH in an extended envelope, and CH_3OH , and sometimes HNCO , have both envelope and core emission components.
3. The inferred molecular emission locations are consistent with rotational temperatures derived from the single dish observations, except for CH_3OH , where single-dish data are dominated by the envelope.
4. The abundances of complex organics with respect to CH_3OH in the warm core regions are indistinguishable for the line-poor MYSOs and the sample of hot core sources from Bisschop et al. (2007). The envelope chemistry also seems similar for both kinds of sources, but this analysis is limited by a lack of CH_3OH envelope data toward the hot core sources.
5. The OCN^- (and possibly NH_3) ice abundances seem to affect the $\text{HNCO}/\text{CH}_3\text{OH}$ gas-phase abundances. This relationship is reproduced by the *MAGICKAL* astrochemical code, assuming fiducial collapse and warm-up rates and initial ice compositions that span the observed range. In contrast to earlier model predictions, the new model and observations show no correlation between OCN^- and NH_3 ice abundances and gas phase $\text{CH}_3\text{CN}/\text{CH}_3\text{OH}$ abundances.

Bibliography

- Aikawa, Y., Umebayashi, T., Nakano, T., & Miyama, S. M. 1997, *ApJ*, 486, L51
- Aikawa, Y., Wakelam, V., Garrod, R. T., & Herbst, E. 2008, *ApJ*, 674, 984
- Andersson, S., Al-Halabi, A., Kroes, G. J., & van Dishoeck, E. F. 2006, *J. Chem. Phys.*, 124, 14
- Andersson, S., Arasa, C., Yabushita, A., et al. 2011, *Phys. Chem. Chem. Phys.*, 13, 15810
- Andersson, S., Kroes, G. J., & van Dishoeck, E. F. 2005, *Chem. Phys. Lett.*, 408, 415
- Andersson, S. & van Dishoeck, E. F. 2008, *A&A*, 491, 907
- Arasa, C., Andersson, S., Cuppen, H. M., van Dishoeck, E. F., & Kroes, G. J. 2010, *J. Chem. Phys.*, 132, 184510
- Arasa, C., Andersson, S., Cuppen, H. M., van Dishoeck, E. F., & Kroes, G. J. 2011, *J. Chem. Phys.*, 164503
- Avouris, P. & Walkup, R. E. 1989, *Annu. Rev. Phys. Chem.*, 40, 173
- Bacmann, A., Taquet, V., Faure, A., Kahane, C., & Ceccarelli, C. 2012, *A&A*, 541, L12
- Bahr, D. A. & Baragiola, R. A. 2012, *ApJ*, 761, 36
- Bejan, D. 2004, *J. OPTOELECTRON. ADV. M.*, 6, 359
- Bennett, C. J. & Kaiser, R. I. 2005, *ApJ*, 635, 1362
- Bergin, E. A., Alves, J., Huard, T., & Lada, C. J. 2002, *ApJ*, 570, L101
- Bergin, E. A., Calvet, N., D'Alessio, P., & Herczeg, G. J. 2003, *ApJL*, 591, L159
- Bergin, E. A., Ciardi, D. R., Lada, C. J., Alves, J., & Lada, E. A. 2001, *Astrophys. J.*, 557, 209
- Bertin, M., Fayolle, E. C., Romanzin, C., et al. 2012, *Phys. Chem. Chem. Phys.*, 14, 9929

- Bertin, M., Romanzin, C., Michaut, X., Jeseck, P., & Fillion, J. H. 2011, *J. Phys. Chem. C*, 115, 12920
- Biham, O., Furman, I., Pirronello, V., & Vidali, G. 2001, *ApJ*, 553, 595
- Bisschop, S. E., Fraser, H. J., Öberg, K. I., van Dishoeck, E. F., & Schlemmer, S. 2006, *A&A*, 449, 1297
- Bisschop, S. E., Fraser, H. J., Öberg, K. I., van Dishoeck, E. F., & Schlemmer, S. 2006, *A&A*, 449, 1297
- Bisschop, S. E., Jørgensen, J. K., van Dishoeck, E. F., & de Wachter, E. B. M. 2007, *A&A*, 465, 913
- Blake, G. A., Sutton, E. C., & Masson, C. R. 1987, *ApJ*
- Bonn, M., Funk, S., Hess, C., et al. 1999, *Science*, 285, 1042
- Boogert, A. C., Pontoppidan, K. M., Knez, C., et al. 2008, *ApJ*, 678, 985
- Bottinelli, S., Boogert, A. C. A., Bouwman, J., et al. 2010, *ApJ*, 718, 1100
- Brith, M. & Schnepp, O. 1965, *Mol. Phys.*, 9, 473
- Brown, W. A. & Bolina, A. S. 2007, *MNRAS*, 374, 1006
- Burke, D. J. & Brown, W. A. 2010, *Physical Chemistry Chemical Physics*, 12, 5947
- Burke, D. J. & Brown, W. A. 2010, *Phys. Chem. Chem. Phys.*, 12, 5947
- Carter, M., Lazareff, B., Maier, D., et al. 2012, *A&A*, 538, 89
- Caselli, P., Benson, P. J., Myers, P. C., & Tafalla, M. 2002, *ApJ*, 572, 238
- Caselli, P., Keto, E., Bergin, E. A., et al. 2012, *ApJL*, 759, L37
- Cazaux, S., Tielens, A. G. G. M., Ceccarelli, C., et al. 2003, *ApJ*, 593, L51
- Ceccarelli, C., Loinard, L., Castets, A., et al. 2001, *A&A*, 372, 998
- Chakarov, D. V., Oesterlund, L., & Kasemo, B. 1995, *Langmuir*, 11, 1201
- Charnley, S. B., Tielens, A. G. G. M., & Millar, T. J. 1992, *ApJ*, 399, L71
- Chavarría, L., Herpin, F., Jacq, T., et al. 2010, *A&A*, 521, L37
- Ciesla, F. J. & Sandford, S. A. 2012, *Science*, 336, 452
- Collings, M. P., Anderson, M. A., Chen, R., et al. 2004, *MNRAS*, 354, 1133
- Collings, M. P., Dever, J. W., Fraser, H. J., & McCoustra, M. R. S. 2003, *Ap&SS*, 285, 633

- Collings, M. P., Dever, J. W., Fraser, H. J., & McCoustra, M. R. S. 2003a, *Astrophys Space Sci*, 285, 633
- Collings, M. P., Dever, J. W., Fraser, H. J., McCoustra, M. R. S., & Williams, D. A. 2003b, *ApJ*, 583, 1058
- Collings, M. P., Dever, J. W., McCoustra, M. R. S., & Fraser, H. J. 2005, *Highlights Astron.*, 13, 491
- Cosby, P. C. 1993, *J. Chem. Phys.*, 98, 9560
- Cottin, H., Moore, M. H., & Bénilan, Y. 2003, *ApJ*, 590, 874
- Coutens, A., Vastel, C., Caux, E., et al. 2012, *A&A*, 539, 132
- Cuppen, H. M., Penteadó, E. M., Isokoski, K., van der Marel, N., & Linnartz, H. 2011, *MNRAS*, 417, 2809
- Cuppen, H. M., van Dishoeck, E. F., Herbst, E., & Tielens, A. G. G. M. 2009, *A&A*, 508, 275
- Daranlot, J., Hincelin, U., Bergeat, A., et al. 2012, *PNAS*, 109, 10233
- Dartois, E. 2005, *Space Sci Rev*, 119, 293
- Dimitrov, A., Seppelt, K., Scheffler, D., & Willner, H. 1998, *J. Am. Chem. Soc.*, 120, 8711
- Dohnálek, Z., Ciolli, R. L., Kimmel, G. A., et al. 1999, *Journal of Chemical Physics*, 110, 5489
- Dominik, C., Ceccarelli, C., Hollenbach, D., & Kaufman, M. J. 2005, *Astrophys. J.*, 635, L85
- Doty, S. D., Schöier, F. L., & van Dishoeck, E. F. 2004, *A&A*, 418, 1021
- Draine, B. T. 2003, *Annu. Rev. Astro. Astrophys.*, 41, 241
- Ehrenfreund, P. & Charnley, S. B. 2000, *Annu. Rev. Astro. Astrophys.*, 38, 427
- Ehrenfreund, P., Dartois, E., Demyk, K., & D'Hendecourt, L. 1998, *A&A*, 339, L17
- Elisabetta Palumbo, M., Baratta, G. A., Collings, M. P., & McCoustra, M. R. S. 2006, *Phys. Chem. Chem. Phys.*, 8, 279
- Ennis, C. P., Bennett, C. J., & Kaiser, R. I. 2011, *Phys. Chem. Chem. Phys.*, 13, 9469
- Fayolle, E. C., Bertin, M., Romanzin, C., et al. 2011, *ApJ*, 739, L36
- Flower, D. R., des Forets, G. P., & Walmsley, C. M. 2006, *A&A*, 456, 215
- Fogel, J. K. J., Bethell, T. J., Bergin, E. A., Calvet, N., & Semenov, D. 2011, *ApJ*, 726, 29

- Fraser, H. J., Collings, M. P., McCoustra, M. R. S., & Williams, D. A. 2001, *MNRAS*, 327, 1165
- Freund, R., Wetzel, R., & Shul, R. 1990, *Phys. Rev. A*, 41, 5861
- Fuchs, G. W., Acharyya, K., Bisschop, S. E., et al. 2006, *Faraday Discuss.*, 133, 331
- Fuchs, G. W., Cuppen, H. M., Ioppolo, S., et al. 2009, *A&A*, 505, 629
- Fuente, A., Neri, R., & Caselli, P. 2005, *A&A*, 444, 481
- Funk, S., Bonn, M., Denzler, D. N., et al. 2000, *J. Chem. Phys.*, 112, 9888
- Garrod, R. T. 2013, *ApJ*, 765, 60
- Garrod, R. T. & Herbst, E. 2006, *A&A*, 457, 927
- Garrod, R. T., Weaver, S. L. W., & Herbst, E. 2008, *ApJ*, 682, 283
- Geppert, W. D., Hamberg, M., Thomas, R. D., et al. 2006, *Chemical Evolution of the Universe*, 133, 177
- Gibb, E. L., Whittet, D. C. B., Boogert, A. C., & Tielens, A. G. G. M. 2004, *ApJS*, 151, 35
- Gillett, F. C. & Forrest, W. J. 1973, *ApJ*, 179, 483
- Goldsmith, P. F. 2001, *ApJ*
- Goldsmith, P. F. & Langer, W. D. 1978, *ApJ*, 222, 881
- Goldsmith, P. F. & Langer, W. D. 1999, *ApJ*, 517, 209
- Goldsmith, P. F., Liseau, R., Bell, T. A., et al. 2011, *ApJ*, 737, 96
- Gottfried, J. M., Schmidt, K. J., Schroeder, S. L. M., & Christmann, K. 2003, *Surf. Sci.*, 536, 206
- Gredel, R., Lepp, S., & Dalgarno, A. 1987, *ApJ*, 323, L137
- Greenberg, L. T. 1973, in *Interstellar dust and related topics*, ed. Greenberg & van de Hulst, 413–419
- Guzmán, V., Pety, J., Goicoechea, J. R., Gerin, M., & Roueff, E. 2011, *A&A*, 534, 49
- Haensel, R., Koch, E. E., Kosuch, N., Nielsen, U., & Skibowski, M. 1971, *Chem. Phys. Lett.*, 9, 548
- Hasegawa, T. I. & Herbst, E. 1993, *MNRAS*, 263, 589
- Herbst, E. & van Dishoeck, E. F. 2009, *Annu. Rev. Astro. Astrophys.*, 47, 427
- Herczeg, G. J., Linsky, J. L., Valenti, J. A., Johns Krull, C. M., & Wood, B. E. 2002, *ApJ*, 572, 310

- Hily-Blant, P., Bonal, L., Faure, A., & Quirico, E. 2013, *Icarus*, 223, 582
- Hily-Blant, P., Walmsley, M., des Forets, G. P., & Flower, D. 2010, *A&A*, 513, 20
- Himpfel, F. J., Schwentner, N., & Koch, E. E. 1975, *phys. stat. sol. (b)*, 71, 615
- Hogerheijde, M. R., Bergin, E. A., Brinch, C., et al. 2011, *Science*, 334, 338
- Hollenbach, D., Kaufman, M. J., Bergin, E. A., & Melnick, G. J. 2008, *ApJ*, 690, 1497
- Horn, A., Møllendal, H., & Sekiguchi, O. 2004, *The Astrophysical ...*
- Hudson, R. L. & Moore, M. H. 2002, *ApJ*, 568, 1095
- Ioppolo, S., Cuppen, H. M., Romanzin, C., van Dishoeck, E. F., & Linnartz, H. 2008, *ApJ*, 686, 1474
- James, G. K., Ajello, J. M., Franklin, B., & Shemansky, D. E. 1990, *J. Phys. B: At. Mol. Opt. Phys.*, 23, 2055
- Janssen, C., Guenther, J., Krankowsky, D., & Mauersberger, K. 1999, *J. Chem. Phys.*, 111, 7179
- Johns Krull, C. M. & Herczeg, G. J. 2007, *ApJ*, 655, 345
- Jørgensen, J. K., Schöier, F. L., & van Dishoeck, E. F. 2005, *A&A*, 435, 177
- Kaiser, R. I., Jansen, P., Petersen, K., & Roessler, K. 1995, *Rev. Sci. Instrum.*, 66, 5226
- Kimmel, G. A., Stevenson, K. P., Dohnálek, Z., Smith, R. S., & Kay, B. D. 2001, *J. Chem. Phys.*, 114, 5284
- Kimmel, G. A., Stevenson, K. P., Dohnálek, Z., Smith, R. S., & Kay, B. D. 2001, *J. Chem. Phys.*, 114, 5284
- Knauth, D. C., Andersson, B. G., McCandliss, S. R., & Warren Moos, H. 2004, *Nature*, 429, 636
- Knez, C., Boogert, A. C., Pontoppidan, K. M., et al. 2005, *ApJL*, 635, L145
- Knez, C., Boogert, A. C. A., Pontoppidan, K. M., et al. 2005, *ApJ*, 635, L145
- Kristensen, L. E., van Dishoeck, E. F., van Kempen, T. A., et al. 2010, *A&A*, 516, 57
- Lee, P. C. & Nee, J. B. 2000, *J. Chem. Phys.*, 112, 1763
- Liseau, R., Goldsmith, P. F., Larsson, B., et al. 2012, *A&A*, 541, A73
- Lu, H.-C., Chen, H.-K., Cheng, B.-M., Kuo, Y.-P., & Ogilvie, J. F. 2005, *J. Phys. B: At. Mol. Opt. Phys.*, 38, 3693
- Mann, A., Cloutier, P., Liu, D., & Sanche, L. 1995, *Phys. Rev. B*, 51, 7200

- Maret, S., Bergin, E. A., & Lada, C. J. 2006, *Nature*, 442, 425
- Mason, N. J., Dawes, A., Holtom, P. D., et al. 2006, *Faraday Discuss.*, 133, 311
- Matar, E., Congiu, E., Dulieu, F., Momeni, A., & Lemaire, J.-L. 2008, *A&A*, 492, L17
- Mathis, J. S., Mezger, P. G., & Panagia, N. 1983, *A&A*, 128, 212
- Mauersberger, K., Krankowsky, D., & Janssen, C. 2003, *Space Sci Rev*, 106, 265
- McKellar, A. 1940, *Publications of the Astronomical Society of the Pacific*
- Megeath, S. T., Wilson, T. L., & Corbin, M. R. 2005, *ApJ*, 622, L141
- Merrill, K. M., Russell, R. W., & Soifer, B. T. 1976, *ApJ*
- Merrill, P. W. 1934, *Publications of the Astronomical Society of the Pacific*, 46, 206
- Mitchell, G. F., Lee, S. W., Maillard, J.-P., et al. 1995, *Astrophys. J.*, 438, 794
- Miyauchi, N., Hidaka, H., Chigai, T., et al. 2008, *Chem. Phys. Lett.*, 456, 27
- Mota, R., Parafita, R., Maneira, M. J. P., et al. 2007, *Radiat. Prot. Dosim.*, 122, 66
- Müller, H., Thorwirth, S., Roth, D. A., & Winnewisser, G. 2001, *A&A*, 370, L49
- Muñoz Caro, G. M., Jiménez-Escobar, A., Martín-Gago, J. Á., et al. 2010, *A&A*, 522, 108
- Muñoz Caro, G. M. & Schutte, W. A. 2003, *A&A*, 412, 121
- Nahon, L., de Oliveira, N., Garcia, G. A., et al. 2012, *J Synchrotron Rad*, 19, 508
- Neufeld, D. A., Lepp, S., & Melnick, G. J. 1995, *ApJ*
- Nomura, H. & Millar, T. J. 2004, *A&A*, 414, 409
- Öberg, K. I., Boogert, A. C. A., Pontoppidan, K. M., et al. 2008, *ApJ*, 678, 1032
- Öberg, K. I., Boogert, A. C. A., Pontoppidan, K. M., et al. 2011a, *ApJ*, 740, 109
- Öberg, K. I., Bottinelli, S., Jørgensen, J. K., & van Dishoeck, E. F. 2010, *ApJ*, 716, 825
- Öberg, K. I., Bottinelli, S., & van Dishoeck, E. F. 2009a, *A&A*, 494, L13
- Öberg, K. I., Fayolle, E. C., Cuppen, H. M., van Dishoeck, E. F., & Linnartz, H. 2009b, *A&A*, 505, 183
- Öberg, K. I., Fuchs, G. W., Awad, Z., et al. 2007, *ApJL*, 662, L23
- Öberg, K. I., Garrod, R. T., van Dishoeck, E. F., & Linnartz, H. 2009a, *A&A*, 504, 891
- Öberg, K. I., Linnartz, H., Visser, R., & van Dishoeck, E. F. 2009b, *ApJ*, 693, 1209

- Öberg, K. I., Murray-Clay, R., & Bergin, E. A. 2011b, *ApJL*, 743, L16
- Öberg, K. I., van Broekhuizen, F., Fraser, H. J., et al. 2005, *ApJ*, 621, L33
- Öberg, K. I., van Broekhuizen, F. A., Fraser, H. J., et al. 2005, *ApJL*, 621, L33
- Öberg, K. I., van Dishoeck, E. F., & Linnartz, H. 2009, *A&A*, 496, 281
- Öberg, K. I., van Dishoeck, E. F., & Linnartz, H. 2009, *A&A*, 496, 281
- Oka, A., Inoue, A. K., Nakamoto, T., & Honda, M. 2012, arXiv
- Oka, A., Nakamoto, T., & Ida, S. 2011, *ApJ*, 738, 141
- Okabe, H. 1978, *Photochemistry of small molecules*, Vol. 431 (Wiley New York)
- Okuzumi, S., Tanaka, H., Kobayashi, H., & Wada, K. 2012, *ApJ*, 752, 106
- Pagani, L., Bourgoïn, A., & Lique, F. 2012, *A&A*, 548, L4
- Pagani, L., Olofsson, A. O. H., Bergman, P., et al. 2003, *A&A*, 402, L77
- Pagani, L., Pardo, J. R., Apponi, A. J., Bacmann, A., & Cabrit, S. 2005, *A&A*, 429, 181
- Parise, B., Ceccarelli, C., Tielens, A. G. G. M., et al. 2006, *A&A*, 453, 949
- Parker, D. H. 2000, *Acc. Chem. Res.*, 33, 563
- Persson, C. M., Black, J. H., Cernicharo, J., et al. 2010, *A&A*, 521, 6
- Persson, C. M., de Luca, M., Mookerjea, B., et al. 2012, *A&A*, 543, 34
- Pickett, H. M., Poynter, R. I., & Cohen, E. A. 1998, *J Quant. Spectrosc. Ra.*
- Pontoppidan, K. M., Boogert, A. C., Fraser, H. J., et al. 2008, *ApJ*, 678, 1005
- Pontoppidan, K. M., Boogert, A. C. A., Fraser, H. J., et al. 2008, *ApJ*, 678, 1005
- Pontoppidan, K. M., Dartois, E., van Dishoeck, E. F., Thi, W. F., & d'Hendecourt, L. 2003, *A&A*, 404, L17
- Pontoppidan, K. M., Fraser, H. J., Dartois, E., et al. 2003, *A&A*, 408, 981
- Pontoppidan, K. M., Fraser, H. J., Dartois, E., et al. 2003, *A&A*, 408, 981
- Qi, C., Wilner, D. J., Calvet, N., et al. 2006, *ApJ*, 636, L157
- Rakhovskaia, O., Wiethoff, P., & Feulner, P. 1995, *Nucl. Instrum. Meth. B*, 101, 169
- Rodgers, S. D. & Charnley, S. B. 2001, *ApJ*, 546, 324
- Rodón, J. A., Beuther, H., Megeath, S. T., & van der Tak, F. F. S. 2008, *A&A*, 490, 213

- Roncin, J.-Y., Damany, N., & Romand, J. 1967, *J. Molec. Spectrosc.*, 22, 154
- Rowland, B., Fisher, M., & Devlin, J. P. 1991, *J. Chem. Phys.*, 95, 1378
- Sandell, G., Goss, W. M., & Wright, M. 2005, *ApJ*, 621, 839
- Sandford, S. A. & Allamandola, L. J. 1988, *Icarus*, 76, 201
- Sandford, S. A. & Allamandola, L. J. 1990, *Icarus*, 87, 188
- Schreyer, K., Semenov, D., Henning, T., & Forbrich, J. 2006, *ApJ*, 637, L129
- Schulz, G. J. 1973, *Rev. Mod. Phys.*, 45, 423
- Shen, C. J., Greenberg, J. M., Schutte, W. A., & van Dishoeck, E. F. 2004, *A&A*, 415, 203
- Shi, H., Cloutier, P., & Sanche, L. 1998, *Low Temp. Phys.*, 24, 742
- Sivaraman, B., Mebel, A. M., Mason, N. J., Babikov, D., & Kaiser, R. I. 2010, *Phys. Chem. Chem. Phys.*, 13, 421
- Stevenson, K. P. 1999, *Science*, 283, 1505
- Stevenson, K. P., Kimmel, G. A., Dohnalek, Z., Smith, R. S., & Kay, B. D. 1999, *Science*, 283, 1505
- Straub, H., Renault, P., Lindsay, B., Smith, K., & Stebbings, R. 1996, *Phys. Rev. A*, 54, 2146
- Swings, P. & Rosenfeld, L. 1937, *ApJ*
- Taquet, V., Peters, P. S., Kahane, C., et al. 2013, *A&A*, 550, 23
- Teolis, B., Loeffler, M., Raut, U., Fam, M., & Baragiola, R. 2007, *Icarus*, 190, 274
- Tercero, B., Kleiner, I., Cernicharo, J., et al. 2013, *ApJL*, 770, L13
- Thrower, J. D., Burke, D. J., Collings, M. P., et al. 2008, *ApJ*, 673, 1233
- Tielens, A. G. G. M. & Hagen, W. 1982, *A&A*, 114, 245
- V. Piétu, A. Dutrey, & S. Guilloteau. 2007, *A&A*, 467, 163
- Valenti, J. A., Fallon, A. A., & Johns Krull, C. M. 2003, *ApJS*, 147, 305
- van Broekhuizen, F. A., Keane, J. V., & Schutte, W. A. 2004, *A&A*, 415, 425
- van de Hulst, H. C. 1949, Utrecht, Drukkerij Schotanus & Jens, 1949., -1
- van der Tak, F. F. S., Tuthill, P. G., & Danchi, W. C. 2005, *A&A*, 431, 993
- van der Tak, F. F. S., van Dishoeck, E. F., & Caselli, P. 2000, *A&A*, 361, 327

- van Dishoeck, E. F. 2006, *Proc. Nat. Acad. Sci. USA*, 103, 12249
- van Dishoeck, E. F., Jonkheid, B., & van Hemert, M. C. 2006, *Faraday Discuss.*, 133, 231
- Vasyunin, A. I. & Herbst, E. 2013, *ApJ*, 762, 86
- Visser, R., van Dishoeck, E. F., Doty, S. D., & Dullemond, C. P. 2009, *A&A*, 495, 881
- Visser, R., van Dishoeck, E. F., Doty, S. D., & Dullemond, C. P. 2009, *A&A*, 495, 881
- Viti, S., Collings, M. P., Dever, J. W., McCoustra, M. R. S., & Williams, D. A. 2004, *MNRAS*, 354, 1141
- Viti, S., Collings, M. P., Dever, J. W., McCoustra, M. R. S., & Williams, D. A. 2004, *MNRAS*, 354, 1141
- Viti, S. & Williams, D. A. 1999, *MNRAS*, 305, 755
- Walsh, C., Millar, T. J., & Nomura, H. 2010, *ApJ*, 722, 1607
- Watanabe, N., Horii, T., & Kouchi, A. 2000, *ApJ*, 541, 772
- Watanabe, N. & Kouchi, A. 2002, *ApJ*, 571, L173
- Watanabe, N., Nagaoka, A., & Shiraki, T. 2004, *ApJ*
- Watanabe, N., Shiraki, T., & Kouchi, A. 2003, *ApJ*, 588, L121
- Westley, M. S., Baragiola, R. A., Johnson, R. E., & Baratta, G. A. 1995a, *Nature*, 373, 405
- Westley, M. S., Baragiola, R. A., Johnson, R. E., & Baratta, G. A. 1995b, *Planetary and Space Science*, 43, 1311
- Willacy, K. & Langer, W. D. 2000, *ApJ*, 544, 903
- Wu, Y.-J., Wu, C. Y. R., Chou, S.-L., et al. 2012, *ApJ*, 746, 175
- Wyrowski, F., Schilke, P., Walmsley, C. M., & Menten, K. M. 1999, *ApJ*, 514, L43
- Yabushita, A., Hama, T., Yokoyama, M., et al. 2009, *ApJL*, 699, L80
- Yang, S., Hill, W. T., & Dixit, S. N. 1994, *J. Chem. Phys.*, 100, 6434
- Yuan, C. & Yates, J. T. 2013, *J. Chem. Phys.*, 138, 4303
- Zhang, Z., Piatkowski, L., Bakker, H. J., & Bonn, M. 2011, *Nat. Chem.*, 3, 888

Nederlandse samenvatting

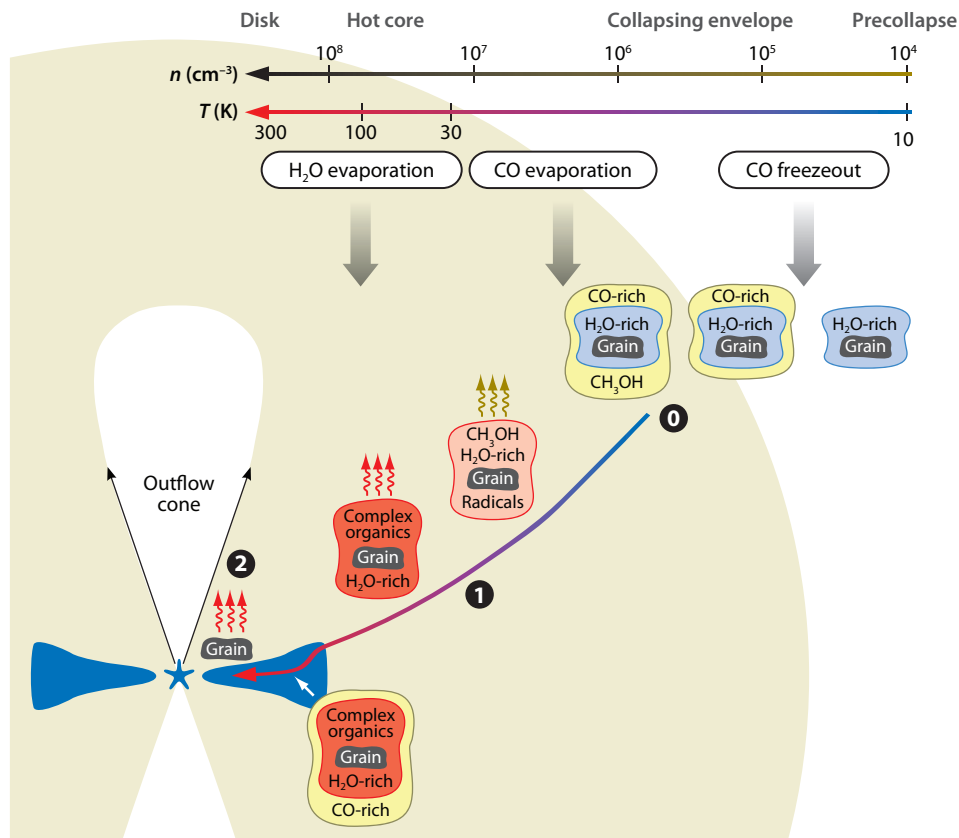
Van ijs tot gas Het onderzoek naar desorptieprocessen van interstellair ijs

Ijs in stervormingsgebieden

Moleculen zijn overal in het heelal aanwezig. In het inter- en circumstellaire medium - de ijle ruimte tussen en rondom de sterren - is een grote diversiteit van moleculen waargenomen, variërend van diatomen tot organische moleculen, grote polycyclische aromatische koolwaterstoffen (PAKs), ionen en radicalen. Door de processen die verantwoordelijk zijn voor hun vorming en afbraak te bestuderen kunnen we meer te weten komen over de fysische omgeving waarin ze worden gevonden. Dit vormt een van de hoofddoelen van de astrochemie, de wetenschap die zich bezig houdt met chemische processen in de ruimte.

Stervormingsgebieden bestaan gewoonlijk uit moleculair gas en stofdeeltjes van submicrometergrootte. In koude omgevingen zoals prestellare kernen, de buitenste delen van een protostellare wolk en het middenvlak van een protoplanetaire schijf kunnen moleculen vormen of vastvriezen op stofdeeltjes en zo een ijsmantel vormen. De ijssamenstelling in verscheidene stervormingsgebieden kan worden vastgesteld m.b.v. mid-infrarood spectroscopie, en deze toont aan dat ijs in de ruimte vooral uit H₂O bestaat, gevolgd door CO and CO₂, evenals NH₃, CH₄, OCN⁻ en CH₃OH. Grotere organische moleculen moeten nog steeds geïdentificeerd worden. Waardevolle informatie over de mogelijke vorming van deze moleculen kan verkregen worden door de veranderingen in de abundantie en de ijscompositie gedurende de verschillende fases van stervorming. Het zwaartepunt van dit proefschrift ligt op de fysische in chemische processen die plaatsvinden in interstellair ijs, en die middels laboratorium experimenten worden gekarakteriseerd.

Figuur 8.1 toont schematisch dat ons huidige begrip van de ijsvorming en -evolutie tijdens het stervormingsproces. Eenvoudige soorten ijs vormen in donkere wolken in



Figuur 8.1: Schematische voorstelling van de ijsevolutie in opeenvolgend een prestellaire kern, een instortende gas wolk en een protoplanetaire schijf. In de prestellaire fase zien we de vorming van de eerste door H₂O gedomineerde ijsmantel, gevolgd door het vastvriezen van gasvormige moleculen tijdens de ineenstorting van de wolk, waardoor een CO-rijke mantel ontstaat. In de protostellaire fase, bewegen de ijzige stofdeeltjes richting de ster. De ijslagen ondergaan dan hydrogenatiereacties als ook hitte en UV straling. Het grootste deel van de ijsmantel verdampt wanneer de stofdeeltjes gebieden van 100 K bereiken. Daarnaast zullen sommige stofdeeltjes richting het middenvlak van protoplanetaire schijf bewegen waar planeten en kometen ontstaan. Deze illustratie is gemaakt door E. van Dishoeck en R. Visser.

de prestellaire fase door het vastvriezen van atomen en kleine moleculen op de stofdeeltjes. CO₂ wordt gevormd in deze fase, naast de hydrogenatie van O, C, en N waaruit H₂O, CH₄, en NH₃ ontstaan. Wanneer de kern onder zijn eigen zwaartekracht instort en de protoster ontstaat, gaat de temperatuur omlaag en zullen de moleculen die nog in de gasfase zaten (voornamelijk CO) vastvriezen bovenop de eerste waterrijke laag en zo een apolaire ijsmantel vormen. Gedurende de protostellaire fase voedt de pasgeboren ster zich met materiaal uit omringende schijf van gas en stof, wat resulteert in de opwarming van de met ijs bedekte stofdeeltjes. In deze fase worden complexere moleculen gevormd door thermisch gedreven reacties en door de toename in mobiliteit van radicalen die zijn gevormd tijdens energetische reacties. De relatie

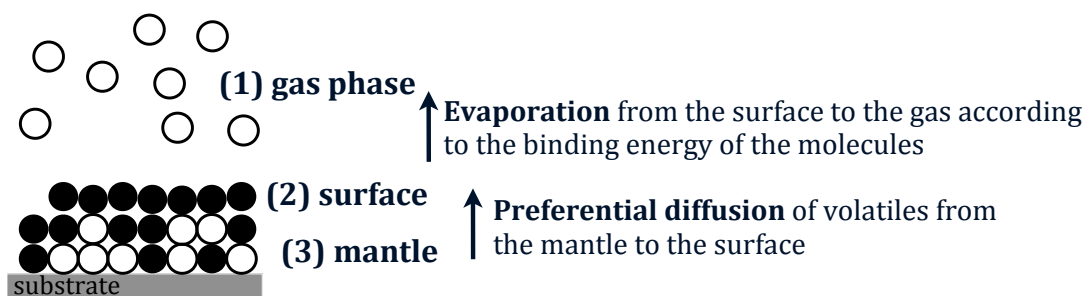
tussen ijssamenstelling en waarnemingen van complexe organische moleculen rond massieve sterren is het onderwerp van hoofdstuk 7. Het ijs op de stofdeeltjes verdampt dichter bij de ster. Bij temperaturen van 100 K zijn de meeste moleculen terug in de gasfase en nemen deel aan gasfase reacties. Daarnaast bewegen sommige ijzige stofdeeltjes richting de protoplanetaire schijf, en mogelijk staan de moleculen die al in eerdere stadia gevormd zijn aan het begin van de route naar moleculaire complexiteit zoals die wordt waargenomen in planetaire systemen. In gebieden zonder thermische desorptie kunnen ook energetische deeltjes en met name UV-fotonen zorgen voor verdamping van ijs. Dit is het geval in prestellaire wolken, in de buitenste delen van protostellaire wolken en in het middenvlak van protoplanetaire schijven.

De studie van thermische en niet-thermische desorptieprocessen is cruciaal voor het begrijpen van gas-stof interacties in stervormingsgebieden. Moleculen in de gasfase worden veelal gebruikt door radioastronomen als indicatoren van fysische omstandigheden. Daarom is het belangrijk om te begrijpen bij welke druk, temperatuur, stralingsveld, enzovoorts, de moleculen van de vaste naar de gasfase overgaan. Vanuit chemisch oogpunt is een goede inschatting van de ijs tot gas verhouding cruciaal doordat chemische reacties drastisch verschillen in beide fases; van sommige reactieproducten wordt meer gevormd in de ene fase in vergelijking tot de andere. Het hoofddoel van dit proefschrift is het experimenteel vaststellen van de thermische en foton-gëinduceerde desorptie processen voor omstandigheden die relevant zijn voor het interstellair medium.

Thermische desorptie van ijs

Thermische desorptie van ijs is een belangrijk proces in de protostellaire fase wanneer de jonge ster groeit door de ineenstorting van haar wolk. De ijzige stofdeeltjes van de wolk warmen op terwijl ze richting ster bewegen en moleculen gaan van de vaste naar de gasfase afhankelijk van hun bindingsenergie aan het ijsoppervlak. Experimenten in het laboratorium die de sublimatie van de ijsmantel simuleren laten zien hoe de desorptie van de interstellair ijs analogen plaatsvindt. Hoofdstuk 2 focust op de vraag hoe H_2O , de hoofdcomponent van interstellair ijs, de thermische desorptie van meer vluchtige moleculen beïnvloedt. $\text{H}_2\text{O}:\text{CO}_2$ ijsmengsels van verschillende diktes en mengverhoudingen worden gegroeid op een koud substraat, dat het stof oppervlak nabootst. Dit wordt gedaan onder ultrahoog vacuum om de dichtheidsomstandigheden in stervormingsgebieden zo goed mogelijk te simuleren. Het gevormde ijs wordt vervolgens in een specifiek tempo opgewarmd en de gedesorbeerde moleculen worden gemeten met een quadrupool massa spectrometer als functie van de temperatuur. Puur CO_2 ijs desorbeert rond 70 K, maar wanneer het gemengd is met H_2O verdampt maar een fractie bij 70 K. De rest desorbeert rond 140 K samen met de watermoleculen. Dit 'vasthoudt' fenomeen wordt beschreven in hoofdstuk 2 m.b.v. een uitgebreid 3-fase model van een ijsanaloog (zie Figuur 8.2).

De laboratorium experimenten worden gebruikt om de migratie van vluchtige moleculen van de ijsmantel naar het oppervlak te begrijpen, omdat dit geen statistisch proces is maar samenhangt met de soort-afhankelijke diffusie in de watermatrix. Met dit model kan de hoeveelheid vluchtige moleculen die vast blijft zitten in het waterijs worden voorspeld voor verschillende ijsdiktes, mengverhoudingen en opwarmings-



Figuur 8.2: Principe van het 3-fase desorptiemodel voor vluchtige moleculen (rode cirkels) in waterrijk ijs (groene cirkels). Desorptie van moleculen naar de gasfase gebeurt aan het oppervlak als functie van de bindingsenergie van de moleculen. Moleculen dieper uit de mantel vullen het oppervlak weer aan na elk desorptie evenement. De aanvulling hangt af van het vermogen van de moleculen om te diffunderen van de bulk naar het oppervlak en is dus gunstiger voor vluchtige soorten omdat deze minder sterk gebonden zijn aan hun omgeving.

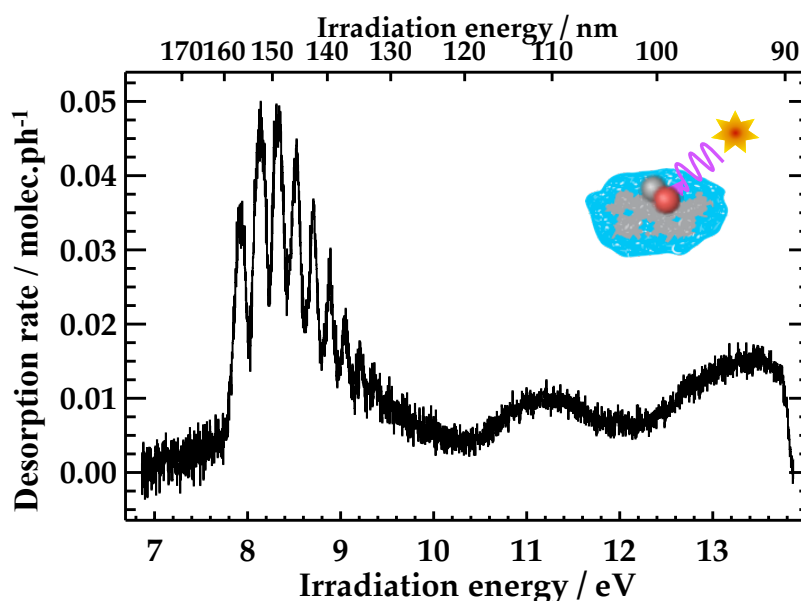
snelheden die specifiek zijn voor protosterren. Door dit model te combineren met huidige gas-stof simulaties kan de overgang van ijs naar gas beter worden benaderd en daarmee ook de chemie beter worden beschreven.

Foton-geïnduceerde desorptie

In koude inter- en circumstellaire omgevingen waar men verwacht dat moleculen volledig uitgevoren zijn, kunnen sommige moleculen nog steeds in de gasfase worden waargenomen a.g.v niet-thermische desorptie processen. Bijvoorbeeld niet-thermische desorptie geïnduceerd door UV fotonen biedt een mogelijke verklaring voor moleculaire abundanties in protoplanetaire schijven. Er zijn laboratorium experimenten gedaan om zowel de efficiëntie als de betrokken mechanismes van fotodesorptie te meten. De meeste fotodesorptie studies gebruiken een H_2 microgolven-ontladingslamp om desorptie te veroorzaken, omdat deze voornamelijk Lyman-alpha straling produceert. De emissieprofielen van deze lampen zijn echter erg gevoelig voor de omstandigheden en de fotodesorptie efficiëntie hangt sterk af van het lamp-specifieke emissieprofiel.

Een nieuwe aanpak, gebruikt in hoofdstuk 3 t/m 6, is daarentegen gebaseerd op afstembare Vacuum-UV straling om de fotodesorptie van interstellaire ijsanalogen te bestuderen. De DESIRS lichtbron bij de SOLEIL synchrotron (Saint-Aubin, Frankrijk) zendt fotonen uit in het astronomisch interessante 7-14 eV spectrale venster, met hoge intensiteit en goede spectrale resolutie. Op deze manier is het mogelijk om de golflengte afhankelijke fotodesorptie te meten. Zulke studies resulteren in kwantitatieve fotodesorptie snelheden voor verschillende energieën, wat bijdraagt aan een betere benadering van fotodesorptie in gebieden in het heelal met verschillende UV stralingsprofielen. Het belangrijkste is echter dat een spectraal opgeloste analyse van fotodesorptie waardevolle inzichten geeft in de onderliggende moleculaire mechanismes, wat boeiend is vanuit een fysisch-chemisch standpunt en bovendien helpt om dit pro-

ces te beschrijven met astrochemische simulaties die gas-stof interacties meenemen.



Figuur 8.3: CO fotodesorptie spectrum voor een 10 ML ijs dik bij 18 K. De vibrationale progressie onder 10 eV komt overeen met de excitatie van de niet-dissociatieve $A^1\Pi$ toestand van CO.

Als eerste is de fotodesorptie van CO-ijs onderzocht, omdat CO een veel bestudeerd molecuul is en CO-rijk ijs aan het oppervlak van interstellaire stofdeeltjes wordt gevonden (zie Figuur 8.1). CO-ijs wordt in ultrahoog vacuum bij 18 K gegroeid en vervolgens bestraald met fotonen met energieën tussen 7 en 14 eV. De gedesorbeerde moleculen worden gemeten met massa spectrometrie als functie van foton energie en dit resulteert in het spectrum in Figuur 8.3. De duidelijke golflengte afhankelijkheid van de fotodesorptie komt door de elektronische structuur van het CO-ijs; dit is Desorptie geïnduceerd door Elektronische Transitie (DIET) (hoofdstuk 2). Door het gebruik van isotopologisch-gelabelde lagen van $^{12}\text{CO}/^{13}\text{CO}$ en een klein verschil in frequentie van de vibratie niveaus van de geëxciteerde toestanden tussen deze twee isotopologen, is het mogelijk om dieper dan ooit op het fotodesorptiemechanisme in te gaan. Het is de energetische excitatie van moleculen in het suboppervlak die op hun beurt energie overdragen aan de moleculen aan het oppervlak, waarmee de desorptie uiteindelijk wordt geïnduceerd (hoofdstuk 3). N_2 fotodesorptie door de niet-dissociatieve elektronische excitatie naar de $A^1\Pi_u$ toestand (boven 12.4 eV) vindt op dezelfde manier plaats als voor CO onder 10 eV. In het geval van O_2 , induceert de VUV straling dissociatie, waardoor zuurstof radicalen ontstaan. Deze radicalen kunnen er voor zorgen dat andere moleculen van de vaste naar gas fase kunnen overgaan, de radicalen zelf kunnen recombineren of chemie induceren die de fotodesorptie kanalen beïnvloedt (hoofdstuk 5). Tenslotte is de energieoverdracht in het niet-dissociatieve fotodesorptiemechanisme onderzocht voor twee verschillende moleculen: CO en N_2 . Het begrijpen van fotodesorptie in ijsmengsels is cruciaal omdat interstellair ijs altijd gemengd is. Hoewel de absorptiespectra van deze moleculen in de vaste fase compleet verschillen,

zijn hun fotodesorptiespectra hetzelfde in een 1:1 mengsel. Wanneer een van de soorten elektronisch geëxciteerd is door een energetisch foton zal het zijn energie naar het oppervlak overdragen ongeacht de aard van het molecuul en zo resulteren in gelijke fotodesorptie profielen. Dit heeft belangrijke astrofysische consequenties aangezien de fotodesorptiesnelheid niet alleen afhangt van de aard van het soort molecuul maar ook van zijn omgeving. Het exacte karakter van de energieoverdracht blijft nog steeds een open vraag die hopelijk in de komende jaren wordt opgelost door het gebruik van laser spectroscopie van desorberende moleculen en de meting van ijsfluorescentie tijdens bestraling. Verder moeten de fotodesorptie mechanismes van organische moleculen nog verder worden onderzocht. Dit is ongetwijfeld het onderwerp van toekomstig onderzoek.

English summary

Ices in star-forming environments

Molecules are present throughout our universe. In the inter- and circumstellar medium, the highly dilute space in between and around stars, a wide variety of molecules have been observed ranging from diatomic species to organic molecules, large PAHs, ions and radicals. Studying their formation, and destruction pathways in the laboratory provides us with clues on the physical environment in which they are found. This constitutes one of the main goals in astrochemistry, the science that focuses on chemical processes in space.

Star-forming regions are typically composed of molecular gas and submicron-sized dust particles. In the cold regions such as prestellar cores, outer parts of protostellar envelopes and mid-planes of protoplanetary disks, molecules can form on or freeze-out onto dust grains, forming an icy mantle. The ice composition along the lines of sight of various star-forming environments can be inferred through mid-IR spectroscopy. Interstellar ice consists mainly of H₂O, followed by CO and CO₂ and also includes NH₃, CH₄, OCN⁻, CH₃OH. Even bigger organic species still have to be identified. The presence of molecules in polar and apolar ices and molecular abundance variations during the various stages of star formation provide valuable clues on their possible formation pathways. The focus in this thesis is on the physical and chemical processes that take place in interstellar ice, and their characterization through dedicated laboratory experiments.

Figure 8.4 presents a simple schematic summarizing the current understanding of how ices form and behave during star formation. Simple ices form at the prestellar stage through accretion of atoms and small gas phase molecules onto the grains. The main molecules that form at this stage are CO₂ and the hydrogenation products H₂O, CH₄, and NH₃. When the core gravitationally collapses to form the protostar, the temperature drops and molecules that were still in the gas phase, mainly CO, will freeze out on top of the first water-rich layer, resulting in an apolar mantle. During the protostellar stage, the newborn star feeds on its accreting envelope, resulting in a warm-up of the icy dust grains. This phase will see the formation of more complex species through heat-activated reactions and through the increase in mobility of rad-

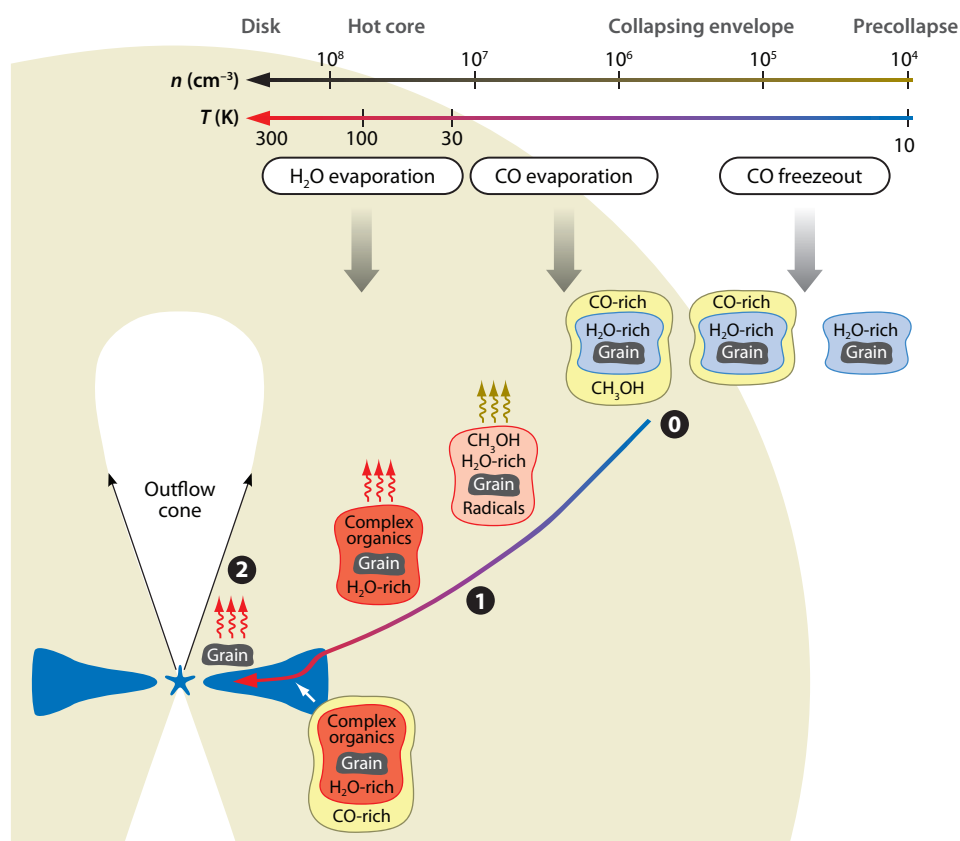


Figure 8.4: Cartoon representation of the ice evolution from the prestellar stage through the collapsing envelope into a protoplanetary disk. The prestellar stage will see the formation of the first H₂O-dominated ice mantles, followed by gas-phase freeze-out during cloud collapse, forming a CO-rich mantle. The icy-grains will undergo hydrogenation, heat and UV activated reactions in the protostellar phase while flowing towards the star. Most of the icy mantle will evaporate when grains reach the 100 K regions, giving rise to an active hot-core chemistry. Alternatively some of the icy grains will flow into the mid-plane of protoplanetary disks where planets and comets are formed and become incorporated into these bodies. Figure by E. van Dishoeck and R. Visser.

icals created by energetic reactions. The icy grains are also subject to sublimation as they get closer to the star. The relationship between ice composition and observation of complex organics around high-mass protostars is the subject of chapter 7. Around $T = 100$ K, most of the molecules sublimate into the gas phase and participate in gas phase reaction networks. Alternatively, some of the icy grains will flow to the protoplanetary disk. Molecules formed at previous stages are thus most likely at the origin of the molecular complexity as observed in planetary systems. In regions where thermal desorption does not occur, energetic particles and especially UV-photons can also induce ice desorption. This is the case in prestellar clouds, before the star is formed, in the outer parts of the protostellar envelope and in the mid-planes of protoplanetary disks.

Constraining thermal and non-thermal desorption processes is crucial to understand the gas-grain interactions in star-forming environments. Molecules in the gas phase are widely used by radio astronomers as tracers of physical conditions. Thus it is vital to understand the parameters - temperature, radiation fields, ice composition, etc - that govern the transition of molecules from the icy grains into the gas phase. From a chemical point of view, a good estimate of the ice and gas partitioning is crucial since chemical reactions are drastically different in both phases ; some daughter species may form in one phase more than in the other. The main goal of this thesis is to experimentally constrain the thermally- and photon-induced desorption processes under conditions that are relevant to the interstellar medium.

Thermal desorption of ice

Thermal ice desorption is a crucial process during the protostellar stage when the young star feeds through the infall of its envelope. The icy grains from the envelope warm up as they flow towards the star and molecules go from solid to gas-phase according to their binding efficiencies to the icy surface. Laboratory experiments simulating the sublimation of the ice mantle are used to understand how the desorption of interstellar ices occurs. Specifically, chapter 2 focuses on how H_2O , the main component of interstellar ices, affects the thermal release of more volatiles ice components. $\text{H}_2\text{O}:\text{CO}_2$ ice mixtures of various thicknesses and ratios are grown on a cold substrate, mimicking the cold grain surface, and under ultra-high vacuum to simulate the density conditions encountered in star forming environments. The ice sample is then warmed up at a linear rate and desorbing molecules are monitored by a mass spectrometer with respect to the temperature. CO_2 in pure ice desorbs around 70 K, but when it is mixed with H_2O , only a certain fraction will desorb at 70 K. The rest desorbs around 140 K together with the water molecules. It is this 'trapping' phenomenon that is captured in chapter 2 through an extended 3-phase model of the ice (see figure 8.5).

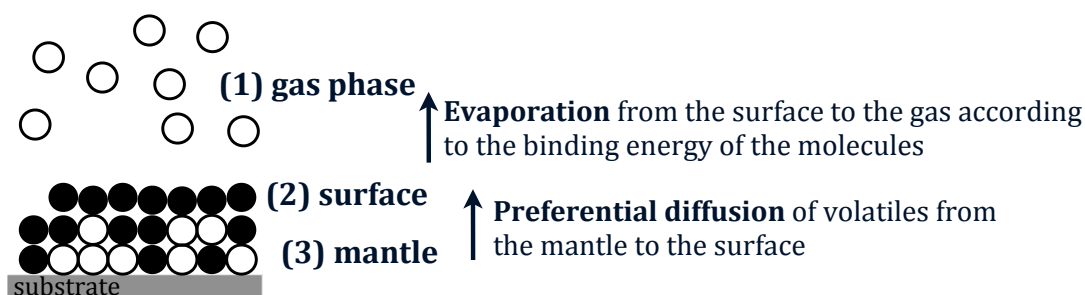


Figure 8.5: Principle of the 3-phase desorption model for volatiles (open circles) in water-rich ice (full circles). Desorption of molecules to the gas phase occurs from the surface according to the binding energy of the molecules and mantle molecules replenish the surface after each desorption event. The replenishment depends on the ability of molecules to diffuse from the bulk to the surface and is more favorable for volatile species since these are less bound to their surroundings.

The laboratory experiments are used to constrain the migration of volatile molecules from the mantle to the surface of the ice. This process is not statistical and instead depends on molecule specific diffusion in water matrix. Using this model, the amount of volatile species trapped within the water can be predicted for various ice thicknesses, mixing ratios, and warm-up rates typical for protostellar environments. Coupling this model to current gas-grain simulations allows for a better estimate of the ice to gas partitioning and thus improve the understanding of both the solid-state and gas-phase chemistry in protostellar environments.

Photon-induced desorption of ice

In cold regions where molecules are expected to totally freeze out, some of them are still observed in the gas-phase due to non-thermal desorption processes. For instance, non-thermal desorption induced by UV photons has been invoked to explain these molecular abundances in protoplanetary disks. Laboratory experiments have been performed to measure the efficiency of photodesorption and investigate its mechanism. Most photodesorption studies so far used an H_2 microwave discharge lamp to induce desorption as it mainly produces Lyman-alpha radiation. The emission profiles of these lamps is, however, very sensitive to the experimental conditions and thus the measured photodesorption efficiencies may depend on the lamps specific emission profile.

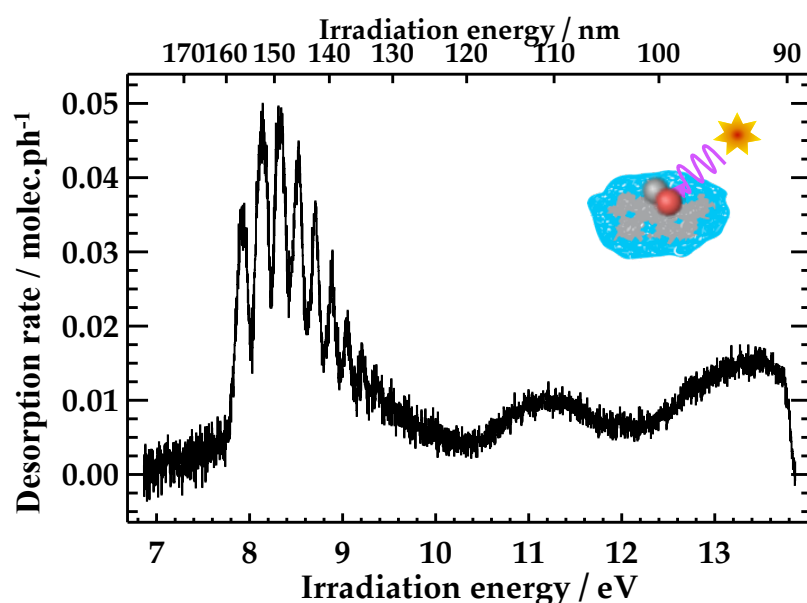


Figure 8.6: CO photodesorption spectrum for a 10 ML ice at 18 K. The vibrational progression below 10 eV correspond to excitation of the non-dissociative $A^1\Pi$ state of CO.

Instead, a new approach used in chapters 3 to 6 relies on the use of tunable Vacuum-UV synchrotron-radiation to study the photodesorption of interstellar ice analogues. The DESIRS beamline at the SOLEIL synchrotron (Saint-Aubin, France) provides photons in the astrophysically interesting 7 - 14 eV spectral window at good flux and resolution to monitor photodesorption efficiency with respect to the incoming photon

energy. Such studies yield quantitative photodesorption rates for a wide energy range, which contributes to a better estimate of the photodesorption over different regions of space where UV fields can have various profiles. But more importantly, such a frequency resolved analysis of photodesorption provides valuable insights on the underlying molecular mechanisms. This is exciting from a physical-chemical point of view and also helps to incorporate this process into gas-grain astrochemical simulations.

The photodesorption of CO ice has been investigated first since CO is a rather well understood molecule and because CO-rich ice is found at the surface of interstellar grains (see figure 8.4). CO ice samples are grown under ultra-high vacuum at 18 K and then irradiated by photons which energy is ranging from 7 to 14 eV. The desorbing molecules are monitored by mass spectrometry with respect to the irradiation energy and yield the photodesorption spectrum presented in figure 8.6. The clear wavelength-dependence of photodesorption is due to the electronic structure of the CO ice; it is a Desorption Induced by Electronic Transition (DIET) process (chapter 3). Using isotopically-labeled layers of $^{12}\text{CO}/^{13}\text{CO}$ and the slight difference in energy observed for the vibrational levels of the excited state of the two isotopologues, it has been possible to go deeper than ever before in the understanding of this photodesorption process. It is found that the electronic excitation of molecules in the sub-surface induces a transfer of energy to the surface where it triggers their desorption (chapter 4). N_2 photodesorption mainly occurs in the same way as for CO below 10 eV. In the case of O_2 , the VUV irradiation induces dissociation in the 7 - 14 eV window and the photodesorption mechanism becomes much more complex since oxygen radicals can induce additional kick-out events, recombine, or induce chemistry affecting the photodesorption channels (chapter 5). In addition, non-dissociative photodesorption mechanism has been investigated for two distinct species in mixed iced: CO and N_2 . Understanding photodesorption for ice mixtures is crucial since interstellar ices are mostly mixed. Even though the photo-absorption spectra of the two species in the solid phase are completely different, their photodesorption spectra are the same when irradiating a 1:1 mixture. These similar desorption profiles are due to the electronic excitation of one specific species and subsequent energy transfer to the surface molecules, regardless of their nature. This has important astrophysical consequences as the photodesorption rates do not only depend on the nature of the species but also on the molecular environment. The exact nature of the energy transfer still remains an open question which will hopefully be answered in the coming years through laser spectroscopy of the desorbing species and measurement of ice fluorescence during irradiation. Finally, the photodesorption mechanisms of organics still have to be investigated, which is challenging, mostly because of the complex role of the radical created upon irradiation. Experimentally constraining the desorption of organics and observing it in the interstellar medium provides a fantastic tool to probe the chemical complexity of interstellar ices. This would definitely be a topic of future work.

Résumé français

De la glace au gaz Comprendre les processus de désorption des glaces interstellaires

Des glaces dans les régions de formation des étoiles.

Les molécules sont présentes partout dans l'univers et sont principalement concentrées dans les nuages moléculaires, siège de formation des étoiles. Une riche variété de molécules a été observée, des plus simples (diatomiques) aux espèces plus complexes (molécules organiques, PAHs), et incluant des ions et des radicaux. Étudier leurs états énergétiques ainsi que leurs voies de destruction permet de connaître les conditions physiques dans lesquelles elles se trouvent et de prédire leur voie de formation et leur abondance dans les différentes régions du milieu interstellaire. Ceci constitue l'un des buts majeurs de l'astrochimie.

Les régions de formation des étoiles sont typiquement composées de gaz moléculaire et de grains de poussière de taille inférieure au micron. Dans les régions froides telles que les cœurs prestellaires, les parties externes des enveloppes protoplanétaires et le plan moyen des disques protoplanétaires, les molécules peuvent se former ou s'accréter sur les grains de poussières, formant ainsi des manteaux de glace. La composition chimique de ces glaces suivant la ligne de visée de différents types d'environnements protostellaires peut être obtenue par spectroscopie infrarouge. Le composé majoritaire est H_2O , suivi de CO , de CO_2 mais aussi de NH_3 , CH_4 , OCN^- , CH_3OH et de molécules plus complexes non encore identifiées. La présence de ces molécules dans différentes phases solides, polaires ou apolaires, et les variations d'abondances moléculaires ont fourni d'importants indices quant à leur possible formation.

La figure 8.7 présente un schéma simplifié du scénario de formation et d'évolution des glaces durant la formation des étoiles. Les glaces simples se forment dans les nuages moléculaires durant l'étape prestellaire par accréation d'atomes et de petites molécules de la phase gazeuse sur les grains. À cette étape, ce sont principalement CO_2 ainsi que les molécules hydrogénées H_2O , CH_4 , NH_3 qui se forment. Cette phase solide dominée par H_2O est dite "polaire". Quand le cœur prestellaire s'effondre pour former

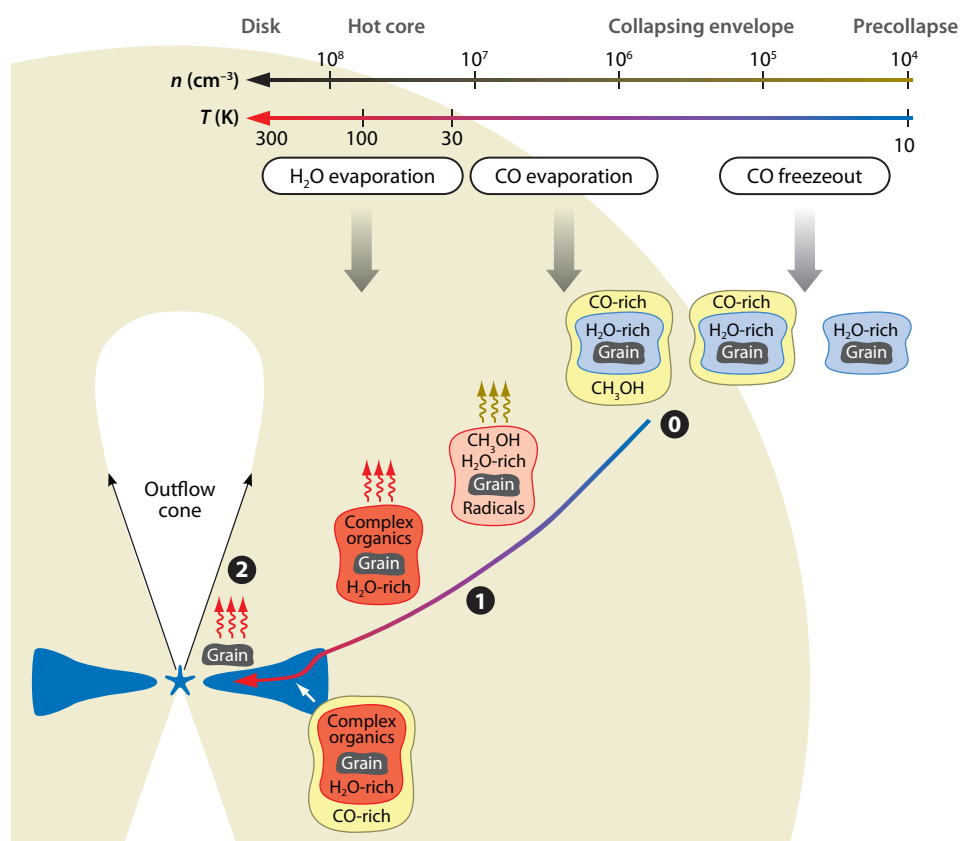


FIGURE 8.7: Schéma représentant l'évolution des glaces interstellaires des cœurs prestellaires, en passant par la phase protostellaire et les disques protoplanétaires. L'étape prestellaire voit la formation d'un premier manteau de glace riche en eau, suivi d'un épisode d'accrétion de molécules de la phase gazeuse durant l'effondrement du cœur prestellaire, formant un manteau de glace riche en CO. Les glaces vont subir des phénomènes d'hydrogénation, de réchauffement, et des réactions induites par les UV pendant la phase protoplanétaire où les grains migrent vers la proto-étoile. La plupart du manteau de glace va s'évaporer lorsque les grains atteignent les régions où les températures sont supérieures à 100 K, ce qui va donner lieu à une chimie riche en phase gazeuse. Alternativement, certains grains migrent dans la région centrale du disque protoplanétaire où les planètes et comètes se forment et ces grains peuvent ainsi être incorporés dans ces mêmes corps. Cette illustration a été élaborée par E. van Dishoeck et R. Visser.

la proto-étoile, la température diminue et les molécules qui se trouvaient encore dans la phase gazeuse - à l'exception de H_2 - viennent se condenser sur la première couche de glace riche en eau. Il en résulte un second manteau de glace, nommé cette fois "apolaire" puisque principalement composé de CO. Durant la phase protostellaire, la jeune étoile se nourrit de son enveloppe qui s'effondre, ce qui entraîne un réchauffement des grains gelés. C'est lors de cette étape que des molécules plus complexes vont pouvoir se former grâce à l'activation de réactions thermiques et à une augmentation de la

mobilité des radicaux formés sous l'effet de particules énergétiques environnantes. À mesure qu'ils s'approchent de la proto-étoile, la température augmente et les grains subissent alors des processus de sublimation. Autour de 100 K, la plupart des molécules condensées dans le manteau de glace sont libérées en phase gazeuse, enrichissent le milieu et participent également aux réactions chimiques. La relation entre la composition des glaces et l'observation d'espèces organiques complexes dans la phase gazeuse est le sujet du chapitre 7 de cette thèse. Néanmoins, une certaine fraction des glaces protostellaires migre dans le plan moyen du disque protoplanétaire, et les molécules formées précédemment sont sans doute à l'origine de la complexité moléculaire observée dans les systèmes planétaires. Dans les régions où la désorption thermique est négligeable, les particules énergétiques - principalement les photons UV - peuvent induire des phénomènes de désorption non-thermiques significatifs. Ce type de désorption peut notamment jouer un rôle dans les cœurs prestellaires (avant formation de l'étoile), les enveloppes protostellaires mais également à la surface des disques protoplanétaires.

Prendre en compte les processus de désorption thermique et non-thermique est fondamental pour comprendre l'interaction gaz-grains dans les régions de formation des étoiles. Les molécules en phase gazeuse sont communément utilisées par les radio astronomes pour sonder les conditions physiques du milieu interstellaire. Il est important de comprendre quels paramètres physiques conditionnent les liens entre les phases solide et gazeuse pour pouvoir utiliser les molécules comme sondes. D'un point de vue chimique, il est également nécessaire de connaître la répartition des molécules entre phase gazeuse et condensée puisque les réactions chimiques peuvent être très différentes d'une phase à l'autre ; certains produits peuvent se former préférentiellement dans une phase plus que dans l'autre. Le but principal de cette thèse est de caractériser et de comprendre les processus de désorption thermique et les processus non-thermiques photo-induits par le rayonnement UV dans les conditions du milieu interstellaire.

La désorption thermique des glaces

La désorption thermique des glaces est un processus important à l'étape protostellaire, lorsque la jeune étoile se nourrit de son enveloppe qui s'effondre. Les grains de l'enveloppe se réchauffent à mesure qu'ils se rapprochent de la proto-étoile et les constituants des manteaux de glaces sont libérés en phase gazeuse de manière sélective selon leurs énergies de liaison. Des expériences de laboratoire sont nécessaires pour comprendre comment ce processus de désorption se produit dans le cas de glaces interstellaires. Plus particulièrement, le chapitre 2 s'intéresse à l'impact de l'eau, principal composant des glaces interstellaires, sur la désorption d'espèces minoritaires plus volatiles. Des dépôts de mélanges $\text{H}_2\text{O} : \text{CO}_2$ de rapports de concentrations et d'épaisseurs variables sont préparés sur un substrat maintenu à très basse température sous ultra-vide, de manière à simuler les conditions rencontrées dans l'espace. La méthode expérimentale repose sur l'application d'une rampe thermique linéaire permettant de chauffer progressivement l'échantillon tout en enregistrant le signal de désorption des espèces triées en masse (spectromètre de masse). Le CO_2 pure désorbe aux alentours de 70 K. Cependant, lorsqu'il est mélangé à H_2O , seule une fraction désorbe à cette température tandis que le reste désorbe vers 140 K avec les molécules d'eau. Ce phénomène de piégeage est reproduit dans le chapitre 2 grâce à un modèle

de glace distinguant trois phases (voir figure 8.8 pour plus de détails sur le modèle).

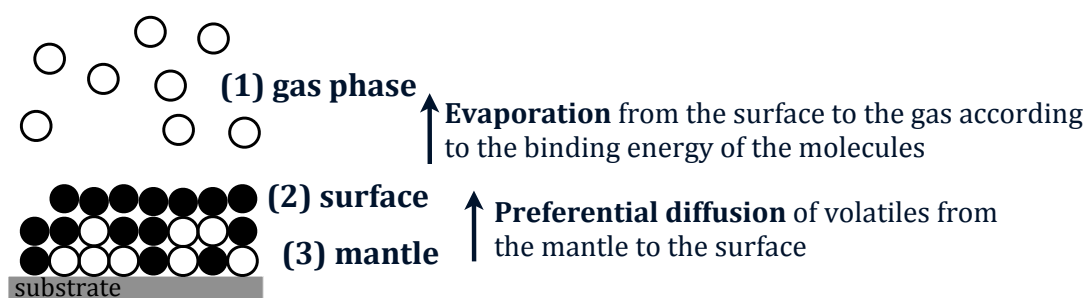


FIGURE 8.8: Principe du modèle de désorption 3-phases pour les volatiles (cercles vides) et les molécules d'eau (cercles pleins). La désorption des molécules vers la phase gazeuse provient de la surface selon l'énergie de liaison des molécules, et les molécules du manteau viennent remplir la surface après chaque événement de désorption. Le remplissage dépend de la facilité pour les molécules à diffuser du manteau vers la surface et est plus favorable pour les espèces volatiles car celles-ci sont moins liées à leur environnement.

Les expériences de laboratoire sont utilisées pour quantifier la migration des espèces volatiles du manteau vers la surface de la glace puisque celle-ci n'est pas statistique mais dépend de la diffusion de ces volatiles en matrice d'eau. En utilisant ce modèle, il est possible d'estimer la quantité de molécules volatiles qui reste piégées avec l'eau à des températures supérieures à leur sublimation en phase pure, et ceci en fonction de l'épaisseur, de la concentration de la glace et du taux de réchauffement spécifique pour une proto-étoile. Coupler ce modèle aux simulations des interactions gaz-grains du milieu interstellaire permet de mieux estimer la répartition entre phase condensée et phase gazeuse des espèces volatiles et donc de prédire de façon précise la chimie protostellaire.

Désorption photo-induite

Dans les régions froides où toutes les molécules - sauf H_2 - devraient se trouver en phase condensée, il est possible d'observer quelques molécules en phase gazeuse sous l'effet de processus de désorption non-thermique. Plus précisément, la désorption non-thermique induite par les photons UV a été invoquée pour expliquer la présence de gaz moléculaire froid dans les disques protoplanétaires. Des expériences de laboratoire ont donc été conduites pour mesurer l'efficacité de la photodésorption et pour comprendre son mécanisme. La plupart des expériences de photodésorption utilise des lampes micro-onde à décharge de H_2 pour induire la désorption car celles-ci produisent principalement des photons UV à la longueur d'onde de l'émission H-alpha et un continuum à plus basse énergie. Les rendements de photodésorption mesurés dépendent à priori du profil spectral de la décharge, très sensible aux conditions expérimentales.

Une nouvelle approche, développée dans les chapitres 3 à 6, consiste à utiliser comme source lumière le rayonnement synchrotron dans le domaine VUV (ultraviolet du vide, $\lambda < 200$ nm) afin d'étudier la photodésorption des glaces interstellaires.

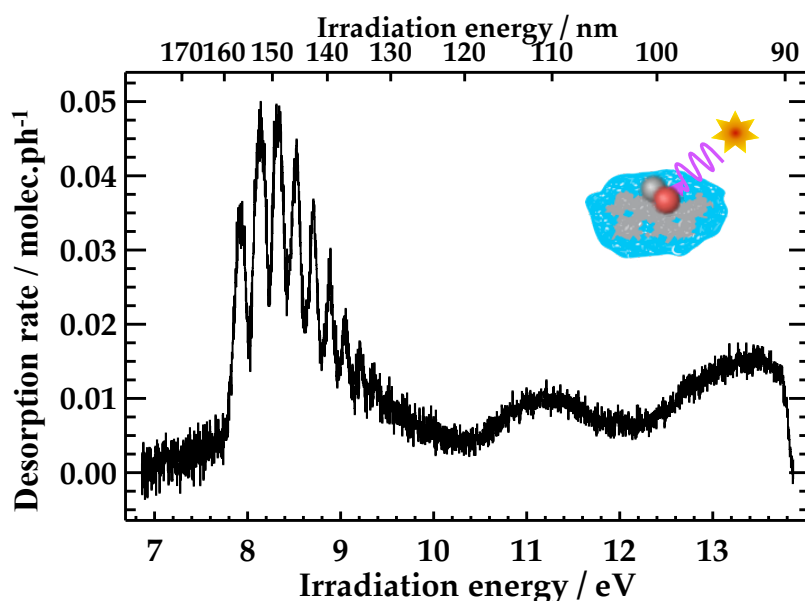


FIGURE 8.9: Spectre de photodésorption d'une glace de CO de 10 ML à 18 K. La progression vibrationnelle sous 10 eV correspond à l'excitation électronique vers l'état non-dissociatif $A^1\Pi$ de CO.

La ligne de lumière DESIRS du synchrotron SOLEIL (Saint-Aubin, France) fournit des photons dans la gamme d'énergie 7 - 14 eV intéressante pour l'astrophysique et à des flux et résolutions suffisants pour sonder la photodésorption en fonction de l'énergie d'irradiation. Ces études permettent d'obtenir des taux de photodésorption sur une large gamme d'énergie, ce qui permet de calculer l'efficacité de photodésorption pour une variété de régions de l'espace ayant différents profils spectraux dans l'UV. Mais l'avantage principal de ces études en fonction de l'énergie d'irradiation est l'obtention d'informations sur le mécanisme de photodésorption, ce qui permet de l'incorporer de façon détaillée dans les simulations astrochimiques d'interaction gaz-grains.

Les premières études résolues en énergie ont porté sur la photodésorption de CO puisque c'est une molécule dont la spectroscopie est connue et que des glaces riches en CO sont communément observées dans le milieu interstellaire. Des échantillons de glace de CO ont été formés sous ultra-vide à 18 K, puis irradiés par des photons dont l'énergie est comprise entre 7 et 14 eV. Les molécules qui désorbent sont sondées par spectrométrie de masse en fonction de l'énergie des photons incidents, ce qui permet d'obtenir un spectre de photodésorption (voir figure 8.9). La nette dépendance de la photodésorption avec la longueur d'onde reflète la structure électronique de la glace de CO; il s'agit donc d'un processus de Désorption Induite par Transition Electronique (DIET, voir chapitre 3). En utilisant des couches de glaces marquées grâce aux isotopologues $^{12}\text{CO}/^{13}\text{CO}$ et en se servant de la différence de fréquences propres des niveaux vibrationnels du premier état excité de ces deux molécules, il est possible de comprendre comme jamais auparavant le mécanisme de photodésorption dans ce domaine de longueur d'onde. Il a ainsi été montré que c'est l'excitation électronique des molécules en sous-couches qui induit de manière indirecte la désorption des molécules de surface

(voir chapitre 4). La photodésorption de N_2 , très efficace au dessus de 12 eV, se produit de façon analogue à celle démontrée pour CO aux énergies inférieures à 10 eV. Dans le cas de O_2 , l'irradiation VUV provoque la dissociation des molécules, ce qui complique le mécanisme de photodésorption puisque les atomes d'oxygène peuvent éjecter d'autres molécules de la glace, se recombiner, ou induire de la chimie (chapitre 5).

La photodésorption de molécules dans cette gamme d'énergie a été étudié dans le cas de deux espèces chimiques mélangées : CO et N_2 . Comprendre le processus de photodésorption pour des mélanges de glace est nécessaire puisque la plupart des glaces interstellaires ne sont pas pures. Les glaces de CO et N_2 ont des spectres d'absorption très distincts. Cependant, en présence d'un mélange de CO : N_2 (1 : 1), les spectres de photodésorption de ces deux espèces sont identiques. Ces profils comparables viennent de l'excitation électronique d'un type de molécule et de la redistribution de l'énergie à toutes les molécules voisines, indépendamment de leur nature (voir chapitre 6). Ces observations ont d'importantes conséquences astrophysiques puisque les taux de photodésorption ne sont pas seulement dus à la nature de l'espèce chimique qui absorbe le rayonnement, mais également à celle de son environnement. La nature du transfert énergétique reste encore une question ouverte mais devrait trouver une réponse prochainement grâce à l'analyse par spectroscopie laser des molécules photodésorbées ainsi que par l'étude de la lumière émise (fluorescence) au cours de l'irradiation. Les expériences de photodésorption devront aussi être étendues à des molécules organiques plus complexes. La photodésorption de ces molécules est encore méconnue étant donné le rôle complexe que jouent les radicaux formés pendant l'irradiation VUV, mais sa quantification expérimentale ainsi que son observation dans le milieu interstellaire constituent un outil formidable pour sonder la complexité chimique des glaces interstellaires.

Curriculum vitae

I was born on the 9th of July 1986 in Clermont-Ferrand, France. I grew up with my parents at the foot of the massif central mountains in Royat, a small town renowned for its roman spa. After receiving my middle school certificate from Collège Theillard de Chardin (Chamalières) and discovering a passion for physics and chemistry, I obtained a high school degree in science from Lycée Polyvant de Chamalières. Following advice from school teachers, I applied successfully for a 2-year post-high school selective training in Physics and Chemistry (Classe préparatoire pour les Grandes Ecoles section Physique Chimie) at Lycée Blaise Pascal de Clermont-Ferrand in order to prepare for the famous French Grandes Ecoles. I moved in with my grandfather who took great care of me and I owe him my success in this highly competitive program. I was accepted into the joint physical chemistry program of Université Paris-Sud and Ecole Normale Supérieure de Cachan as a university student to get a magister degree in molecular physical chemistry ; a combined bachelor and master degree with additional courses. The stimulating multidisciplinary research performed here inspired me to exchange my carrier choice as a teacher for the exciting world of research. Astrochemistry came up as the natural field of study for me as it ties together my fascination for interstellar space and my chemical physics background. I left France for the first time to perform my master internship at the Sackler Laboratory for Astrophysics, Leiden Observatory in April 2008. This life changing experience exposed me to new scientific approaches, cultures and personal challenges. I greatly enjoyed this international experience and accepted a PhD position at the same institute in the group of Prof. Harold Linnartz starting August 2009. I carried out my research at the Sackler Laboratory for Astrophysics in Leiden, in the group of Prof. Jean-Hugues Fillion and with Dr. Mathieu Bertin at Université Pierre et Marie Curie in Paris, and with Dr. Karin Öberg in Cambridge, MA and Charlottesville, VA. Over the last four years, I have presented my PhD research at various national and international meetings in Kerkrade (NL), Glasgow (UK), Gothenburg (Sweden), Groningen (NL), Grenoble (France), Toledo (Spain), Paris (France), Leiden (NL) and at several institutes in Paris (France), Cambridge (USA), Charlottesville (USA), Münster (Germany), Milton Keynes (UK), Pasadena (USA), Mountain View (USA), Stanford (USA), and Berkeley (USA). After the defense of this thesis, I will continue to pursue my research in astrochemistry as a postdoctoral scholar at the Harvard Smithsonian Center for Astrophysics in Cambridge, Massachusetts.

Publications

Peer-reviewed articles

E. C. Fayolle, K. I. Öberg, S. E. Bisschop, R. T. Garrod, E. F. van Dishoeck, "Organic molecules around high-mass protostars : linking gas observations to the initial ice content", in preparation

M. Bertin, **E. C. Fayolle**, C. Romanzin, H. A. M. Poderoso, X. Michaut, L. Philippe, P. Jeseck, K. I. Öberg, H. Linnartz, J.-H. Fillion, "Indirect UV photodesorption from CO :N₂ binary ices - an efficient grain-gas process", submitted to The Astrophysical Journal

E. C. Fayolle, M. Bertin, C. Romanzin, H. A. M. Poderoso, L. Philippe, X. Michaut, P. Jeseck, H. Linnartz, K. I. Öberg, J.-H. Fillion, "Wavelength-dependent UV photodesorption of pure N₂ and O₂ ices", *Astronomy and Astrophysics*, 556, A122, 2013

K. I. Öberg, M. Dufie Boamah, **E. C. Fayolle**, R. T. Garrod, C. Cyganowski, F. van der Tak, The Spatial Distribution of Organics toward the High-Mass YSO NGC 7538 IRS9, *The Astrophysical Journal*, 771, 95, 2013

M. Bertin, **E. C. Fayolle**, C. Romanzin, K. I. Öberg, X. Michaut, A. Moudens, L. Philippe, P. Jeseck, H. Linnartz, J.-H. Fillion, "UV photodesorption of interstellar CO ice analogues : from subsurface excitation to surface desorption", *Physical Chemistry Chemical Physics*, 14, 9929, 2012

E. C. Fayolle, M. Bertin, C. Romanzin, X. Michaut, K. I. Öberg, H. Linnartz, J.-H. Fillion, "CO Ice Photodesorption : A Wavelength-dependent Study", *The Astrophysical Journal Letters*, 739, L36, 2011

E. C. Fayolle, K. I. Öberg, H. M. Cuppen, R. Visser, H. Linnartz, "Laboratory H₂O :CO₂ ice desorption data : entrapment dependencies and its parameterization with an extended three-phase model", *Astronomy and Astrophysics*, 529, A74, 2011

K. I. Öberg, **E. C. Fayolle**, H. M. Cuppen, E. F. van Dishoeck, H. Linnartz, "Quantification of segregation dynamics in ice mixtures", *Astronomy and Astrophysics*, 505, 183-194, 2009

Proceedings

E.C. Fayolle, K.I. Öberg, H.M. Cuppen, R. Visser, H. Linnartz,
"Laboratory H₂O :CO₂ ice desorption data : entrapment dependencies and its parameterization with an extended three-phase model", in *Proceedings* EAS Publications Series, 58, 327-331 2012

H. Linnartz, J.-B. Bossa, J. Bouwman, H. M. Cuppen, S. H. Cuyllé, E. F. van Dishoeck, E. C. Fayolle, G. Fedoseev, G. W. Fuchs, S. Ioppolo, K. Isokoski, T. Lamberts, K.I. Öberg, C. Romanzin, E. Tenenbaum, J. Zhen, "Solid State Pathways towards Molecular Complexity in Space", in *Proceedings* of IAU Symposium, vol. 280 of IAU Symposium, pp. 390-404, Dec. 2011.

Acknowledgments

The data, results and ideas presented here are the outcome of work performed by many people. Moreover I enjoyed the support and help of colleagues, friends, and family. Here I acknowledge all of these people and hope the list below is as complete as possible.

My thanks go out to the people I met and had the chance to work with at the Sackler Laboratory for Astrophysics. Jordy, Lou, you have been the first people who made me feel welcome in the lab five years ago. Thank you for showing me how much fun laboratory astrophysics can be. Martijn, thank you for being such a super-hero; each time something goes wrong in the lab, you're always there to pick up the pieces. Claire, Sergio, Gleb, Thanja, you have built such an impressive and innovative machine gun to tackle these atom addition reactions, I really look up to you. Herma, many thanks for giving me this invaluable understanding of the big picture regarding astrochemistry. Jean-Baptiste, it was fantastic to have someone to talk so openly about science and other subjects. You're a terrific labmate! Anton, your hilarious and somehow disarming sense of humor brought a refreshing feeling to the group. Daniel P., thanks for coming back to the lab, you are such a talented scientist. Niels, I wish you all the best for your PhD and I have no doubts you will do wonders. Steven, Karoliina, Nadine Joseph, Dongfeng, Junfeng, Emily, your help and discussions were very much appreciated and helped me to develop as an experimentalist.

Dear Lars, having 'le grand Danois' with me for the first time I stayed in a foreign country has been such a blessing. I can't wait to be reunited and continue celebrating our anniversaries. De Ruud die ik ken is een echte Nederlander. Hij drinkt heel veel melk en heeft een Noord-Afrikaans accent als hij Frans spreekt. Nienke, you have been my officemate all along. Our chats, trips and nights out brought so much fun to my life here in Leiden. Daniel H., I thank you for all the laughs we shared at the office late at night and for our friendly/crazy discussions. You are, wait for it, legendary! Pam, you're such an incredible, fearless woman. You are a role model for us, lady astronomers. Joe, your British sense of humor and kindness are bringing so much to the astrochem group, many thanks for that. Stephanie Cazaux, Elisabetta M., Dave, Kalle, Umut, Geoff, Catherine, Xiaohu, Alan, Markus, Irene, Magnus, Christian, Jeanette, Mihkel, Carina, Olivier, thank you for the astrochem chats and coffee breaks!

My acknowledgments go out to the staff and support staff at the sterrewacht for their invaluable computational and organizational support and to the university fine

mechanical and electronic workshop and the glassblowing team at the Leidse Instrumentmakers School for their technical support. My deepest acknowledgments go out to Prof. John Yates, Dr. Emmanuel Dartois, Prof. Xander Tielens and Prof. Röttgering for reading this thesis and allowing me to defend it. Life as a scientist is pretty frenetic so thank you for taking the time to promote the work of a junior researcher. Many thanks to my officemates Dominik, Simon, Nienke, Marinus, Remko, Jan and Frank for supporting my craziness, my terribly annoying voice, and for sharing some good laughs. Shannon, Isa, Roderik, Ben, Lisa, Simone, Christian, Adam, Suzanne, Rob, Renske, Jayne, Freeke, Remco, Margaret, Pink E., Elisabetta S., thank you for all the good nights out we shared in Leiden, Den Haag, and Amsterdam. You made my life in the Netherlands be so funky!

Most of my thesis work has been performed at the SOLEIL synchrotron through a very fruitful collaboration with the Laboratoire de Physique Moléculaire pour l'Atmosphère et l'Astrophysique (LPMAA) at Université Pierre et Marie Curie in Paris. Mathieu, Claire, Xavier, Chef, we started this amazing adventure together and I could never thank you enough for the beautiful and elegant science that came out of it. Dear Mathieu, you have been essential to the success of this thesis. Your name would have deserved to be on page 4 of this booklet, next to the 3 other key people. Dr. Xavier, mille mercis pour ton humour grinçant et ta rigueur scientifique. Laurent, Pascal, Mishal, Hugo, Audrey, Aline, Jozef, your help has been crucial to this whole enterprise and I thank you for staying all night long or coming early to take over the morning shifts! Many thanks to Laurent Nahon, head of the DESIRS beamline at SOLEIL, Nelson, Gustavo, Jean-Francois, Barbara and Marcel, for letting us use their cutting edge technology and helping us along the way. I deeply acknowledge the technical support at SOLEIL and special thanks to the amazing cooks who made these week-ends, holidays, birthdays spent there a fun time!

I visited multiple times the LPMAA in Paris and I acknowledge Marie-Lise Dubernet for welcoming me into her laboratory. The homy feeling I got there, I owe it to Salem, Patrick, Corinne, Michele, Christiane, Yao, Christian, and Pascal.

Isa, Claire, you can't imagine how lucky I feel to have you as friends. You welcomed me to your homes, helped me with work when things became hectic and had the patience to accompany me through my very emotional approach to life. Thank you Claire for your discrete but efficient guidance during these last five years. Isa, I would never have dreamed of such a wonderful, supportive BFF. It will be a true honor to have you by my side to defend this thesis.

My parents and grandparents supported me in every enterprise I undertook, regardless of what life and career choices I made. This unconditional love is the foundation of who I am today and I couldn't have imagined more beautiful gifts from them. Papa, maman, pépé, votre soutien inconditionnel dans tous les choix qui m'ont menés jusqu'ici est pour moi la plus belle preuve d'amour qu'il soit. Merci d'avoir fait de moi une personne généreuse qui partage autour d'elle tous les bonheurs qu'elle a reçus.

I shared these last couple of years with an amazing human being who made me believe in myself, supported me during the difficult times, and pushed me to be a better person. Thank you, my pink elephant, for making my life such an amazing story.